

ISSN 2071-4726
2071-0305

Magazine of Civil Engineering

95(3), 2020





ПОЛИТЕХ
Санкт-Петербургский
политехнический университет
Петра Великого

Инженерно-строительный институт
Центр дополнительных профессиональных программ
195251, г. Санкт-Петербург, Политехническая ул., 29,
тел/факс: 552-94-60, www.stroikursi.spbstu.ru,
stroikursi@mail.ru

**Приглашает специалистов организаций, вступающих в СРО,
на курсы повышения квалификации (72 часа)**

Код	Наименование программы	Виды работ*
Курсы по строительству		
БС-01-04	«Безопасность и качество выполнения общестроительных работ»	п.1,2, 3, 5, 6, 7, 9, 10, 11, 12, 13, 14
БС-01	«Безопасность и качество выполнения геодезических, подготовительных и земляных работ, устройства оснований и фундаментов»	1,2,3,5
БС-02	«Безопасность и качество возведения бетонных и железобетонных конструкций»	6,7
БС-03	«Безопасность и качество возведения металлических, каменных и деревянных конструкций»	9,10,11
БС-04	«Безопасность и качество выполнения фасадных работ, устройства кровель, защиты строительных конструкций, трубопроводов и оборудования»	12,13,14
БС-05	«Безопасность и качество устройства инженерных сетей и систем»	15,16,17,18,19
БС-06	«Безопасность и качество устройства электрических сетей и линий связи»	20,21
БС-08	«Безопасность и качество выполнения монтажных и пусконаладочных работ»	23,24
БС-12	«Безопасность и качество устройства мостов, эстакад и путепроводов»	29
БС-13	«Безопасность и качество выполнения гидротехнических, водолазных работ»	30
БС-14	«Безопасность и качество устройства промышленных печей и дымовых труб»	31
БС-15	«Осуществление строительного контроля»	32
БС-16	«Организация строительства, реконструкции и капитального ремонта. Выполнение функций технического заказчика и генерального подрядчика»	33
Курсы по проектированию		
БП-01	«Разработка схемы планировочной организации земельного участка, архитектурных решений, мероприятий по обеспечению доступа маломобильных групп населения»	1,2,11
БП-02	«Разработка конструктивных и объемно-планировочных решений зданий и сооружений»	3
БП-03	«Проектирование внутренних сетей инженерно-технического обеспечения»	4
БП-04	«Проектирование наружных сетей инженерно-технического обеспечения»	5
БП-05	«Разработка технологических решений при проектировании зданий и сооружений»	6
БП-06	«Разработка специальных разделов проектной документации»	7
БП-07	«Разработка проектов организации строительства»	8
БП-08	«Проектные решения по охране окружающей среды»	9
БП-09	«Проектные решения по обеспечению пожарной безопасности»	10
БП-10	«Обследование строительных конструкций и грунтов основания зданий и сооружений»	12
БП-11	«Организация проектных работ. Выполнение функций генерального проектировщика»	13
Э-01	«Проведение энергетических обследований с целью повышения энергетической эффективности и энергосбережения»	
Курсы по инженерным изысканиям		
И-01	«Инженерно-геодезические изыскания в строительстве»	1
И-02	«Инженерно-геологические изыскания в строительстве»	2,5
И-03	«Инженерно-гидрометеорологические изыскания в строительстве»	3
И-04	«Инженерно-экологические изыскания в строительстве»	4
И-05	«Организация работ по инженерным изысканиям»	7

*(согласно приказам Минрегионразвития РФ N 624 от 30 декабря 2009 г.)

**По окончании курса слушателю выдается удостоверение о краткосрочном повышении
квалификации установленного образца (72 ак. часа)**

Для регистрации на курс необходимо выслать заявку на участие, и копию диплома об образовании по телефону/факсу: 8(812) 552-94-60, 535-79-92, , e-mail: stroikursi@mail.ru.

Magazine of Civil Engineering

SCHOLAR JOURNAL

ISSN 2071-0305

Свидетельство о государственной регистрации:
Эл № ФС77-77906 от 19.02.2020,
выдано Роскомнадзором

Специализированный научный журнал. Выходит с
09.2008.

Включен в Перечень ВАК РФ

Индексируется в БД Scopus

Периодичность: 8 раз в год

Учредитель и издатель:

Санкт-Петербургский политехнический университет
Петра Великого

Адрес редакции:

195251, СПб, ул. Политехническая, д. 29

Главный редактор:

Екатерина Александровна Линник

Научный редактор:

Николай Иванович Ватин

Выпускающий редактор:

Анастасия Крупина

Редакционная коллегия:

д.ф.-м.н., доцент Р.А. Абдикаримов;
д.т.н., проф. В.В. Бабков;
к.т.н., проф. А.И. Боровков;
д.т.н., проф. А. Бородинец;
д.т.н., проф. Н.И. Ватин;
PhD, проф. М. Вельжкович;
к.т.н., М.Р. Гарифуллин;
д.т.н., проф. Э.К. Завадскас;
д.ф.-м.н., проф. М.Н. Кирсанов;
D.Sc., проф. М. Кнежевич;
д.т.н., проф. В.В. Лалин;
д.т.н., проф. Б.Е. Мельников;
д.т.н., академик М.М. Мирсаидов;
д.т.н., проф. Р.Б. Орлович;
Dr. Sc. Ing., professor Л. Пакрастиньш;
Dr.-Ing. Habil., professor X. Пастернак;
д.т.н., проф. А.В. Перельмутер;
д.т.н., проф. М.Р. Петриченко;
д.т.н., проф. В.В. Сергеев;
д.ф.-м.н., проф. М.Х. Стрелец;
д.т.н., проф. О.В. Тараканов;
д.т.н., проф. Б.Б. Телтаев;
д.т.н., проф. В.И. Травуш;
д.т.н., проф. Д. Унгерман;
д.т.н., проф. С.В. Федосов

Magazine of Civil Engineering

SCHOLAR JOURNAL

ISSN 2071-0305

Peer-reviewed scientific journal

Start date: 2008/09

8 issues per year

Publisher:

Peter the Great St. Petersburg Polytechnic University

Indexing:

Scopus, Russian Science Citation Index (WoS),
Compendex, EBSCO, Google Academia, Index
Copernicus, ProQuest, Ulrich's Serials Analysis System,
CNKI

Corresponding address:

29 Polytechnicheskaya st., Saint-Petersburg, 195251,
Russia

Editor-in-chief:

Ekaterina A. Linnik

Science editor:

Nikolay I. Vatin

Technical editor:

Anastasia Krupina

Editorial board:

R.A. Abdikarimov, D.Sc., associate professor
V.V. Babkov, D.Sc., professor
A.I. Borovkov, PhD, professor
A. Borodinecs, Dr.Sc.Eng., professor
M. Veljkovic, PhD, professor
M. Garifullin, PhD, postdoctorant
E.K. Zavadskas, D.Sc., professor
M.N. Kirsanov, D.Sc., professor
M. Knezevic, D.Sc., professor
V.V. Lalin, D.Sc., professor
B.E. Melnikov, D.Sc., professor
M.M. Mirsaidov, D.Sc., professor
R.B. Orlovich, D.Sc., professor
L. Pakrastinsh, Dr.Sc.Eng., professor
H. Pasternak, Dr.-Ing.habil., professor
A.V. Perelmuter, D.Sc., professor
M.R. Petrichenko, D.Sc., professor
V.V. Sergeev, D.Sc., professor
M.Kh. Strelets, D.Sc., professor
O.V. Tarakanov, D.Sc., professor
B.B. Teltayev, D.Sc., professor
V.I. Travush, D.Sc., professor
S.V. Fedosov, D.Sc., professor

Дата выхода: 19.05.2020

Date of issue: 19.05.2020

© Peter the Great St. Petersburg Polytechnic University.
All rights reserved.

© Coverpicture – Ilya Smagin

© ФГАОУ ВО СПбПУ, 2020

© Иллюстрация на обложке: Илья Смагин

Contacts:

E-mail: mce@spbstu.ru

Web: <http://www.engstroy.spbstu.ru>

Contents

Ebadi, P., Farajloomanesh, S. Seismic design philosophy of special steel plate shear walls 1	3
Gravit, M.V., Serdjuks, D., Vatin, N., Lazarev, Y.G., Yuminova, M.O. Single burning item test for timber with fire protection	19
Kiss, L.P. Stability of fixed-fixed shallow arches under arbitrary radial and vertical forces	31
Travush, V.I., Karpenko, N.I., Erofeev, V.T., Vatin, N., Erofeeva, I.V., Maksimova, I.N., Kondrashchenko, V.I., Kesarijskij, A.G. Destruction of powder-activated concrete with fixation of destruction by a laser interferometer	42
Kolesnikov, A.O., Kostiuk, T.N., Popov, V.N. Attenuation of the soil vibration amplitude at pile driving	49
Rusanov, A.E., Baiburin, A. Kh., Baiburin, D.A., Bianco, V. Heat loss from defects of hinged facade systems of buildings	57
Zolina, T.V., Sadchikov, P.N. Loads for the design of the industrial building frame	66
Polyankin, A.G., Korolev, K.V., Kuznetsov, A.O. Analysis of reinforced soil sustainability while tunnel construction	80
Tyukalov, Yu.Ya. Method of plates stability analysis based on the moments approximations	90
Usanova, K., Barabanshchikov, Yu.G. Cold-bonded fly ash aggregate concrete	104
Maltseva, T.V., Trefilina, E.R., Saltanova, T.V. Deformed state of the bases buildings and structures from weak viscoelastic soils	119
Pavlov, M.V., Karpov, D.F., Sinitsyn, A.A., Gudkov, A.G. Winter greenhouse combined heating system	131



DOI: 10.18720/MCE.95.1

Seismic design philosophy of special steel plate shear walls

P. Ebadi*, S. Farajloomanesh

Department of Civil Engineering, Shahr-e-Qods Branch, Islamic Azad University, Tehran, Iran

* E-mail: parviz.ebadi@gmail.com

Keywords: seismic, steel plate shear wall, capacity design, optimization, ductility

Abstract. Steel plate shear walls are usually designed by devoting total story shear to plates and designing peripheral frames for total transferred forces from the plates to the peripheral frames. Therefore, the participation of frames in the story shear neglected conservatively. In this research, a design methodology is presented based on the real sharing of steel walls and peripheral frames in story shear. Steel walls are designed using Plate-Frame Interaction (PFI) theory for different percentages of story shear and their seismic parameters compared together by numerical modeling in nonlinear analysis software. The obtained results indicated that using the conventional design methods, devoting total story shear to the steel walls and neglecting the shear capacity of the peripheral frame could lead to the over-designed (conservative) sections. In contrast, if the seismic design of this system was performed considering the sum of the capacity of steel plate and peripheral frame and their real sharing in story shear, the system design would be efficient and economical.

1. Introduction

Numerous studies have been conducted on Steel Plate Shear Walls (SPSW) in recent years. Roberts and Sabouri-Ghomi [1] tested 16 steel shear panels at the University of Wales and showed that all the panels had sufficient ductility during large inelastic cycles. The Plate-Frame Interaction (PFI) theory introduced for analyzing SPSW with and without stiffener and opening [1, 2]. In this theory, the behavior of the frame and plate are investigated independently and their interactions are taken into consideration. Gholhaki [3] tested two specimens of SPSW with hinge and rigid connections for end of beams and found that the effect of the beam-column connection type on the initial stiffness of the walls could be ignored. But, the strength of the specimen with rigid connection was higher than that of the hinge one by almost 26 percent. Furthermore, the energy absorption capacity of the specimen with rigid connection was higher than that of the specimen with hinge connection. Moreover, the effect of the beam-column connection on the angle of the diagonal tension field was insignificant. Darvishi et al. [4] tested three models with the panel width-to-height ratio of smaller than 1, equal to 1, and higher than 1 and concluded that, in the first case, the increased stiffness of the column increased the ductility of the overall structure as well as the over-strength factor. In the second case, had no significant effect, while in the third case, reduced ductility and over-strength factor. Based on the studies conducted by Alinia and Dastfan [5–7] on SPSW, it can be concluded that high energy absorption of the steel shear wall system depends on the stiffness of the boundary elements. Several laboratory studies were conducted at the laboratory of Assessment and Planning Center of Construction and Transportation Industry in South Korea in order to investigate the bearing capacity variations of the shear walls made of steel plates with various construction details [8]. Kharrazi et al. [9] proposed the Modified Plate-Frame Interaction (M-PFI) theory, in which the effect of -bending on the SPSW system response was taken into account in the load-displacement diagram. Chen and Jhang [10] examined the effect of using steel with Low Yield Point (LYP) on designing steel shear walls and demonstrated that limiting the plate's width-to-thickness ratio to below 80 would improve the wall's performance. In addition, the use of beam-column moment connection, instead of shear connection, would increase the system's strength and energy dissipation capacity by 28 % and 18 %, respectively. Hosseinzadeh and Tehranizadeh [11] studied SPSW with different stories and width-to-height ratios. They concluded that the plate yield in the panels with a smaller number of stories would occur greatly earlier than the peripheral frame, while in the case of more number of stories, the full yield of plates would be

Ebadi, P., Farajloomanesh, S. Seismic design philosophy of special steel plate shear walls. Magazine of Civil Engineering. 2020. 95(3). Pp. 3–18. DOI: 10.18720/MCE.95.1



This work is licensed under a [CC BY-NC 4.0](https://creativecommons.org/licenses/by-nc/4.0/)

postponed. Furthermore, since the steel walls could only work in tension, not compression, the axial tensile forces in the columns would be less than their axial compressive forces. Moradinejad et al. [12] investigated the effect of the location of the SPSW on progressive collapse. The results of the nonlinear static analyses showed that the location of SPSW at the corner of the plan improved the structure's behavior against the progressive collapse. Ebadi et al. [13, 14] examined the effect of the steel wall contribution to the lateral load transfer and represented that the more the plate's contribution to the lateral load, the more the thickness of the plate and the more non-economic and conservative design of the structure would be. Purba and Bruneau [15] tested a 1/3-scale model of three-story SPSW specimen and suggested that development of in-span hinges should be explicitly avoided in the design of Horizontal Boundary Elements (HBE) and mentioned that, in some instances, the ordinary-type connection specified by the code to be used in SPSWs might not be sufficient to sustain large rotation demand that could occur in the connections. Moghimi and Driver [16] studied performance of SPSW under accidental blast loads and found that despite the inherent slenderness of the steel members, the SPSW system would be an effective potential protective structure in industrial plants. The side wall subjected to in-plane blast load is a strong and reliable system, and the front wall subjected to out-of-plane blast load can be sized to provide acceptable design for industrial plant applications. Guo et al. [17] studied the influence of hinged, rigid and semi-rigid beam-column connection types on the behavior of SPSW structures. They concluded that the semi-rigid composite frame with SPSW is an effective lateral load resisting system. So that, the semi-rigid frame and the shear wall work together to satisfy higher safety margins.

Du et al [18] made Pseudo-static test on SPSW specimen and studied method of anchoring stiffeners to the steel plate to reinforce the structure.

Wang et al [19] observed that the lateral stiffness and bearing capacity of horizontal corrugated SPSWs are higher than those of vertical corrugated SPSWs, in contrast to the case of corrugated steel plate reinforced concrete composite shear walls.

Jalali and Darvishan [20] enhanced modelling of self-centering steel plate shear walls. They used a set of 44 earthquake ground motions by comparative nonlinear response history analyses.

Yu et al [21] investigated SPSWs with different types of stiffener and found that the performance of SPSWs enhanced by using multiple ribs and precast concrete panel. In addition, out-of-plane deformation of plate decreased by increasing restraining stiffness.

Pachideh et al [22] analyzed 27 frames, including 18 frames with thin steel plate shear walls, as lateral load resisting system along with 9 special moment-resisting frames with three different heights in short, intermediate and tall configurations. The observations demonstrated that the damage index for SPSW in taller frames led to better results and higher safety compared to other frames.

Hajimirsadeghi et al [23] conducted a full scale cyclic experiment on an enhanced modular shear wall SPSW and continued up to fail. Test results revealed high initial stiffness, excellent ductility, and significant energy dissipation capacity of the system.

Mu and Yang [24] proposed SPSWs with oblique channel-shaped stiffeners. They studied Seismic behaviors of obliquely stiffened SPSWs with openings. They observed that the multi-oblique stiffening form could effectively improve the buckling load of plates and delay the formation of tension field.

In Seismic Provisions for Structural Steel Buildings [25] and Steel Plate Shear Wall Design Guide [26], the design of the beams and columns depends on tension field forces resulted from the plates. In other words, the increased thickness of the steel plate would lead to the increased transitional force caused by the plate's tension field on the wall's boundary elements, resulting in the increased size of the columns. In the conventional design methods for steel walls, the steel plate is designed for the total story shear and the effect of the frame on the story shear is ignored, while the peripheral frame can transfer a considerable lateral force. Thus, it is expected that assigning total story shear to the plate would increase the thickness of the plate, imposes additional forces to the beams and columns, and finally, leads to the over-designed (conservative) sections of the beams and columns.

In this paper, in order to evaluate the lateral load bearing capacity of stories in conventional design methods, a 10-story steel building designed. Then, the sketched PFI diagrams for different stories indicated much higher capacity of each story relative to the required story shear. Afterwards, a repetitive trial-and-error design philosophy was proposed by precisely determining the contribution of the steel plate and its' peripheral frame to the total story shear of SPSW. At the next stage, in order to examine the effect of the contribution of the wall and frame to the story shear, the steel walls and peripheral frames re-designed for 75 % and 50 % of the demand story shear. Therefore, the transferred tension field forces from the steel wall to peripheral frame decreased. At the final stage and according to the proposed design method, the actual contribution of the steel walls to the story shear was calculated and the optimal design contributions was presented. PFI diagrams sketched for all the specimens and the seismic parameters of the frames, including ductility, response modification factor, over-strength factor, and energy absorption capacity were calculated.

2. Methods

2.1. Plate-Frame Interaction (PFI) theory

The PFI theory is one of the most powerful tools for calculating the capacity of SPSW. Thus, it was used to evaluate the capacity of the studied frames. In PFI theory, the capacity diagrams of the frame and plate are evaluated separately, and the capacity of SPSW is calculated by summing up the capacity diagrams of the plate and frame. PFI parameters for the frame are defined in Fig. 1.

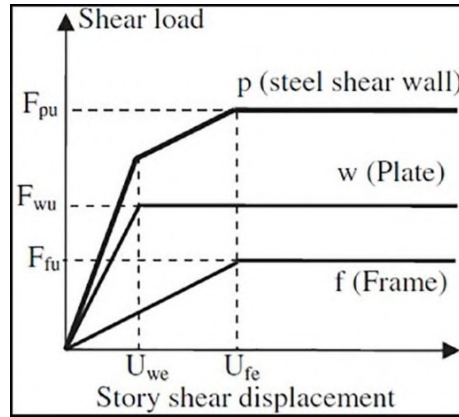


Figure 1. PFI parameters [1].

Where F_{wu} is the ultimate shear strength of plate, U_{we} is the shear yield displacement of the plate, F_{fu} is the ultimate shear strength of the frame, and U_{fe} is shear yield displacement of the frame, calculated using Eq (1–4).

$$F_{wu} = b.t \left(\tau_{cr} + 0.5\sigma_y \sin 2\theta \right) \quad (1)$$

$$U_{we} = \frac{2\sigma_y}{E \sin 2\theta} d \quad (2)$$

$$F_{fu} = \frac{4M_{fp}}{d} \quad (3)$$

$$U_{fe} = \frac{M_{fp} d^2}{6EI_f} \quad (4)$$

Where b and d indicate the panel's width and height, respectively, t is the plate's thickness, E is the steel plate modulus of elasticity, σ_y is the uniaxial yield stress of the steel plate, τ_{cr} is the plate's critical shear stress, and θ is the angle of tension field inclined respect to the horizontal line, M_{fp} is the plastic moment of columns, I_f is the moment of inertia of columns, F_{fu} and F_{wu} are shear capacity of peripheral frame and steel plate, respectively, and U_{wf} and U_{we} are lateral yield displacement of peripheral frame and steel plate, respectively.

The system's total capacity (F_{pu}) is calculated by Eq (5).

$$F_{pu} = F_{fu} + F_{wu} \quad (5)$$

2.2. Optimal design of SPSW

In the conventional design method of SPSWs, total story shear is allocated in the wall. Therefore, the peripheral frame's contribution to the story shear is neglected conservatively.

However, in the optimal design of the SPSW, which was investigated in this paper, the lateral load capacity of the peripheral frame is also considered. In other words, the trial-and-error method implemented to determine the actual contribution of the steel wall and peripheral frame in the story shear. It should be noted that the contribution of steel wall and frame is not constant on all the stories. Accordingly, since the dimensions of the lower columns

depend on the thickness of the steel wall in the upper stories, it is necessary to start the optimization from the highest stories and, eventually, end it on the ground story.

According to Clause-17.2 of AISC341 [25], the nominal shear strength for the SPSW is calculated by Eq (6).

$$V_n = \phi \times 0.42 \times F_y \times L_{cf} \times t_w \times \sin 2\alpha \quad (6)$$

Where ϕ is the strength reduction factor and is equal to 0.9, F_y , L_{cf} , t_w , and α indicate specified minimum yield-stress of steel, clear distance between columns, steel wall thickness, and angle formed by tension field on the vertical wall, respectively.

According to PFI equations, the shear strength and displacement corresponding to the plate, frame, and panel are obtained by Eq (1–4).

AISC has considered the ratio of the expected tensile strength to the specified minimum tensile strength ($R_t = 1.2$) in Eq (6); in other words, being divided by 1.2. Therefore, the coefficient of 0.5 in Eq (1) from PFI theory has been changed to 0.42 in Eq (6) from AISC341 ($0.5/1.2 = 0.42$). Furthermore, the plate's critical shear stress (τ_{cr}) is insignificant in Eq (1), which has been neglected in AISC equations. Thus, if Eq (1) is multiplied by $(\phi/1.2) = (0.9/1.2) = 0.75$ and also $\tau_{cr} = 0$ is taken into account, Eq (1) and (6) will be equivalent.

Since the AISC load method and ultimate strength have been used in designing the wall, it is necessary to apply the following changes for drawing the PFI diagrams:

$$\frac{0.9}{1.2} (PFI) \approx V_{demand} \quad (7)$$

Where V_{demand} is the design base shear from building code. In other words, Eq (7) can be rewritten as follows:

$$F_{pu} = F_{wu} + F_{fu} = 1.33 \times V_{demand} \quad (8)$$

Thus, in order to use PFI in design, demand shear (V_{demand}) should be multiplied by 1.33 and the steel wall and frame must be designed such that their total capacity exceeds the required base shear of the story by 1.33 times.

The process of the optimal design of the SPSW is as follows:

1. Optimization is started from the highest story and ends on the ground story.
2. Assumption of the certain percentage of the plate and frame sharing on each story shear is considered.
3. Thickness of the steel wall is determined by Equations (6), (7), and (8).
4. The maximum force transferred from the steel wall to the peripheral frame is determined and combined with gravitational loads.
5. Frames are designed for the applied loads in Step 4.
6. The capacity of the frame and wall is calculated and compared with the story's required base shear.
7. If the calculated capacity in Step 6 is higher than the story's required capacity, the wall thickness must be reduced and steps 2–6 must be repeated; however, if the capacity is less, thickness of the wall must be increased and the aforementioned steps must be repeated.
8. After optimizing the story, the optimization process is carried out for the lower stories, respectively. It should be noticed that the forces of the upper stories are transferred to the lower stories after optimization.

2.3. Design of frames

The studied building was a 10-story residential building with local soil type 3 (shear wave velocity of 175–375 m/s), story height of 3 meters and located in a high seismic hazard zone. Plans of the stories are shown in Fig. 2 and the steel walls were located around the plan. By assuming the uniform lateral load distribution according to the structure's weight on each wall, only a part of the structure plan with the affected weight for design of one of the walls is shown in Fig. 2.

The materials of the SPSW were of the S235J type with the minimum yield strength of 235 MPa and materials of the beams and columns were of the S350J type with the minimum yield strength of 350 MPa. Dead load of the stories and roof, live load of the stories, and live load of the roof were equal to 5, 2, and 1.5 kN/m², respectively. Structural response modification factor was considered equal to 7 in accordance with Minimum Design Loads for Buildings and Other Structures (ASCE7-10) [27]. Cross-section of the columns was considered as a hollow square section; besides, to ensure the plastic hinge in the beams (strong column-weak beam principle), the beam-column connection of RBS¹ type was used. The SPSW was designed based on the requirements of Seismic Provisions for Structural Steel Buildings (AISC 341) [25] and AISC Design Guide 20 [26] using Load and Resistance Factor Design (LRFD) method.

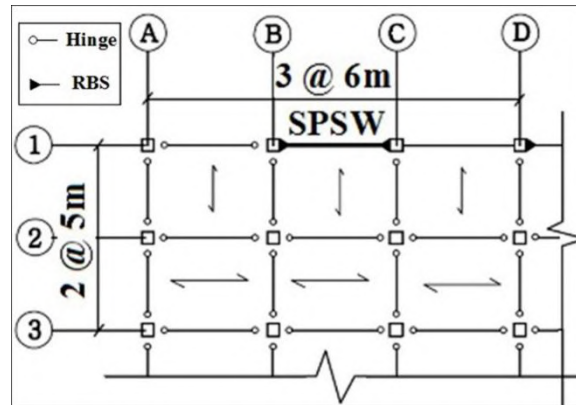


Figure 2. Plan of buildings.

The studied frames were named as SPSW-xx, where xx indicate the portion of the total shear load of the story (in percent), which was used for the wall design and was selected equal to 50, 75, and 100 percent. The optimal design was also shown by "opt" symbol. Furthermore, in order to prevent increased seismic demand of the system, the computational thickness was used for the steel walls.

In Table 1, the wall's contribution to the lateral load transfer is specified for four studied specimens on various stories. It can be seen that in the optimal design, the plate's contribution to the system shear strength was much less than the conventional design method, which is on average about 33 % (instead of 100 %). In addition, on the highest story, the contribution of the plate was reduced compared to other stories, which was due to using larger dimensions for columns because of executive problems. According to Table 1, by reducing the plate's contribution to the story shear, the thickness of the plate and dimensions of the boundary elements reduced. As will be discussed in the following sections, the system's capacity in specimens SPSW-100, SPSW-75, and SPSW-50 was still higher than the story shear, while in the optimal frame, the capacity of the system became equal to the structural story shear demand.

In Table 2, the designed sections of the frame on axis 1 between axes B and C are shown (see Fig. 2). The designed sections were named based on the nominal dimensions and the thicknesses of the sections. For instance, in the third column of this Table, B360x25 refers to the Hollow Square Section (HSS) with outside dimension of 360 mm and thickness of 25 mm. In addition, in the fourth column, b600x-310x-25x-12 indicates the plate girder with the height of 600 mm, flange width of 310 mm, flange thickness of 25 mm, and web thickness of 12 mm.

Table 1. Percentage of the plate's contribution in shear strength of each story.

Story	SPSW-100	SPSW-75	SPSW-50	SPSW-Opt
	Percentage of the Plate's Contribution (%)			
10				13
9				28
8				34
7				38
6				34
5	100	75	50	33
4				33
3				33
2				32
1				34

¹ Reduced Beam Section

Table 2. Design sections of frames*.

Story	Plate Thickness	Column	Beam	Story	Plate Thickness	Column	Beam
SPSW-100				SPSW-75			
10	1	B360x25	b600x-310x-25x-12	10	0.8	B300x25	b600x-220x-25x-10
9	2	B360x25	b600x-310x-25x-12	9	1.5	B300x25	b600x-250x-20x-10
8	2.8	B400x30	b600x-310x-25x-12	8	2.1	B350x30	b600x-250x-20x-10
7	3.6	B400x30	b550x-280x-25x-10	7	2.7	B350x30	b550x-250x-20x-10
6	4.2	B450x35	b550x-280x-25x-10	6	3.1	B400x30	b550x-250x-20x-10
5	4.7	B450x35	b550x-220x-20x-10	5	3.5	B400x30	b450x-260x-20x-8
4	5.2	B500x35	b550x-220x-20x-10	4	3.9	B450x35	b450x-260x-20x-8
3	5.5	B500x35	b450x-210x-20x-10	3	4.1	B450x35	b400x-190x-20x-8
2	5.7	B550x40	b450x-210x-20x-10	2	4.2	B500x35	b400x-190x-20x-8
1	5.8	B550x40	b450x-150x-20x-10	1	4.3	B500x35	b400x-190x-20x-8
SPSW-50				SPSW-Opt			
10	0.5	B250x20	b550x-210x-20x-10	10	0.1	B210x20	b350x-200x-20x-6
9	1	B300x25	b550x-210x-20x-10	9	0.5	B260x20	b450x-280x-20x-8
8	1.4	B300x25	b450x-280x-20x-10	8	0.9	B290x20	b450x-280x-20x-8
7	1.8	B340x30	b450x-280x-20x-10	7	1.3	B290x25	b450x-280x-20x-8
6	2.1	B340x30	b450x-280x-20x-10	6	1.4	B320x25	b450x-240x-20x-8
5	2.3	B340x30	b400x-220x-20x-8	5	1.5	B320x30	b450x-240x-20x-8
4	2.5	B360x30	b400x-220x-20x-8	4	1.7	B330x30	b450x-240x-20x-8
3	2.7	B360x30	b350x-200x-20x-8	3	1.8	B340x30	b450x-240x-20x-8
2	2.8	B410x35	b350x-200x-20x-8	2	1.8	B350x30	b400x-150x-15x-8
1	2.9	B410x35	b350x-180x-15x-8	1	1.9	B360x30	b400x-150x-15x-8

* All dimensions are in mm.

3. Results and Discussion

3.1. Force-displacement diagrams

3.1.1. First story

Force-displacement diagrams of the first, fifth, and tenth stories for the studied panels are shown in Figures 3 to 5. Diagrams of the other stories and system behavior were the same and neglected in order to summarize the paper. In these diagrams, the PFI theory is used, where P, F, and W indicate Panel, Frame, and Wall, respectively. Therefore, the total capacity of the structure in SPSW-100 in Fig. 3a was almost 3 times as the required shear capacity of the story.

In Fig. 3b and 3c, in which the plates were designed for 75 % and 50 % of the story shear, the total capacity of the structure was obtained equal to 8482 and 4989 kN, which was 2.3 and 1.3 times as the story's shear demand (equal to 3681 kN), respectively. In Fig. 3d, the optimal value for the plate's shear sharing (equal to 34 %) is calculated using the trial-and-error method. Besides, the total capacity of the structure in SPSW-100 was 1.3 times of SPSW-75. It is also 2.3 and 3 times of SPSW-50 and SPSW-Opt specimens, respectively. As shown in Fig. 3d, the total capacity of the structure was equal to the story's shear demand.

Panel's stiffness in SPSW-100 was 1.4, 2.8, and 4 times as those of SPSW-75, SPSW-50, and SPSW-Opt specimens, respectively. The plate-to-frame initial stiffness ratio in SPSW-75, SPSW-50, and SPSW-Opt was equal to 0.7, 0.8, and 1.1, respectively.

As observed, the less the wall plate contribution to the story shear capacity, the smaller the peripheral frame and the higher the yield deformation of the frames would be. Therefore, by increasing the distance between the yield deformations of the frame and wall, the system's energy absorption capacity would be increased as well. It is also notable that by allocating the whole story shear to the steel wall, the frame's initial stiffness in Fig. 3a was more than that of the wall, and the dominant behavior of the system would be the peripheral frame.

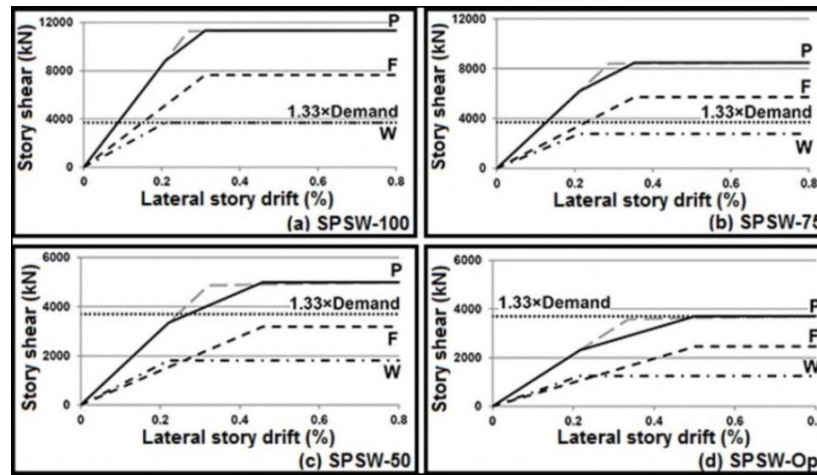


Figure 3. PFI diagram of the first story and comparison with design story shear demand; a) SPSW-100, b) SPSW-75, c) SPSW-50, d) SPSW-Opt.

3.1.2. Fifth story

In order to summarize the results, some stories investigated as a sample. In this section, the results for the fifth story are discussed. Force-displacement diagram of the fifth story for the studied frames is shown in Fig. 4. According to Fig. 4a, the total capacity of the structure was 2.6 times of the story's shear demand. It indicates that the design of steel wall for the total base shear of the story and neglecting the bearing capacity of the peripheral frame leads to over-design procedure. In Fig. 4b and 4c, the total capacity of the structure was obtained equal to 5706 and 3884 kN, which was 1.8 and 1.3 times of the story's demand shear (equal to 3053 kN), respectively. The percentage of the plate's contribution to the fifth story of the optimum specimen was calculated as 33 percent.

Panel stiffness on the fifth story in SPSW-100 was 1.5 times of that in SPSW-75, and 2.5 and 3.5 times of SPSW-50 and SPSW-Opt, respectively. The total capacity of the structure in SPSW-100 was 1.4, 2.1, and 2.6 times of those in SPSW-75, SPSW-50, and SPSW-Opt, respectively. The plate-frame stiffness ratio in SPSW-100 was equal to 1. Furthermore, in SPSW-75, SPSW-50, and SPSW-Opt specimens, it was equal to 1.2, 1.4, and 1.1, respectively.

Frame-to-plate yield stress ratio in SPSW-100, SPSW-75, SPSW-50, and SPSW-Opt specimens was equal to 1.7, 1.9, 2.2, and 2.4, respectively. In other words, by reducing the wall's contribution to the story shear, this ratio was increased, which was consistent with the philosophy of the peripheral frame contribution in the story shear.

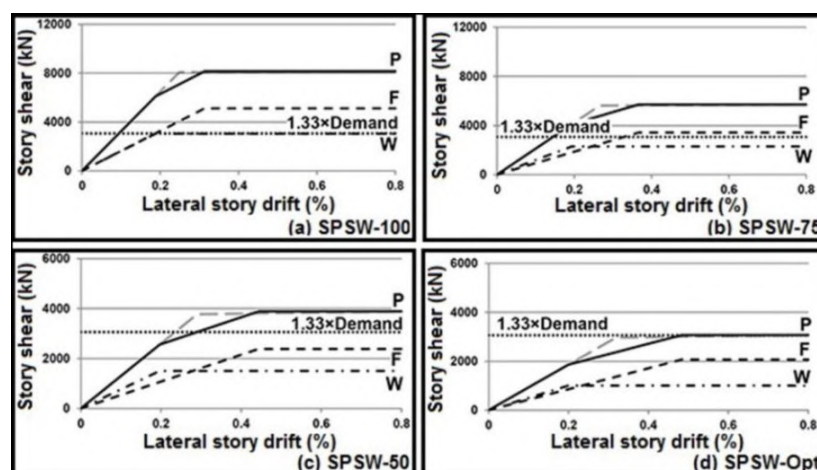


Figure 4. PFI diagram of the fifth story and comparison with design story shear demand; a) SPSW-100, b) SPSW-75, c) SPSW-50, d) SPSW-Opt.

3.1.3. Tenth story

Force-displacement diagrams of the tenth story for the studied specimens are shown in Fig. 5. Total capacity of the structure in Fig. 5a was 4.7 times of the demand shear capacity of the story. In Fig. 5b and 5c, the structure's total capacity was obtained as 2185 and 1244 kN, which was 3.2 and 1.8 times of the demand

shear capacity of the story (681 kN), respectively. In Fig. 5d, the percentage of the plate's optimal contribution to the story shear was calculated equal to 13 percent. Panel stiffness in SPSW-100 was 1.7, 3.3, and 9.1 times of the ones in SPSW-75, SPSW-50, and SPSW-Opt, respectively. Furthermore, the structure's total capacity in SPSW-100 was 1.5, 2.6, and 4.7 times of the ones in SPSW-75, SPSW-50, and SPSW-Opt, respectively.

The plate-to-frame stiffness ratio in SPSW-100, SPSW-75, SPSW-50, and SPSW-Opt was 0.4, 0.7, 1, and 0.5, respectively. As expected, by reducing the plate's contribution to the lateral load, the plate-to-frame stiffness ratio was increased. The reduction in the plate-to-frame stiffness ratio in SPSW-Opt was due to the application of executive limitations on the minimum dimension size of the columns in 10th story as well as the plate's low contribution (13 %) to the panel shear strength. The frame-to-plate yield stress ratio in SPSW-100, SPSW-75, SPSW-50, and SPSW-Opt was 1.9, 2.3, 2.9, and 3.7, respectively.

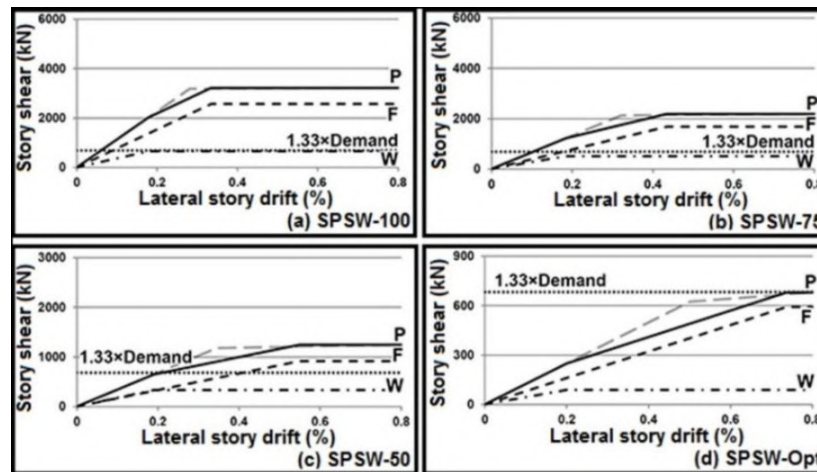


Figure 5. PFI diagram of the tenth story and comparison with design story shear demand; a) SPSW-100, b) SPSW-75, c) SPSW-50, d) SPSW-Opt.

3.1.4. Comparison of the design methods

Fig. 6 represents the comparison between the panel force-displacement diagrams on the studied sorties. It can be seen that by reducing the wall's contribution to the story shear capacity, the stiffness of the panel reduced. Moreover, the system's capacity in the optimum specimen (SPSW-Opt) was equalized with the demand story shear. Interestingly, in the studied diagrams, the steel plate's yield displacement was almost constant, while the yield displacement of the frame was increased. In other words, the increase in the distance between the yield displacement of the steel plate and frame led to the increased energy absorption capacity in this region. Details of the calculations of these displacements on different stories of the studied specimens are presented in Table 3.

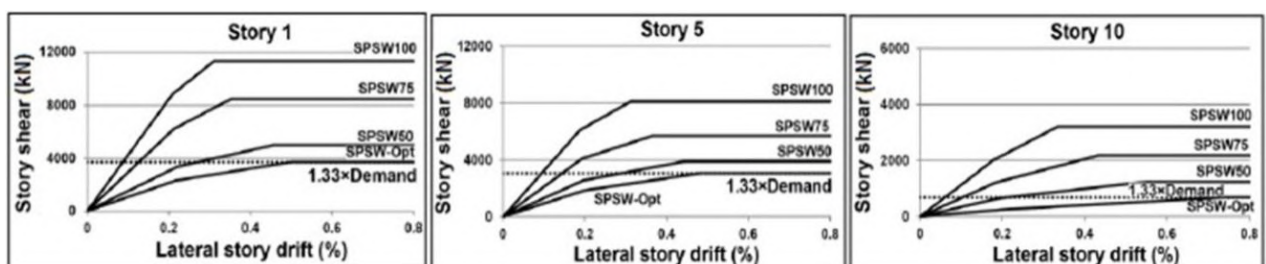


Figure 6. Comparing panel force-displacement diagrams in the studied specimens.

As seen in Table 3, owing to the 25 % reduction in the plate's contribution to the lateral load, the average plate yield displacement (U_{we}) and average frame yield displacement (U_{fe}) were increased by 3 % and 20 %, respectively.

Regarding the investigation of the PFI diagrams on the stories of the structure, in contrast to the conventional conservative design method, shear capacity of the frame was much higher than that of the steel plate. In other words, the plate's contribution to the story shear was less than the peripheral frame and neglecting the frame shear capacity in calculations might result in the overdesigned sections. It should be noted that the lateral stiffness of the frame was also higher than that of the steel plate.

Table 1. Plate-frame yield displacement in PFI diagrams*.

Story	U_{we}	U_{fe}	U_{we}	U_{fe}	U_{we}	U_{fe}	U_{we}	U_{fe}
	SPSW-100	SPSW-75	SPSW-75	SPSW-50	SPSW-50	SPSW-50	SPSW-Opt	SPSW-Opt
10	5.3	10	5.5	13	5.7	16.5	6	22.1
9	5.3	10	5.6	13.3	5.8	14.2	6	17.3
8	5.4	9.5	5.6	11.6	5.9	14.8	5.8	14.7
7	5.5	10	5.7	11.9	5.9	13.1	5.9	15.6
6	5.6	9.2	5.7	10.6	5.9	13.2	5.9	14
5	5.6	9.4	5.8	11	5.9	13.3	6	14.5
4	5.6	8.5	5.8	9.9	6	13	5.9	13.7
3	5.6	8.5	5.9	10.1	6.1	13.6	6	13.5
2	5.7	7.7	5.8	9	6.2	12.1	6	13.4
1	6.3	9.3	6.4	10.6	6.6	13.7	6.5	15.1

* All dimensions are in mm.

3.2. Seismic evaluation of system

The major seismic parameters of the system, including ductility, response modification factor, over-strength factor, and energy absorption capacity of the frames, are calculated in this section and the effects of the design philosophy are investigated based on determining the actual contribution of the steel plate and frame to these parameters.

3.2.1. Ductility

According to ATC-24 [28], the displacement ductility factor of a system can be calculated using Eq. 9.

$$\mu = \frac{U_{max}}{U_y} \quad (9)$$

Where μ is ductility factor, U_{max} is a maximum inelastic displacement that the system can experience before failure (supposed to be $0.02h$ in accordance with ASCE7-10 [27]), and U_y is the system's yield displacement.

The ductility of the frames in various stories is shown in Fig. 7. As can be seen, the less the plate's contribution to the story shear-capacity, the less the system's ductility would be. In other words, by reducing the plate's contribution from 100 % to the optimal value in different stories, the average ductility would be reduced from 8 to 6.3. According to Fig. 7, for every 25 % reduction in the plate's contribution relative to the SPSW-100 specimen, the system's ductility would be reduced by 9 %.

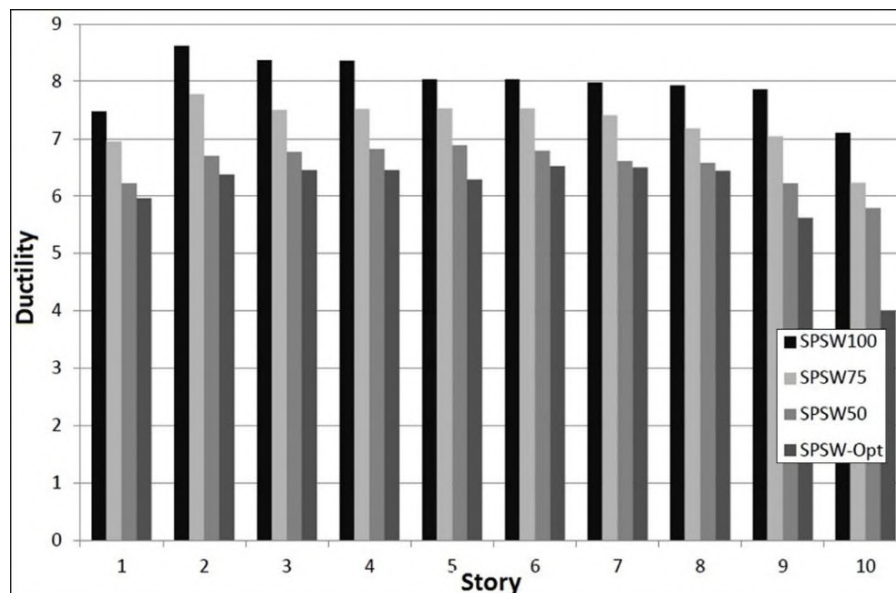


Figure 7. Ductility of the frames in different stories.

3.2.2. Energy absorption capacity

The area under the force-displacement diagram was equal to the system's energy absorption capacity [29]. In Fig. 8, the structure's energy absorption capacity on various stories for the studied specimens was calculated up to the displacement of 2 %.

The reduction in the steel plate's contribution to the story shear capacity led to the significant reduction of the system's energy absorption, which was mainly due to the reduction in the size of the peripheral frames as well as a reduction in the steel plate's thickness. In other words, the conventional overdesign (conservative) method would lead to a significant increase in the size of the columns and the thickness of the middle plate. It can be seen that in the optimal design, energy absorption capacity was less than the one in the conventional design, which does not mean the structure's inefficiency for earthquake energy absorption, and the energy absorbed by the system should be compared with the structural demand for various earthquakes. It should also be noted that the reduced frame dimensions and steel plate thickness would result in the reduced system stiffness and seismic demand. As previously mentioned, in this research, the designs were carried out by assuming the equal seismic requirements for the studied frames. According to Fig. 8, it can be seen that for every 25 % reduction in the plate's contribution relative to SPSW-100, the system's energy absorption capacity was reduced by 27 %.

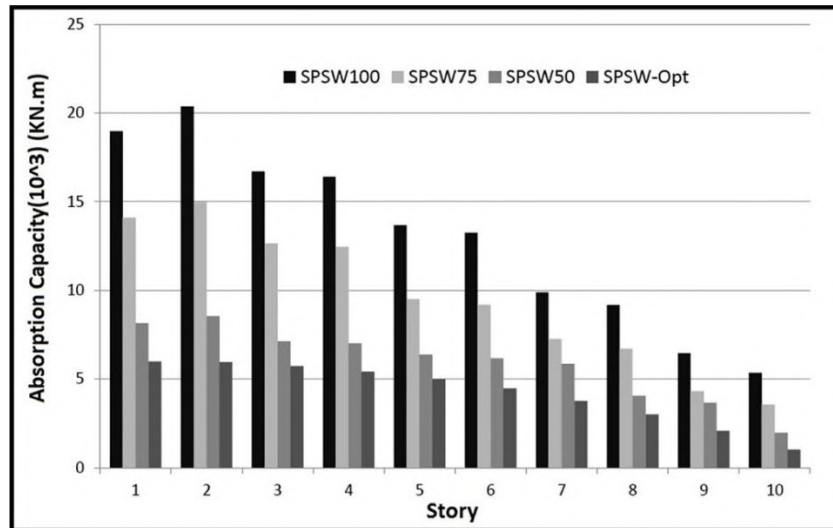


Figure 8. Energy absorption capacity of the frames in different stories.

3.2.3. Ductility reduction factor

One of the common methods to determine the reduction caused by ductility factor (R_μ) is Newmark and Hall method, which is calculated using Eq. 10. The median values of the periods (T) are calculated through interpolation [30].

$$\begin{aligned}
 T \leq 0.03 & \quad R_\mu = 1 \\
 0.12 \leq T \leq 0.5 & \quad R_\mu = \sqrt{2\mu - 1} \\
 T \geq 1 & \quad R_\mu = \mu
 \end{aligned} \tag{10}$$

Ductility reduction factors for the studied frames are shown in the second column of Table 4. It can be seen that by reducing the plate's contribution to the story shear, the ductility reduction factor would be also reduced. Therefore, the ductility reduction factor of the structure would be decreased by 6.8 on average for each 25 % reduction in the plate's contribution to the story shear.

Table 4. Seismic parameters of the frames.

Specimen	R_μ	Ω_0	R_u
SPSW-100	5.01	1.4	7.01
SPSW-75	4.67	1.5	7.01
SPSW-50	4.33	1.6	6.93
SPSW-Opt	4.2	1.65	6.94

3.2.4. Over-strength factor

Over-strength factor (Ω_0) is the strength that the structure demonstrates after forming the first plastic hinge (C_s) up to the mechanism (C_y), which is obtained using Eq. 11.

$$\Omega_0 = \frac{C_y}{C_s} \quad (11)$$

The over-strength factors were calculated for each story considering the PFI diagrams and, then, the average values were proposed on various stories of the studied frames in the third column of Table 4. It can be seen that by reducing the plate's contribution to the story shear capacity, the over-strength factor was increased so that, for every 25 % reduction in the plate's contribution to the story shear, the over-strength factor was increased by 7 %.

3.2.5. Response modification factor

Response modification factor in LRFD level was determined according to the following equation.

$$R_u = R_\mu \Omega_0 \quad (12)$$

Where R_u and Ω_0 indicate the ductility reduction and over-strength factors of the system. The mean values of the response modification factor on different stories of the studied frames are presented in the fourth column of Table 4. In this table, the behaviors of SPSW-100 and SPSW-75 were equal to 7.01, while for SPSW-50 and SPSW-Opt, they were 6.93 and 6.94, respectively. The interesting point about the mean values of the response modification factor in the studied frames was that, despite the reduction in the steel plate's contribution to the story shear capacity and the significant reduction in the size of the columns, beams, as well as the steel plate's thickness, the value of the computational response modification factor did not change significantly. In other words, the reduction in the value of the ductility reduction factor in the specimens with less contribution of the steel plate was compensated for by the increased over-strength factor of the structure.

3.3. Numerical study

Finite element analysis of the studied specimens was used to investigate the distribution of the forces in the steel wall and its peripheral frame at various drifts as well as the accuracy of the PFI diagrams and the obtained results.

For this purpose, ANSYS finite element software was used to model and investigate the specimens undergoing nonlinear static analysis (pushover). The thickness of the wall plate was very low in SPSW-50 and SPSW-Opt specimens. Furthermore, since the specimens were modeled with small computational thicknesses and actual dimensions of the frames in the software, the lateral deformations of plate were relatively too high. Therefore, it was so difficult to converge the models. In addition, due to the huge volume of the calculations in modeling a 10-storey structure in software, only the first two stories were modeled for two SPSW-100 and SPSW-75 specimens in the software in order to investigate the shear behavior of the first story. It was necessary to model the second story to investigate the correct beam role for the tensile force of the lower and upper stories due to tension field in steel walls. Therefore, the two-story model was used for studying the ground story.

3.3.1. Finite element modeling

The steel wall and frame elements were selected by SHELL181 element type, which included 4 nodes with 3 degrees of translational freedom as well as 3 degrees of rotational freedom. Besides, it was capable of modeling large buckling deformations. The column base-to-ground connection, plate-to-beam and column connection, as well as beam-to-column connections were continuous. The out-of-plane deformation of the frame was prevented. The S350J steel materials with the minimum yield strength of 350 MPa were used for the beams and columns and S235J steel with the minimum yield strength of 235 MPa were used for the steel wall. The reason for using the steel with higher yield stress for the peripheral frame was to reduce the size of columns and beams to the minimum possible dimensions. Materials were considered bilinear with the strain-hardening slope of 1 % and the optimum mesh size was considered equal to 200 mm. Fig. 9 shows the two-story model built in software. As demonstrated in this figure, due to the use of RBS in the beam-column connection, meshing at the end of the beam and also at the points adjacent to the columns was finer. Moreover, in order to prevent the concentration of the stresses in the panel zone, the continuity plates were used in the columns.

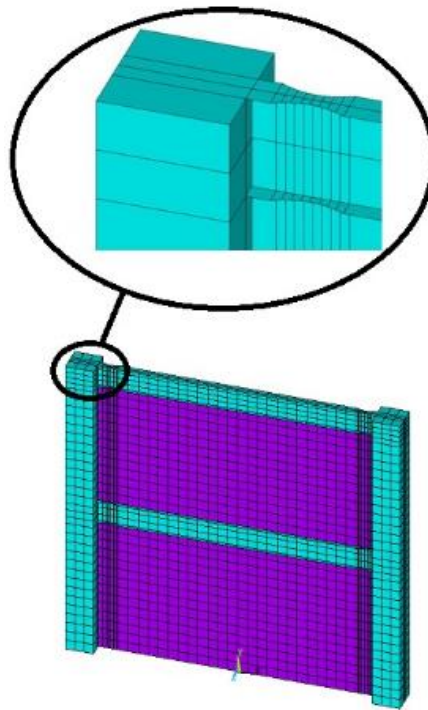


Figure 9. Finite element model.

3.3.2. Force-displacement diagrams

The force-displacement curves of the software models and the PFI diagrams of the studied specimen are compared in Fig. 10. As can be seen, the diagrams obtained from the software were compatible with PFI diagrams.

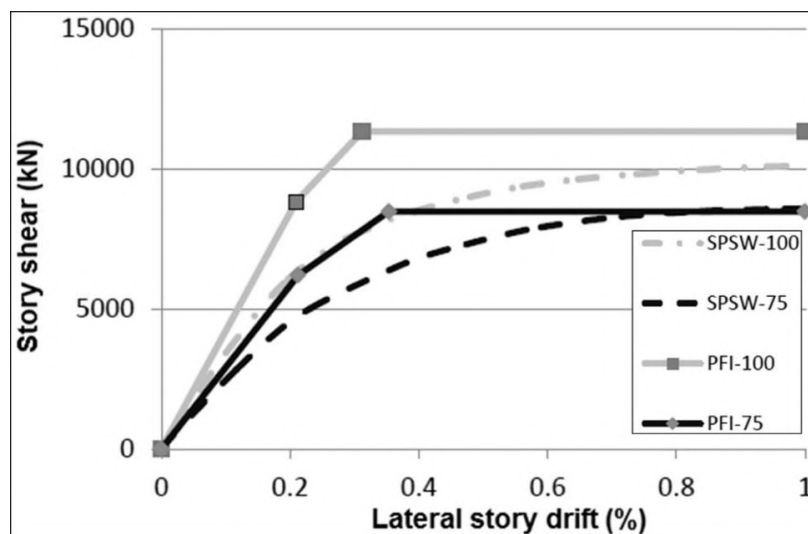


Figure 10. Comparing software and PFI pushover diagrams.

3.3.3. Stress distribution in steel wall

Fig. 11 and 12 represent the distribution and the values of stresses (in MPa) inside the steel wall at different drifts. As shown in these figures, the stresses began to increase from the corner of the plate toward center. A larger area of the plate was yielded by increasing the lateral story drift. Finally, a major part of the wall was yielded at 1 % drift in SPSW-100 and SPSW-75 specimens.

First yield point of the plate in SPSW-100 occurred at 0.13 % drift, while the yield point in the SPSW-75 was at 0.09 % drift. In other words, the reduction in the contribution of the steel wall led to smaller drifts for the first yield of the steel plate. For example, the total yield point of the wall in SPSW-100 occurred at the displacement of 4.3 mm, while the yield point in SPSW-75 was at the displacement of equal to 5 mm.

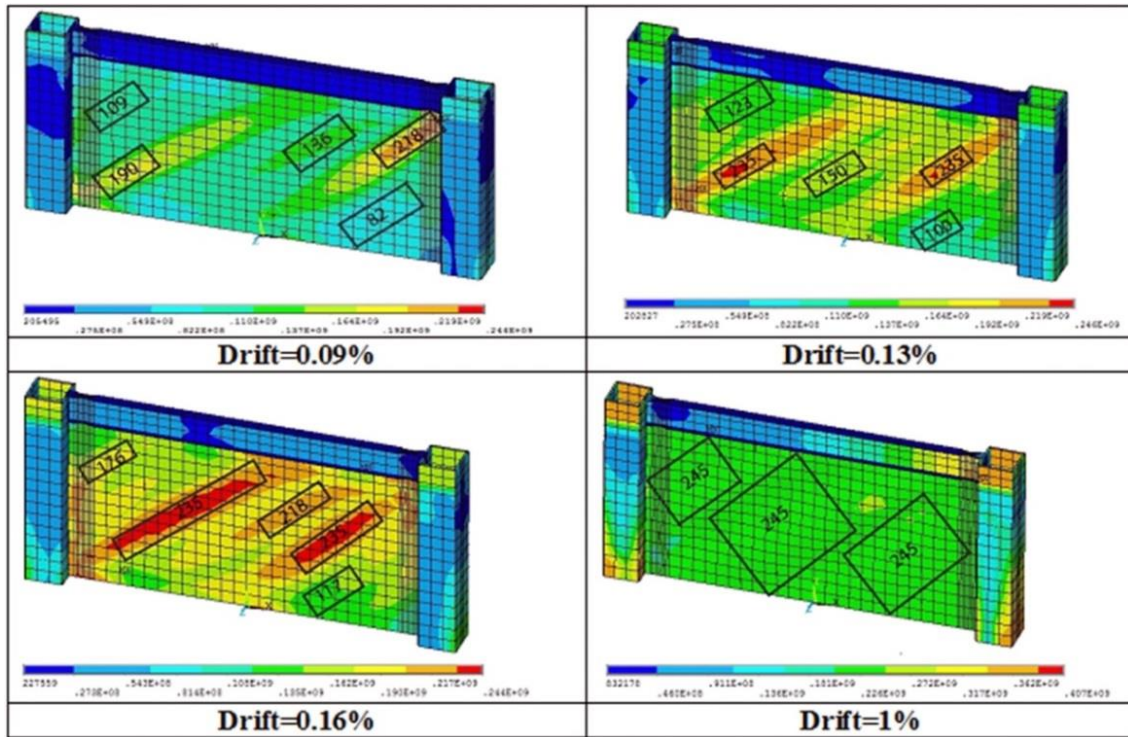


Figure 11. Von-Mises stress distribution in various drifts in SPSW-100.

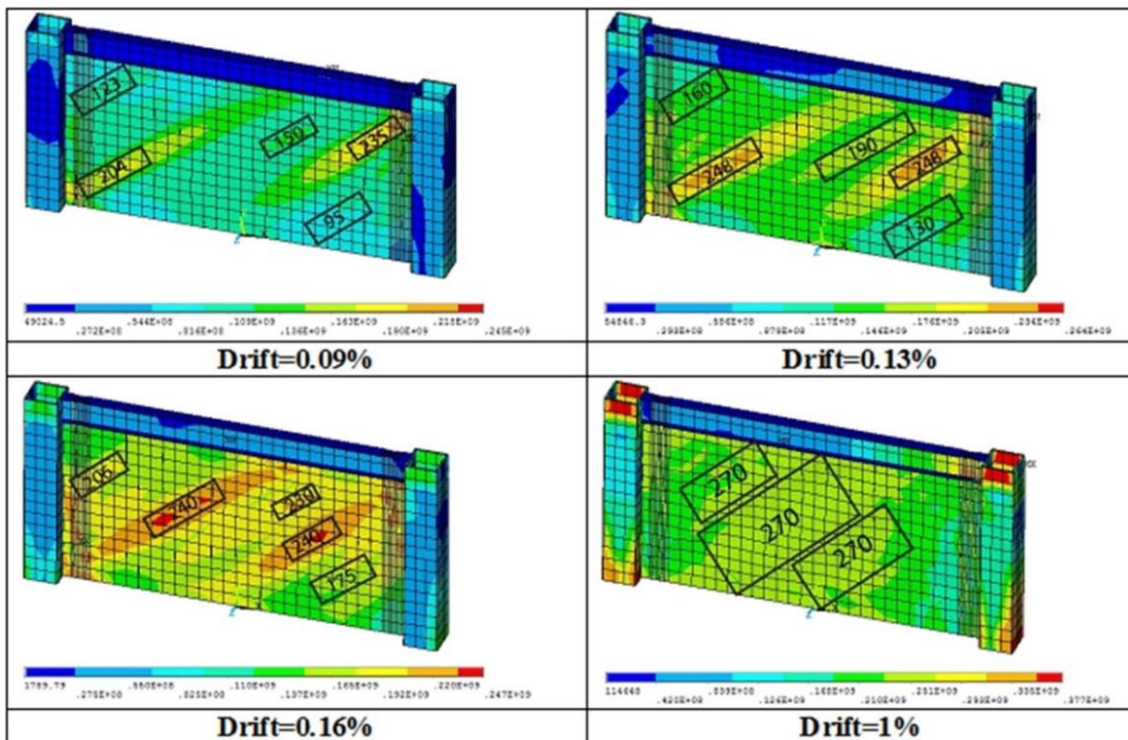


Figure 12. Von-Mises stress distribution in various drifts in SPSW-75.

3.3.4. Behavior of RBS connection

In order to follow the strong column-weak beam philosophy in accordance with AISC358 [31] requirements, the RBSs were provided at the ends of beams.

The Von-Mises stress distribution in RBS connections at various drifts is shown in Fig. 13. The average stress values are written on the figure. The use of RBS led to the increased stress in the reduced area, formation of plastic hinges in the beams, as well as prevention of the formation of the plastic hinge in the columns. It can be seen that the first yield point of the RBS connection was occurring at 0.4 % drift, which protected the column against unfavorable effects of stress concentration adjacent columns' face.

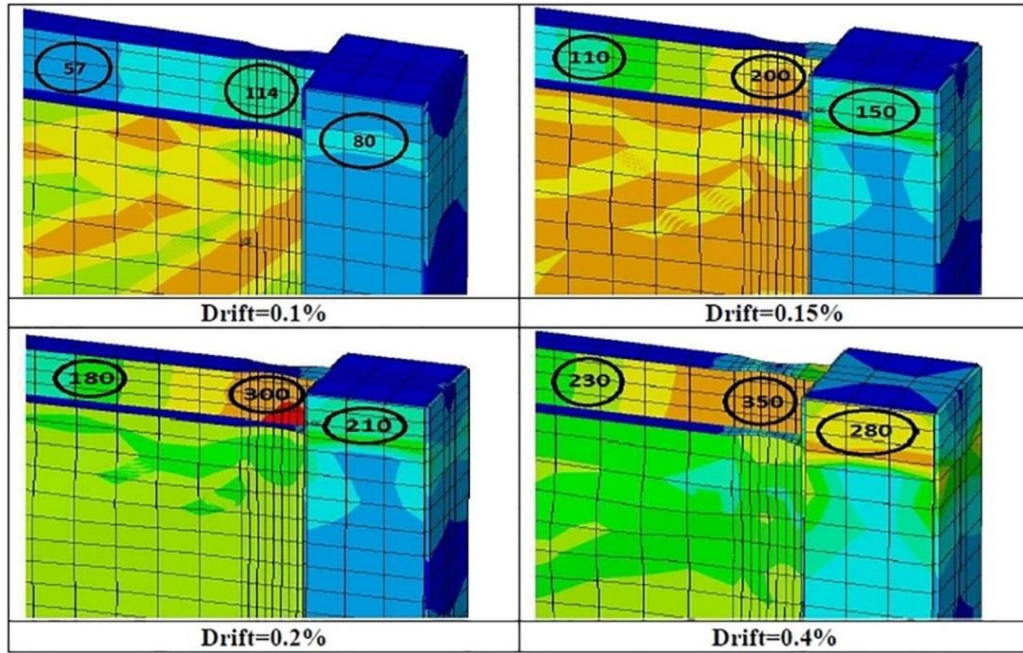


Figure 13. Von-Mises stress distribution in RBS connections at various drifts.

3.3.5. Out-of-plane displacements of steel wall

The out-of-plane deflections of steel wall is shown in Fig. 14. In SPSW-100, the thickness of the steel plate on the first story was 5.8 mm, where the maximum out-of-plane displacement at 1 % drift was 40 mm. In SPSW-75, the thickness of the steel plate on the first story was 4.3 mm, while the maximum displacement at 1 % drift was 36.5 mm. It is observed that, despite the considerable reduction in the steel plate's thickness in SPSW-75 compared to SPSW-100, the value of the out-of-plane deformation of the plate did not change significantly. In other words, by reducing the wall's contribution to the lateral load transfer, the number of the out-of-plane deformation waves of the plate (number of protrusions and indentations of the plate) was increased, while the maximum displacement value along the out-of-plane direction of the steel plate was reduced.

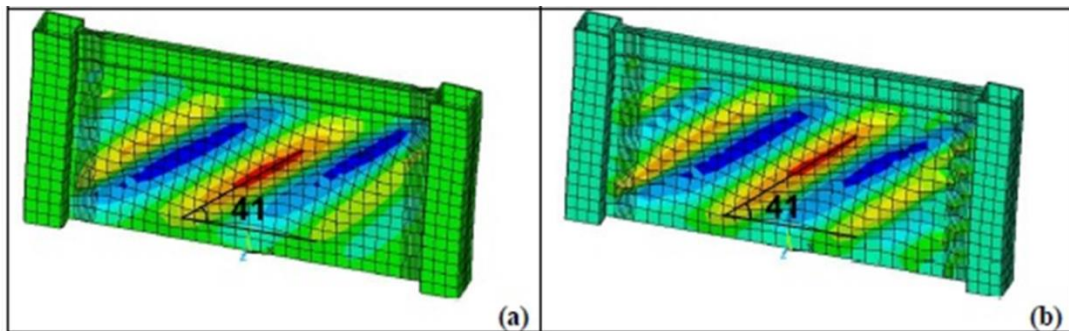


Figure 14. Out-of-plane deflection of steel wall in 1 % drift, a) SPSW-100, b) SPSW-75.

3.3.6. Tension field angle

As shown in Fig. 14, the diagonal tension field angles in both SPSW-100 and SPSW-75 were 41° . Therefore, by decreasing the plate's contribution to the lateral load transfer, the value of the tension field angle did not change significantly.

3.3.7. Contribution of steel plate and peripheral frame in the story shear

To determine the value of transferring shear by the steel wall and its peripheral frame, the value of horizontal forces of the wall at the wall's node connection to the foundation at various drifts was added and the remaining shear was tolerated by the peripheral frame (see Fig. 15).

According to Fig. 15, by increasing the structure's drift, the contribution of the steel plate to the story's shear transfer was reduced. Furthermore, the contribution of the plate in SPSW-75 was more. Therefore, in SPSW-100, the steel plate and its peripheral frame transferred about 54 % and 46 % of the total story's shear

at the beginning of loading, respectively, while at 1 % drift, the steel plate and its peripheral frame transferred about 38 % and 62 % of the shear, respectively. In SPSW-75, the steel plate and its peripheral frame transferred about 54 % and 46 % of the total story's shear (similar to SPSW-100), respectively, while at 1 % drift, the steel plate and its peripheral frame transferred about 33 % and 67 % of the story's shear, respectively. In other words, by increasing the structure's drift, the contribution of the steel wall to the story's shear capacity in SPSW-75 was decreased much more than the one in SPSW-100. It should be noted that in designing SPSW-100, the total story shear was allocated to the steel wall, while the contribution of the steel wall varied only between 38 % and 54 %. Similarly, in SPSW-75, in which the steel wall was designed to transfer 75 % of the total story shear, the contribution of the steel wall was between 33 % and 54 % of the system's total capacity. The diagrams indicated that the shear percentage allocated for designing the steel walls was over-estimated and, in practice, the walls had less contribution in story shear. Furthermore, a large amount of the story shear was transmitted by columns and neglecting the role of peripheral frame in the story shear would lead to the non-economic design of the SPSW system.

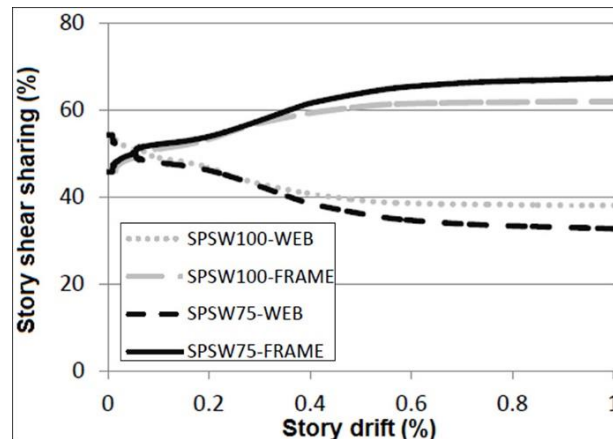


Figure 15. Contribution of steel plate and peripheral frame in the story shear versus drift.

4. Conclusion

Four specimens of steel shear wall in a 10-story building were designed for 100, 75, 50 %, and the optimal percentage of shear transfer and the capacity of each frame was compared with the demand shear capacity of each story. According to the results, designing the wall for higher shear percentage and neglecting the role of columns in the story shear capacity would increase the frame's thickness and the peripheral frame dimensions, leading to the non-economic system. Furthermore, according to the PFI diagrams and finite element modeling of the specimens, in the specimens with less contribution of the steel plate to the story shear, the value of the ductility reduction factor was decreased and the structure over-strength factor was increased, while the mean value of the structure's response modification factor did not change significantly. In general, it can be concluded that by determining the precise contribution of the steel plate and its peripheral frame for the earthquake demand story shear, it would be possible to design SPSW for more optimized sections.

Finite element analysis of the studied specimens also indicated much less contribution of the steel plate to the story shear. In order to complete the discussions presented in this research, it is necessary to conduct further studies on the structures with different numbers of stories as well as on the behavior of the structures under nonlinear time history analysis and incremental dynamic analysis (IDA). Moreover, providing an optimal design requires further studies in this regard. In addition, the accurate definition of earthquake demands considering the reduced stiffness of the system and decreased base shear may result in more optimized system.

5. Acknowledgments

The research described in this paper was supported by Shahr-e-Qods Branch of Islamic Azad University.

References

1. Roberts, T.M., Sabouri-Ghomi, S. Hysteretic Characteristics of Unstiffened Plate Shear Panels. *Thin Walled Structures*, 1991. 12(2). Pp. 145–162.
2. Sabouri-Ghomi, S., Ventura, C.E., Kharrazi, M.H.K. Shear Analysis and Design of Ductile Steel Plate Walls. *Journal of Structural Engineering*, ASCE, 2005. 131(6). Pp. 878–889.

3. Gholhaki, M. Investigating behavior of ductile steel shear walls and effect of type of beam-column joint. Ph.D. thesis, Department of Civil and Environmental Engineering, K.N. Tousi University of Technology, 2008.
4. Darvishi, A., Jamshidi, M., Qaffari, H., Mir-Babaei, S.A. Investigating effect of column's stiffness on load bearing capacity of steel shear walls, National Conference on Structure-Road-Architecture, Islamic Azad University, Chalous Branch, Chalous-Iran, 2011.
5. Alinia, M.M., Dastfan, M. The Effects of Surrounding Members on Post-Buckling Behavior of Thin Steel Plate Shear Walls (TSPSW). *Advances in Steel Structures*, Elsevier Ltd, 2005. 2. Pp. 1427–1432.
6. Alinia, M.M., Dastfan, M. Behavior of Thin Steel Plate Shear Walls Regarding Frame Members. *Journal of Constructional Steel Research*, 2006. 62(7). Pp. 730–738.
7. Alinia, M.M., Dastfan, M. Cyclic Behavior, Deformability and Rigidity of Stiffened Steel Shear Panels. *Journal of Constructional Steel Research*, 2007. 63(4). Pp. 554–563.
8. Choi, L., Park, H. Cyclic Test for Framed Steel Plate Walls with Various Infill Plate Details. *Proceedings, the 14th World Conference in Earthquake Engineering, Beijing-China, 2008.*
9. Kharrazi, M.H., Ventura, C.E., Prion, H.G. Analysis and Design of Steel Plate Walls: Analytical Model. *Canadian Journal of Civil Engineering*, 2010. 38(1). Pp. 49–59.
10. Chen, S.h., Jhang, C.h. Experimental Study of Low-Yield-Point Steel Plate Shear Wall Under in-Plane Load. *Journal of Construction Steel Research*, 2011. 67. Pp. 977–985.
11. Hosseinzadeh, S.A.A., Tehranizadeh, M. Behavioral Characteristics of Code Designed Steel Plate Shear Wall Systems. *Journal of Construction Steel Research*, 2014. 99. Pp. 72–84.
12. Moradinejad, Z., Gholampour, S., Vaseghi Amiri, J. Investigating effect of position of steel shear wall on progressive failure using nonlinear static analysis. 6th National Congress on Structure and Steel, Tehran-Iran, 2014.
13. Ebadi, P., Farajloomanesh, S., Pishbin, M. Required ductility and capacity for designing steel buildings with special steel shear wall system without stiffener, International Conference on Architecture – Civil Engineering and Urban Planning in 3rd Millennium, Tehran-Iran, 2014.
14. Ebadi, P., Farajloomanesh, S., Pishbin, M. Effect of plate's contribution to shear tolerance of story in special steel shear wall system without stiffener. 6th National Conference on Structure and Steel, Tehran-Iran, 2014.
15. Purba, R., Bruneau, M. Experimental investigation of steel plate shear walls with in-span plastification along horizontal boundary elements. *Engineering Structures*, 2015. 97. Pp. 68–79.
16. Moghimi, H., Driver, R.G. Performance assessment of steel plate shear walls under accidental blast loads. *Journal of Constructional Steel Research*, 2015. 106. Pp. 44–56.
17. Guo, H.C., Hao, J.P., Liu, Y.H. Behavior of stiffened and unstiffened steel plate shear walls considering joint properties. *Thin-Walled Structures*, 2015. 97. Pp. 53–62.
18. Du, Y., Hao, J., Yu, J., Yu, H., Deng, B., Lv, D., Liang, Z. Seismic performance of a repaired thin steel plate shear wall structure. *Journal of Constructional Steel Research*, 2018. 151. Pp. 194–203.
19. Wang, W., Ren, Y., Lu, Z., Song, J., Han, B., Zhou, Y. Experimental study of the hysteretic behaviour of corrugated steel plate shear walls and steel plate reinforced concrete composite shear walls. *Journal of Constructional Steel Research*, 2019. 160. Pp. 136–152.
20. Jalali, S.A., Darvishan, E. Seismic demand assessment of self-centering steel plate shear walls. *Journal of Constructional Steel Research*, 2019. 162. P. 105738.
21. Yu, J.G., Liu, L.M., Li, B., Hao, J.P., Gao, X., Feng, X.T. Comparative study of steel plate shear walls with different types of unbonded stiffeners. *Journal of Constructional Steel Research*, 2019. 159. Pp. 384–396.
22. Pachideh, G., Gholhaki, M., Daryan, A.S. August. Analyzing the damage index of steel plate shear walls using pushover analysis. In *Structures-Elsevier*, 2019. 20. Pp. 437–451.
23. Hajimirsadeghi, M., Mirtaheri, M., Zandi, A.P., Hariri-Ardebili, M.A. Experimental cyclic test and failure modes of a full scale enhanced modular steel plate shear wall. *Engineering Failure Analysis*, 2019. 95. Pp. 283–288.
24. Mu, Z., Yang, Y. Experimental and numerical study on seismic behavior of obliquely stiffened steel plate shear walls with openings. *Thin-Walled Structures*, 2020. 146. P. 106457.
25. ANSI/AISC 341, Seismic Provisions for Structural Steel Buildings. American Institute of Steel Construction, 2005.
26. AISC Steel Design Guide 20, Steel Plate Shear Walls. American Institute of Steel Construction, 2007.
27. ASCE/SEI 7-10, Minimum Design Loads for Buildings and Other Structures. American Society of Civil Engineering, 2010.
28. ATC-24, Guidelines for Seismic Testing of Components of Steel Structures. Report-24, Applied Technology Council, 1992.
29. ATC-40, Seismic evaluation and retrofit of concrete buildings. Applied Technology Council, 1996.
30. Borzi, B., Elnashai, A.S. Refined force reduction factors for seismic design *Engineering Structures*, 1991. 22. Pp. 1244–1260.
31. ANSI/AISC 358-10, Prequalified Connections for Special and Intermediate Steel Moment Frames for Seismic Applications. American Institute of steel construction Inc., 2010.

Contacts:

Parviz Ebadi, parviz.ebadi@gmail.com

Saeid Farajloomanesh, s.farajloomanesh@gmail.com

© Ebadi, P., Farajloomanesh, S., 2020



DOI: 10.18720/MCE.95.2

Single burning item test for timber with fire protection

M.V. Gravit^a, D. Serdjuks^b, N. Vatin^a, Y.G. Lazarev^a, M.O. Yuminova^{a*}

^a Peter the Great St. Petersburg Polytechnic University, St. Petersburg, Russia

^b Riga Technical University, Riga, Latvia

* E-mail: maria.yuminova@mail.ru

Keywords: building products, timber constructions, fire protection for wood, fire retardants, single burning item test, combustible, flammability, smoke production, SBI

Abstract. Fire protection of timber structures and finishing structural materials is actual due to the high combustibility of these materials. The technical characteristics for protected timber structures in case of fire, determined by the single burning item test (SBI), are considered in the paper. Nine thin-layered lacquers and paints fire protections, which were differed by the type of fire resistance and chemical contents, were analyzed. The timber specimens treated by such fire protections as the paints, impregnations, lacquers and water glass were tested by SBI method. It was shown, that the lacquer on the base of the acryl resin has a significant influence on the fire growth rate indices FIGRA and smoke growth rate SMOGRA on the initial stage of combustion (FIGRA – 2948.78 W/s, SMOGRA – 101.28 m²/s²). Traditional fire protection by the water glass shows the high fire growth rate indices FIGRA (268.63 W/s) and total smoke production TSP600s (163.13 m²). The low levels of the both values did not confirm a classic consideration of the water glass as effective fire protection of timber members. Type of timber base and assembling method (with or without air gap) has a significant influence on the effectiveness of fire protection. Analogous results obtained for the intumescent paint and two types of lacquers. The modern water impregnations that contains phosphoric acids characterized by the low expenditure (mean value 250 g/m²) and low values of smoke growth rate and total smoke production in 3MJ and 33 m², correspondingly. These impregnations provides a class Bs1d0 of fire protection by the European classification.

1. Introduction

The methods for determination of technical characteristics of finishing structural materials in case of fire actions and its classification by the fire hazard are differed in Russian Federation and Europe at the present moment [1]. A lack of direct correlation of European and Russian codes regulating determination of fire hazard of structural materials is the major difficulty in the harmonization of the methods [1–4].

European method Single Burning Item (SBI) [5] is used for determination of technical characteristics of structural materials in case of fire and class of fire-resistance [6].

Two sub-systems (structural and finishing materials so as ceiling coverings) includes the seven classes of the fire hazard starting from the class A (noncombustible materials) until the class F (highly combustible materials).

The SBI method is considered in current work for the determination of technical characteristics of timber structures in case of fire action because timber is a structural material, which is characterized by the variety of shapes and dimensions and widely used for the structural purposes now [7–10]. The low fire resistance and high ability for ignition are the critical disadvantages of the timber as a structural material. The timber member treated by the fire protective agents, including fire-retardant treatment, must strongly corresponds to the requirements of standards by the heat and smoke growth rate so as the fire protective agents can increase the fume developing ability of the base. It is very significant in the cases, if the timber member is placed in the probable ways of the evacuation. So, structural products are classified basing on the determined class and additional class by the smoke growth rate [6]. The SBI method cannot be considered as an etalon in some

Gravit, M.V., Serdjuks, D., Vatin, N., Lazarev, Y.G., Yuminova, M.O. Single burning item test for timber with fire protection. Magazine of Civil Engineering, 2020. 95(3). Pp. 19–30. DOI: 10.18720/MCE.95.2



This work is licensed under a CC BY-NC 4.0

unstandardized cases, when the national standards enables to obtain the results with the increased precision [11–19].

A special attention should be payed to assembling process and fasteners so as both the factors have the significant influence on the obtained results. The methods of fastening should be reflected in the specifications. Assembling in accordance with the standard provides determination of fire hazard class with the increased precision. Several deviations during the assembling leads to misrepresentation of the classification [18, 19]. Results of the classification can be differed dependently from the type of the base. Therefore, the results obtained in the case of the gypsum boards base without air gap can be different from the results obtained in the case of clearances existence between the specimen and noncombustible base. Conditions of the test will be more rigid in the second variant with the air gap. The timber, non-treated by the fire protective agents, products with the minimum thickness in 22 mm and minimum density in 350 kg/m², are classified without the further testing in accordance [20]. Structural timber relates to the class D-s2, d0 in accordance with [20]. The class of fire hazard of the timber increases until the B2 by the using of fire protective agents [21]. The unprotected timber structures are related in Russian Federation to 5th class of fire hazard (strongly combustible materials with the highest rates of ability to ignition, combustibility, total smoke production, gase toxicity rate and fire growth rate) [1–4]. Intermediate variants from class A to class F are characterized by the lack of correlation with the adopted in Russia classification and methods of confirmation of the classification. Toxicity of burning products is determined by the laboratorian mouses in Russia and by the gas analysers in SBI method, for example [1, 2].

The target of current paper is to analyses the technical characteristics of the fire protected timber structures by the SBI method. Nine different fire protection agents for wood and plywood with different chemical nature are considered in order to understand the best fire-technical characteristics.

2. Methods

The SBI method suppose fire action from one side on the external surface of the whole specimen of the structure (Fig. 1 and 2). A chamber for the tests is the closed space (room) with the single source of ignition (gas burner) in one of the corners and air hole system with sensors for taking the indications. The material is subjected by the flame with the exposure rate in 100 kW in course of the first ten minutes and in 300 kWt in course of the next ten minutes [5]. The indications of materials behavior (expenditure of oxygen, output of carbon dioxide, and values of temperatures) are determined. The behavior than can be used for the determination of parameters for the classification of materials. The parameters give the full-scale information about the dynamic of the fire development including the heat emission and capability of the smoke production.

- THR – total heat release (MJ) from the specimen in the first 600 seconds of exposure to the main (primary) burner flames.

- HRR – heat release rate (kW/m²) – velocity of heat emission from the combustion of specimen and gas in the burner.

- FIGRA – fire growth rate indices (W/s) – maximum of the quotient of heat release rate from the specimen and the time of its occurrence.

- TSP – total smoke production from the specimen (m²) – the value, which characterize the total smoke production from the specimen in the first 600 seconds of exposure to the main (primary) burner flames.

- SMOGRA – smoke growth rate (m²/s²) – maximum of the quotient of smoke production rate from the specimen and the time of its occurrence.

- LFS – lateral flame spread on the long specimen wing – the length of the flame spread on the long specimen wing.

The results enables to evaluate the fire growth rate indices and critical heat emission. The values enables to classify the material in accordance with the standard EN 13501-1 and to determine a class of the fire hazard of the structural material. The algorithm of the classification of structural material is consists from three components:

1. Classification on the base of the total heat release and fire growth rate indices. Class A-F is determined on the base of the values of parameters FIGRA and THR.
2. Additional classification by the smoke growth rate. Class s1-3 is determined on the base of the values of parameters SMOGRA and TSP.
3. Additional classification by the development of firing drops/particles. Class d0-2 is determined dependently on the development of the firing drops/particles in course of the 600 s during the test.

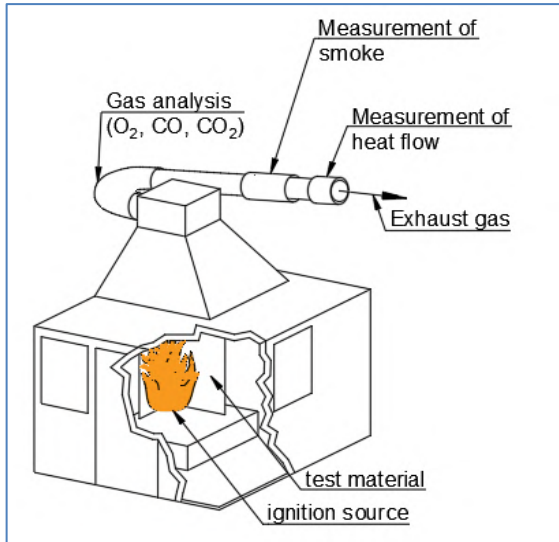


Figure 1. Scheme of the chamber for the tests.

Figure 2. Process of the samples testing.

Timber or plywood boards made of such species as a pine, spruce or a larch with moisture 8–10 %. The small board with dimensions 1.5×0.5 m and big board with dimensions 1.5×1.0 m developing the direct angle.

Products performance determined on gypsum plasterboard substrate A2-s-1-d0 reaction to fire class and classification is valid for product mounting on substrates at least reaction to fire class A2-s-1-d0.



Figure 3. Sample 1 before the test.



Figure 4. Sample 1 at the tenth minute of the test.

Plywood and timber of such species as a larch and spruce were used as the materials of the samples. The species of timber were indicated in the laboratorian protocols. Thickness of the samples changes within the limits from 17 to 19 mm. The following types of the fire protection were considered:

1. Aqueous alkaline solution of sodium silicate $\text{Na}_2\text{O}(\text{SiO}_2)_n$ is a viscous substance of the grey colour without admixtures. It decrease the fire hazard of timber and it efficiency depends on the amount of the borrowed layers. The samples shown on Fig. 3-5 were treated by three layers.
2. Priming on the base of water glass in two layers and lacquer on the base of stirol-acryl resin, melamin and paraffin chlorine (three layers).
3. Lacquer with the decreased combustability consisting from the stirol-acryl resin, ammonoum poliphosphat melamin and paraffin chlorine (three layers). The lacquer is analogous to the same for the sample 2.
4. Lacquer on the base of carbomideformaldehyde resin with the admixture of classic fire retardants (three layers) [22]. A homogeneous suspension with the colours from white to pale yellow without external admixtures. The completed finishing has a lustre and is turbid. The charring of the fire-protective layer occurs under the fire action. The fire protective layer gat a structure of the foamed

coil and the surface of the material is protected from the influence of oxygen (Fig. 6). So, process of combustion is retarded.



Figure 5. Sample 1 at the end of the test.



Figure 6. Sample 4 – bloating of the lacquer.

5. Intumescent water based paint (two layers). The high porous foamed coil is developed at the temperature in 300°C and it protect the structure from the further heat action. The paint is a white color finedispersion suspension of functional admixtures and a pigment in the polivinilacetate dispersion or an acryle latex with admixture of several additional agents [22].
6. Traditional impergnation on the base of the soluble salts which are based on the roasted carbonate of potassium. The fire retardant is a color-less liquid with non-sufficient precipitate. The fire retardant is applied on the surface or the protected material is deeply impergnated under pressure. It fire retarding action is joined with ability of the fire retardants to develop the protective layer on the surface of the timber and to produce non-combustable gases which prevents expansion of the fire and it penetration in the protected material. The effect is obtained by the retarding if the fire expansion by the surface of protected material in the case if surface impergnation.
7. Impergnation «NEOHIM», produced by the Russian company «NEOHIM» LTD, is the water based solution with the fire retardants. Impergnation «NEOHIM» possess an effect of intumescention (Fig. 7). The samples shown on the Fig. 7 are made of the larche.



Figure 7. Development of foamed coil after the testing of sample 7.

8. Impergnation Palonot. The content is patented [23], it includes the water based solution of the fire retarding material «PALONOT F1», which is produced by the company Palonot, Finland. It contains

acids with the high content of phosphorus (30.1 %). Using of the ethanolamine as the nitrogen containing compounds is in the base impregnation Palonot application. The components are used in the proportion which possess a synerhism in case of the fire protective action. The specimens treated by the fire retardant Palonot F1 were produced of the birch plywood FSF. Peculiarities of assembling in accordance with the protocol of the test: valid for product mounting with air gap between product and substrate. Valid also product mounting on substrates without air gap.

9. Water based impregnation Flamex, which is produced by the Norwegian company Thermax as. The water based impregnation Flamex contains amino phosphates (30–60) %, amino chlorides (1–5) %, carbomide (5–10)%, glycerine (1–5)% and other admixtures. The specimens with the thickness in 21 mm were made from the spruce timber. Peculiarities of assembling in accordance with the protocol of the test: valid for product mounting with or without air gap between product and substrate, for ventilated and unventilateted applications.

The authors possess the following information about group of combustability for the tested specimens [23]. One of the targets for the test was determination of one of the four group of combustability. The groups were determined as follows:

- Group of combustability 1 – slightly combustible materials, which are not burning without source of fire. The materials produce the smoke gases with the temperature up till the 135°C in case of burning. The length of the damaged area does not exceeds the 65 %. Only 20% of the material mass can be destroyed by the fire action.
- Group of combustability 2 – medium combustible materials, which are burning without source of fire not longer, than half of the minute. The nominal tempherature of the developed smoke gases is equal to 235°C. The length of the damaged area does not exceeds the 85 %. Only 50 % of the material mass can be destroyed by the fire action.
- Group of combustability 3 – normally combustible materials, which are burning without source of fire not longer, than five minutes. The nominal tempherature of the developed smoke gases is equal to 450°C. The length of the damaged area does not exceeds the 85%. Only 50 % of the material mass can be destroyed by the fire action.
- Group of combustability 4 – strongly combustible materials, which are burning without source of fire not longer, than five minutes. The nominal tempherature of the developed smoke gases exceeds 450°C. The length of the damaged area does not exceeds the 85 %. Only 50 % of the material mass can be destroyed by the fire action.

Unfortunately, such parameters as a combustability, total smoke production, fire growth rate and gase toxicity rate (on the combustible timber and noncombustible asbestos plates) are unknown. So the class of the fire hazard from 0 to 5 in accordance with the Russian classification can not be determined. The tests for the determination of the group of combustability should be conducted for the structural materials exclude the finishing coverings of the ceilings and carpet coverings in the case if the material should be certified in the field of the fire safety.

The considered in the course of current study samples related to 1–2 groups of combustability. It is slightly combustible materials on the noncombustable base.

The parameters determined by the SBI method and by the method of determination of combustability groups [23] are shown in the Table 1. Several parameters determined by the SBI method are shown on the Fig. 8–13 dependently from the duration of the tests.

3. Results and Discussion

Table 1. Results of the specimens testing by the method SBI and its comparison with the group of combustibility [23].

Investigated parameters and classification in EN and Russia	Sample 1.	Sample 2.	Sample 3.	Sample 4.	Sample 5.	Sample 6.	Sample 7.	Sample 8.	Sample 9.
Expenditure on the board (g/m ²) big / small	336 / 346	252+542 / 261+486	410 / 400	486 / 393	691 / 533	303 / 253	250 / 250	240 / 240	200
FIGRA _{0.2}									
- fire growth rate indices (W/s)	268.63	2948.78	2729.07	76.40	49.78	200.83	31.6	21.9	95.0
FIGRA _{0.4} (THR(t) threshold of 0.4MJ)	268.63	2659.13	2729.07	74.76	30.41	186.35	30.5	21.9	66.7
THR ₆₀₀									
- total heat production (MJ)	20.101	13.997	6.531	11.70	2.602	21.483	3.8	3.0	5.4
SMOGRA									
- smoke growth rate (m ² /s ²)	15.82	101.28	88.28	32.93	13.58	9.94	-	1.4	7.9
TSP _{600s}									
- total smoke production (m ²)	163.13	60.88	79.89	152.91	48.66	97.33	33.0	34.9	41.9
Group of combustibility GOST 32244 [24]	1	2	2	1	1	2	-	-	1
Supposed class EN 13501-1	D s2 d0	E s2 d0	E s2 d0	C s2 d0	A2/B s1 do	D s2 do	A2/B s1 do	A2/B s1 do	B s1 d0

Note. The results for the sample 9 were absent in the protocol of the tests; «-» – results are unknown; FIGRA – maximum relation $HRR_{cp}(t)/(t - 300)$, multiplied by 1000. The maximum relation should be determined when the threshold levels of HRR_{cp} and THR were exceeded only. Indices of FIGRA is equal to zero if one or the both of its threshold levels were not exceeded during the time of action. Two different THR threshold values are used, which give finally FIGRA 0,2MJ and FIGRA 0,4MJ.

Basing on the results shown in Table 1, three types of fire protection are strongly differed: the water glass (nonorganic material), lacquers with the decreased combustibility and paints, which are close to water impregnations so as water impregnations.

Traditional impregnation on the base of the soluble salts which are based on the roasted carbonate of potassium (sample 6) possess the worst fire protective properties among the recently developed impregnations. The maximum smoke growing rate (SMOGR), as it was expected, was observed for the fire protections with the organic components. The water glass also shows high maximum smoke growing rate (sample 1), what can be explained by the rapid combustion of the specimen made of pine wood.

The specimens 2, 3 and 6 are related to the medium combustible materials of group of combustibility 2 and possess the enough high fire rate growth indexes FIGRA_{0.4}. But the specimen 1 also possess the fire rate growth index equal to 268.63 W/s. Foamed paint containing the organic combustible components, which was used for treatment of the sample 5, have the low values of all the parameters due to the bloating effect.

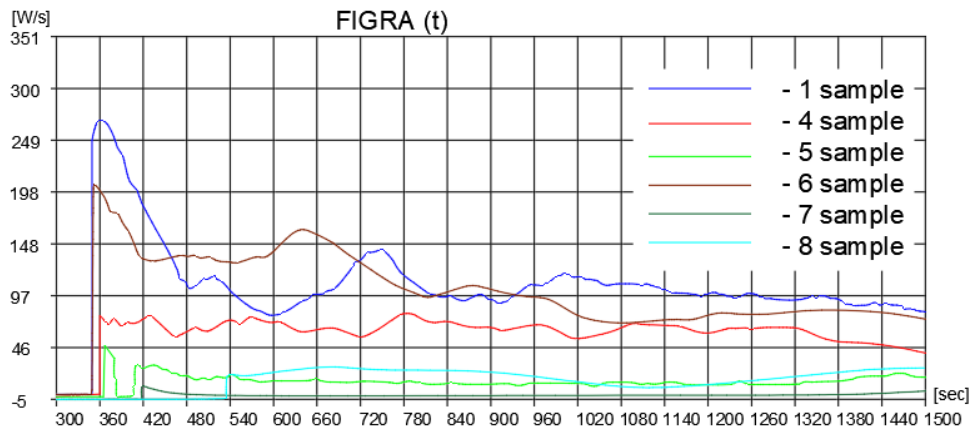


Figure 8. Fire growth rate indices FIGRA as a function of the time for the samples 1 and 4-8.

The fire growth rate indices FIGRA as a function of the time has a shock type shape for all the samples. The sample 1 is characterized by the highest fire growth rate indices probably due to the combustibility of the pinewood, which was used as a base material.

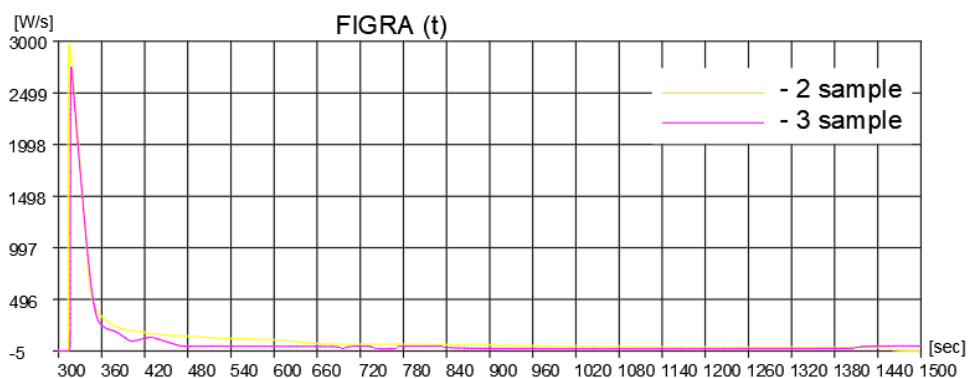


Figure 9. Fire growth rate indices FIGRA as a function of the time for the samples 2 and 3.

The base of the water glass does not have a significant influence on the fire growth rate indices FIGRA. The rapid shock in 300-540 s corresponding to the heat emission in 2.5–3 kW/s was observed at the initial stage. Then the fire growth rate indice tends to zero due to the fusion of the top layer and development of noncombustible gases. The water glass protective layer did not allows the heat emission. The small shock in 360 s than slightly decreased 2 times with the small oscillations, as it is shown on the chart. The similar character of the chart with the shock in 350 swas observed for the sample 6. The chart of the sample 4 has the shock starting from zero on the 360-th second and than it developed with the small oscillations from 46 to 97 Wt/s. The chart of the sample 8 has the similar shape with the shock on the 540-th second up to 22 W/s and than the value of the fire growth rate was stable. The graph for the sample 5 has two shocks at 360-th and 420-th seconds and than it has the shape similar to the grapf for the sample 4 with the mean value of the fire growth rate indices FIGRA equal to 30 W/s.

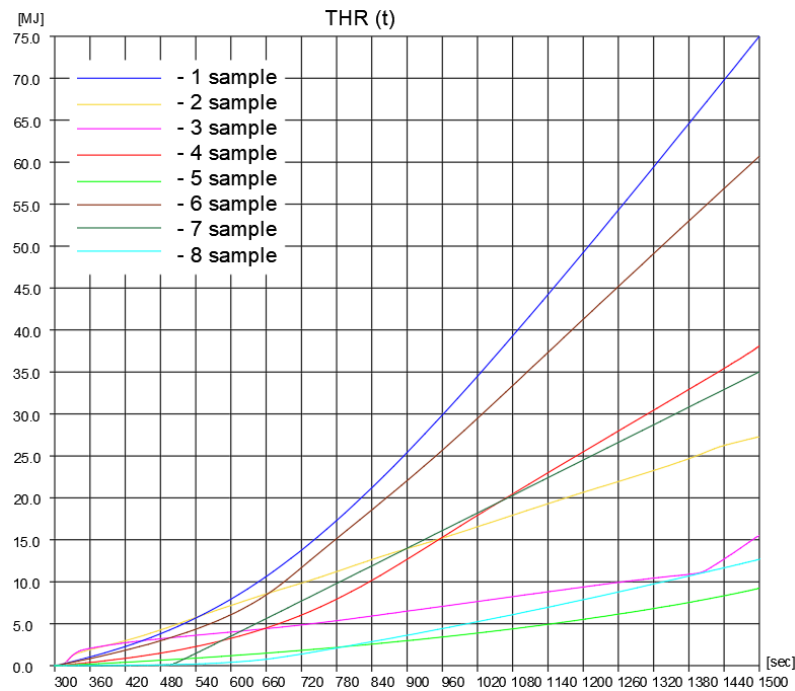


Figure 10. Total heat release THR as the function from the time.

All the charts shown on the Fig. 10 shows that the total heat releases are the directly proportional to the time. The maximum heat release was observed for the sample 1 and sample 6 with the fire protection of the water glass and salt impregnation due to the constant heat release. The least heat release and least temperature of combustion were observed for the sample 4.

The fire growth rate indices quickly decreases and process of combustion developed more slowly for the samples 2 and 3. The samples 5 and 8 have the minimum fire growth rate indices and, correspondingly, minimum total heat releases.

The direct dependence between the fire growth rate indices and total heat release was not observed for the sample 7. The mean value of the total heat release corresponds to the minimum value of the fire growth rate indices.

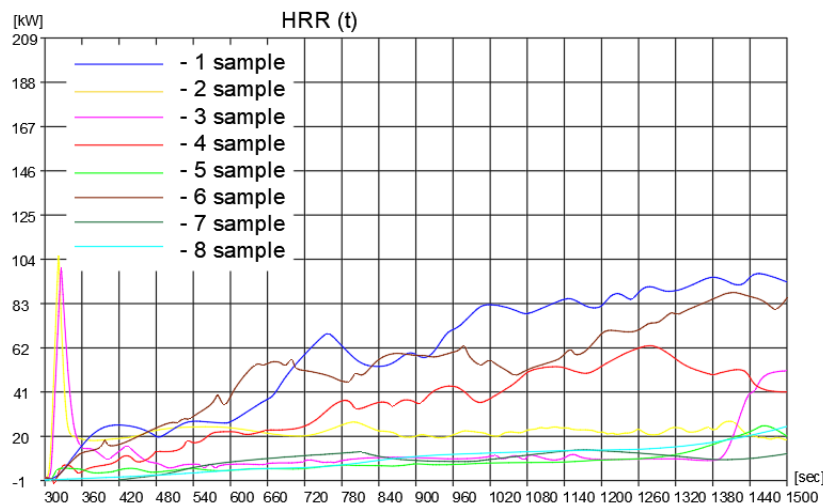


Figure 11. Total heat release rate HRR as the function from the time.

The total heat release rate for the samples 1, 6 and 8 is growing gradually with the time due to warming and damages of the protective layer. The charts for the samples 2 and 3 repeat the dependences of FIGRA on the time, which are shown on the Fig. 9. The shock in 300-360 s was observed at combustion and then the fire growth rate indices rapidly decreases due to the limiting of the oxygen level due to the changing of the structure of the protective layer.

The rapid increase of the fire growth rate indices was observed at the final stage of the testing of sample 3 (1380–1500 s), which is based by the charring of the protective layer and ending of it functions.

The dependence obtained for the sample 4 shows that the total heat release rate is directly proportional to the time until the 1260-th second and start to decrease than.

The sample 5 was characterized by the constant in the time total heat release rate with the slight increase starting from the 1320-th second. The total heat release rate for the sample 7 is growing till the 700-th second and then was constant with the non-sufficient oscillations.

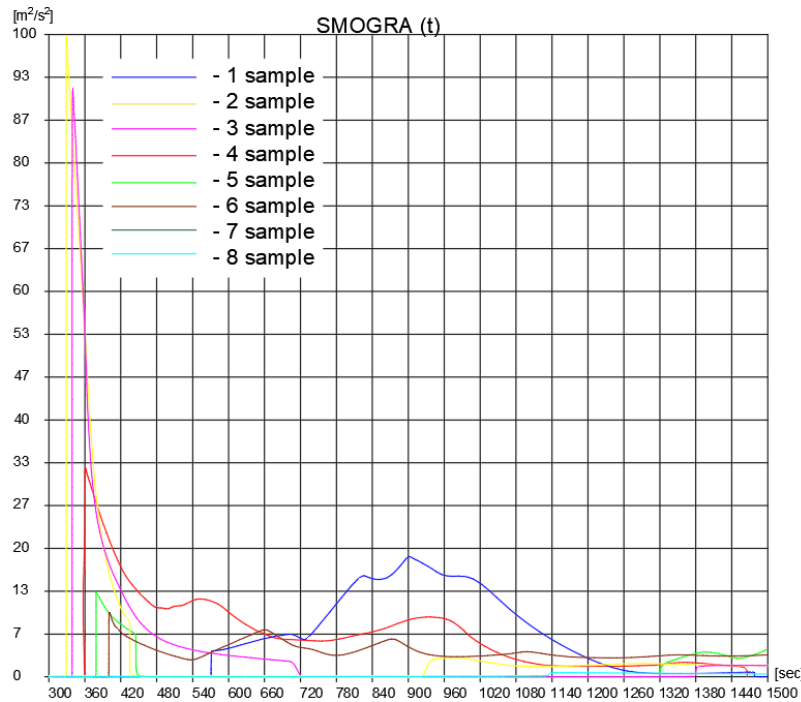


Figure 12. Smoke growth rate SMOGRA as the function from the time.

The smoke growth rate as a function from the time for the samples from 1 to 8 are shown on the Fig. 12. The dependences obtained for the samples 2 and 3 repeat the shape of the dependences obtained for the fire growth rate indices due to the charring of the upper layer and decrease the amount of the oxygen on the surface of the protected material. The smoke growth rate impetuously decreases in the case.

The dependence obtained for the sample 1 shows the slight increase of the smoke growing rate due to the surface warming with the further decrease. The dependences obtained for the samples 4, 5 and 6 have the shocks from 360 to 420 s. The smoke growth rate is slightly decrease until zero at the 1500-th second for the sample 4. The smoke growth rate is equal to zero starting from the 420-th second and slightly increase from 1340-th second for the specimen 5. The dependence of the smoke growth rate is slightly decreases with the no significant oscillations for the sample 6. The dependence obtained for the sample 8 is characterized by the small shock on the 1100-th second. It reaches a maximum in $1.8 \text{ m}^2/\text{s}^2$, what is the minimum value of the smoke growth rate in comparison with the other tested specimens.

The dependence for the sample 7 was not shown, so as smoke growth rate is insufficient and threshold sensitivity was not obtained.

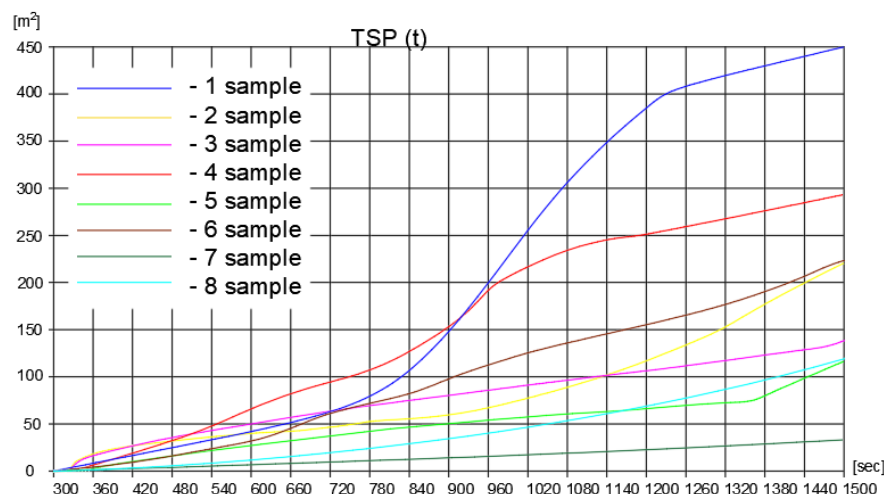


Figure 13. Total smoke production TSP as the function from the time.

The maximum total smoke production observed for the sample 4 due to the existence of the organic substances in the content of the fire protective material. The rapid increase of the total smoke production for the sample 1, which was treated by the water glass, on the 540-th second can be explained by the charring of the protective layer and firing of the base made of the pine wood with the high content of the resin.

Investigations conducted by the SBI method of the timber samples of the same type and assembling scheme probably, will enable to identify the content of fire protective impregnations (paints and lacquers) at the same methods of the specimens treatment. Research on fire retardants for wood-plastic composites has been attracting more attention in recent years; however, most results are preliminary because of the difficulty in identifying or formulating a fire-retardant system that is effective for both wood and plastics [25–29].

4. Conclusions

1. Correlation between the parameters determined by the European and Russian standards for classification of the fire hazard of the structural materials is difficult for evaluation due to the difference in the choice of the values of the criterias, which are necessary for the classification. The additional data characterizing combustibility, smoke growth rate, fire growth rate indices and materials toxicity are necessary. Additional tests should be conducted at the similar conditions to get the information for the more precise comparison of the materials. The type of base, existence or absence of the air gap, spice of timber, its treatment should be considered as the conditions for the test.

2. Composition on the base of the acryl resin has a significant influence at the fire growth rate indices FIGRA (W/s) and the smoke growth rate SMOGRA (m^2/s^2) at the initial stage of fire. The maximum values of the FIGRA and SMOGRA observed for the nine specimens differed by the base materials and fire protection, were equal to 2948.78 W/s and 101.28 m^2/s^2 , correspondingly.

3. The minimum values of the parameters were obtained for the water based bloated paint used as the fire protection. The paint expenditure which is necessary for the treatment of the board was the maximum at the same time and equal to 691 and 533 g/m^2 for the big and small boards, correspondingly.

4. The impregnations NEOMID 450-1 and Palonot have enough high characteristics as the fire protection which is characterized by the minimum smoke growth rate. It was equal to 1.4 m^2/s^2 for the Palonot and low undetermined on the chart value of smoke growth rate for the NEOMID 450-1.

5. The further investigations are necessary for the determination of fire protective materials consumption, defining of their types by the development of protective films and influence of the content on the technical characteristics of protected timber structures in case of fire, gotten by the SBI method.

References

1. Gravit M.V., Nedryshkin O.V., Vaytitskiy A.A., Shpakova A.M., Nigmatullina D.G. Pozharno-tehnicheskiye kharakteristiki stroitelnykh materialov v yevropeyskikh i rossiyskikh normativnykh dokumentakh. Problemy garmonizatsii metodov issledovaniya i klassifikatsii. Pozharovzryvobezopasnost/Fire and Explosion Safety. 2016; 25(10):16-29. <https://DOI.org/10.18322/PVB.2016.25.10.16-29>
2. Trushkin D.V. Problems of classification of construction materials on fire hazard. part 2. comparative analysis of experimental methods for fire hazard assessment of construction materials accepted in russia and the european union countries. determination of combustibility for construction materials. Pozharovzryvobezopasnost/ Fire and Explosion Safety, 2014. 23(4). Pp. 24–32.
3. Gravit, M., Vaititckii, A., Imasheva, M., Nigmatullina, D., Shpakova, A. Classification of fire-technical characteristic of roofing materials in European and Russian regulation documents. MATEC Web of Conferences 53, 01031, 2016. DOI: 10.1051/mateconf/20165301031.
4. Khasanov I.R. Osobennosti pozharnej opasnosti zdaniy iz derevyannykh konstrukcij [Features of fire hazard of buildings made of wooden structures]. Pozharovzryvobezopasnost/Fire and Explosion Safety. 25 (11). 2016. Pp. 51–60. DOI: 10.18322/PVB.2016.25.11.51-60.
5. European Standard EN (SBI) 13823-2010. Tests of building materials on fire. Building products, except for flooring materials, are exposed to thermal heat from a gas burner.
6. European Standard EN13501-1-2007. Classification of building products and materials for fire safety.
7. Polishchuk, E.Yu., Sivenkov, A.B., Kenzhehan, S.K. Heating and charring of timber constructions with thin-layer fire protection. Magazine of Civil Engineering, 2018. 81(5). Pp. 3–14. DOI: 10.18720/MCE.81.1.
8. Buka-Vaivade, K., Serdjus, D., Goremikins, V., Pakrastins, L., Vatin, N.I. Suspension structure with cross-laminated timber deck panels. Magazine of Civil Engineering, 2018. 83 (7). Pp. 126–135. DOI: 10.18720/MCE.83.12.
9. Gravit, M.V., Serdjus, D., Bardin, A.V., Prusakov, V., Buka-Vaivade, K. Fire Design Methods for Structures with Timber Framework. Magazine of Civil Engineering, 2019. 85(1). Pp. 92–106. DOI: 10.18720/MCE.85.8.
10. Lipinskas, D., Mačiulaitis, R. Further opportunities for development of the method for fire origin prognosis. Journal of Civil Engineering and Management, 2005. 11(4). Pp. 299–307. DOI: 10.3846/13923730.2005.9636361.
11. Bartlett, A.I., Hadden, R. M., Bisby, L. A. A review of factors affecting the burning behavior of wood for application to tall timber construction. Fire Technology, 2018. Pp. 1–49. DOI: 10.1007/s10694-018-0787-y.
12. Ostman, B., Mikkola, E. European Classes for the Reaction to Fire Performance of Wood Products (except Floorings). Holz als Roh- und Werkstoff, 2004. 36 p. DOI: 10.1007/s00107-006-0116-x.
13. Frangi, A., Fontana, M. Fire safety of multistorey timber buildings. Proceedings of the Institution of Civil Engineers. Structures and Buildings. 2010. 163(4). Pp. 213–226. DOI: 10.1680/stbu.2010.163.4.213.

14. Ostman, B., Tsantaridis, L., Mikkola, E., Hakkarainen, T., Nilsen, T.N., Evans, F., Grexa, O. Durability of fire retardant wood. New test methods and round robin. Nord test-project 1527-01. Stockholm, 2002. 38 p.
15. Steen-Hansen, A., Kristoffersen, B. Prediction of fire classification for wood based products. A multivariate statistical approach based on the cone calorimeter. *Fire and Materials*. 2007. 31(3). Pp. 207–223. DOI: 10.1002/fam.934.
16. Messerschmidt, B. The capabilities and limitations of the single burning item (SBI) test. *Fire and Building Safety in the Single European Market*. 2008. Pp. 70–81.
17. White, R.V. Testing and Evaluation of Fire-retardant-treated Wood Products. *Lignocellulosic Fibers and Wood Handbook*. 2016. Vol. 23. Pp. 583–593. DOI: 10.13073/0015-7473-60.7.668.
18. Sundstrom, B., Axelsson, J. Development of a common European system for fire testing of pipe insulation based on EN 13823 (SBI) and ISO 9705 (Room/Corner Test). Swedish Natl. Test. Res. Institute. Fire Technology SP report 2002:21, 2002. 101 p.
19. Axelsson, J., Van Hees, P. New data for sandwich panels on the correlation between the SBI test method and the room corner reference scenario. *Fire and Materials*. 2005. Vol. 29. №1. Pp. 53–59. DOI: 10.1002/fam.879.
20. Commission 2000/147 / YeS. CWFT - Classification without further testing. Commission decisions published in Official Journal 2003-2007 for five wood products.
21. NB-CPD/SH02/12/096. Reaction to fire testing and classification of untreated and fire retardant treated wood construction products. Coordination of the Group of Notified Bodies for the Construction Products Directive 89/106/EEC, 2012. 13 p.
22. Korotkov, A.S., Gravit, M.V. 3D-map modelling for the melting points prediction of intumescent flame-retardant coatings. SAR and QSAR in Environmental Research. 2017. 28(8). Pp. 677–689. DOI: 10.1080/1062936X.2017.1370725.
23. Patent FI 127667B. Finland, Kilterinkulma 2 D1, 01600 VANTAA. «PALONOT OY». Kukkonen Jari, Nissinen Timo. 09.03.2017. 41 p.
24. Interstate standard (countries of the independent community) GOST 30244 Building materials. Methods for combustibility test.
25. Fengqiang Wang, Qingwen Wang, and Xiangming Wang (2010) Progress in Research on Fire Retardant–Treated Wood and Wood-Based Composites: A Chinese Perspective. *Forest Products Journal*: November/December, Vol. 60, No. 7-8, pp. 668-678. <https://DOI.org/10.13073/0015-7473-60.7.668>
26. Hu La, Chen Zhilin, Fu Feng and Fan Mizi. (2015) Investigation of Factory Fire Retardant Treatment of Eucalyptus Plywood. *Forest Products Journal* 65:7-8, 320-326.
27. Palatinskaya I.P., Borovik S.I., Orlov A.A., Dementyeva E.S., Sintiyeva V.A., Redkina N.E. Study of Influence of Fire Retardant Coatings on Expanded Polystyrene Properties. *Bulletin of the South Ural State University. Ser. Construction Engineering and Architecture*. 2018, vol. 18, no. 1, pp. 47–52. (in Russ.). DOI: 10.14529/build180104.
28. Zemitis J., Terekh M. Optimization of the level of thermal insulation of enclosing structures of civil buildings. *MATEC Web of Conferences* 245, 06002 (2018).
29. Saknite, T., Serdjuks, D., Goremikins, V., Pakrastins, L., Vatin, N.I. Fire design of arch-type timber roof. *Magazine of Civil Engineering*. 2016. 64(4). Pp. 26–39. DOI:10.5862/MCE.64.3.

Contacts:

Marina Gravit, marina.gravit@mail.ru

Dmitrijs Serdjuks, Dmitrijs.Serdjuks@rtu.lv

Nikolai Vatin, vatin@mail.ru

Yuri Lazarev, Lazarev-yurij@yandex.ru

Maria Yuminova, maria.yuminova@mail.ru

© Gravit M.V., Serdjuks D., Vatin N., Lazarev Y.G., Yuminova M.O., 2020



DOI: 10.18720/MCE.95.3

Stability of fixed-fixed shallow arches under arbitrary radial and vertical forces

L.P. Kiss*

Institute of Applied Mechanics, University of Miskolc, Miskolc, Hungary

* E-mail: mechkiss@uni-miskolc.hu

Keywords: buckling, stiffness, strength, design, composite materials

Abstract. In the present paper the planar stability of fixed-fixed shallow circular arches is investigated. The arches are made of linearly elastic, functionally graded material and are subject to a concentrated radial or vertical dead force at an arbitrary position. To describe the behaviour, the one-dimensional Euler-Bernoulli kinematic hypothesis is used. The effect of the bending moment on the membrane strain is incorporated into the model. The related coupled differential equations of the problem are derived from the principle of virtual work. Exact solutions are found both for the pre- and post-buckling displacements. Closed-form analytical solution is given for the buckling load when the load is radial while for vertical force, the solution is numerical. It is found that for fixed-fixed members, only limit point buckling is possible. Such shallow arches are not sensitive to small imperfections in the load position or in the load direction. It turns out that the material composition and geometry have significant effects on the behaviour and buckling load. If the load is placed far enough from the crown point, the load bearing abilities become better than for crown-load. Comparisons with an analytical literature model and commercial finite element software confirm the validity of the new findings.

1. Introduction

Curved members (arches, shells) are often used in engineering applications, e.g., in aerospace structures or in civil engineering structures [1, 2]. These elements are preferred because of their advantageous mechanical behaviour under various loading conditions and partially because of their favourable design.

Compared to classical homogeneous materials, composites have such advantageous properties like the increased durability or reduced weight [3–5]. Functionally graded materials (FGM) have a further notable benefit, that is the smooth stress distribution because of the continuously changing material properties. For these previous reasons, such composite materials are being used more and more frequently [6–9] by civil engineers. Thus, it is important to be able to predict the mechanical behaviour of such members.

Buckling is a well-known phenomenon, which can occur for various structural members [10–12]. Thus, the in-plane stability of arches is not a new topic as there is a bunch of available works, like [13–15] in the open literature. It is well-known that their behaviour is nonlinear since the pre-buckling deformations are significant. There are many arch problems that have been solved either analytically or by means of a numerical method [16–22]. These issues involve the effect of the foundation stiffness, remote unconnected equilibria, inclusion of geometric imperfections, elastic horizontal and rotational end restraints. The preferred numerical methods include the analog equation method, the modified Riks method and the Galerkin method as well.

Studies [23–27] report about analytical solutions on the stability of shallow arches with multiple stiffness regions along the centroidal axis. The Euler-Bernoulli hypothesis is considered and various load and support conditions are investigated. Articles [28–30] focus on FGM arches analytically using the classical shallow arch theory.

It is found that simple crown-point loads are preferred in the literature. However, in practice, other load positions are also possible. Early articles [31, 32] investigate the effect of the load position on arches but the later one neglects the effect of the axial compressive force. There is a recent article series about the in-plane stability of arches under arbitrary concentrated radial load [33–35] by using the same hypotheses as in [36–37]. These works present analytical investigations for homogeneous material but the effect of the bending

Kiss, L.P. Stability of fixed-fixed shallow arches under arbitrary radial and vertical forces. Magazine of Civil Engineering. 2020. 95(3). Pp. 31–41. DOI: 10.18720/MCE.95.3



This work is licensed under a [CC BY-NC 4.0](https://creativecommons.org/licenses/by-nc/4.0/)

moment on the membrane strain is neglected. An improved kinematical hypothesis is presented and evaluated in the likes of [38–40].

According to the literature review, it is an open question how fixed-fixed FGM shallow arches behave under a radial or vertical dead load at an arbitrary position. The aim of the current article is to find the answer to this issue. The related tasks, therefore, are:

1. to introduce a new geometrically nonlinear beam model, incorporating the effect of the bending moment on the membrane strain;
2. to find the related static equilibrium equations using a suitable variational principle and to solve these coupled equations in closed-form;
3. to derive the buckling equations and investigate the possibility and conditions of bifurcation and limit point buckling;
4. to show the effect of various geometrical and material parameters on the buckling load;
5. to verify the outcomes, i.e., compare the new results with the literature and finite element computations.

2. Methods

2.1. Kinematics

A fixed-fixed shallow FG circular arch is considered. Its (E -weighted) centroidal axis is shown in Fig. 1. The axis ξ coincides with the circumferential direction, while the cross-sectional coordinates are η, ζ . The cross-section is symmetric to ζ , i.e., η is a principal axis. The initial radius of the centroidal axis is ρ and the included angle of the arch is 2ϑ with ϕ being the angle coordinate. The external load Q is a dead concentrated force at $\phi = \alpha$ and is either radial ($\gamma = 0$) or vertical ($\gamma = \alpha$). The FG material composition is a mixture of metallic (subscript m) and ceramic (subscript c) phases. The material constituents – like the Young modulus E are assumed to follow a power-law distribution (e.g., the Voigt rule of mixture) along the thickness as

$$E(\zeta) = (E_c - E_m) \left(\frac{\zeta}{b} \right)^k + E_m \quad (1)$$

with b being the height of the cross-section and k is the volume fraction index [42].

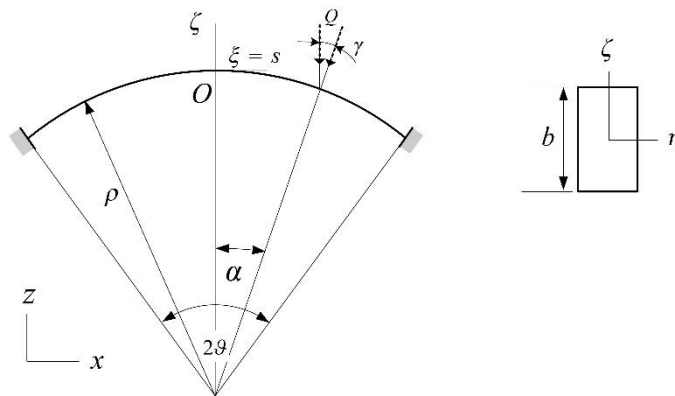


Figure 1. A fixed-fixed shallow arch with radius ρ and included angle 2ϑ under a concentrated radial/vertical load Q .

Using the Euler-Bernoulli hypothesis, the longitudinal strain at an arbitrary point is [41] expressed by

$$\varepsilon_{\xi} = \frac{\rho}{\rho + \zeta} \left[\frac{du}{ds} + \frac{w}{\rho} + \zeta \left(\frac{du}{\rho ds} - \frac{d^2w}{ds^2} \right) \right] + \frac{1}{2} \left(\frac{u}{\rho} - \frac{dw}{ds} \right)^2, \quad (2)$$

with the nonlinear membrane strain – $\zeta = 0$ – and the cross-sectional rotation being

$$\varepsilon = \frac{du}{ds} + \frac{w}{\rho} + \frac{1}{2}\psi^2; \quad \psi = \frac{u}{\rho} - \frac{dw}{ds}. \quad (3)$$

The circumferential and lateral displacements are denoted by u and w .

According to the Hooke law, the axial force and bending moment are as follows [41]:

$$N = \int_A \sigma_\xi dA = E_1 \varepsilon - \frac{E_3}{\rho} \left(\frac{1}{\rho} \frac{du}{ds} - \frac{d^2 w}{ds^2} \right), \quad (4a)$$

$$M = \int_A \zeta \sigma_\xi dA = -E_3 \left(\frac{d^2 w}{ds^2} + \frac{w}{\rho^2} \right), \quad N + \frac{M}{\rho} = E_1 \varepsilon. \quad (4b)$$

Thus, clearly, the effect of the bending moment on the membrane strain is accounted, unlike in some previous models. In the expressions of the inner forces the various stiffnesses are defined by

$$E_j = \int_A E \zeta^{j-1} dA. \quad (5)$$

At the points of the centroidal axis $E_2 = 0$.

2.1.1 Equilibrium equations

The principle of virtual work is used to find the nonlinear pre-buckling equilibrium configuration. It requires that equation

$$\int_V \sigma_\xi \delta \varepsilon_\xi dV - \mathbf{Q} \cdot \delta \mathbf{w} \Big|_{\phi = \alpha} = 0 \quad (6)$$

to be satisfied by any kinematically admissible virtual field $\delta(\cdot)$. Due to the shallowness of the arch, only the virtual work done by the external force on the radial displacement field is accounted. From the above principle, the following coupled differential equation (DE) system can be found [40]:

$$\frac{dN}{ds} + \frac{1}{\rho} \left[\frac{dM}{ds} - \left(N + \frac{M}{\rho} \right) \psi \right] = 0, \quad (7)$$

$$\frac{d}{ds} \left[\frac{dM}{ds} - \left(N + \frac{M}{\rho} \right) \psi \right] - \frac{N}{\rho} = 0. \quad (8)$$

These equations can be given in terms of the dimensionless displacement $W = w/\rho$ and the notation $d(\cdot)/ds = (\cdot)'$ as

$$\varepsilon' = 0, \quad W'''' + (\chi^2 + 1)W'' + \chi^2 W = \chi^2 - 1, \quad (9)$$

with the strain- and geometrical-material parameters being defined as

$$\chi^2 = 1 - \mu\varepsilon; \quad \mu = \frac{E_1 \rho^2}{E_3} = \frac{\rho^2}{r^2}; \quad r^2 = \frac{E_3}{E_1}. \quad (10)$$

So, the effect of the material composition is incorporated into the model through these quantities. Furthermore, it is found that the membrane strain is constant. Equilibrium equations are comparable to, e.g., [28, 43].

Focusing now on the post-buckling equilibrium state, the typical increments – noted by a hat symbol ($\hat{\cdot}$) – are [38]

$$\hat{\varepsilon}_\xi = \frac{\rho}{\rho + \zeta} \left[\frac{d\hat{u}}{ds} + \frac{\hat{w}}{\rho} + \zeta \frac{d\hat{\psi}}{ds} \right] + \psi \hat{\psi}, \quad \hat{\psi} = \frac{\hat{u}}{\rho} - \frac{d\hat{w}}{ds}, \quad (11)$$

$$\hat{\varepsilon} = \frac{d\hat{u}}{ds} + \frac{\hat{w}}{\rho} + \left(\frac{u}{\rho} - \frac{dw}{ds} \right) \left(\frac{\hat{u}}{\rho} - \frac{d\hat{w}}{ds} \right), \quad (12)$$

$$\hat{N} = E_1 \hat{\varepsilon} - \frac{\hat{M}}{\rho}, \quad \hat{M} = -E_3 \left(\frac{d^2 \hat{w}}{ds^2} + \frac{\hat{w}}{\rho^2} \right). \quad (13)$$

From the principle of virtual work for the buckled equilibrium configuration, equation

$$\int_V \sigma_{\xi}^* \delta \varepsilon_{\xi}^* dV - \mathbf{Q}^* \cdot \delta \mathbf{w}^* \Big|_{\phi=\alpha} = 0 \quad (14)$$

is to be satisfied. Here $(\)^* = (\) + (\hat{\ })$ is the sum of the pre- and post-buckling components of any quantity. The following DEs are found from this principle [41]:

$$\frac{d\hat{N}}{ds} + \frac{1}{\rho} \frac{d\hat{M}}{ds} - \frac{1}{\rho} \left(N + \frac{M}{\rho} \right) \hat{\psi} - \frac{1}{\rho} \left(\hat{N} + \frac{\hat{M}}{\rho} \right) \hat{\psi} = 0, \quad (15a)$$

$$\frac{d^2 \hat{M}}{ds^2} - \frac{\hat{N}}{\rho} - \frac{d}{ds} \left[\left(N^* + \frac{M^*}{\rho} \right) \hat{\psi} + \left(\hat{N} + \frac{\hat{M}}{\rho} \right) \hat{\psi} \right] = 0, \quad (15b)$$

which are actually

$$\hat{\varepsilon}' = 0, \quad (16)$$

$$\hat{W}'''' + (\chi^2 + 1)\hat{W}'' + \chi^2 \hat{W} = \mu \hat{\varepsilon} \left[1 - (W'' + W) \right], \quad \hat{W} = \hat{w} / \rho. \quad (17)$$

These results are again comparable to previous models, like [28, 44].

3. Results and Discussion

3.1. Solution – pre-buckling state

The following closed-form general solution was found to satisfy Eq. (9)₂

$$W_i(\phi) = \frac{\chi_i^2 - 1}{\chi_i^2} + C_{1i} \cos \phi + C_{2i} \sin \phi - \frac{C_{3i}}{\chi_i^2} \cos \chi_i \phi - \frac{C_{4i}}{\chi_i^2} \sin \chi_i \phi, \quad (18)$$

with $C_{1i} - C_{4i}$ being integration constants, χ_i being the membrane strain parameter defined by

$$\chi_i = \sqrt{1 - \mu \varepsilon_i} \quad (19)$$

and furthermore, here and now on, subscript $i = \{r, l\}$ if ϕ is $\{\geq \alpha; < \alpha\}$.

When the load is radial, the strain is constant on the whole centroidal axis while for vertical load, the strain has a jump at $\phi = \alpha$. The jump (discontinuity) magnitude is found from the variational principle as

$$\chi_l^2 = \chi_r^2 + \frac{2P \sin \gamma}{g}; \quad P = \frac{Q \rho^2 g}{2E_3} \quad (20)$$

with P being a dimensionless load. Thus, the average membrane strain – recalling (19) and (20) – is

$$\bar{\varepsilon} = -\frac{1}{\mu} \frac{(\chi_l^2 - 1)(g + \alpha) + (\chi_r^2 - 1)(g - \alpha)}{2g} \quad (21)$$

with $\chi_l = \chi_r$ for radial load. As a consequence, the solution for the displacement field is sought separately on the two sides of the external load. Based on the virtual work principle, the following boundary, continuity and discontinuity conditions are valid for the arch:

$$W_l|_{-g} = W_l'|_{-g} = W_r|_g = W_r'|_g = 0, \quad (22)$$

$$W_l|_\alpha = W_r|_\alpha \quad W_l'|_\alpha = W_r'|_\alpha, \quad (23)$$

$$W_l''|_\alpha = W_r''|_\alpha \quad -W_l'''|_\alpha + W_r'''|_\alpha = -\frac{2P \cos \gamma}{g}. \quad (24)$$

All these above fields are continuous except the third derivative, which is proportional to the shear force. It has a jump for both radial and vertical load. Substituting here solutions (18), the system of linear equations is found:

$$\begin{bmatrix} \cos g & -\sin g & -\frac{\cos \chi_l g}{\chi_l^2} & \frac{\sin \chi_l g}{\chi_l^2} & 0 & 0 & 0 & 0 \\ -\chi_l \sin g & -\chi_l \cos g & \sin \chi_l g & \cos \chi_l g & 0 & 0 & 0 & 0 \\ \cos \alpha & \sin \alpha & -\frac{\cos \chi_l \alpha}{\chi_l^2} & -\frac{\sin \chi_l \alpha}{\chi_l^2} & -\cos \alpha & -\sin \alpha & \frac{\cos \chi_r \alpha}{\chi_r^2} & \frac{\sin \chi_r \alpha}{\chi_r^2} \\ \chi_l \sin \alpha & -\chi_l \cos \alpha & -\sin \chi_l \alpha & \cos \chi_l \alpha & -\chi_r \sin \alpha & \chi_r \cos \alpha & \sin \chi_r \alpha & -\cos \chi_r \alpha \\ -\cos \alpha & -\sin \alpha & \cos \chi_l \alpha & \sin \chi_l \alpha & \cos \alpha & \sin \alpha & -\cos \chi_r \alpha & -\sin \chi_r \alpha \\ -\sin \alpha & \cos \alpha & \chi_l \sin \chi_l \alpha & -\chi_l \cos \chi_l \alpha & \sin \alpha & -\cos \alpha & -\chi_r \sin \chi_r \alpha & \chi_r \cos \chi_r \alpha \\ 0 & 0 & 0 & 0 & \cos g & \sin g & -\frac{\cos \chi_r g}{\chi_r^2} & -\frac{\sin \chi_r g}{\chi_r^2} \\ 0 & 0 & 0 & 0 & \chi_r \sin g & -\chi_r \cos g & -\sin \chi_r g & \cos \chi_r g \end{bmatrix} \cdot \begin{bmatrix} C_{1l} \\ C_{2l} \\ C_{3l} \\ C_{4l} \\ C_{1r} \\ C_{2r} \\ C_{3r} \\ C_{4r} \end{bmatrix} = \begin{bmatrix} -\frac{\chi_l^2 - 1}{\chi_l^2} \\ \frac{\chi_r^2 - 1}{\chi_r^2} - \frac{\chi_l^2 - 1}{\chi_l^2} \\ 0 \\ 0 \\ 0 \\ -\frac{2P \cos \gamma}{g} \\ -\frac{\chi_r^2 - 1}{\chi_r^2} \\ 0 \end{bmatrix}.$$

The coefficients C_{ji} can now be calculated in closed-form.

Because of equilibrium Eq. (9)₁, the membrane strain is constant on the centroidal axis, so it is equal to the average membrane strain given by:

$$\varepsilon = \bar{\varepsilon} = \frac{1}{g + \alpha} \int_{-g}^{\alpha} \varepsilon_l(\phi) d\phi + \frac{1}{g - \alpha} \int_{\alpha}^g \varepsilon_r(\phi) d\phi = \text{constant}. \quad (25)$$

Recalling Eq. (3) and assuming $w \gg u$ due to the shallowness, which is generally accepted in the literature [33], a quadratic equation in P is established for fixed-fixed shallow arches under arbitrary radial ($\chi_l = \chi_r$; $\gamma = 0$) load as:

$$G_0 + G_1 P + G_2 P^2 = 0. \quad (26)$$

The constants G_0 - G_2 are functions of $\mu, \alpha, \vartheta, \chi$. This previous equation can be solved analytically for any given strain-, geometrical and material parameter.

When the load is vertical – $\chi_l \neq \chi_r$; $\gamma = \alpha$ – the above equation becomes strongly nonlinear in the dimensionless load because of Eq. (20) and

$$H_0(\mu, \alpha, \gamma, \vartheta, P, \chi_l, \chi_r) = 0 \quad (27)$$

can only be tackled numerically.

3.2. Buckled equilibrium

The general solution to the inhomogeneous post-buckling equilibrium equation (17) is

$$\hat{W}_i(\phi) = D_{1i} \cos \phi + D_{2i} \sin \phi + D_{3i} \sin \chi_i \phi + D_{4i} \cos \chi_i \phi - \frac{\mu \hat{\varepsilon}_i}{2 \chi_i^3} \left(\frac{2}{\chi_i} + C_{3i} \phi \sin \chi_i \phi - C_{4i} \phi \cos \chi_i \phi \right) \quad (28)$$

with the unknown constants $D_{1i} - D_{4i}$. The related boundary and continuity conditions are

$$\hat{W}_l|_{-\vartheta} = \hat{W}_l'|_{-\vartheta} = \hat{W}_r|_{\vartheta} = \hat{W}_r'|_{\vartheta} = 0, \quad (29)$$

$$\hat{W}_l|_{\alpha} = \hat{W}_r|_{\alpha}, \quad \hat{W}_l'|_{\alpha} = \hat{W}_r'|_{\alpha}, \quad (30)$$

$$\hat{W}_l''|_{\alpha} = \hat{W}_r''|_{\alpha}, \quad \hat{W}_l'''|_{\alpha} = \hat{W}_r'''|_{\alpha} \quad (31)$$

with all the typical fields being continuous at $\phi = \alpha$ as there is no load increment ($\hat{Q} = 0$). These conditions determine an inhomogeneous linear equation system which can be solved in closed-form. According to (16), the strain increment is constant, thus, with (12) and the inequality $\hat{w} \gg \hat{u}$ used on (16) it is found that

$$\hat{\varepsilon} = \frac{1}{2\vartheta} \int_{-\vartheta}^{\vartheta} (\hat{U}' + \hat{W} + W' \hat{W}') d\phi. \quad (32)$$

It is again a quadratic equation in the dimensionless load when the force is radial:

$$J_0 + J_1 P + J_2 P^2 = 0 \quad (33)$$

with $J_1; J_2; J_3$ being functions of $\mu, \alpha, \vartheta, P, \chi$ and it leads to a strongly nonlinear relationship for vertical load:

$$K_0(\mu, \alpha, \gamma, \vartheta, P, \chi_l, \chi_r) = 0. \quad (34)$$

Solution for limit point (of snap-through) buckling can be evaluated for any geometry and material distribution by solving simultaneously nonlinear Eqs. (26); (33) for radial load and (27); (34) for vertical load. Or, alternatively, since limit points are local maxima on the equilibrium path [42], the very same results can be found by differentiating Eq. (26) or (27) with respect to the strain parameter.

In theory, it is also possible for fixed-fixed shallow arches under concentrated load to undergo bifurcation buckling [38]. During bifurcation, the load and membrane strain remain constant [36] and the arch buckles to an infinitesimally close bifurcation equilibrium configuration. In this case, solution to DE (17) with $\hat{\varepsilon} = 0$ is

$$\hat{W}_i(\phi) = S_{1i} \cos \phi + S_{2i} \sin \phi + S_{3i} \sin \chi_i \phi + S_{4i} \cos \chi_i \phi. \quad (35)$$

This solution and the conditions (29)–(31) determine a homogeneous linear system of equations. Nontrivial solution exists if the determinant of the coefficient matrix vanishes, therefore

$$\begin{vmatrix}
 \cos \vartheta & -\sin \vartheta & -\sin \chi_1 \vartheta & \cos \chi_1 \vartheta & 0 & 0 & 0 & 0 \\
 \sin \vartheta & \cos \vartheta & \chi_1 \cos \chi_1 \vartheta & \chi_1 \sin \chi_1 \vartheta & 0 & 0 & 0 & 0 \\
 \cos \alpha & \sin \alpha & \sin \chi_1 \alpha & \cos \chi_1 \alpha & -\cos \alpha & -\sin \alpha & -\sin \chi_r \alpha & -\cos \chi_r \alpha \\
 -\sin \alpha & \cos \alpha & \chi_1 \cos \chi_1 \alpha & -\chi_1 \sin \chi_1 \alpha & \sin \alpha & -\cos \alpha & -\chi_r \cos \chi_r \alpha & \chi_r \sin \chi_r \alpha \\
 -\cos \alpha & -\sin \alpha & -\chi_1^2 \sin \chi_1 \alpha & -\chi_1^2 \cos \chi_1 \alpha & \cos \alpha & \sin \alpha & \chi_r^2 \sin \chi_r \alpha & \chi_r^2 \cos \chi_r \alpha \\
 \sin \alpha & -\cos \alpha & -\chi_1^3 \cos \chi_1 \alpha & \chi_1^3 \sin \chi_1 \alpha & -\sin \alpha & \cos \alpha & \chi_r^3 \cos \chi_r \alpha & -\chi_r^3 \sin \chi_r \alpha \\
 0 & 0 & 0 & 0 & \cos \vartheta & \sin \vartheta & \chi_r^2 \sin \chi_r \vartheta & \chi_r^2 \cos \chi_r \vartheta \\
 0 & 0 & 0 & 0 & -\sin \vartheta & \cos \vartheta & \chi_r^3 \cos \chi_r \vartheta & -\chi_r^3 \sin \chi_r \vartheta
 \end{vmatrix} = 0$$

This determinant, in fact, yields the critical strain for bifurcation buckling. However, recalling the solutions of [33] and [38], it is clear that, for fixed-fixed shallow arches under a concentrated load, bifurcation buckling is possible only when $\alpha = 0$ and in this case, the bifurcation point is always located on the unstable equilibrium branch. It means that only limit point buckling can occur.

3.3. Analytical and numerical solutions

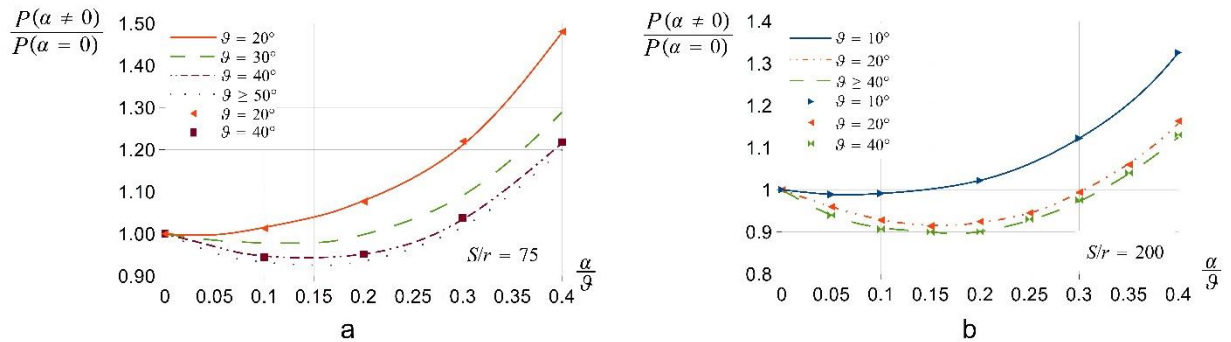


Figure 2. The critical load ratio for non-crown and crown loads in terms of the relative load position parameter α / ϑ for arches with: a – $S/r = 75$; b – $S/r = 200$.

First, the effect of the load position α on the lowest critical load is investigated for multiple semi-vertex angles ϑ . Results are plotted in Fig. 2a and 2b for two S/r ratios – S is the length of the centroidal axis and r is the E -weighted radius of gyration. $P(\alpha = 0)$ is the critical dimensionless load at the crown and $P(\alpha \neq 0)$ is the critical load when the force is placed elsewhere. Different line types are drawn for radial load while markers are used to show the findings for vertical force. When the load is in the small vicinity of the crown point $\alpha \ll 2\vartheta$ the buckling load changes (decreases) slowly for all the selected geometries. Thus, fixed-fixed arches, unlike pinned-pinned members [39], are not sensitive to small imperfections in the load position. In general, replacing the load from the crown makes the buckling load decrease for a while. Then it is always followed by an increase and if the load is exerted sufficiently far from the crown point, the load bearing abilities become better than for $\alpha = 0$. Overall, smaller included angle means smaller change in the buckling load. When $S/r = 75$, the semi-vertex angle and load position have greater effects compared to $S/r = 200$. Above a certain angle, the behaviour seems to become independent of the angle as well.

It is also found that in the investigated range it does not really matter if the load is vertical or radial, i.e., fixed-fixed shallow arches are not sensitive to small imperfections in the load direction in relation to the radial one.

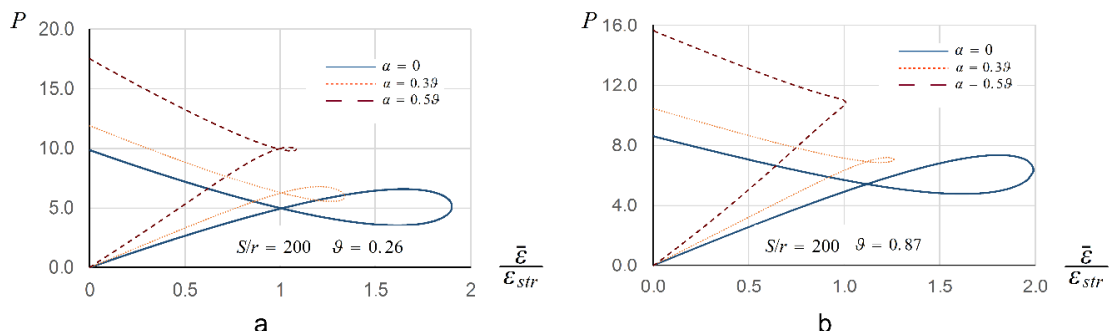


Figure 3. Dimensionless load vs membrane strain parameter to depict the effect of load position α on the behaviour of arches with $S/r=200$: a – $\vartheta=0.26$; b – $\vartheta=0.87$.

Next, it is investigated how the load position can affect the behaviour of arches as shown in Fig. 3a and 3b. Here, ε_{str} is the buckling strain of a straight column under compression with the same material composition, length and cross-section as the arch. Independently of the angle, it is common in the diagrams that as the strain is increased from zero, there is a possible stability loss where the tangent is horizontal. Furthermore, increasing α makes the strain ratio decrease at the moment of buckling and at the same time the dimensionless buckling load gradually becomes greater. One branch always starts from the origin and the other one from a different level. The later one is greater in the dimensionless load P if α is greater and ϑ is smaller. These diagrams are plotted for radial load but can be considered valid for vertical force also with a good accuracy.

Fig. 4-5 give information about the effect of the ratio S/r on the in-plane behaviour when the load is radial. The dimensionless displacement at the application point of the force is $W_\alpha = W(\phi = \alpha)$. As S/r decreases, the loop always becomes smaller with lower critical load and strain ratio as well. The different branches start from a same point, independently of S/r and intersect each other again at a same point as shown in Fig. 4a and 4b. This later intersection point is close to the strain ratio 1. In Fig. 5a and 5b, there are three equilibrium branches: a primary stable, a remote stable and an unstable between them. (When there is no possibility of buckling, there is only one stable branch.) It is somewhat different to pinned-pinned members [39, 40] as then, the number of equilibrium branches showed an increases with α and could reach a number quite more than three, but for fixed-fixed members the number of equilibrium branches seems to be always three. It is set down to the fact that fixed supports are stiffer. When $\alpha = 0$, the unstable branches are very flat but still there is limit point buckling at smaller dimensionless displacement compared to $\alpha = 0.2\vartheta$.

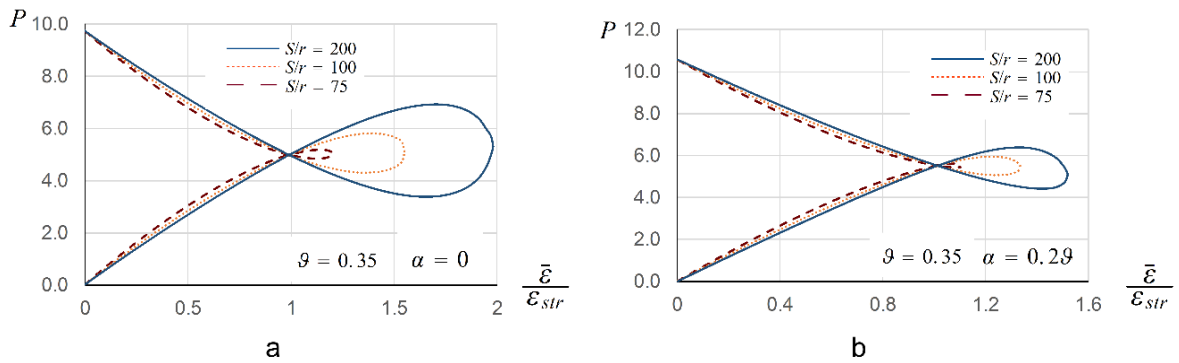


Figure 4. Dimensionless load vs membrane strain parameter to depict the effect of ratio S/r on the behaviour of arches with $\vartheta=0.35$ when: a – $\alpha = 0$; b – $\alpha = 0.2\vartheta$.

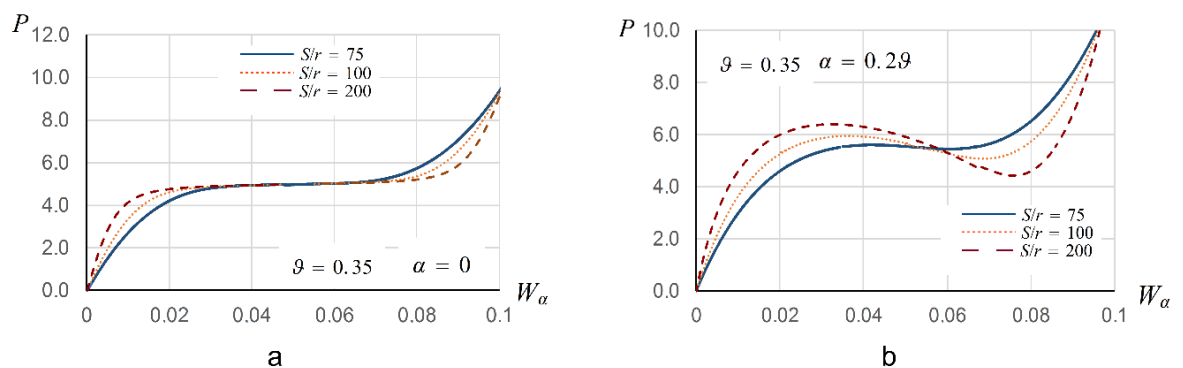


Figure 5. Dimensionless load vs dimensionless displacement at $\phi = \alpha$ to depict the effect of ratio S/r on the behaviour of arches with $\vartheta=0.35$ when: a – $\alpha = 0$; b – $\alpha = 0.2\vartheta$.

In what follows, the lowest buckling loads are plotted in terms of the included angle as shown in Fig. 6a and 6b. The various lines represent radial load and markers are used for vertical force. Clearly, the buckling load increases with S/r . It makes no real sense if the load is radial or vertical – the maximum difference between them is only a few percent at most. Increasing S/r makes the typical curves shift to the left – the possibility of buckling appears for smaller included angles.

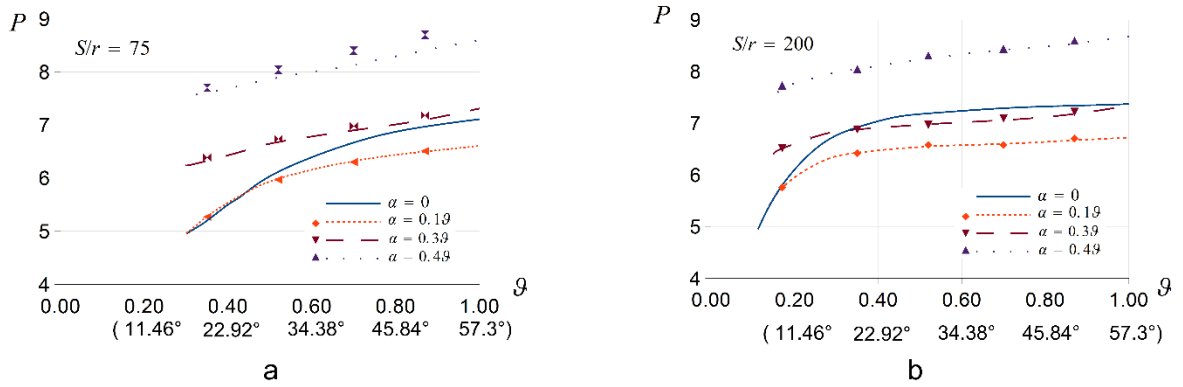


Figure 6. Lowest critical loads for multiple load positions in terms of the semi-vertex angle: a – $S/r=75$; b – $S/r=200$.

3.4. Verification of the results

For radial load, comparisons were carried out with [33] assuming homogeneous material. Results for arches with the same geometrical and material parameters are gathered in Table 1. The correlation is really good. Differences are greatest when g and α are greatest. Since the new model of this article accounts for the effect of the bending moment on the membrane strain, it is assumed to be more reliable.

The new results for vertical load are also verified by the commercial finite element software Abaqus 6.13. A geometrically nonlinear model was used with the Riks method to find the limit points on the equilibrium path. A one-dimensional model was created with eighty B21 beam elements. A doubly symmetric I -section was selected [34]. The related geometrical data were the following: depth 256 mm, flange width 146 mm, flange thickness 10.9 mm, web thickness 6 mm. The moment of inertia is $54,255,292 \text{ mm}^4$ and the modulus of section is $423,869.469 \text{ mm}^3$ to the bending axis η while these values are $5,657,929 \text{ mm}^4$ and $77,505.875 \text{ mm}^3$ to the other principal axis ζ . So the radius of gyration r to the bending axis is 108 mm. Since $S/r = 200$ was selected, the centerline length is 21,600 mm. The Young modulus was 210 GPa. Comparisons of the models with some further geometrical data are gathered in Table 2, indicating that the results of the current model are reliable.

Table 1. Comparison of the lowest radial dimensionless buckling loads with [33] for arches with $S/r = 75$ and 200.

g	ρ [m]	span [m]	altitude [m]	P	P in [33]
$S/r = 75, \alpha = \{0/0.2/0.4\} g$					
0.38	10.65	7.90	0.76	5.20/5.61/7.62	5.15/5.56/7.35
0.69	5.87	7.47	1.34	6.67/6.35/8.14	6.57/6.26/7.89
1.05	3.85	6.69	1.94	7.16/6.68/8.67	7.06/6.41/7.99
$S/r = 200, \alpha = \{0/0.2/0.4\} g$					
0.38	28.42	21.08	2.03	6.92/6.38/8.05	6.92/6.37/7.97
0.69	15.65	19.92	3.58	7.29/6.54/8.42	7.28/6.49/8.05
1.05	10.28	17.84	5.17	7.39/6.76/8.74	7.34/6.51/8.07

Table 2. Comparison of the lowest dimensionless buckling loads for vertical load with Abaqus for arches with $S/r=200$.

g	P	P , Abaqus
$S/r = 200, \alpha = \{0.1/0.2/0.3\} g$		
0.38	6.42/6.40/6.88	6.30/6.29/6.78
0.69	6.61/6.54/7.09	6.72/6.62/7.04
1.05	6.76/6.77/7.30	7.07/6.93/6.84

4. Conclusion

1. In this article a new geometrically nonlinear model was established to investigate the in-plane behaviour and stability of fixed-fixed shallow arches under the effect of a concentrated radial or vertical dead load. The arches are made of functionally graded material. The Euler-Bernoulli kinematical hypothesis was applied. Account for the effect of the bending moment on the membrane strain was made.
2. The related pre-buckling and buckled equilibrium equations were derived from the principle of virtual work. Analytical evaluations were carried out for radial load and numerical ones for vertical force.
3. It was found that only limit point buckling is possible with three equilibrium branches: two stable and one unstable for any geometry and material composition.
4. Unlike pinned-pinned arches, fixed-fixed members are not sensitive to small imperfections in the load position and in the load direction.
5. At the same time, the load position can have a significant effect on the buckling load. Generally, the buckling load decreases for a while when the force is moved from the crown point but as it is placed close enough to the supports, the load bearing abilities become even better.
6. In limit case, the presented model is also capable of predicting the buckling load for homogeneous materials.
7. The new results were confirmed by comparisons with literature and finite element computations.

5. Acknowledgements

The described article was carried out as part of the EFOP-3.6.1-16-2016-00011 „Younger and Renewing University – Innovative Knowledge City – institutional development of the University of Miskolc aiming at intelligent specialisation” project implemented in the framework of the Szechenyi 2020 program. The realization of this project is supported by the European Union, co-financed by the European Social Fund.

References

1. Gusevs, J., Serdjuks, D., Ardebjaki, G., Afanasjeva, E., Goremikins, V. Behaviour of load-carrying members of velodromes' long-span steel roof. *Magazine of Civil Engineering*. 2016. 65(5). Pp. 3–16. DOI: 10.5862/MCE.65.1
2. Hirkovskis, A., Serdjuks, D., Goremikins, V., Pakrastins, L., Vatin, N. Behaviour analysis of load-bearing aluminium members. *Magazine of Civil Engineering*. 2015. 57(5). Pp. 86–117. DOI: 10.5862/MCE.57.8
3. Sharbatdar, M., Ehsani, R., Kheyroddin, A. Ductility and moment redistribution capacity of two-span RC beams. *Magazine of Civil Engineering*. 2019. 90(6). Pp. 104–118. DOI: 10.18720/MCE.90.10
4. Duc, N.D., Cong, P.H., Tuan, N.D., Tran, P., Thanh, N.V. Thermal and mechanical stability of functionally graded carbon nanotubes (FG CNT)-reinforced composite truncated conical shells surrounded by the elastic foundations. *Thin-Walled Structures*. 2017. 115. Pp. 300–310. DOI: 10.1016/j.tws.2017.02.016
5. Kumar, S.K., Siddiraju, S. Effect of steel and polypropylene fiber on mechanical properties of concrete. *International Journal of Civil Engineering and Technology*. 2016. 7(3). Pp. 342–346.
6. Klyuev, S., Klyuev, A., Vatin, N. Fiber concrete for the construction industry. *Magazine of Civil Engineering*. 2018. 84(8). Pp. 41–47. DOI: 10.18720/MCE.84.4
7. Bespalov, V., Ucer, D., Salmanov, I., Kurbanov, I., Kupavykh, S. Deformation compatibility of masonry and composite materials. *Magazine of Civil Engineering*. 2018. 78(2). Pp. 136–150. DOI: 10.18720/MCE.78.11
8. Kanishchev, R. Analysis of local stability of the rectangular tubes filled with concrete. *Magazine of Civil Engineering*. 2016. 64(4). Pp. 59–68. DOI: 10.5862/MCE.64.6
9. Mashhadban, H., Kutanaei, S.S., Sayarinejad, M.A. Prediction and modeling of mechanical properties in fiber reinforced self-compacting concrete using particle swarm optimization algorithm and artificial neural network. *Construction and Building Materials*. 2016. 119. Pp. 277–287. DOI: 10.1016/j.conbuildmat.2016.05.034
10. Zhang, J., Zhang, M., Tang, W., Wang, W., Wang, M. Buckling of spherical shells subjected to external pressure: A comparison of experimental and theoretical data. *Thin-Walled Structures*. 2017. 111. Pp. 58–64. DOI: 10.1016/j.tws.2016.11.012
11. Godoy, L.A. Buckling of vertical oil storage steel tanks: Review of static buckling studies. *Thin-Walled Structures*. 2016. 103. Pp. 1–21. DOI: 10.1016/j.tws.2016.01.026
12. Yu, T., Yin, S., Bui, T.Q., Xia, S., Tanaka, S., Hirose, S. NURBS-based isogeometric analysis of buckling and free vibration problems for laminated composites plates with complicated cutouts using a new simple FSDT theory and level set method. *Thin-Walled Structures*. 2016. 101. Pp. 141–156. DOI: 10.1016/j.tws.2015.12.008
13. Timoshenko, S.P., Gere, J.M. *Theory of Elastic Stability*. Engineering Societies Monographs. McGrawHill, 1961. 541 p.
14. Szeidl, G. *Effect of Change in Length on the Natural Frequencies and Stability of Circular Beams*. PhD Thesis. Department of Mechanics. University of Miskolc, Hungary. 1975. (in Hungarian).
15. Simitses, G.J. *An Introduction to the Elastic Stability of Structures*. Prentice-Hall. Englewood Cliffs, 1976. 253 p.
16. Plaut, R.H. Snap-through of arches and buckled beams under unilateral displacement control. *International Journal of Solids and Structures*. 2015. 63. Pp. 109–113. DOI: 10.1016/j.ijsolstr.2015.02.044
17. Zhou, Y., Chang, W., Stanciulescu, I. Non-linear stability and remote unconnected equilibria of shallow arches with asymmetric geometric imperfections. *International Journal of Non-Linear Mechanics*. 2015. 77. Pp. 1–11. DOI: 10.1016/j.ijnonlinmec.2015.06.015
18. Han, Q., Cheng, Y., Lu, Y., Li, T., Lu, P. Nonlinear buckling analysis of shallow arches with elastic horizontal supports. *Thin-Walled Structures*. 2016. 109. Pp. 88–102. DOI: 10.1016/j.tws.2016.09.016
19. Tsiatas, G.C., Babouskos, N.G. Linear and geometrically nonlinear analysis of non-uniform shallow arches under a central concentrated force. *International Journal of Non-Linear Mechanics*. 2017. 92. Pp. 92–101. DOI: 10.1016/j.ijnonlinmec.2017.03.019

20. Abdelgawad, A., Anwar, A., Nassar, M. Snap-through buckling of a shallow arch resting on a two-parameter elastic foundation. *Applied Mathematical Modelling*. 2013. 37(16). Pp. 7953–7963. DOI: 10.1016/j.apm.2013.03.016
21. Liu, N., Plucinsky, P., Jeffers, A.E. Combining load-controlled and displacement-controlled algorithms to model thermal-mechanical snap-through instabilities in structures. *Journal of Engineering Mechanics*. 2017. 143(8). Article No. 04017051. DOI: 10.1061/(ASCE)EM.1943-7889.0001263
22. Lalin, V., Dmitriev, A., Diakov, S. Nonlinear deformation and stability of geometrically exact elastic arches. *Magazine of Civil Engineering*. 2019. 89(5). Pp. 39–51. DOI: 10.18720/MCE.89.4
23. Yan, S.-t., Shen, X., Chen, Z., Jin, Z. On buckling of non-uniform shallow arch under a central concentrated load. *International Journal of Mechanical Sciences*. 2017. 133. Pp. 330–343. DOI 10.1016/j.ijmecsci.2017.08.046
24. Yan, S.-t., Shen, X., Chen, Z., Jin, Z. Collapse behavior of non-uniform shallow arch under a concentrated load for fixed and pinned boundary conditions. *International Journal of Mechanical Sciences*. 2018. 137. Pp. 46–67. DOI: 10.1016/j.ijmecsci.2018.01.005
25. Yan, S.-t., Shen, X., Chen, Z., Jin, Z. On collapse of non-uniform shallow arch under uniform radial pressure. *Engineering Structures*. 2018. 160. Pp. 419–438. DOI: 10.1016/j.engstruct.2018.01.027
26. Yan, S.-t., Shen, X., Chen, Z., Jin, Z. Symmetric snap-through and equal potential energy load of non-uniform shallow arch under a concentrated load considering imperfection effect. *International Journal of Mechanical Sciences*. 2018. 146-147. Pp. 152–179. DOI: 10.1177/0954406219855105
27. Yan, S.-t., Shen, X., Jin, Z. Static and dynamic symmetric snap-through of non-uniform shallow arch under a pair of end moments considering critical slowing-down effect. *Proceedings of the Institution of Mechanical Engineers, Part C: Journal of Mechanical Engineering Science*. 2019. 233(16). Pp. 5735–5762. DOI: 10.1177/0954406219855105
28. Bateni, M., Eslami, M.R. Non-linear in-plane stability analysis of FGM circular shallow arches under central concentrated force. *International Journal of Non-Linear Mechanics*. 2014. 60. Pp. 58–69. DOI: 10.1016/j.ijnonlinmec.2014.01.001
29. Bateni, M. Eslami, M.R. Non-linear in-plane stability analysis of FG circular shallow arches under uniform radial pressure. *Thin-Walled Structures*. 2015. 94. Pp. 302–313. DOI: 10.1016/j.tws.2015.04.019
30. Babaei, H., Kiani, Y., Eslami, M.R. Thermomechanical nonlinear in-plane analysis of fix-ended FGM shallow arches on nonlinear elastic foundation using two-step perturbation technique. *International Journal of Mechanics and Materials in Design*. 2019. 15(2). Pp. 225–244. DOI: 10.1007/s10999-018-9420-y
31. Schreyer, H.L. The effect of initial imperfections on the buckling load of shallow circular arches. *Journal of Applied Mechanics*. 1972. 39(2). Pp. 445–450.
32. Plaut, R.H. Influence of load position on the stability of shallow arches. *Zeitschrift für angewandte Mathematik und Physik ZAMP*. 1979. 30(3). Pp. 548–552. DOI: 10.1007/BF01588902
33. Pi, Y.-L., Bradford, M.A., Liu, A. Nonlinear equilibrium and buckling of fixed shallow arches subjected to an arbitrary radial concentrated load. *International Journal of Structural Stability and Dynamics*. 2017. 17(8). Art. No. 1750082. DOI: 10.1142/S0219455417500821
34. Liu, A., Bradford, M.A., Pi, Y.-L. In-plane nonlinear multiple equilibria and switches of equilibria of pinned–fixed arches under an arbitrary radial concentrated load. *Archive of Applied Mechanics*. 2017. 87(11). Pp. 1909–1928. DOI: 10.1007/s00419-017-1300-7
35. Pi, Y.-L. Non-linear in-plane multiple equilibria and buckling of pin-ended shallow circular arches under an arbitrary radial point load. *Applied Mathematical Modelling*. 2020. 77. Pp. 115–136. DOI: 10.1016/j.apm.2019.07.021
36. Bradford, M.A., Uy, B., Pi, Y.-L. In-plane elastic stability of arches under a central concentrated load. *Journal of Engineering Mechanics*. 2002. 128(7). Pp. 710–719. DOI: 10.1061/(ASCE)0733-9399(2002)128:7(710)
37. Pi, Y.-L., Bradford, M. A. Dynamic buckling of shallow pin ended arches under a sudden central concentrated load. *Journal of Sound and Vibration*. 2008. 317. Pp. 898–917. DOI: 10.1016/j.jsv.2008.03.037
38. Kiss, L., Szeidl, G. In-plane stability of fixed-fixed heterogeneous curved beams under a concentrated radial load at the crown point. *Technische Mechanik*. 2015. 35(1). Pp. 31–48. DOI: 10.24352/UB.OVGU-2017-067
39. Kiss, L.P. Sensitivity of FGM shallow arches to loading imperfection when loaded by a concentrated radial force around the crown. *International Journal of Non-Linear Mechanics*. 2019. 116. Pp. 62–72. DOI: 10.1016/j.ijnonlinmec.2019.05.009
40. Kiss, L.P. Nonlinear stability analysis of fgm shallow arches under an arbitrary concentrated radial force. *International Journal of Mechanics and Materials in Design*. May 2019. DOI: 10.1007/s10999-019-09460-2
41. Kiss, L., Szeidl, G. Nonlinear in-plane stability of heterogeneous curved beams under a concentrated radial load at the crown point. *Technische Mechanik*. 2015. 35(1). Pp. 1–30. DOI: 10.24352/UB.OVGU-2017-066
42. Bateni, M., Eslami, M.R. Non-linear in-plane stability analysis of FGM circular shallow arches under central concentrated force. *International Journal of Non-Linear Mechanics*. 2014. 60. Pp. 58–69. DOI: 10.1016/j.ijnonlinmec.2014.01.001
43. Yan, S-t, Shen, X., Jin, Z. Instability of imperfect non-uniform shallow arch under uniform radial pressure for pinned and fixed boundary conditions. *Thin-Walled Structures*. 2018. 132. Pp. 217–236. DOI: 10.1016/j.tws.2018.08.018
44. Pi, Y.-L., Bradford, M.A., Tin-Loi F. Non-linear in-plane buckling of rotationally restrained shallow arches under a central concentrated load. *International Journal of Non-Linear Mechanics*. 2008. 43. Pp.1–17. DOI: 10.1016/j.ijnonlinmec.2007.03.013

Contacts:

Laszlo Peter Kiss, mechkiss@uni-miskolc.hu

© Kiss L.P., 2020



DOI: 10.18720/MCE.95.4

Destruction of powder-activated concrete with fixation of destruction by a laser interferometer

V.I. Travush^a, N.I. Karpenko^a, V.T. Erofeev^{b*}, N. Vatin^c, I.V. Erofeeva^b, I.N. Maksimova^d,
V.I. Kondrashchenko^e, A.G. Kesarijskij^f

^a Russian Academy of Architecture and Building Sciences, Moscow, Russia

^b Ogarev Mordovia State University, Saransk, Russia

^c RUDN University, Moscow, Russia

^d Penza State University of Architecture and Construction, Penza, Russia

^e Russian University of Transport, Moscow, Russia

^f LLC "Laboratory of integrated technology", Pavlograd, Ukraine

* E-mail: yerofeevvt@mail.ru

Keywords: self-compacting concrete, fracture testing, stress-strain curves, crack propagation, laser interferometry

Abstract. The article is devoted to the identification of the patterns of deformation and destruction of powder-activated concrete under the action of power loads. As research concrete, powder-activated concrete of a new generation was considered in comparison with materials of the old and transitional generations. To carry out such studies, laser holographic interferometry methods were used, the physical essence of which consists in recording wave fields synchronously with the application of the load reflected by the surface under study at various points in time and then comparing these wave fields with each other. Using the complete equilibrium deformation diagrams and 3D graphs, we determined the parameters of the diagram (cyclicality, ultimate tensile strength), and the parameters of surface deformation (photographs with waves of strains and cracks). Using laser interferometry methods, it was found that the introduction of microquartz, especially in combination with amorphous active silica fume, significantly delays the onset of microcrack formation in cement samples, which exhibit a uniform deformation field up to a stress level of 0.90–0.95 from destructive. A sample based on a cement-sand mortar without finely dispersed fillers distinguishes a lower level of crack formation, corresponding to a stress level of 0.5–0.6 from destructive ones, and with an increase in load, the fracture of the sample has a block character.

1. Introduction

The composition of concrete in various proportions includes aggregates, a binder, water and modifying additives (plasticizing, reactive microbiological, etc.), included depending on the required strength and its functional purpose [1–8]. High-quality concretes (HQC) classification combine a wide range of concretes for various purposes: high-strength (HSB, HochfesterBeton – HFB) and ultrahigh-strength (UVB, UltrahochfesterBeton – UHFB), self-compacting (SUB, Selbstverdichtender Concrete); joint-stock powder, dispersion-reinforced (ReaktionspulverBeton – RPB or ReactivePowderConcrete – RPC) and others. These types of concrete satisfy the high requirements for compressive and tensile strength, crack resistance, impact strength, wear resistance, corrosion resistance, frost resistance and other key performance indicators [2, 6, 9–12].

Travush, V.I., Karpenko, N.I., Erofeev, V.T., Vatin, N., Erofeeva, I.V., Maksimova, I.N., Kondrashchenko, V.I., Kesarijskij, A.G. Destruction of powder-activated concrete with fixation of destruction by a laser interferometer. Magazine of Civil Engineering. 2020. 95(3). Pp. 42–48. DOI: 10.18720/MCE.95.4



The development of concrete science is connected with the concept of highly functional concretes (High Performance Concrete – LDC). One of its developers, the Canadian scientist P.-K. Aichin notes its difference from the concept of high-strength concrete (High Strength Concrete (HSC)). P.-K. Aichin and his followers [13, 14] saw the development of high-functional concrete technology [13, 14] when they achieved the highest possible strength indicators ($R_s = 140$ MPa), manufacturability, density and durability. The use of high-strength concrete is the most effective way to reduce the mass of structures, the complexity and cost of their construction, which necessitates the creation of new types of them with increased strength and durability. Important in this case is the physicochemical dispersion of highly concentrated mineral powders of various chemical and mineralogical nature for the production of building materials with extremely long aggregate stability.

Experimental evidence of the achievement of water-reducing effects equal to 8–15 versus 1.8–2.0 in cement dispersions is given in [5]. In these experiments, the gravitational fluidity of plasticized mineral suspensions was maintained while reducing water consumption by 8–15 times! It is such cardinal changes in the rheological properties and water-reducing effects that served as the basis for the creation of high-strength and ultra-high-strength concrete of the new generation [5, 14–16]. A new progress strategy was formulated in obtaining highly filled and highly economical concrete of ordinary grades M200–M600 and high-strength concrete M600–M1000, high-strength and ultra-high-strength: “Through a rational rheology into the future of concrete” [14, 15]. For enhanced implementation of the construction of new varieties of concrete in practice, it is necessary to take into account all their advantages in comparison with traditional materials. For the successful implementation of the construction of new varieties of concrete in practice, it is necessary to take into account all their advantages in comparison with traditional materials, in connection with which an important direction is to conduct research on materials to optimize them in terms of static and dynamic strength, durability. At the same time, along with the establishment of physic-mechanical parameters of cement composites, it is necessary to identify the patterns of their deformation and fracture under the action of power loads [17–21].

Traditional methods for studying the mechanics of concrete fracture involves loading the test sample and recording its deformation response depending on the magnitude of the load. This approach is quite simple and convenient, but gives information only about the limiting states of the object. At the same time, for specialists in the field of mechanics of a deformed solid and the calculation of building structures, an important role is played by an understanding of the process of destruction of a material and its behavior at all stages of testing.

The objects of research were powder-activated concretes with a high proportion of the suspension component, which included, along with cement, sand and water, superplasticizer, rheologically active and reactive additives. Concrete of transitional and old generations were considered as compared materials. Old-generation concretes were formed from a cement-sand mixture, with a superplasticizer, of a transitional type – with the addition of a reactive active additive – silica fume.

The goal of our work was to study the stages of development of the processes accompanying the destruction of samples, with the fixation of the fields of deformation movements synchronously with the application of the load.

The objectives of the research were:

1. Investigate the stage of destruction of samples of powder-activated concrete;
2. To compare the performance of powder-activated concrete with concrete of the old and transitional generations;
3. To identify the effect of water-cement ratio, the content of superplasticizer, finely dispersed fillers on crack formation.

2. Methods

The tests were performed using laser holographic interferometry methods, the promisingness of which for the study of building materials of complex structures was confirmed by a number of successful experimental studies that revealed previously unknown features of the fracture mechanics of various building materials, including those based on cement binders [22–27].

Cement composites were made on CEM I 42.5 N cement of the Ulyanovsk cement plant of the Russian Federation: cement composite with Melflux 1641F hyperplasticizer filled with sand of fractions 0–0.63 and 0.63–2.5 mm (composition No. 6); cement composite with Melflux 1641F hyperplasticizer, filled with sand fractions 0–0.63 and 0.63–2.5 mm with the addition of microquartz (composition No. 4); cement composite with Melflux 1641F hyperplasticizer filled with sand of fractions 0–0.63 and 0.63–2.5 mm with the addition of microquartz and silica fume (composition No. 5).

To load the samples, a press with a force of up to 200 kN equipped with a power hydraulic cylinder was used.

The analysis of interferograms was performed according to the method described in [8, 22], where the displacement at a point was determined by the formula:

$$\vec{d}(\vec{r}_i + \vec{r}_o) = \lambda n, \quad (1)$$

where \vec{d} is the vector of displacement of a point on the investigated surface;

\vec{r}_i is a single vector of illumination of the investigated surface;

\vec{r}_o is a single observation vector of the investigated surface;

λ is wavelength of laser radiation;

n is the order of the interference band.

The experimental data were processed using the AutoCAD graphic complex. In Fig. 1 shows one of the interferograms at the stage of decryption.

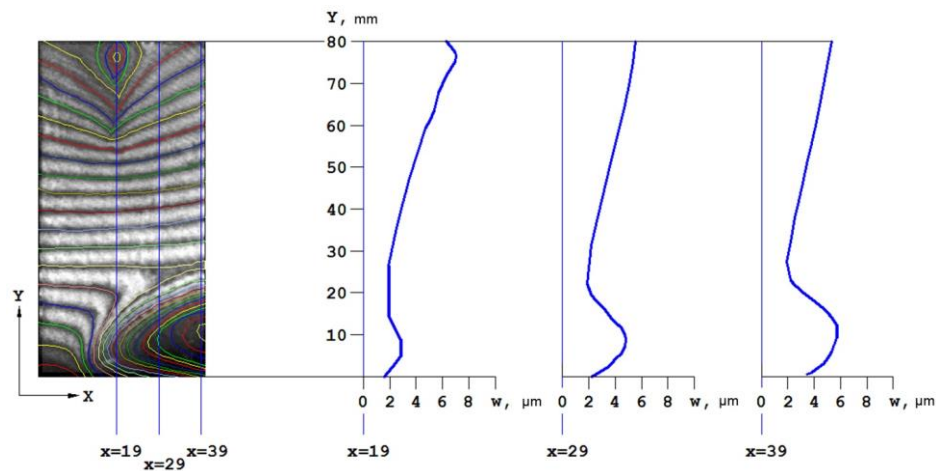


Figure 1. Interpretation of the interferogram with the construction of graphs of the field of movement along the sections.

For a more visual representation of the deformation of the sample, 3D visualization of the displacement field, shown in Fig. 2, which significantly reduces the analysis time of interferograms.

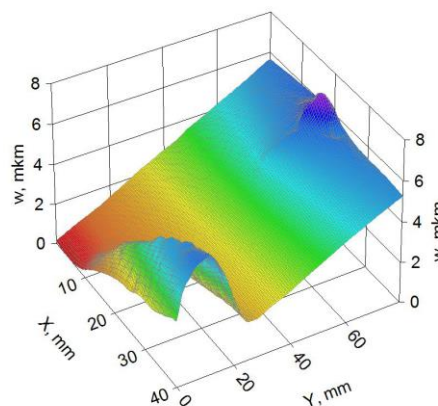


Figure 2. Presentation of data on the field of movement of the sample in the form of 3D graphics.

The effect of microquartz (composition No. 4) or a mixture of microquartz with silica fume (composition No. 5) on the properties of sand concrete was studied by comparison with a control composition that does not contain finely dispersed quartz (composition No. 6). In all the studied compositions, in addition to cement and water, Melflux 1641F brand hyperplasticizer and two-fraction quartz sand were used. To ensure equal mobility of the cement-sand mortar, the water-cement ratio of the control composition was 14 % lower than that of the composition on microquartz, and 9.5 % lower than that of the composition on a mixture of microquartz and silica fume. The latter is explained by the plasticizing effect of microquartz.

3. Results and Discussion

Interferograms, 3D-graphs, surface deformations and deformations for samples of compositions 6, 4 and 5 are shown in Figs. 3, 4 and 5.

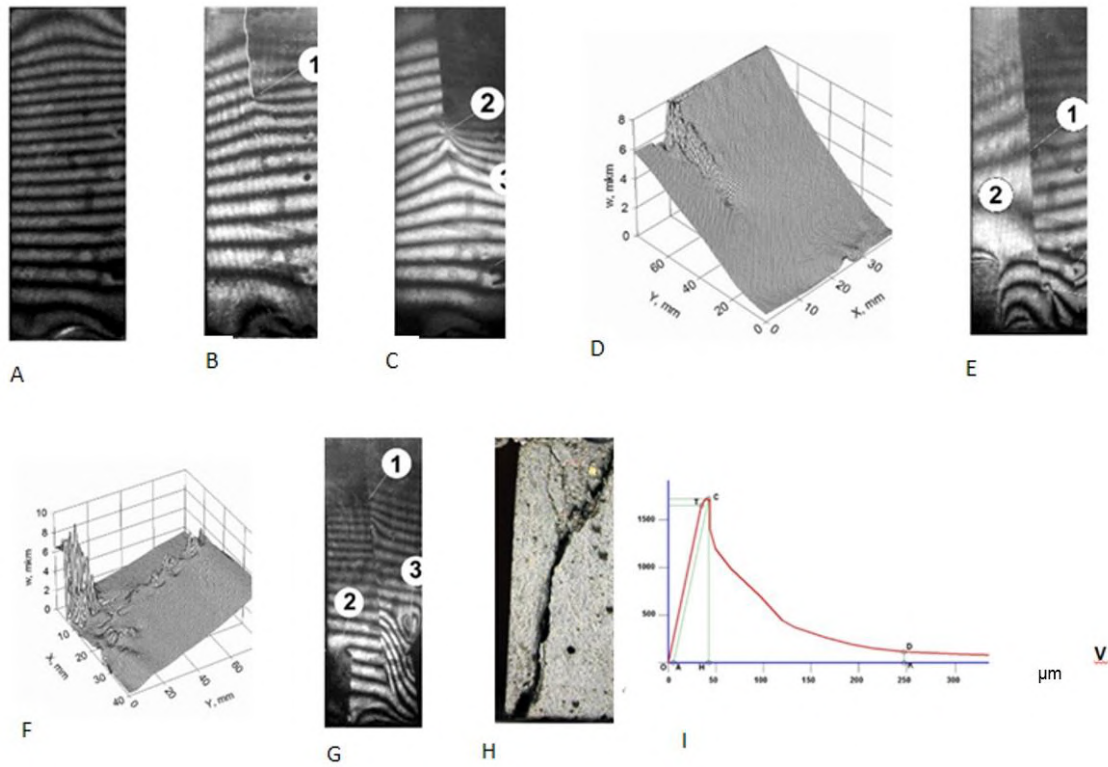


Figure 3. Interferograms (A–C, E, G), 3D-graphs (D, F) of surface deformations and a photograph (H) complete equilibrium deformation diagram (I) of sample No. 6 ($\Delta\sigma = 1.53$ MPa, other explanations are given in the text).

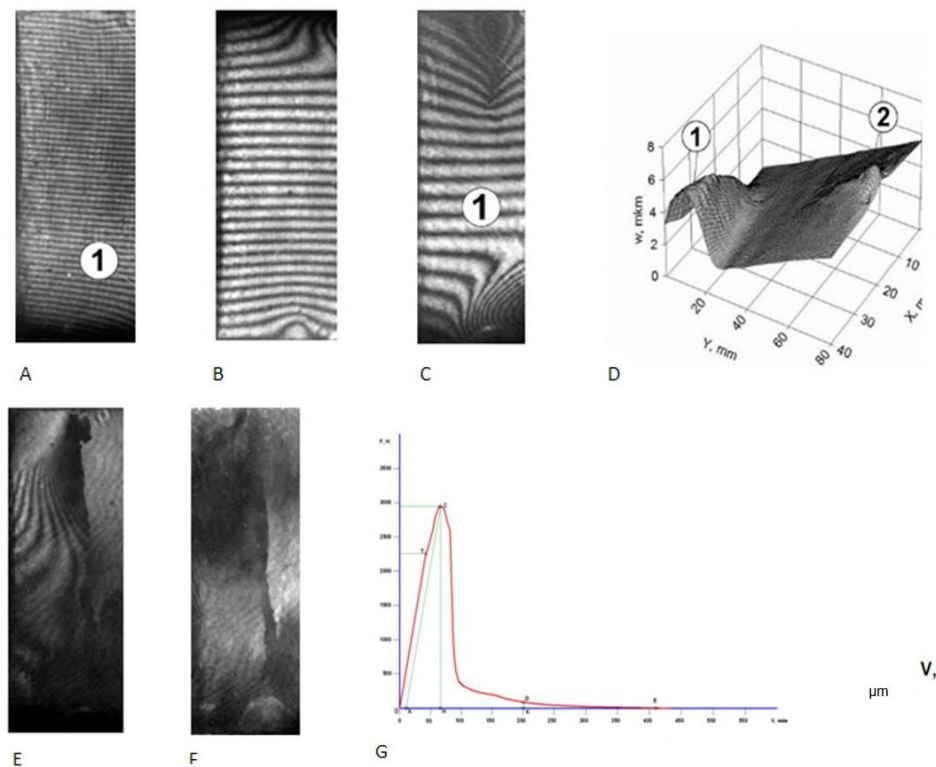


Figure 4. Interferograms (A–C, E, F) and 3D-graph (D) of surface deformations, complete equilibrium deformation diagram (G) of specimen composition No. 4 ($\Delta\sigma = 1.53$ MPa, other explanations are given in the text).

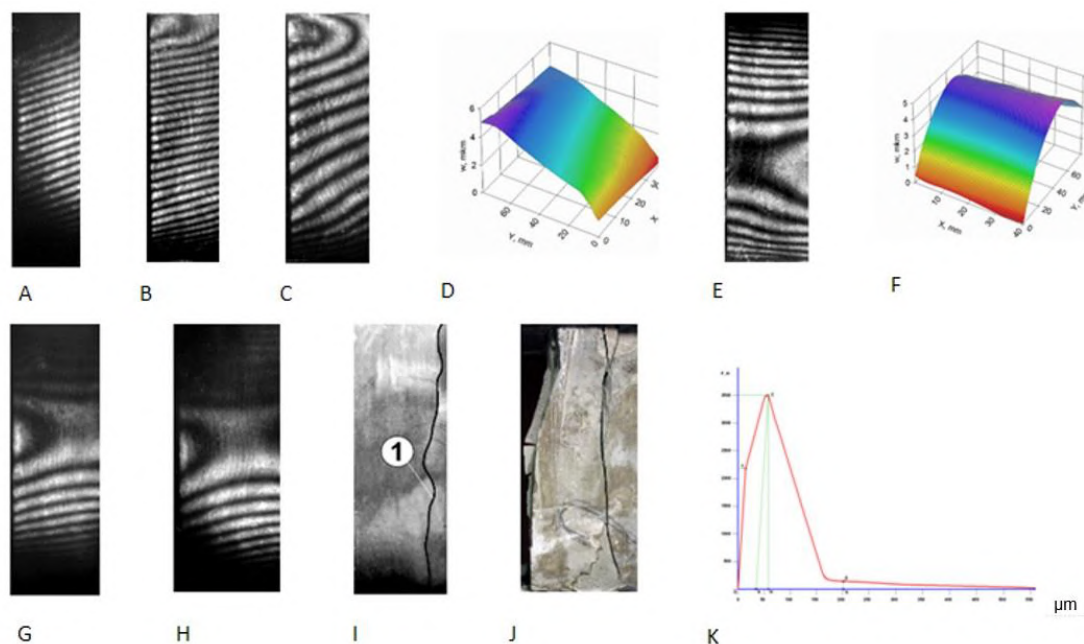


Figure 5. Interferograms (A–C, E, G–I), 3D-graphs (D, F) of surface deformations and a photograph (K) complete equilibrium deformation diagram (I) of sample No. 5 ($\Delta\sigma = 1.53$ MPa, others explanations are given in the text).

In concrete without quartz micro-filler (composition No. 6) at a stress level of 0.27σ size. Deformation of the sample is observed as an isotropic body with minor anomalies in the zone of its contact with the loading plates of the press (Fig. 3). With an increase in load to 0.59σ a zone of increased plastic deformations is identified, identified as a visually unobservable crack, and a slight anomaly appears in the zone of local deformation of the sample, which, with an increase in stresses up to 0.72σ , develops with the formation of new anomalous zones. At a stress level of 0.82σ the vertical zone of plastic deformation almost completely intersects the surface of the sample, dividing it into two blocks, but is inhibited by the structural element of the material. In the lower left part of the sample, a zone of high gradient deformation develops, parallel to the crack, dividing it into two subunits. The previously observed anomaly forms a local crack. The formed blocks behave as separate elastic elements with substantially different deformation fields. At a stress level of 0.95σ the main crack develops along the entire length of the sample.

A fragment in the lower left corner of the sample undergoes continuous movement. The abnormal zone in this case generates a third vertical crack, which provides freedom of movement to the newly formed block. The destruction of the sample is observed, in which large blocks are held by a geometric closure at the boundary of their surfaces before its physical disintegration into fragments by a main crack.

In samples with microquartz at a stress level of $0.15\sigma_{destr}$ local microfractures are observed in the zone of their contact with the loading plates, associated with roughnesses in the end surfaces and their hugging with increasing load, which develop with increasing load and manifest themselves at a stress level of $\approx 0.5\sigma_{destr}$, leading to the onset of the formation of a main crack along the compressive load and initially not visually detectable even at a stress level of $0.91\sigma_{destr}$, and then clearly observed on the interferogram at a stress level of $\approx \sigma_{destr}$.

For a sample with microquartz and silica fume with an increase in the load from the stress level $0.13\sigma_{destr}$ до $0.26\sigma_{destr}$ the field of displacements over the entire surface of the sample remains uniform, without local anomalies.

At a stress level of 0.47σ the local annular structure of interference fringes in the upper left corner of the sample indicates a shift in the contact forces to this zone, which is explained by the ongoing pressure testing of its surfaces in contact with the press plate. For most of the sample, uniform deformation is observed without signs of abnormal plastic deformations. Increment of stresses by 38 % – from level $0.47\sigma_{destr}$ до $0.65\sigma_{destr}$ caused deformation of the central part of the sample, which is explained by the manifestation of the "cage effect" – its cramped deformations in the zone of contact with the press plates.

At this level of stress, zones of abnormal plastic deformations are still not observed, in contrast to the composition with microquartz, which has a stress level of $\approx 0.5\sigma_{destr}$ the beginning of the formation of a main crack, or a control composition, was observed, in which, at a stress level of $0.59\sigma_{destr}$, a zone of increased

plastic deformation appeared, identified as a visually unobservable crack and a zone of local deformation of the sample.

At a voltage level of $0.78\sigma_{destr}$ up to $0.91\sigma_{destr}$ the nature of the displacement field does not change significantly – there are no local anomalies, there are no signs of crack nucleation, which fundamentally distinguishes the behavior of the composition with microquartz and silica fume from other studied compositions. In this case, the loss of contrast of the interference bands in the upper and lower parts of the sample is explained by the beginning of its destruction in the contact zone with the reference and loading plate presses. Such a uniform deformation of the sample up to a load of more than $0.9\sigma_{destr}$ resulted at a stress level of $\approx 1.0\sigma_{destr}$ spontaneous development, apparently, from the zones of contact of the sample with the support and loading plates of the press of a vertically directed main crack, which divided the sample into two equal fragments.

4. Conclusion

1. The relevance of researching the durability of concrete is shown, since structures based on them are subject to cracking during operation. The purpose of the study was to study the stages of development of the processes accompanying the destruction of concrete samples by laser interferometry with fixation of the fields of displacements synchronously with the application of the load.

2. As a result of the research revealed the following:

- A decrease in W / C causes a more elastic behavior of the material under load, a significant (4–5 times) lengthening of the descending branch of the full equilibrium diagram of the deformation of cement stone and a change in the fracture mechanism of the material, with W / C 0.267, through the formation of a main crack in the early stages of loading and its subsequent development up to the fragmentation of the sample, and at W / C 0.350 – through the formation of a block structure with the subsequent closure of transverse cracks in the blocks and the merging of longitudinal block cracks into a main crack;
- Laser interference studies generally confirmed the block nature of the prefracture of the specimen with the Melflux 1641F hyperplasticizer, followed by the formation of a main (main) crack, leading to its physical destruction and fragmentation into separate plates.

Using laser interferometry methods, it was found that the introduction of microquartz, especially in combination with amorphous active silica fume, significantly delays the onset of microcrack formation in cement samples, which exhibit a uniform deformation field up to the stress level of $0.90\sigma_{destr} - 0.95\sigma_{destr}$. Cement-sand stone without finely dispersed quartz distinguishes a lower level of crack formation, corresponding to a stress level of $0.5\sigma_{destr} - 0.6\sigma_{destr}$ from destructive ones, and with an increase in load, the fracture of the sample has a block character.

References

1. Bazhenov, Yu.M., Chernyshev, Ye.M., Korotkikh, D.N. Konstruirovaniye struktur sovremennykh betonov: opredelyayushchiye printsipy i tekhnologicheskiye platform [Structural engineering of modern concrete: defining principles and technological platforms]. Stroitelnyye materialy. 2014. No. 3. Pp. 6–15. (rus)
2. Erofeev, V.T., Rodin, A.I., Yakunin, V.V., Bogatov, A.D., Bochkin, V.S., Chegodajkin, A.M. Alkali-activated slag binders from rock-wool production wastes. Magazine of Civil Engineering. 2018. 82(6). Pp. 219–227. DOI: 10.18720/MCE.82.20
3. Zhao, Q., Cheng, P., Wei, Y., Wang, J. Factors effecting the recovery process of self-repairing concrete. Magazine of Civil Engineering. 2019. 88(4). Pp. 52–59. DOI: 10.18720/MCE.88.5
4. Igawa, H., Eguchi, H., Kitsutaka, Y. A fundamental study for the self-healing performance of heavyweight concrete. Journal of Structural and Construction Engineering. 83(748). Pp. 763–772. DOI: 10.3130/aajs.83.763.
5. Kalashnikov, V.I. Terminologiya nauki o betone novogo pokoleniya [New Generation Concrete Science Terminology]. Stroitelnyye materialy. 2011. No. 3. Pp. 103–106. (rus)
6. Kapriyev, S.S., Chilin, I.A. Sverkhvysokoprochnyy samouplotnyayushchiysya fibrobeton dlya monolitnykh konstruksiy [Ultra-high-self-sealing fiber concrete for monolithic constructions]. Beton i zhelezobeton – vzhlyad v budushcheye : nauchnyye trudy III Vserossiyskoy (II Mezhdunarodnoy) konferentsii po betonu i zhelezobetonu: v 7 t. T. 3 [Concrete and reinforced concrete – a look into the future: scientific papers of the III All-Russian (II International) conference on concrete and reinforced concrete: in 7 vol. V. 3]. Moscow : MGSU, 2014. Pp. 158–164. (rus)
7. Makar, J., Margeson, J., Luh, J. Carbon nanotube/cement composites – early results and potential applications. 3-rd International Conference on Construction Materials: Performance, Innovations and Structural Implications. Vancouver, B.C. 2005. Pp.1–10.
8. Cwirzen, A., Habermehl-Cwirzen, K., Penttala, V. Surface decoration of carbon nanotubes and mechanical properties of cement/carbon nanotube composites. Advances in Cement Research. 2008. 20(2). Pp. 65–73. DOI: 10.1680/adcr.2008.20.2.65
9. Kalinovskiy, M.I. Primeneniye fibry dlya povysheniya treshchinostoykosti betona [The use of fiber to increase the crack resistance of concrete]. Transportnoye stroitelstvo. 2008. No. 3. Pp. 7–9. (rus)
10. Akimov, L., Ilenko, N., Mizharev, R., Cherkashin, A., Vatin, N., Chumadova, L. Influence of Plasticizing and Siliceous Additives on the Strength Characteristics of Concrete. Applied Mechanics and Materials. 2015. No. 725–726. Pp. 461–468. DOI: 10.4028/www.scientific.net/AMM.725-726.461

11. Beygi, M.H.A., Kazemi, M.T., Nikbin, I.M., Amiri, J.V. The effect of water to cement ratio on fracture parameters and brittleness of self-compacting concrete. *Materials and Design*. 2013. No. 50. Pp. 267–276. DOI: 10.1016/j.matdes.2013.02.018
12. Carpinteri, A., Brighenti, R. Fracture behaviour of plain and fiber-reinforced concrete with different water content under mixed mode loading. *Materials and Design*. 2010. 31(4). Pp. 2032–2042. DOI: 10.1016/j.matdes.2009.10.021
13. Aitcin, P.-C., Neville, A. High Performance Concrete Demystified. *Concrete International*. 1993. 15(1). Pp. 21–26.
14. Kalashnikov, V., Kornienko, P., Gorshkova, L., Gakshteter, G., Sarsenbayeva, A. Development of compositions of self-compacting fine-grained refractory concrete. *Journal of Advanced Concrete Technology*. 2014. 12(9). Pp. 299–309. DOI: 10.3151/jact.12.299
15. Yerofeyeva, I.V. Fiziko-mekhanicheskiye svoystva, biologicheskaya i klimaticheskaya stoykost poroshkovo-aktivirovannykh betonov: avtoreferat dissertatsii kand. tekhn. nauk [Physico-mechanical properties, biological and climatic resistance of powder-activated concrete: abstract of the thesis of Cand. tech. sciences]. Penza, 2018. 28 p. (rus)
16. Zhang, X.X., Ruiz, G., Yu, R.C., Tarifa, M. Fracture behaviour of high-strength concrete at a wide range of loading rates. *International Journal of Impact Engineering*. 2009. 36(10-11). Pp. 1204–1209. DOI: 10.1016/j.ijimpeng.2009.04.007
17. Sprince, A., Pakrastinsh, L., Vatin, N. Crack Formation in Cement-Based Composites. *IOP Conference Series: Materials Science and Engineering*. 2016. 123(1). 012050. DOI: 10.1088/1757-899X/123/1/012050
18. Muralidhara, S., Prasad, B.K.R., Eskandari, H., Karihaloo, B.L. Fracture process zone size and true fracture energy of concrete using acoustic emission. *Construction and Building Materials*. 2010. 24(4). Pp. 479–486. DOI: 10.1016/j.conbuildmat.2009.10.014
19. Shah, S.G., Kishen, J.M.C. Fracture Properties of Concrete-Concrete Interfaces Using Digital Image Correlation. *Experimental Mechanics*. 2011. 51(3). Pp. 303–313. DOI: 10.1007/s11340-010-9358-y
20. Zhang, X.X., Yu, R.C., Ruiz, G., Tarifa, M., Camara, M.A. Effect of loading rate on crack velocities in HSC. *International Journal of Impact Engineering*. 2010. 37(4). Pp. 359–370. DOI: 10.1016/j.ijimpeng.2009.10.002
21. Dong, W., Zhou, X., Wu, Z. On fracture process zone and crack extension resistance of concrete based on initial fracture toughness. *Construction and Building Materials*. 2013. No. 49. Pp. 352–363. DOI: 10.1016/j.conbuildmat.2013.08.041
22. Vest, Ch. Golograficheskaya interferometriya [Holographic interferometry]. Moscow: Mir, 1982. 504 p. (rus)
23. Chernyshov, Ye.M., Korotkikh, D.N. Modifitsirovaniye struktury tsementnogo kamnya mikro- i nanorazmernymi chastitsami kremnezema (voprosy teorii i prilozheniy) [Modification of the structure of a cement stone by micro- and nanosized particles of silica (theory and application issues)]. *Stroitelnyye materialy, oborudovaniye i tekhnologii XXI veka*. 2008. No. 5. Pp. 30–32. (rus)
24. Matallah, M., La Borderie, C., Maurel, O. A practical method to estimate crack openings in concrete structures. *International Journal for Numerical and Analytical Methods in Geomechanics*. 2010. 34(15). Pp. 1615–1633. DOI: 10.1002/nag.876
25. Alam, S.Y., Saliba, J., Loukili, A. Fracture examination in concrete through combined digital image correlation and acoustic emission techniques. *Construction and Building Materials*. 2014. No. 69. Pp. 232–242. DOI: 10.1016/j.conbuildmat.2014.07.044
26. Skarzyński, Ł., Kozicki, J., Tejchman, J. Application of DIC Technique to Concrete-Study on Objectivity of Measured Surface Displacements. *Experimental Mechanics*. 2013. 53(9). Pp. 1545–1559. DOI: 10.1007/s11340-013-9781-y
27. Alam, S.Y., Loukili, A., Grondin, F. Monitoring size effect on crack opening in concrete by digital image correlation. *European Journal of Environmental and Civil Engineering*. 2012. 16(7). Pp. 818–836. DOI: 10.1080/19648189.2012.672211

Contacts:

Vladimir Travush, travush@mail.ru

Nikolaj Karpenko, karpenko@raasn.ru

Vladimir Erofeev, yerofeevvt@mail.ru

Nikolai Vatin, vatin@mail.ru

Irina Erofeeva, ira.erofeeva.90@mail.ru

Irina Maksimova, maksimovain@mail.ru

Valerij Kondrashchenko, kondrashchenko@mail.ru

Aleksandr Kesarijskij, algeo57k@gmail.com

© Travush V.I., Karpenko N.I., Erofeev V.T., Vatin N., Erofeeva I.V., Maksimova I.N., Kondrashchenko V.I., Kesarijskij A.G., 2020



DOI: 10.18720/MCE.95.5

Attenuation of the soil vibration amplitude at pile driving

A.O. Kolesnikov^{a*}, T.N. Kostiuk^a, V.N. Popov^b

^a Novosibirsk State University of Architecture and Civil Engineering (Sibstrin), Novosibirsk, Russia

^b Khristianovich Institute of Theoretical and Applied Mechanics SB RAS, Novosibirsk, Russia

* E-mail: ao_kolesnikov@mail.ru

Keywords: pile driving, attenuation of vibration, soil vibration, wave dispersion, portable vibration apparatus, structural damage, dynamic effect zone

Abstract. The paper presents the solution of the wave equation describing the attenuation of the vibration amplitude in the soil during pile driving. It is suggested that in the soil there is the area around the pile where the energy dissipates due to plastic deformations, and then the areas of the elastic state where surface waves propagate. In the framework of the wave model, the connections have been determined between vertical vibrations of the embedded solid body circular in plane and the motions in the area of the elastic soil state which is described by an integrity of infinitely thin layers. The interaction of the pile and soil in the plastic deformations area is beyond our consideration, though its size is of high importance for the problem solution. The formula has been derived, which permits, having the result of amplitude measurement in any point by a vibrometer and the position of surface wave propagation boundary, evaluating the soil vibrations at different distances from the pile driving point. The quantitative and qualitative agreement of the measured amplitudes and results of analysis obtained during test pile embedment performed during field measurements and found in references proves that the proposed model can be used to increase the accuracy of evaluation of the vertical soil vibrations.

1. Introduction

Equipment used in construction works is usually the source of vibrations propagating around. Regarding the type of the dynamic loading, the vibrations with high amplitudes and low frequencies may appear (for example, pile embedment in the soil), or the vibrations with relatively low amplitudes and high frequencies (for example, vibration embedment of pile curtains, vibrating rollers performance, etc.) Builders often do not have enough data on the choice of the equipment for pile or sheet pile embedment, nor on the parameters of the equipment performance needed to minimize the action of the propagating vibrations on buildings and people. Along with it, according to [1], the accuracy of vibration prediction by modern methods is insufficient. Errors in the choice of the equipment generating vibrations and the distance to the pile embedment site may cause not only worse conditions of existing buildings and constructions performance, but also the damages provoking the faster wear of these objects. Each worksite is unique, so one must take into account its specific conditions. Calculations and predictions, along with the dynamic monitoring of soils, buildings and constructions prevent troubles related with vibrations in building objects.

Thus, the modern standards [2–5] specify the requirements limiting the level of vibrations for neighboring buildings. In the case when the pile driving is performed close to them, there are restrictions of the velocity and acceleration of the foundation vertical vibrations with due regard to the soil type and construction peculiarities of the building and structure. However, according to [6], damages of buildings are related with the maximal shears which area not necessarily coincides with the area of the maximal values of the shear velocities. Today, any information about the minimal distances safe for the neighboring buildings foundations during the pile driving is missing. In spite of the fact that vibrations during the pile driving or sheet pile vibrating embedment are being studied for quite a long time [6–38], further investigations of the wave propagation in the soil from the source are still needed.

Bornitz [8] offers the Golitsin formula [7] for the evaluation of the varying vibration amplitudes of the surface waves A between two points within the distances r_0 and r from the embedded pile

Kolesnikov, A.O., Kostiuk, T.N., Popov, V.N. Attenuation of the soil vibration amplitude at pile driving. Magazine of Civil Engineering. 2020. 95(3). Pp. 49–56. DOI: 10.18720/MCE.95.5



This work is licensed under a [CC BY-NC 4.0](https://creativecommons.org/licenses/by-nc/4.0/)

$$A = A_0 \sqrt{\frac{r_0}{r}} e^{-\delta(r-r_0)}, \quad (1)$$

where A_0 is the amplitude, for example at $r_0 = 0.5$ m, δ is the vibration damping coefficient which varies within the range of 0.02–0.10 m⁻¹ regarding the soil properties. Formula (1) was initially found for the evaluation of damping low-frequency Rayleigh waves with big lengths generated by earthquakes, for which the damping coefficient δ weakly depends on the properties of the upper soil layers. However, from 1930ties, the formula is used for the evaluation of the soil shear amplitudes during the vibrations propagating from the pile driving [8], and the long-term practical verification of this formula showed the satisfactory agreement with the full-scale research data [9].

Today, there is no common approach in the aspect of evaluation of the soil vibration parameters during the impact pile embedment. There are however certain problems in the Golitsin formula application for the soil vibration determination during building from various industrial sources, since the generated waves have higher frequencies and shorter length as compared to the surface waves from earthquakes; the first ones propagate in the upper soil layers near the earth surface [10]. The information resulting from the researches shows that the coefficient δ depends on the vibration source energy, frequency of the waves propagating in the soil, the distance from the vibration source, and soil formation thickness. Experimental data show that the values of δ may vary by more than one order and even change the sign in different points on the earth surface.

According to [11], the parameter δ can be evaluated by the formula

$$\delta = 2\pi fD/V, \quad (2)$$

where D is the soil damping (Hz·s)⁻¹ ($D \ll 1$), f is the vibration frequency (Hz), V is the velocity of wave propagation (m/s), which depends either on the surface wave velocity V_R , or on the transversal wave velocity V_s .

It follows from (2) that δ reduces along with the decrease of the vibration frequency and increase of the wave propagation rate, i.e. the low-frequency wave damps less than the high-frequency one [12]. The dependence of δ on the material characteristics is evident. With the aid of measurements in [13] it is shown that soft soil decreases the vibration level faster than the hard soil. According to [14], the soil damping value depends on the vibration amplitude, soil type, humidity and temperature. For example, humid sand damps the vibrations weaker than dry sand, and frozen soil weakens the vibrations worse than thawed soil.

The authors of [6, 15–17, 33] consider the soil vibration during the impact pile embedment and detect two zones – the near one (nonlinear-plastic) and the far one (elastic). It is believed that the energy dissipates in the near zone due to the plastic flows in the soil. In the far zone, the vibrations mainly consist of the surface waves, and the soil works in the elastic state [18, 19]. In [20–23] it is shown that near the source causing the vertical vibrations, the vertically polarized shear waves dominate, but, as the distance from the source rises, the Rayleigh waves are generated faster. In the near zone, the amplitude attenuation is stronger, than in the far zone.

The near zone is not studied well enough. Neither wave propagation inside this zone, nor its boundaries are detected precisely. As a rule, the width of the near zone is evaluated to range from one to several meters from the pile embedded [6, 20, 24]. It was found in [17] by means of simulation that the calculation results agreed better with the experimental data when the distance from the far zone start was equal to the half of the Rayleigh wave length $r_f = 0.5L_R$, which coincides with the conclusions of [25]. The Rayleigh wave length is determined as

$$L_R = \frac{V_R}{f},$$

f is the pile vibration frequency (Hz), V_R is the Rayleigh wave velocity which can be found with the aid of [26]

$$V_R \approx V_s \frac{0.87 + 1.12\nu}{1 + \nu},$$

where V_s is the transversal wave velocity (m/s), ν is the Poisson ratio. The value V_s is calculated in accordance with [27]

$$V_s = \sqrt{\frac{\mu}{\rho}} = \sqrt{\frac{E}{2\rho(1+\nu)}}.$$

Here, μ is the Lamé coefficient equivalent to the shear module G , (Pa), ρ is the soil density (kg/m^3), E is the elasticity module (Pa).

When detecting the distance from the far zone start, the following approach is also applicable [28]. As the pile is being embedded in soil, the boundary r_f position changes. Each section of the pile lying at the depth h , is and source of longitudinal and transversal waves which impact over the earth surface and transform a part of energy into the Rayleigh waves. The distance from the pile to the point on the soil r_h , where the Rayleigh waves come from the source at the depth h is found by the expression

$$r_h = h \frac{V_R}{\sqrt{V_p^2 - V_R^2}},$$

where V_p is the longitudinal wave velocity calculated according to

$$V_p = \sqrt{\frac{\lambda + 2\mu}{\rho}}, \lambda = \frac{\nu E}{(1+\nu)(1-2\nu)}.$$

In this case, the position of the elastic zone boundary can be evaluated as $r_f < r_H$,

$$r_H = H \frac{V_R}{\sqrt{V_p^2 - V_R^2}},$$

where H is the depth of pile embedment in the soil.

Thus, since the evaluation of the dynamic actions is an important and urgent engineering task not only for the pile foundations construction but also for the design of the foundations for machines with dynamic loadings, the more accurate solutions of this task remains topical [29–31, 38]. In practice, it is desirable to have reliable results using quite simple relations in calculations. In this context, the present paper offers the formula to determine the law of vibrations attenuation as the distance from the source rises. The calculation results obtained by the formula are compared both with the experimental findings presented in [6, 24] and with the authors' results.

2. Methods

2.1. Theoretical method

We assume that, according to [6], the maximal soil shears are caused mainly by the waves propagating from the side pile surface. To determine the vibration attenuation law in the far zone, the wave model is used; in the framework of this model, we detect the links between the motions at the vertical vibrations of the embedded circular in plane absolute solid body and the motions in the surrounding soil. The contact with the medium is realized through the side surface of the embedded body. The medium described by the integrity of infinitely thin layers is considered as the soil. Hence, we solve the task of the vertical vibrations of the infinite plate with a circular cut.

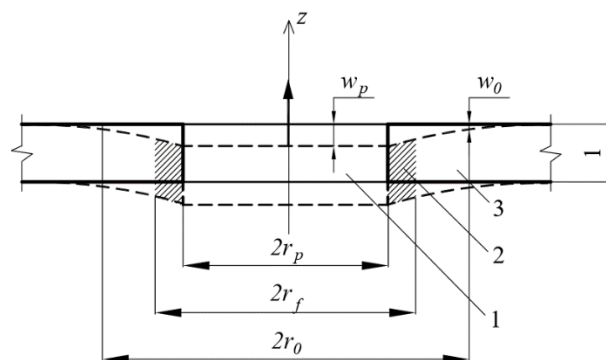


Figure 1. Schematic of the circular cut position in the vibrating thin plate:
1 – cut, 2 – nonlinear-plastic (near) zone, 3 – elastic (far) zone.

Let us consider the warping axisymmetric vibrations of the infinitely thin layer with one circular cut, it radius r_p (Fig. 1). In this case, the equation of elastic medium motion without volume forces in the cylindrical system of coordinates (r, θ, t) is written as:

$$\mu \left(\frac{1}{r} \frac{\partial}{\partial r} r \frac{\partial w}{\partial r} + \frac{1}{r^2} \frac{\partial^2 w}{\partial \theta^2} \right) = \rho \frac{\partial^2 w}{\partial t^2}. \quad (3)$$

Here, $w = w(r, \theta, t)$ is the motion along the axis z , ρ is density. Proceeding from the medium motion character, presuming that every point remains on its straight line during the vibration ($r, \theta = const$), and the distance between them does not change, the equation (3) can be transformed as

$$\frac{1}{r} \frac{\partial}{\partial r} r \frac{\partial w}{\partial r} = \frac{\rho}{\mu} \frac{\partial^2 w}{\partial t^2}, \quad (4)$$

under the condition of the space $r_0 \geq r_p$ in a certain point

$$w(r_0, t) = w_0 e^{i\omega t}. \quad (5)$$

Since we consider the vibrations of the absolute solid body, every point of which in plane ($0 \leq r \leq r_p$) shear by the same value, let us pass to the coordinate $r = r - r_p$. In this case, the equation (4) remains as it is written. This would be enough when considering the embedded solid body under the dynamic loadings, assuming the properties of the elastic medium in the near and far zones. If we presume the presence of the near (nonlinear-plastic) zone with the external boundary $r = r_f$, it is advisable (4) to consider in the area $r \geq r_f$ at $r_0 \geq r_f$ and to pass to the new coordinate like $r = r - r_f$.

The solution of (4), (5) is carried out by the variable separation method and, according to [39], can be presented as

$$w = e^{i\omega t} \sum_{n=0}^{\infty} [A_n H_n^{(1)}(kr) + B_n H_n^{(2)}(kr)]. \quad (6)$$

where $k = \omega / \sqrt{\mu / \rho}$, $H_n^{(1)}$, $H_n^{(2)}$ are the first and second kind Hankel functions, and A_n , B_n are the constant coefficients to be determined.

Since we consider the plane with one cut, and there are no other source of vibration, then (6) describes only divergent waves at $r \rightarrow \infty$. It follows from the asymptotic expansions of the Hankel functions [39] that this conditions at the time factor $e^{i\omega t}$ is satisfied by the function $H_n^{(2)}$ and hence, $A_n = 0$. It follows from the axial symmetry condition that $n = 0$. Then we have $w = e^{i\omega t} B_0 H_0^{(2)}(kr)$, where, according to (5)

$$B_0 = w_0 / H_0^{(2)}(kr_0),$$

and hence,

$$w = e^{i\omega t} w_0 H_0^{(2)}(kr) / H_0^{(2)}(kr_0).$$

Let us evaluate the relative motion of the soil w/w_0 using the relation

$$w/w_0 = H_0^{(2)}(kr) / H_0^{(2)}(kr_0) = S_R(kr) + iS_I(kr),$$

where

$$S_R(kr) = \frac{J_0(kr)J_0(kr_0) + Y_0(kr)Y_0(kr_0)}{J_0^2(kr_0) + Y_0^2(kr_0)}, \quad S_I(kr) = \frac{J_0(kr)Y_0(kr_0) - Y_0(kr)J_0(kr_0)}{J_0^2(kr_0) + Y_0^2(kr_0)}.$$

In the initial system of coordinates, $S_R(kr)$ and $S_I(kr)$ look like

$$S_R(kr) = \frac{J_0[k(r-r_f)]J_0[k(r_0-r_f)] + Y_0[k(r-r_f)]Y_0[k(r_0-r_f)]}{J_0^2[k(r_0-r_f)] + Y_0^2[k(r_0-r_f)]},$$

$$S_I(kr) = \frac{J_0[k(r-r_f)]Y_0[k(r_0-r_f)] - Y_0[k(r-r_f)]J_0[k(r_0-r_f)]}{J_0^2[k(r_0-r_f)] + Y_0^2[k(r_0-r_f)]}.$$

Thus, the varying vibration amplitudes can be described by the formula

$$A = A_0(S_R^2 + S_I^2)^{0.5}, \quad (7)$$

where A_0 is the amplitude in the point r_0 . Fig. 2 shows the results obtained in accordance with (7) at different dimensionless frequencies $a_0 = kr_0$ in the case $r_f = r_p$, $r_0 = r_p$. The calculation data illustrate the dynamics of amplitude variation in the medium, and particularly show that the low-frequency wave damps weaker than the waves with higher frequencies, which agrees with [12].

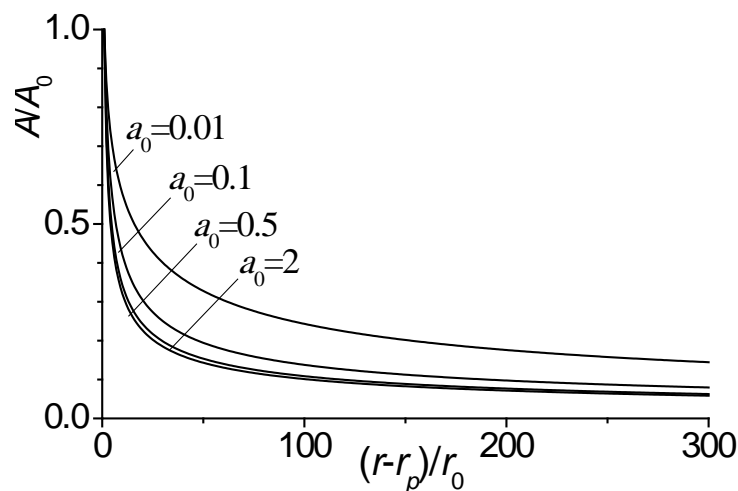


Figure 2. Attenuation of vibration amplitudes at various dimensionless frequencies a_0 .

2.2. Experimental method

Experiments were carried out to analyze the dynamic actions occurring during the pile driving. Three similar-procedure series of tests were carried out. In each case, one prismatic assembled reinforced-concrete pile CP-1, CP-2, CP-3, the length 7.0 m, the cross section 30x30 cm, was embedded by the hydraulic hammer ROPAT. The vibration amplitudes and frequencies were registered on the soil surface in four points simultaneously with the embedment. The distances from the embedded pile center to the probe 1 was 1.5 m, to the probes 2, 3, 4 it was 10 m, 20 m, and 30 m, respectively. Every test pile was embedded directly in the soil from the ditch bottom.

The soil in the worksite from the ditch bottom surface down to the depth of 3.6 m consisted of non-subsiding solid sand clay with the average water saturation degree and density $\rho = 1.78 \text{ t/m}^3$, the deformation module $E_0 = 8.5 \text{ MPa}$ and Poisson ratio $\nu = 0.33$, subsoiled with fine uniform sand with the density $\rho = 2.01 \text{ t/m}^3$, the deformation module $E_0 = 17.6 \text{ MPa}$. The subterranean water at the test moment was at the depth of 3.5 m from the ditch bottom surface.

To register the vibration amplitudes and frequencies we used the vibration-measuring apparatus AVM-1, which includes 3D probes with vibrating accelerometers ADXL, AD/DA converter and PC. AVM-1 permits registering the vibrations and simultaneously process the gathered information. The probe presents a metal case shaped as a cube which can be fastened on the soil surface, with boards with integral two-channel accelerometers inside. The probes were connected to the AD/DA converter via cables. The external module E14-140 made by L-CARD was used as the AD/DA converter. The major engineering characteristics of the used apparatus are presented in the Table below. The data were registered for each embedded pile.

Table 1. Engineering characteristics of apparatus.

Frequency measurement range, Hz	1 – 100
Amplitude measurement range, mm	0.0005–20
The limit of allowed main relative error in the amplitude measurement, %	± 3
The limit of allowed main relative error in the frequency measurement in the range of 1–100 Hz	± 0.2 Hz
Amount of axis in the vibrating probe	3
Probe amount, pcs.	4
Process temperature range	From –10°C to +80°C

3. Results and Discussion

Fig. 3 shows the measurement and calculation results obtained by the formula (7): the rated vibration amplitudes A/A_{\max} for various distances from the source $r = 1.5; 10; 20; 30$ m. The point within 10 m from the vibration source is used as r_0 , for A_{\max} we used the amplitude values at $r = 1.5$ m. The start of the elastic medium zone $r_f = 1$ m was chosen in the same way as in [24], where the soil vibration was studied during the embedment of the similar size pile. The solid lines in Fig. 3–5 show the calculation results obtained with the aid of (7), the dotted lines present the results obtained with the formula (1).

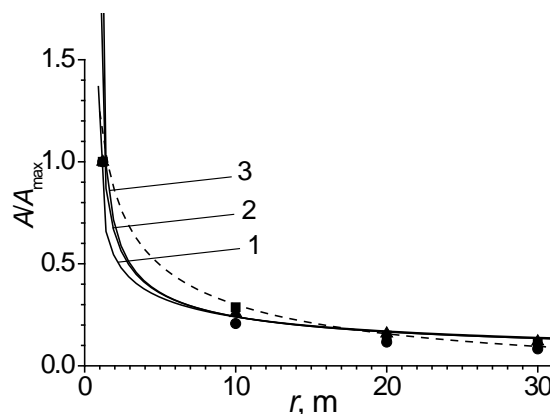


Figure 3. Attenuation of the relative vibration amplitude of the soil at various $k = 0.1$ (1), 0.5 (2), 2 (3) ■, ▲, ● – measurement data.

Fig. 3 demonstrates the satisfactory agreement between the calculations and measured data. It follows from the results of the full-scale and numerical experiments that, as the distance from the vibration source increases, the vibration amplitudes decrease monotonically. The fastest decreases of the amplitude takes place in the area close to the vibration source. For example, in respect to the nearest measurement point ($r = 1.5$ m) within 5 m from the vibration source, the amplitude decreases approximately by three times, by 4 times within 10 m, by 7 times within 20 m and by 10 times within 30 m. The strongest effect of the parameter k on the amplitude variation is observed at $r \leq 8$ m. At low k (for example, at the constant frequency and low density of the medium), the vibrations damp faster. As k rises, the damping is slower, and at $k \geq 0.5$, the obtained solutions feasibly coincide. In the area at $r > 8$, the attenuation does not depend on k . The curves in the figure going above $A/A_{\max} = 1$ describe the variations of the vibration amplitudes in the area between $r = 1.5$ m and $r = r_f$. The results obtained by the formula (1) at $\delta = 0.03 \text{ m}^{-1}$ [6] agree satisfactory with the data obtained during the measurements at $r \geq 10$ m. In the area of $3 \text{ m} \leq r \leq 9 \text{ m}$, the discrepancy between the results given by the formulas (1) and (7) ranges from 20 to 30 %. However, no experimental data makes impossible to confirm the advantages of any method.

To evaluate the applicability of (7), the results of soil vibration amplitudes presented in [6, 24] were used. Fig. 4 demonstrates the measurement results [24] within different distances from the source $r = 1.5; 5; 10; 15; 20; 25; 30$ m and calculations of the rated vibration amplitudes A/A_{\max} . Similarly to the above version, $r_0 = 10$ m. The amplitude values at $r = 1.5$ m were used as A_{\max} . The start of the elastic medium zone $r_f = 1$ m as determined in [24] in accordance with the results of research of the soil vibrations during the pile driving. The calculations by the formula (1) were performed at $\delta = 0.04 \text{ m}^{-1}$ [6].

Figure 5 illustrates the measurement results from [6] at the distances from the source $r = 3, 5, 10, 20, 30$ m and calculations, according to (7), of the rated vibration amplitudes A / A_{\max} . The amplitude values at $r = 3$ m were used as A_{\max} . Again, $r_0 = 10$ m. The start of the elastic medium zone $r_f = 2$ m was chosen in [6] in accordance with the results of research of the soil vibrations during the pile driving. According to [6], the calculations with the formula (1) were carried out at $\delta = 0.07 \text{ m}^{-1}$.

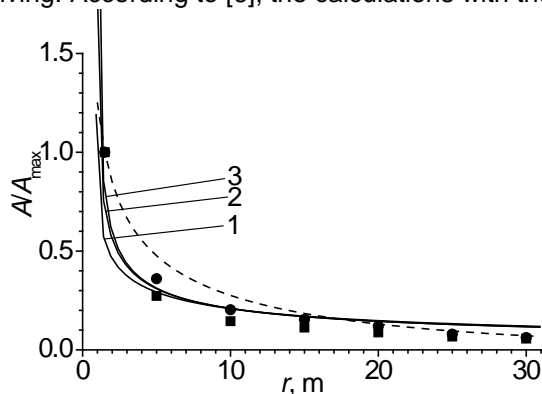


Figure 4. Attenuation of the relative vibration amplitude of the soil at $k = 0.1$ (1), 0.5 (2), 2 (3) ■, ● – measurement data [24].

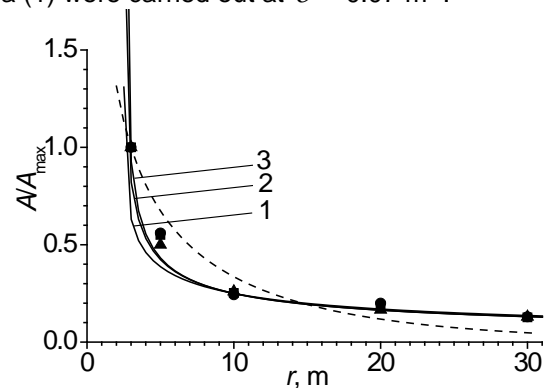


Figure 5. Attenuation of the relative vibration amplitude of the soil at $k = 0.1$ (1), 0.5 (2), 2 (3) ■, ▲, ● – measurement data [6].

According to the results presented in Fig. 4, 5, there is the satisfactory agreement between the data calculated by the formula (7) and the data from [6, 24] to describe the variations in the vertical soil vibration amplitude versus the distance from the vibration source. The Golitsin's formula (1) gives a discrepancy between the experimental and calculation data; to reduce this discrepancy, one need information to correct the vibration attenuation coefficient δ which varies versus the distance from the source. Extra analysis of the soil vibration is needed. Thus, the wave model solution has an advantage over the formula (1).

4. Conclusions

The following conclusions are derived from the performed investigation:

1. The solution (7) of the wave model describes the variation in the soil vertical vibration amplitude versus the distance from the vibration source. To use this solution, it is enough to have the data of only one measurement of the vibration amplitude and the size of the non-linear-plastic area around the driven pile. The vibration amplitude should be measured within the distance exceeding the width of the non-linear-plastic zone, or on its boundary. The size of the non-linear-plastic area around the pile is evaluated approximately either by the half of the Rayleigh wave, or as a distance from 1 to 3 m.
2. Application of the formula (7) gives the satisfactory agreement of the calculation and measurement data in the field measurement and solutions of elastic-plastic problems involving big soft packages.

5. Acknowledgements

The research has been carried out within the Program of Fundamental Research of the State Academies of Sciences 2013-2020 (project No. AAAA-A17-117030610136-3).

References

1. Holscher, P., Waarts, P.H. Reliability of vibration prediction and reducing measures [Online]. Report Delft Cluster. Delft. 2003. URL: <http://resolver.tudelft.nl/uuid:05863abb-5090-4399-a48b-ee04d26cd883>
2. ISO 4866:2010. Mechanical vibration and shock – Vibration of fixed structures – Guidelines for the measurement of vibrations and evaluation of their effects on structures.
3. DIN 4150-3:2016-12. Vibrations in buildings – Part 3: Effects on structures.
4. BS 7385-2:1993. Evaluation and measurement for vibration in buildings – Part 2: Guide to damage levels from groundborne vibration.
5. NS 8141-1:2012+A1:2013 Vibration and shock – Guideline limit values for construction work, open-pit mining and traffic – Part 1: Effect of vibration and air blast from blasting on constructions, including tunnels and rock caverns.
6. Kalyuzhnyuk, M.M., Rud', V.K. Svaebnojnye raboty pri rekonstrukcii [Piling works during reconstruction] [Online]. Saint-Petersburg: Strojizdat, 1989. 160 p. URL: <http://science.totalarch.com/book/4482.rar> (rus)
7. Golitsin, B.B. On dispersion and attenuation of seismic surface waves. Russian Academy of Science News. 1912. 6(2).
8. Bornitz, G. Über die ausbreitung der von großkolbenmaschinen erzeugten bodenschwingungen in die tiefe [Online]. Berlin. Springer-Verlag, 1931. 56 p. URL: <https://DOI.org/10.1007/978-3-642-99597-2>
9. Vasil'evskij, YU.I. Dinamika pogruzheniya zhelezobetonnyh svaj pri zabivke [Dynamics of reinforced concrete piles immersion during driving]. Trudy koordinacionnyh soveshchanij po gidrotekhnike. 1971. No. 66. Pp. 47–51. (rus)
10. Svinkin, M.R. Soil and structure vibrations from construction and industrial sources [Online]. Proceedings of the Sixth International Conference on Case Histories in Geotechnical Engineering. Omni Press, Arlington, Virginia. 2008. Pp. 1–14. URL: <https://scholarsmine.mst.edu/icchge/6icchge/session13/8>

11. Athanasopoulos, G.A., Pelekis, P.C., Anagnostopoulos, G.A. Effect of soil stiffness in the attenuation of Rayleigh-wave motions from field measurements. *Soil Dynamics and Earthquake Engineering*. 2000. 19(4). Pp. 277–288. DOI: 10.1016/S0267-7261(00)00009-9
12. Auersch, L., Said, S. Attenuation of ground vibrations due to different technical sources. *Earthquake Engineering and Engineering Vibration*. 2010. 9(3). Pp. 337–344. DOI: 10.1007/s11803-010-0018-0
13. Clough, G.W., Chameau, J-L. Measured effects of vibratory sheet pile driving [Online]. *Journal of Geotechnical Engineering*. Division, ASCE. 1980. 106(GT10). Pp. 1081–1099. URL: [https:// search-works.stanford.edu/view/486385](https://search-works.stanford.edu/view/486385)
14. Amick, H., Gendreau, M. Construction vibrations and their impact on vibration-sensitive facilities. *Proceedings of the 6th ASCE Construction Congress*. 2000. DOI: 10.1061/40475(278)80
15. Barkan, D.D. *Dynamics of bases and foundations* [Online]. New York: McGraw-Hill Book Company Inc., USA, 1962. 478 p. URL: <https://archive.org/details/dynamicsofbasesf00bark>
16. Massarsch, K.R. Effects of vibratory compaction [Online]. *TransVib 2002 – International Conference on Vibratory Pile Driving and Deep Soil Compaction*. 2002. Pp. 33–42. URL: https://www.researchgate.net/publication/292792536_Effects_of_vibratory_compaction
17. Darius, M., Stefan, V.B. A simple engineering soil surface vibration prediction method. *Civil Engineering Research Journal*. 2018. 4(2). DOI: 10.19080/CERJ.2018.04.555632
18. Massarsch, K.R. Vibrations caused by pile driving [Online]. *The Magazine of the Deep Foundations Institute*. Part 1: Summer Edition. 2004. Pp. 1–8. URL: <https://ru.scribd.com/document/355361734/Vibrations-Caused-by-Pile-Driving>
19. Whenham, V. Power transfer and vibrator-pile-soil interactions within the framework of vibratory pile driving. *Doctoral Thesis* [Online]. University of Louvain. Belgium. 2011. URL: <http://hdl.handle.net/2078.1/75975>
20. Head, J.M., Jardine, F.M. Ground-borne vibrations arising from piling [Online]. CIRIA Technical Note 142. *Construction Industry Research and Information Association (CIRIA)*. London. 1992. URL: <https://www.thenbs.com/PublicationIndex/documents/details?Pub=CIRIA&DocID=53095>
21. Svinkin, M.R. Overcoming soil uncertainty in prediction of construction and industrial vibrations [Online]. *Uncertainty in the geologic environment: from theory to practice*. ASCE, *Geotechnical Special Edition*. 1996. No. 58. Pp. 1178–1194. URL: https://www.researchgate.net/publication/287095145_Overcoming_soil_uncertainty_in_prediction_of_construction_and_industrial_vibrations
22. Svinkin, M.R. Minimizing construction vibration effects. *Practice Periodical on Structural Design and Construction*, ASCE. 2004. 9(2). Pp. 108–115. DOI: 10.1061/(ASCE)1084-0680(2004)9:2(108)
23. Masoumi, H.R., Degrande, G. Numerical modeling of free field vibrations due to pile driving using a dynamic soil-structure interaction formulation. *Journal of Computational and Applied Mathematics*. 2008. 215(2). Pp. 503–511. DOI: 10.1016/j.cam.2006.03.051
24. Vasenin, V.A. Ocenka parametrov kolebanij grunta pri udarnom pogruzenii svaj. Osnovnye sledstviya [Estimation of ground vibrations parameters during impact pile driving. The main investigation] [Online]. *Rekonstrukciya gorodov i geotekhnicheskoe stroitel'stvo*. 2003. No 7. Pp. 210–223. URL: <https://cyberleninka.ru/article/n/eksperimentalnye-issledovaniya-parametrov-kolebaniy-grunta-pri-zabivke-svaj> (rus)
25. Wolf, J.P. *Foundation vibration analysis using simple physical models*. Prentice Hall, Upper Saddle River, USA, 1994. 464 p.
26. Holmberg, R., Arnberg, P.W., Bennerhult, O., et al. *Vibrations generated by traffic and building construction activities*. Swedish Council for Building Research. Stockholm, Sweden. 1984.
27. Massarsch, K.R. Settlements and damage caused by construction-induced vibrations [Online]. *Proceedings of the International Workshop Wave 2000*. Bochum, Germany. 2000. Pp. 299–315. URL: <https://ru.scribd.com/document/37007330/Settlements-and-Damage-Caused-by-Construction-Induced-Vibrat>
28. Dowding, C.H. *Construction Vibrations*. Prentice Hall. Upper Saddle River, USA, 1996. 620 p.
29. Cleary, J.C., Steward, E.J. Analysis of ground vibrations induced by pile driving and a comparison of vibration prediction methods. *DFI Journal – The Journal of the Deep Foundations Institute*. 2016. 10(3). Pp. 125–134. DOI: 10.1080/19375247.2017.1288855
30. Rahman, N., Musir, A.A., Dahalan, N., Ghani, A., Khalil, M. Review of vibration effect during piling installation to adjacent structure. *AIP Conference Proceedings*. 2017. No. 1901. 110009. DOI: 10.1063/1.5010550
31. Deckner, F., Viking, K., Hintze, S. Wave Patterns in the Ground: Case Studies Related to Vibratory Sheet Pile Driving. *Geotechnical and Geological Engineering*. 2017. 35(6). Pp. 2863–2878. DOI 10.1007/s10706-017-0285-x
32. Massarsch, K.R., Fellenius, B.N., Bodare, A. Fundamentals of the vibratory driving of piles and sheet piles. *Geotechnik* 40. 2017. No. 2. Pp. 126–141. DOI: 10.1002/gete.201600018
33. Khoubani, A., Ahmadi, M.M. Numerical study of ground vibration due to impact pile driving. *Geotechnical Engineering*. 2014. 167(1). Pp. 28–39. DOI: 10.1680/geng.11.00094
34. Jayawardana, P., Achuhan, R., Subashi De Silva, G.H.M.J., Thambiratnam, D.P. Use of in-filled trenches to screen ground vibration due to impact pile driving: experimental and numerical study. *Heliyon*. 2018. 4(8). DOI: 10.1016/j.heliyon.2018.e00726
35. Dungca, J.R., Acosta, D.Y., Juego, M.B., Sanchez, H.M., Sanchez, I.S. The propagation behavior of pile-driving-induced vibration done on soil at varying distances and its effects on existing structures. *International Journal of GEOMATE*. 2016. 10(21). Pp. 1877–1883. DOI: 10.21660/2016.21.5223
36. Li, Q., Shu, W., Cao, L., Duan, W., Zhou, B. Vertical vibration of a single pile embedded in a frozen saturated soil layer. *Soil Dynamics and Earthquake Engineering*. 2019. No. 122. Pp. 185–195. DOI: 10.1016/j.soildyn.2019.03.032
37. Dai, D., El Naggar, M.H., Zhang, N., Gao, Yu., Li, Zh. Vertical vibration of a pile embedded in radially disturbed viscoelastic soil considering the three-dimensional nature of soil. *Computers and Geotechnics*. 2019. No. 111. Pp. 172–180. DOI: 10.1016/j.compgeo.2019.03.013
38. Ter-Martirosyan, Z.G., Ter-Martirosyan, A.Z., Sobolev, E.S. Interaction of the pile and surrounding soil during vibration driving. *IOP Conf. Series: Materials Science and Engineering*. 2018. No. 456. DOI: 10.1088/1757-899X/456/1/012093
39. Tihonov, A.N., Samarskij, A.A. *Uravneniya matematicheskoy fiziki* [Equations of mathematical physics]. Moscow: Nauka, 1966. 724 p. (rus)

Contacts:

Aleksei Kolesnikov, ao_kolesnikov@mail.ru

Tatiana Kostiuk, tanyakostuk26@gmail.com

Vladimir Popov, popov@itam.nsc.ru



DOI: 10.18720/MCE.95.6

Heat loss from defects of hinged facade systems of buildings

A.E. Rusanov^a, A.Kh. Baiburin^{a*}, D.A. Baiburin^a, V. Bianco^b

^a South Ural State University, Chelyabinsk, Russia

^b University of Genoa, Genoa, Italy

* E-mail: abayburin@mail.ru

Keywords: buildings, energy efficiency, hinged facade system, thermal insulation, heat loss, heat transfer factors, mathematic simulation

Abstract. The object of investigation hinged facade systems (HFS) used in buildings. Characteristic violations of the HFS technology were identified. The heat loss which depends on a range of structural features of HFS, such as geometrical, thermal, and physical properties of HFS elements, was analyzed. The effect of HFS properties on changes in heat flow and temperature fields was studied. An experiment was designed, computer simulation and laboratory tests were conducted. Different types of HFS defects were analyzed. Finite-element models were developed in the software ELCUD. Laboratory tests proved the adequacy of finite-element models. The comparative results obtained from tests and numerical models were consistent. Mathematical models of the joint effect of these factors were developed. An analysis of the factors' effect on heat loss through HFS elements was performed. An effective way to ensure the energy efficiency of buildings – energy certification with control at the construction stage, was considered. The results can be used for the energy classification of buildings.

1. Introduction

The object of study was the hinged facade systems of civil buildings. The purpose of the study was to determine the effect of defects in the HFS on heat loss. Scientific findings were used to improve the quality control of the HFS and increase the energy efficiency of buildings.

The objectives of the study were:

- to analyze damage to the structure of HFS affecting the heat-shielding properties of structures, and the rationale for computer simulation of defects;
- to determine the combined effect of defects of HFS on the level of thermal protection of building envelopes;
- to develop organizational and technological solutions for HFS aimed at ensuring standardized indicators of energy efficiency of buildings.

Recently, more and more attention has been paid to studying the energy efficiency of buildings, the temperature and humidity conditions of building envelopes, as well as improving their heat-shielding properties [1–41]. The variety of applied hinged facade systems (HFS) and materials for their elements is noted [1, 5, 12, 13, 16, 17, 21, 25, 28–31]. In the construction industry of Russia, the number of tenders for the construction of HFS is 16 %, and the total area of the facades erected in one year reaches 20 million square meters [32]. At the same time, studies of the influence of design features of HFS on the amount of heat loss have become important [2, 11, 13, 22, 27, 29, 33, 36–40], including when taking into account the operation of ventilated channels [20, 24, 26, 30]. In addition to the estimated energy efficiency of buildings with consideration of their life cycle [2, 9, 10, 31] experimental analysis and construction control are required [3, 4, 6–8, 18, 19, 36–40].

During the construction of new buildings or thermal renovation of old buildings, it is necessary to confirm the class of their energy efficiency by various methods [3, 6–8, 14, 15, 19, 23, 36, 38]. As practice shows, in the applied HFS there are numerous violations of the project during construction which negatively affect the



energy efficiency of buildings [1, 18, 19, 31–34, 36–40]. Construction control during the installation of building envelopes is often carried out without the use of scientifically based quality control cards or quantitative assessments of the effects of defects on the level of thermal protection.

The analysis of the results of the statistical processing of thermovision control data [36–39] shows that more than a half of the structures examined (62 %) have defects, which indicates their massive occurrence. The overwhelming majority of defects (90 %) are traced at the connection nodes of window units and wall apertures [34, 37].

Neglecting thermal bridges presence can lead to significant underestimation of actual heat flows which can account for 5 % to almost 20 % of total heat flows through the building envelope [40]. Studies have shown, that the value of the point thermal transmittance, which depended on the thermal properties of the envelop and thickness of the layers, might increase to 35 % [39].

The thermograms obtained through thermovision control [34, 36–40] allowed revealing thermotechnical defects:

- local defects of building envelope;
- defects of translucent building envelope elements;
- temperature anomalies in the junction nodes of external wall;
- defects of erection joints in the connection nodes of window units and wall apertures.

The joint effect of defects on heat loss through HVF has not been studied enough. The study [34] was based on similar methods, but focused on a different structure HVF.

It is necessary to conduct research on the assessment of construction discrepancies due to the need to establish a balance between the design decisions made and the actual execution. The compliance of the actual values of the energy passport of the building with design decisions is established by the results of field tests after construction has been completed. The existing practice of applying energy passport, as a rule, boils down to determining heat loss. Defects in thermal protection must be identified in the process of construction control and their significance must be evaluated promptly.

2. Methods

The study of the effect of defects on the thermal protection of HFS was carried out using computer simulation in the ELCUT software package (certificate of compliance for use in construction No. RU.SP15.H00904).

To confirm the adequacy of the computer calculation, the most characteristic defects in the laboratory were simulated on a fragment of the HFS. The tests were carried out in a certified research laboratory at South Ural State University (Chelyabinsk, Russia). The test procedure was in accordance with State Standard of Russia 56623-2015 “Non-destructive testing. The method for determining the heat transfer resistance of building envelopes”, State Standard of Russia 54853-2011 “Buildings and structures. The method for determining the heat transfer resistance of enclosing structures using a heat meter”, and State Standard 25380-2014 “Buildings and structures. The method for measuring heat fluxes passing through a structural enclosure.” These standards establish methods for measuring the density of heat fluxes through single-layer and multi-layer building envelopes and their resistance to heat transfer in laboratory and field conditions.

The conditions of stationary heat flow were provided by the LTHC-24.0 climatic chamber with a useful volume of 24 m³. The experiment was carried out in the climatic conditions of the city of Chelyabinsk, Russia (55 degrees N, heating degree-day of 6000). The temperature in the room was 21 °C and -34 °C in the chamber. The set of instrumentation equipment included: a FLIR E60 thermal imager; a ITP-MG4.03.10 Potok 10-channel device; a TGTs-MG4 thermohygrometer; a TEMP-3.2 thermohygrometer; a ISP-MG4 Zond heat conductivity meter, etc.

The object of the laboratory study was a fragment of the building envelope of the HFS. Fragment dimensions: height – 1275 mm, width – 1255 mm, thickness – 300 mm, usable area – 1 m². As a carrier layer, masonry from tongue-and-groove aerated 625×250×200 mm D500 concrete blocks was used. Vertical and horizontal masonry joints were made with 5 mm thick Ceresit CT 21 glue. LINEROCK mineral wool boards $\gamma = 80 \text{ kg/m}^3$ of 1000×500×100 mm were used as the heat-insulating layer. To fasten the insulation, 160×8 mm Mungo MDD-S plate-shaped dowels with a metal nail were used. The HFS guide rails were fastened using a 150-50×50 mm KR Alternative bracket and wall dowel with a 10×100/50 MBK-STB screw. The values of the thermal conductivity coefficients of the materials used: D500 gas concrete block – 0.181 W/(m °C); insulation – 0.037 W/(m °C).

After obtaining the results of the laboratory experiment, numerical simulation was performed using the ELCUT software package and the consistency of the results was evaluated.

3. Results and Discussion

Industrial studies of the quality of the HFS were performed on 20 precast-monolithic, monolithic, and brick civil buildings in Chelyabinsk (Russia). The main defects of thermal protection were established: gaps in the joint of insulation boards; gaps at the junction of the bracket with the insulation board; detachment of the insulation from the foundation; gaps in the expansion joint between the foundation and the floor slab; deviations of insulation thickness; and deviations of thermal conductivity coefficients of foundation materials, heat-insulating layer, bracket, and expansion joint. Industrial studies have established that the first four defects are the most characteristic (Fig. 1).



Figure 1. Defects in thermal protection: from top to bottom and from left to right: gap at the junction of the insulation boards; gap at the junction of the bracket with insulation; detachment of the insulation from the foundation; defects in materials; level defects.

The defectiveness characteristics for technological deviations from tolerances were studied during the construction of the HFS (Table 1). The defect level in some parameters reaches 35–45 %. The identified defects can reduce the level of thermal protection of walls to 30–50 %, which is confirmed by research data [7, 11, 18, 22, 31, 32, 37] on significant differences between the design and actual thermal characteristics of building shells.

Table 1. Defectiveness in some quality parameters.

Monitored parameters	\bar{X}	S_x	δX_n	Q
Gap at the junction of insulation boards	0.63	0.70	2.00	0.45
Gap at the junction of the bracket with the insulation board	1.47	0.62	5.00	0.41
Peeling of insulation boards from the foundation	1.58	0.52	6.00	0.35
Gap in the expansion joint between the foundation and the floor slab	3.36	0.25	30.00	0.43

Notes: \bar{X} is average value of the parameter; S_x is standard deviation; δX_n is standard deviation of the parameter; Q is defective level.

Simulations were carried out in the program ELCUT to study the effect of these defects on the level of thermal protection. The adequacy of the simulation was verified through laboratory studies and subsequent analysis of the reliability and consistency of the results. The influence of thermal protection defects was modeled using typical HFS defects: gaps ($t = 10$ mm) at the junction of the insulation boards, gaps ($t = 15$ mm) at the junction of the bracket with the insulation board, and peeling ($t = 10$ mm) of the insulation boards from the load-bearing foundation (Fig. 2).

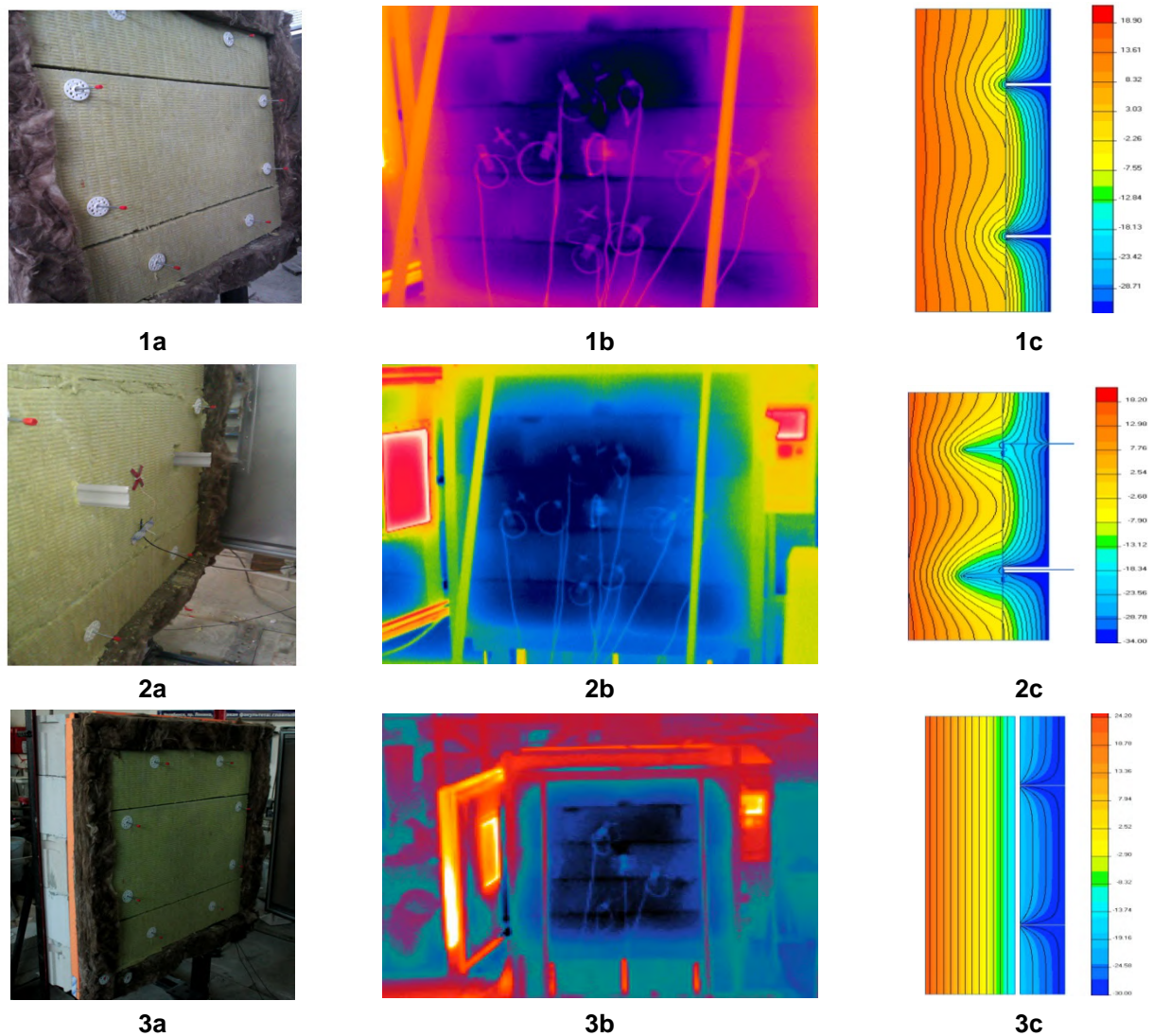


Figure 2. Tested wall fragments with defects in thermal protection:
1) gap at the junction of the insulation boards;
2) gap at the junction of the insulation boards and the bracket;
3) peeling of insulation boards from the foundation;
a) fragment of the enclosing structure; b) thermogram of the fragment;
c) temperature field of the cross section of the fragment.

Computer modeling of the wall fragments was carried out subject to the equality of geometric and physical and technical characteristics, boundary conditions of the computer model, and the experimental fragment. Generalized results of the level of thermal protection were obtained through laboratory research and modeling (Table 2). The reduction in the heat transfer resistance was from 5 to 52 %, which correlates with research data [32] on the influence of such defects – up to 52–55 %. The discrepancy between the results of laboratory studies in the climate chamber and computer simulation ranged from 0.65 to 6.64 %. Thus, we can conclude that the numerical models used are adequate.

Table 2. Generalized results of the assessment of the impact of separate defects.

Object of study	$R_o^{np\ exp},$ (m ² .°C)/W	$R_o^{np\ ELCUT},$ (m ² .°C)/W	Discrepancy, %
Fragment of structure without defects	3.24	3.39	4.63
Fragment with peeling of insulation boards from the foundation ($t = 10$ mm)	1.56	1.58	1.28
Fragment with a gap at the junction of insulation boards ($t = 10$ mm)	2.26	2.41	6.64
Fragment with a gap at the junction of the bracket with the insulation board ($t = 15$ m)	3.08	3.10	0.65

Based on the results obtained on the reliability of computer modeling in ELCUT, a mathematical experiment was conducted to determine the combined effect of the main defects of thermal protection.

A numerical experiment was conducted for a blank section of the outer wall (Fig. 3a) and for a plot in the zone of the floor slab (Fig. 3b). Based on the results of calculating the temperature field and the heat flux power, the reduced heat transfer resistance of the HFS wall fragment was determined.

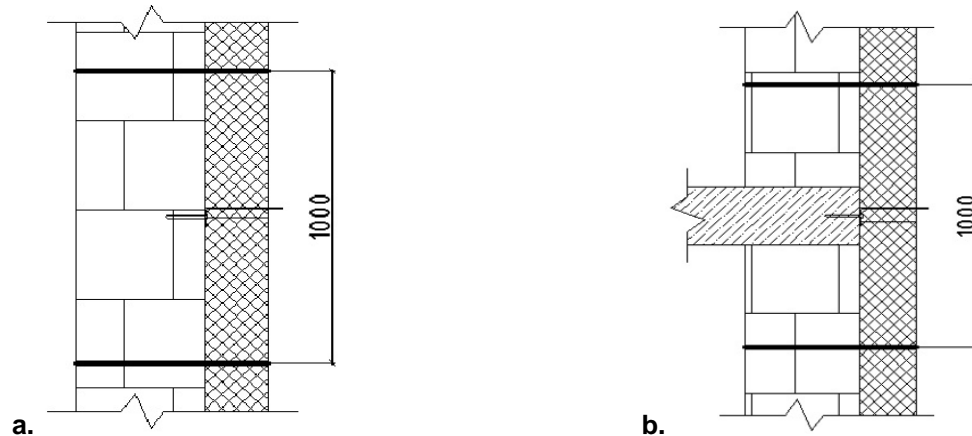


Figure 3. Fragment of the outer wall with the HFS:
a) scheme of the blind section; b) scheme of the section in the area of the floor slab.

A multifactor model was implemented by the methods of planning the experiment, in which the characteristic defects of the thermal protection of the HFS were taken as factors. The values of the levels of variation of factors were determined based on the results of production studies of the quality of work, as well as from analysis of regulatory documents and technical certificates for HFS.

After eliminating insignificant factors, mathematical models were constructed of the combined influence of significant defects on the level of thermal protection of the blind section of the HFS wall (1) and the section in the zone of the floor slab (2). The adequacy of the constructed mathematical models is proved using the Fisher criterion:

$$\begin{aligned}
 k_I = & 0.6684 - 0.0837 \cdot X_1 - 0.0163 \cdot X_2 - 0.1761 \cdot X_3 + 0.0287 \cdot X_4 - \\
 & - 0.0768 \cdot X_5 - 0.1676 \cdot X_6 + 0.0829 \cdot X_7 + 0.0441 \cdot X_1 \cdot X_3 - 0.0266 \cdot X_1 \cdot X_5 - \\
 & - 0.0471 \cdot X_1 \cdot X_6 + 0.0165 \cdot X_1 \cdot X_7 + 0.0160 \cdot X_3 \cdot X_4 - 0.0324 \cdot X_3 \cdot X_5 - \\
 & - 0.0698 \cdot X_3 \cdot X_6 + 0.0503 \cdot X_3 \cdot X_7 - 0.0334 \cdot X_4 \cdot X_5 + 0.0229 \cdot X_4 \cdot X_6
 \end{aligned} \quad (1)$$

$$\begin{aligned}
 k_{II} = & 0.4920 - 0.0896 \cdot X_1 - 0.1696 \cdot X_3 + 0.0687 \cdot X_5 - 0.1683 \cdot X_6 + \\
 & + 0.0736 \cdot X_7 - 0.1003 \cdot X_{10} + 0.0497 \cdot X_1 \cdot X_3 - 0.0391 \cdot X_1 \cdot X_6 + \\
 & + 0.0236 \cdot X_1 \cdot X_{10} - 0.0425 \cdot X_3 \cdot X_6 + 0.0336 \cdot X_3 \cdot X_7 + 0.0433 \cdot X_3 \cdot X_{10} - \\
 & - 0.0284 \cdot X_5 \cdot X_6 + 0.0531 \cdot X_5 \cdot X_{10} - 0.0232 \cdot X_6 \cdot X_7
 \end{aligned} \quad (2)$$

where k_I is the coefficient of the combined influence of factors on the thermal protection of the blind part of the outer wall of the HFS; k_{II} is coefficient of the joint influence of factors on the thermal protection of the HFS wall section in the area of the floor slab; X_1 is the gap at the junction of the insulation boards; X_2 is the gap at the junction of the bracket and insulation board; X_3 is detachment of the insulation from the foundation; X_4 is deviation of the thickness of the foundation; X_5 is deviation of the coefficient of thermal conductivity of the foundation material; X_6 is deviation of the thickness of the insulating layer; X_7 is deviation of the coefficient of thermal conductivity of the material of the insulating layer; X_8 is deviation of the thickness of the bracket; X_9 is deviation of the coefficient of thermal conductivity of the material of the bracket; X_{10} is gap in the expansion joint between the foundation and the floor slab; X_{11} is deviation of the coefficient of thermal conductivity of the material filling the expansion joint between the foundation and the slab. The influence of these factors on the level of thermal protection is presented in Fig. 4.

X_1 , X_2 and X_3 are significant defects for the blind sections of the HFS walls and X_1 , X_3 , and X_{10} for sections of HFS walls in the area of the floor slab. Of the characteristic defects, the greatest influence on the reduced heat transfer resistance is exerted by: peeling of 10 mm of insulation boards from the foundation is 52 %; a gap of 10 mm at the junction of insulation boards is 15 %; a gap of 15 mm at the junction of the bracket and insulation is 3 %, and combined defects. The results obtained nearly coincided with the data of [32] – a

decrease in heat transfer resistance by 10–16 % with a gap at the junction of 8 mm single-layer insulation boards.

In addition to the defects studied, a great influence on the thermal protection of HFS is exerted by:

- filling masonry voids with mortar using hollow brick – a decrease of 13–41 % [18];
- use of single-layer thermal insulation with an increase in the gaps between the insulation boards to 4–8 mm – a decrease of 4–16 % [32] as calculated by taking into account the highly ventilated gap according to DIN EN ISO 6946 [35];
- heat engineering heterogeneities of the mounting frame (substructure) [12, 13, 31, 33] – reduction by 30–40 % (coefficient of heat engineering heterogeneity $r = 0.6–0.7$); heat loss through window sills [34];
- geometric and thermophysical characteristics of the ventilated gap – the effect depends on the conditions of heat and moisture transfer in the gap [1, 30, 33].

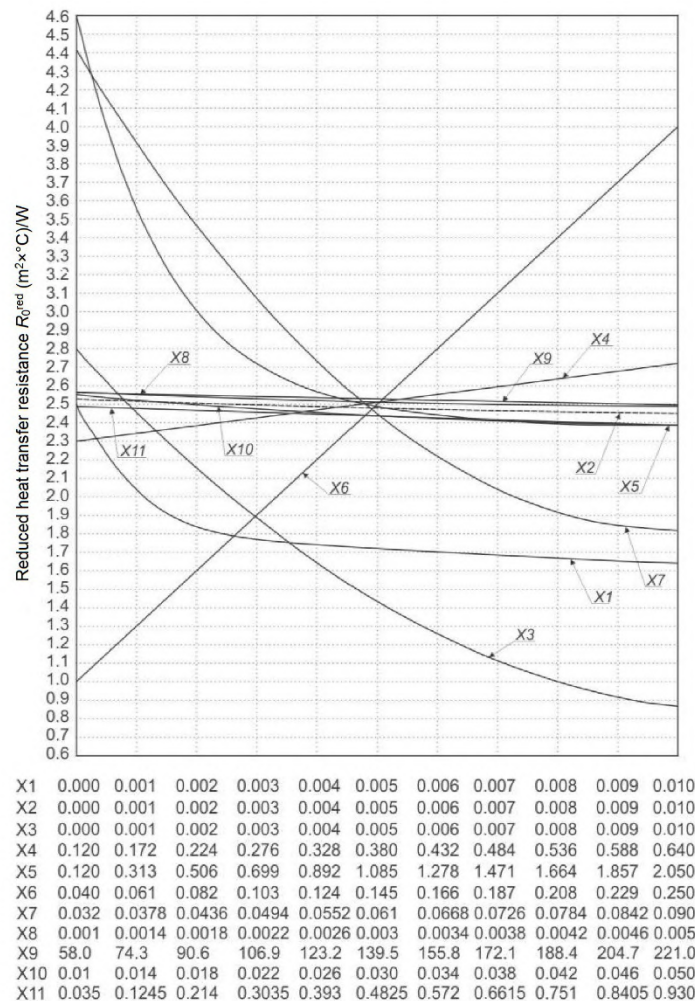


Figure 4. Dependence of the reduced heat transfer resistance of the external wall with the HFS on the factors X1–X11: X1 is gap at the junction of the insulation boards; X2 is gap at the junction of the bracket with the insulation plate; X3 is peeling of the insulation boards from the foundation; X4 is deviation of the thickness of the foundation; X5 is deviation of the thermal conductivity of the foundation material; X6 is deviation of the thickness of the insulating layer; X7 is deviation of the coefficient of thermal conductivity of the insulation material; X8 is deviation of the thickness of the bracket; X9 is deviation of the thermal conductivity of the bracket; X10 is gap in the expansion joint between the foundation and the floor slab; X11 is deviation of the coefficient of thermal conductivity of the material filling the expansion joint between the foundation and the slab.

To reduce the defectiveness of the HFS, it is necessary to develop organizational and technological measures: strengthen technological discipline; regulate operational control using special control cards; justify tolerances and confirmation of energy passport data taking into account technological deviations.

In the course of construction, checklists for the registration of thermal protection defects should be drawn up. These sheets are part of the as-built documentation for the HFS, represented by sections of three

types: *I* – the blind section of the outer wall; *II* – the section of the outer wall in the area of the floor slab, *III* – sections of the wall with a window. The sheets indicate: controlled work zones; type of section of the outer wall; thermal conductivity coefficients of wall materials; wall layer thicknesses; window construction; and defects of thermal protection with an indication of their values and quantity on a controlled work zone. If defects are corrected, sheet inspection should be repeated.

Upon receipt of the work zone, the coefficient of the combined influence of significant heat protection defects is calculated and the actual value of the reduced heat transfer resistance is determined:

$$R_{w,i} = R_w \cdot k_{j,i} \quad (3)$$

where R_w is calculated value of the reduced heat transfer resistance of the outer wall; i is work zone number; $R_{w,i}$ is value of the reduced heat transfer resistance of the outer wall, taking into account the combined influence of significant defects on the i -th work zone; $k_{j,i}$ is coefficient of joint influence of significant defects on the i -th work zone of the j -th wall section (type *I*, *II* or *III*).

For example, for the wall sections of type *I* and *II*:

$$k_{I,i} = k_{I,i}^{X_1} \cdot k_{I,i}^{X_2} \cdot k_{I,i}^{X_3}; \quad k_{II,i} = k_{II,i}^{X_1} \cdot k_{II,i}^{X_3} \cdot k_{II,i}^{X_{10}}, \quad (4)$$

where $k_{I,i}^{X_1}, k_{I,i}^{X_2}, k_{I,i}^{X_3}$ are coefficients of influence factors X_1, X_2, X_3 on thermal protection of the i -th work zone of a blank section of the outer wall the HFS; $k_{II,i}^{X_1}, k_{II,i}^{X_3}, k_{II,i}^{X_{10}}$ are coefficients of influence factors X_1, X_3, X_{10} on thermal protection of the i -th work zone of the HFS wall section in the area of the floor slab.

Tolerances in the performance of work are assigned based on the conditions:

$$k_I^{X_1} \cdot k_I^{X_2} \cdot k_I^{X_3} > k_{cal}; \quad k_{II}^{X_1} \cdot k_{II}^{X_3} \cdot k_{II}^{X_7} > k_{cal}, \quad (5)$$

where k_{cal} is calculated boundary value of the coefficient of influence of defects, at which the heat-shielding properties of the outer walls satisfy the requirements of thermal protection established by the norms:

$$k_{cal} = \max \{ R_{min}, R_{req} \} / R_w, \quad (6)$$

where R_{min} is minimum permissible value of reduced heat transfer resistance; and R_{req} is boundary value of the reduced heat transfer resistance, which provides a sanitary-hygienic indicator of thermal protection.

Acceptance control for HFS is carried out through construction control by the client as part of the assessment of the compliance of building envelopes with the requirements of design documentation, including the requirements of thermal protection and energy efficiency. In some cases, by decision of the client or the state construction supervision body, continuous or selective instrumental control may be assigned to determine the actual values of the monitored parameters and for filling out the energy passport of the building upon commissioning.

Due to the design features of HFS, instrumental control of thermal protection of external walls is time-consuming and expensive. It is possible to complete this control with satisfactory error level only after the completion of construction. An alternative is to calculate the value of the reduced heat transfer resistance during the construction process, which makes it possible to quickly make decisions to eliminate possible violations. In case of violations during construction control that affect the thermal protection of the external walls, it may be necessary to recalculate the value of the reduced resistance to heat transfer of the external walls, which is entered in the energy passport.

The results of this study are reflected in the standard "Union of construction companies of the Urals and Siberia" 02–2013 "Assessment of the energy efficiency of buildings. Monitoring compliance with the requirements of thermal protection of building envelopes." Energy certification with control at the construction stage made it possible to increase the reliability of assessing the compliance of buildings with energy saving requirements. The research results can be used for the energy classification of buildings, both in Russia and abroad (taking into account the requirements of national standards).

4. Conclusions

1. We studied the main defects of thermal protection through HFS which have a significant impact on the energy efficiency parameters of civil buildings. Production studies of defects were carried out in the city of Chelyabinsk (Russia, 55 deg. N) in summer and winter conditions. The main defects: gaps in the junction of insulation boards; gaps at the junction of the bracket with the insulation plate; detachment of the insulation from the foundation; gaps in the expansion joint between the foundation and the floor slab. For some

parameters, the level of defectiveness reaches 35–45 %, which, given combined manifestation of defects, can significantly reduce the heat transfer resistance of the shell. Laboratory experiments in the climate chamber on fragments of real structures substantiated the reliability of the assessment of the influence of defects on the level of thermal protection by numerical simulation in ELCUT.

2. The dependencies of the influence of the main defects on the reduced heat transfer resistance of the wall are revealed and mathematical models of the combined effect of the defects of the HFS on the level of their thermal protection are constructed. The reduction in reduced heat transfer resistance was from 5 to 52 %. Models make it possible to quickly assess the significance of defects, substantiate regulatory tolerances, and draw up scientifically based quality control cards.

3. Organizational and technological solutions for quality control of the device of enclosing structures are proposed, aimed at increasing the energy efficiency of buildings. Based on these solutions, regulations were developed to confirm the energy passport of the building, taking into account the real-world execution of design decisions. The methodology for assessing manufacturing defects with corrections to buildings' energy passport of can be used not only in Russia, but also in other countries, taking into account national standards for energy saving in construction.

5. Acknowledgments

The work was supported by Act 211 Government of the Russian Federation, contract № 02.A03.21.0011.

References

1. Nemova, D.V. Navesnyye ventiliruyemye fasady: obzor osnovnykh problem [Ventilated facades: overview of major issues]. Magazine of Civil Engineering. 2010. No. 5. Pp. 7–11. (rus)
2. Vatin, N.I., Gorshkov, A.S., Nemova, D.V., Staritsyna, A.A., Tarasova, D.S. The energy-efficient heat insulation thickness for systems of hinged ventilated facades. Advanced Materials Research. 2014. No. 941–944, Pp. 905–920.
3. Danilevsky, L.N., Danilevsky, S.L. The algorithm and accuracy of definition of heattechnical indicators of buildings. Magazine of Civil Engineering. 2017. No. 5. Pp. 49–61. DOI: 10.18720/MCE.73.5
4. Petritchko, M.R., Kotov, E.V., Nemova, D.V., Tarasova, D.S., Sergeev, V.V. Numerical simulation of ventilated facades under extreme climate conditions. Magazine of Civil Engineering. 2018. No. 77(1). Pp. 130–140.
5. Ananin, M., Perfilyeva, N., Vedishcheva, I., Vatin, N. Investigation of different materials usage expediency for a low-rise public building from the energy efficiency standpoint. IOP Conf. Series: Materials Science and Engineering 365 (2018).
6. Vasilyev, G.P., Lichman, V.A., Yurchenko, I.A., Kolesova, M.V. Method of evaluation of thermotechnical uniformity coefficient by analyzing thermograms. Magazine of Civil Engineering. 2016. No. 6. Pp. 60–67. DOI: 10.5862/MCE.66.6
7. Korniyenko, S.V., Vatin, N.I., Gorshkov, A.S. Thermophysical field testing of residential buildings made of autoclaved aerated concrete blocks. Magazine of Civil Engineering. 2016. No. 4. Pp. 10–25. DOI: 10.5862/MCE.64.2
8. Korniyenko, S.V. The experimental analysis and calculative assessment of building energy efficiency. Applied Mechanics and Materials. 2014. Vol. 618. Pp. 509–513.
9. Tarasova, D., Staritsyna, A., Nemova, D., Andreev, K. The using feasibility Russian and European software products at thermal calculations. MATEC Web of Conferences, 53. 2016. art. no. 01007.
10. Gorshkov, A., Vatin, N., Nemova, D., Shabaldin, A., Melnikova, L., Kirill, P. Using life-cycle analysis to assess energy savings delivered by building insulation. Procedia Engineering. 2015. 117(1). Pp. 1085–1094. DOI: 10.1016/j.proeng.2015.08.240.
11. Vatin, N.I., Nemova, D.V., Rymkevich, P.P., Gorshkov, A.S. Vliyaniye urovnya teplovoy zashchity ograzh-dayushchikh konstruksiy na velichinu poter teplovoy energii v zdanii [Influence of building envelope thermal protection on heat loss value in the building]. Magazine of Civil Engineering. 2012. No. 8(34). Pp. 4–14. DOI: 10.5862/MCE.34.1 (rus)
12. Bikas, D. et al. Ventilated facades: requirements and specifications across Europe. Procedia Environmental Sciences 38, International Conference on Sustainable Synergies from Buildings to the Urban Scale, SBE16. Greece, 2017. Pp. 148–154.
13. Protosevich A.M., Krutilin A.B. Klassifikatsiya ventiliruyemykh fasadnykh sistem. Vliyaniye teploprovodnykh vkluycheniy na ikh teplozashchitnyye kharakteristiki [Ventilated facade systems classification. Influence of Thermal bridges on their heat-resistant characteristics]. Magazine of Civil Engineering. 2011. No. 8. Pp. 7–11. (rus)
14. Yeromin, A., Kolosov, A. Modeling of energy efficient solutions regarding the heating system and the facade heat insulation in the implementation of thermomodernization. Eastern European Journal of Enterprise Technologies. 2018. No. 1(8–91), Pp. 49–57.
15. Filonenko, O., Yurin, O., Kodak, O. Thermal modernization of the panel buildings external walls. International Journal of Engineering and Technology (UAE). 2018. No. 7(3). Pp. 116–122.
16. Ryabukhina, S., Simankina, T., Koshkarova, M., Sokolovskii, N., Ryzhkov, O. Combined Thermal Insulating Module of Mounted Vented Facades. MATEC Web of Conferences, 73. 2016. art. no. 02005.
17. Lu Tszin. Effektivnyye energosberegayushchiye ograzhdayushchiye konstruksii zdaniy [Efficient energy-saving enclosing structures of buildings]. Industrial and civil engineering. 2017. No. 2. Pp. 66–69. (rus)
18. Gorshkov, A.S., Gladkikh, A.A. Vliyaniye rastvornykh shvov kladki na parametry teplotekhnicheskoy odnorodnosti sten iz gazobetona [Influence of mortar joints in aerocrete-work on the thermotechnical homogeneity of walls]. Magazine of Civil Engineering. 2010. No. 3. Pp. 39–42. (rus)
19. Taylor, T., Counsell, J., Gill, S. Energy efficiency is more than skin-deep: Improving construction quality control in new-build housing using thermography. Energy and Buildings. 2013. No. 66. Pp. 222–231.
20. Nemova, D.V., Yemelyanova, V.A., Miftakhova, D.R. Extremal calculation problems of free convective movements in ventilated facades. Magazine of Civil Engineering. 2013. No. 43 (8), Pp. 46–53.
21. Carbary, L., Yee, S., Bagatelos, N. Thermal and Structural Performance for Use in Curtainwall Constructions. Architecture Insulation Modules. 2014. Pp. 1–18.

22. Gagarin, V.G., Kozlov, V.V., Lushin, K.I., Plyushchenko, N.Yu. Uchet teploprovodnykh vklucheniy i ventiliruyemoy prosloyki pri raschetakh soprotivleniya teploperedache steny s navesnoy fasadnoy sistemoy (NFS) [Consideration of heat-conducting inclusions and a ventilated layer when calculating the resistance to heat transfer of hinged facade system (HFS)]. *Stroitelnyye materialy*. 2016. No. 6. Pp. 32–35. (rus)
23. Basińska, M., Koczyk, H., Błotnicka-Smyk, A. Assessment of thermo-modernization in a multifamily building. *E3S Web of Conferences*, 49. 2018. art. no. 00004. DOI: 10.1051/e3sconf/20184900004
24. Statsenko, E.A., Ostrovaia, A.F., Olshevskiy, V.Y., Petrichenko, M.R. Temperature and velocity conditions in vertical channel of ventilated facade. *Magazine of Civil Engineering*. 2018. No. 80(4). Pp. 119–127.
25. Ryabukhina, S., Simankina, T., Koshkarova, M., Sokolovskii, N., Ryzhkov, O. Combined Thermal Insulating Module of Mounted Vented Facades. *MATEC Web of Conferences*, 73, 2016. art. no. 02005.
26. Olshevskiy, V., Statsenko, E., Musorina, T., Nemova, D., Ostrovaia, A. Moisture Transfer in Ventilated Facade Structures. *MATEC Web of Conferences*, 53, 2016. art. no. 01010.
27. Mashenkov, A.N., Cheburkanova, Ye.V. Opredeleniye koeffitsiyenta teplotekhnicheskoy odnorodnosti navesnykh fasadnykh sistem s vozdushnym zazorom [Determination of coefficient of heat engineering uniformity of hinged facade systems with an air gap]. *Stroitelnyye materialy*. 2007. No. 6. Pp. 10–12. (rus)
28. Vieira, G.B., Petrichenko, M.R., Musorina, T.A., Zaborova, D.D. Behavior of a hollowed-wood ventilated facade during temperature changes. *Magazine of Civil Engineering*. 2018. No. 3. Pp. 103–111.
29. Tushina, O.A., Emelianov, A.A., Tushina, V.M. Thermal insulation properties of various ventilated facade systems. *Magazine of Civil Engineering*. 2013. No. 43 (8). Pp. 54–63.
30. Emelianova, V.A., Nemov, D.V., Miftakhova D.R. Optimized structure of ventilated facades. *Magazine of Civil Engineering*. 2014. No. 50 (6). Pp. 53–66.
31. Gorshkov, A.S., Popov, D.Yu., Glumov, A.V. Konstruktivnoye ispolneniye ventiliruyemogo fasada povyshennoy nadezhnosti // *Inzhenerno-stroitelnyy zhurnal*. 2010. № 8. S. 5–8.
32. Yelokhov, A.Ye., Verkhovskiy, A.A., Borisov, V.A. Sravneniye effektivnosti utepleniya v sistemakh navesnykh ventiliruyemykh fasadov [Efficiency Comparison of Thermal Insulation schemes in the Hinged Ventilated Facades Systems]. *Academia. Arkhitektura i stroitelstvo*. 2018. No. 4. Pp. 116–122. (rus)
33. Gagarin, V.G. O nekotorykh teplotekhnicheskikh oshibkakh, dopuskayemykh pri proyektirovanii ventiliruyemykh fasadov [About some heat engineering errors made when designing ventilated facades]. *AVOK*. 2005. No. 2. Pp. 52–58. (rus)
34. Baiburin, A.Kh., Rybakov, M.M., Vatin, N.I. Heat loss through the window frames of buildings. *Magazine of Civil Engineering*. 2019. No. 85(1). Pp. 3–14. DOI: 10.18720/MCE.85.1
35. DIN EN ISO 6946 Building components and building elements. Thermal resistance and thermal transmittance Calculation method (ISO 6946:2007). German version EN ISO 6946:2007.
36. Taylor, T., Counsell, J., Gill, S. Combining thermography and computer simulation to identify and assess insulation defects in the construction of building facades. *Energy and Buildings*. 2014. No. 76, Pp. 130–142.
37. Korniyenko, S.V. Evaluation of Thermal Performance of Residential Building Envelope. *Procedia Engineering*. 2015. No.117, Pp. 191–196.
38. Mozgalev, K.M., Taran, E.Yu. Confirming the Actual Energy Efficiency for Commissioned Buildings. *Procedia Engineering*. 2016. No. 150, Pp. 2128–2132.
39. Šadauskienė, J., Šeduikytė, L., Ramanauskas, J., Buska, A. Assessment of buildings with ventilated facade systems and evaluation of point thermal bridges. *Journal of Sustainable Architecture and Civil Engineering*. 2015. No. 2(11), Pp. 59–71.
40. Theodosiou, T., Tsikaloudaki, K., Kontoleon, K., Bikas, D. Thermal bridging analysis on cladding systems for building facades. *Energy and Buildings*. 2015. No. 109, Pp. 377–384.
41. EN ISO 14683:2008 Thermal bridges in building construction – Linear thermal transmittance – Simplified methods and default values.

Contacts:

Alexey Rusanov, tyarus@mail.ru

Albert Baiburin, abayburin@mail.ru

Denis Baiburin, dbayburin@mail.ru

Vincenzo Bianco, vincenzo.bianco@unige.it

© Rusanov A.E., Baiburin A. Kh., Baiburin D.A., Bianco V., 2020



DOI: 10.18720/MCE.95.7

Loads for the design of the industrial building frame

T.V. Zolina, P.N. Sadchikov*

Astrakhan State Architectural and Construction University, Astrakhan, Russia

* E-mail: pn_sadchikov@mail.ru

Keywords: industrial building, load combination, probabilistic model, numerical methods, stress-strain state

Abstract. The article considers the issues of assessing the reliability of structures of an industrial building equipped with bridge cranes. The implementation of the research concept is based on a probabilistic approach as the most appropriate to the random nature of technogenic and extreme impacts. A mathematical model is constructed that takes into account the random nature of the formation and perception of the framework structure of the totality of loads. To substantiate the method, an extensive amount of statistical data was generated on the loads of bridge cranes of various types and meteorological information on wind and snow for individual climatic regions of Russia. The stationary probabilistic models for crane and quasistationary models for snow and wind loads are substantiated. The proposed algorithms for their implementation are adapted for the automation of calculations using the software developed by the authors of the article "DINCIB-new". Numerical calculations of the operability of the frame structures of the operated buildings of production shops under the action of a combination of loads. A comparative analysis of the obtained results with the normative allowed us to conclude that it is necessary to include when forming combinations of loads that affect the change in the stress-strain state of the frame structures of an industrial building, lateral forces. As a result of experimental and theoretical studies, refinements were made to the previously proposed calculation schemes and calculation methods, allowing to design the supporting structures of the frames in accordance with the actual conditions of their actual work.

1. Introduction

One of the main tasks in the design of industrial buildings and structures is to ensure their durability, reliability and stability against both external influences and the impacts that directly arise during their operation [1–8]. The purpose of this study is to clarify the design schemes and methods for calculating an industrial building for crane and atmospheric loads under the real conditions of the actual operation of the frame structures, taking into account the random nature of their manifestation.

During the study of changes in the stress-strain state of an industrial building equipped with bridge cranes, it is necessary to consider internal technological factors that have a significant impact on the performance and safe operation of framework structures. Impacts caused by these factors may be static and dynamic. Their weight in the magnitude of the generalized load is significant and depends on a large number of conditions and parameters of operation of bridge cranes when transferring vertical and horizontal loads on the structures of an industrial facility [9]. In [7], a method was proposed for solving a dynamic problem from the influence of a harmonic load on structures, based on the static accounting of higher vibration modes.

The calculation of industrial buildings for various types of impact correlates with their pronounced random properties. Among the main parameters of the presented perturbations, the following should be highlighted:

- the maximum amplitude of oscillations;
- spectral composition;
- the focus of action;
- duration of the intensive phase.



When designing and operating such facilities, it is possible to provide the required security with a certain degree of probability. As correctly noted in the article [10], the development of probabilistic methods for calculating building structures follows the path of accumulating factual material on the statistical properties of impacts, while nothing new appears in the formulation of the goals of probabilistic calculation and methods for its implementation. And that's why, when implementing the research concept of authors' article, preference is given to methods for calculating the maximum permissible risk using probabilistic models and reliability theory methods.

For the possibility of constructing a probabilistic calculation of structures with joint application of loads, a promising model for correlating a sequence of random loads [11] based on the generalized covariance method [12, 13]. For the numerical implementation of the calculation algorithm, it is necessary to construct generalized probabilistic models of crane, snow, and wind loads that actually act on the frame of an industrial building. The results of modeling the aerodynamic parameters of structures obtained in [8] were taken into account in the course of this study, since they allow excluding unreasonable reserves of wind load.

To achieve the goal set for the study, the following tasks are required:

1. to identify beyond design basis impacts on the frame of an industrial building arising from the operation of bridge cranes, and their weight in the amount of the generalized load;
2. to clarify the design schemes and methods for calculating the components of the crane load and the components of the atmospheric effects in a probabilistic setting, as the most appropriate for the random nature of their manifestation;
3. adapt the calculation algorithms of an industrial building to the effect of snow and wind loads for software implementation using computer tools.

2. Methods

It is extremely rare that individual elements and the frame of a building as a whole are affected by only one load. In most cases, when calculating, you must immediately take into account several components \tilde{Q}_i [10], the combination of which in accordance with the objectives of the study is considered as the sum of stationary and quasistationary random processes:

$$\tilde{Q} = \sum_{i=1}^n c_i \tilde{Q}_i, \quad (1)$$

where c_i is the proportion of the i load when converting to the component of the design effort.

Numerical characteristics of the generalized load, presented in the form of a mathematical expectation and a standard, can be defined as:

$$\bar{Q} = \sum_{i=1}^n c_i \bar{Q}_i, \quad s_Q = \sqrt{\sum_{i=1}^n (c_i \bar{Q}_i \text{Var}(Q_i))^2}, \quad (2)$$

where $\text{Var}(Q_i)$ is the coefficient of variation of a random variable Q_i .

Its effective frequency in the absence of a correlation dependence between the individual components of the aggregate, according to the conclusions of V.V. Bolotin [14], expressed as:

$$\omega_Q = \frac{\sqrt{\sum_{i=1}^n (\omega_i c_i \bar{Q}_i \text{Var}(Q_i))^2}}{\sqrt{\sum_{i=1}^n (c_i \bar{Q}_i \text{Var}(Q_i))^2}}. \quad (3)$$

Industrial building under the action of a combination of a large number of loads involved in the oscillatory process. Each of the components of the load factor makes its more or less significant contribution to the joint work of a set of interrelated structures that determine the physical model of the object of study [15–23].

The components of the dynamic load vector vary at different points in time. As one of the options in the automation of calculations, the entire possible range of values may arise from the generation of random numbers according to the normal distribution law with a known expectation \bar{X} and standard s . Because of

this approach to determining the range of variation, the random value of the crane load X most fully described by a probabilistic model of a normal stationary random process. In this case, the normalized load deviation γ can be defined as:

$$\gamma = \frac{(X - \bar{X})}{s}, \quad (4)$$

and the corresponding emission frequency of random crane load values:

$$v_+(\gamma) = \frac{\omega e^{-\frac{\gamma^2}{2}}}{2\pi}, \quad (5)$$

where ω is the effective frequency of stationary random process.

The probability of exceeding the normalized level of crane load over time t :

$$Q(\gamma, t) \cong v_+(\gamma) t = \frac{\omega t e^{-\frac{\gamma^2}{2}}}{2\pi}. \quad (6)$$

In addition to crane loads, both at the design and construction stages and at the stage of their operation, a quantitative risk assessment of buildings and structures can be given only when carrying out probabilistic calculations, especially when it comes to extreme impacts on the structures of buildings. When conducting research, the calculated values of crane loads are considered by the authors in the form of random parameters, while assumptions are made about the stochastic representation of their potential deviations determined based on numerous field tests [24, 25].

Except for the considered crane load industrial building is experiencing a number of influences, wearing the natural character of education. These include snow load and wind pressure on the lateral surface of the object.

The value of the snow load has a random nature of changes over time both during a single winter and during long-term seasonal fluctuations of climatic conditions. Consequently, the most acceptable form of its mapping is a probabilistic model of a random process, the parameters of which vary depending on the territorial affiliation of a specific snow region.

According to the results of numerous studies [26] to all known models formalizing a probabilistic approach to the formation of snow load, the most preferred revealed. It consists of presenting a selective sequence of annual highs (S_{mi}) in the form of a continuous random variable distributed according to the Gumbel law. Its probability density is defined as:

$$f(S_m) = \frac{1}{\beta} \exp \left[\frac{\alpha - S_m}{\beta} - \exp \left(\frac{\alpha - S_m}{\beta} \right) \right], \quad (7)$$

and the corresponding distribution function:

$$F(S_m) = \exp \left[-\exp \left(\frac{\alpha - S_m}{\beta} \right) \right]. \quad (8)$$

In the study of the wind load, the preferred form of representation of a turbulent flow is the decomposition of its velocity into two components:

$$v = \bar{v} + v' \quad (9)$$

where \bar{v} is the average wind speed, v' is the flow rate pulsations.

Any obstacle in the path of the turbulent flow is affected by the corresponding wind load. It refers to the number of short-term loads that do not have a low regulatory value. To assess the forces caused by wind on the object of study, the corresponding load, as in the case of the velocity of the turbulent flow, is decomposed into the sum of two components: the average and the pulsating.

To find the average wind load at a height z above the surface of the earth it is regulated to use the formula

$$w_M = w_0 k C, \quad (10)$$

where w_0 is the standard wind pressure at 10 m above the ground; k is the coefficient to estimate the change in wind pressure in height; C is the aerodynamic coefficient.

The value w_0 determined in accordance with the map of territorial zoning, which shows the distribution of zones of calculated values of wind pressure when choosing the averaging interval $\Delta t = 10$ min, exceeded on average once every 50 years. This map is the result of the implementation of a probabilistic model presented in the form of a nonstationary random velocity field of wind flow at a height z_0 above ground. It displays the territorial variability of the parameter under study, the mathematical expectation of the values of which is the result of smoothing the data of long-term observations of meteorological stations, and the standard – the result of processing deviations during such smoothing.

The currently existing methods [2, 10, 27] and the software and settlement systems developed on their basis do not consider all possible components of external influences. They do not always allow one to take into account the spatial work of the structures of buildings and structures, as well as the calculations under the simultaneous action of a whole set of components of the generalized load in a probabilistic formulation.

3. Results and Discussion

The results of experimental studies of vertical crane loads in existing production workshops, processed in the technique of random variables and random processes, revealed their probabilistic features [28]. These should include:

1. stationary random crane load, which is manifested in rapid stabilization and further immutability distributions ordinate and the numerical characteristics;
2. consistency of emission frequencies and frequency characteristics of random processes;
3. the insignificance of deviations of the crane load ordinate (solid line), considered as a continuous random variable X , from the Gauss curve (dashed line), which displays a graph of the probability density function according to the normal distribution law (Fig. 1);

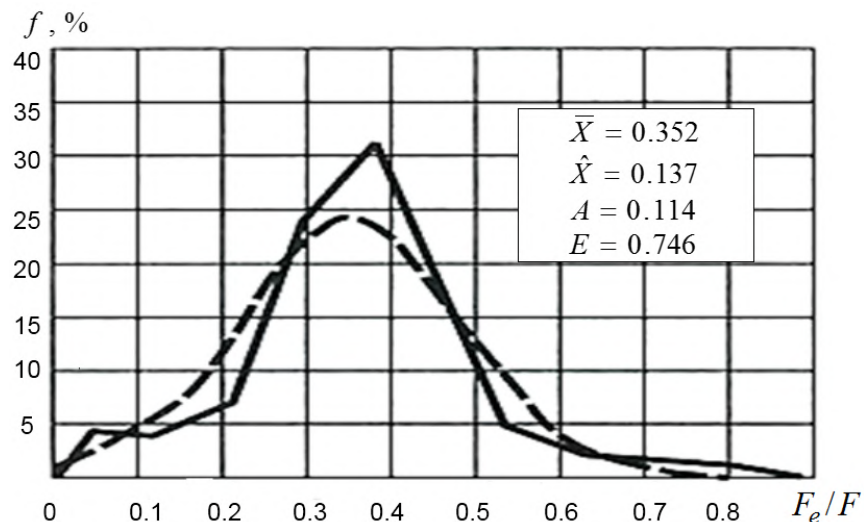


Figure 1. Example of distribution of vertical crane load.

Designations: \bar{X} is the average value, \hat{X} is the coefficient of variation, A is the asymmetry index, E is the excess.

4. high-frequency mixing of random crane load and the absence of a periodic component;
5. allocation of the extreme tail parts corresponding to operations with loads close to the carrying capacity in the distribution of loads caused by the operation of bridge cranes with a flexible suspension.

The analysis of statistical data also indicates the random nature of the dynamics of changes in the magnitude of horizontal loads during the movement of bridge cranes for various purposes [28]. As in the case of vertical loads, these distributions are characterized by the properties of stationarity, elongation of tail parts and normality of statistical representations (Fig. 2).

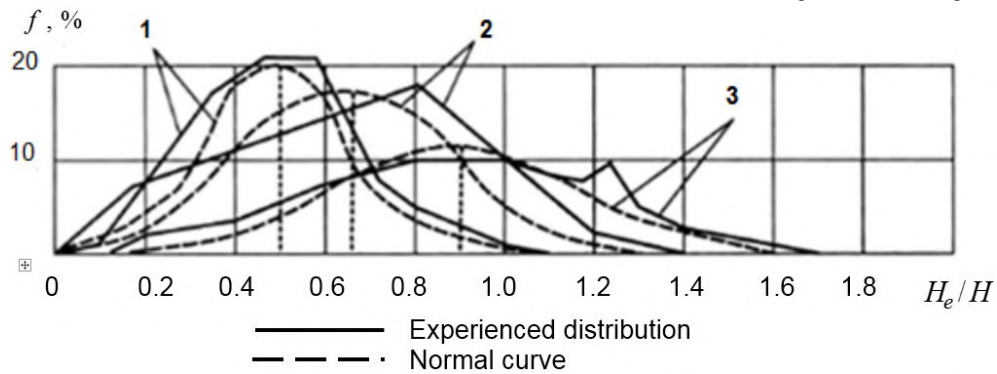


Figure 2. Examples of horizontal crane load distributions:
1 – for cranes with flexible load suspension in areas with a normal gauge;
2 – for cranes with flexible suspension with narrowing and widening of ways;
3 – for cranes with a rigid load suspension.

When analyzing the statistical data obtained during surveys, on the joint distribution of vertical and horizontal crane loads, the following was revealed:

- for sections of tracks with a normal gauge, there is a correlation between the components of the crane load;
- for sections with narrowing and widening of paths, a similar correlation dependence is absent.

It is revealed that between the values of the mathematical expectations of the vertical \bar{F} and horizontal \bar{H} components of the crane load are linear [28]. The equation of this dependence can be represented as: $\bar{H} = k\bar{F}$, in which k is the coefficient of proportionality.

The values of the proportionality coefficients for the main groups of bridge cranes according to the results of processing a large amount of statistical data obtained from surveys of industrial buildings are determined in intervals:

- $k = 0.133 \dots 0.167$ for a crane with a hard suspension;
- $k = 0.050 \dots 0.061$ for a multi-wheel crane with a flexible suspension (the number of wheels is 8 or more);
- $k = 0.16 \dots 0.46$ for the four-wheel crane with flexible suspension.

Expected value \bar{X} and standard s random vertical crane loads were obtained by summarizing the results of the experiments performed with a security of 0.99:

- for cranes with a rigid suspension, a dependence is revealed

$$\bar{X} = \left(0.66 - 0.243 \frac{Q}{Q_{cr} + Q_{tr}} \right) F_0^s; \quad s = 0.131 F_0^s, \quad (11)$$

where F_0^s is the standard vertical pressure on the crane wheel; Q is the crane capacity; Q_{cr} , Q_{tr} are the weight of the crane bridge and crane truck, respectively;

- for cranes with flexible hanger

$$\bar{X} = 0.758 F_0^s; \quad s = 0.274 F_0^s. \quad (12)$$

These characteristics with the effective frequency ω , completely describe the random vertical crane load and allow solving the problems of probabilistic calculation and evaluation of the reliability of structures under these influences.

So, for example, for a two-span, equal-height building of the ship's hull workshop of the Astrakhan Marine Plant, equipped with bridge cranes with a lifting capacity of 50 tons each with flexible suspensions, the results on the action of vertical crane loads are obtained. Fig. 3 shows the values of bending moments that occur at the vertical pressure of two cranes in probabilistic (solid line) and normative (dashed line) calculations.

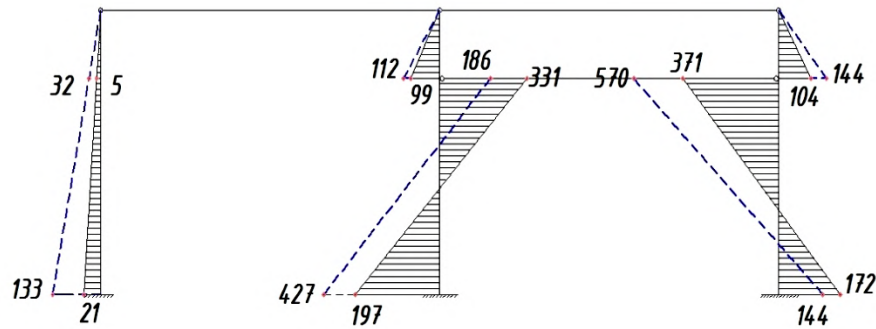


Figure 3. Diagram of bending moments from the vertical pressure of the crane (kN m).

Based on the analysis of experimental data, generalized numerical characteristics of the probability distributions of horizontal loads of the main groups of bridge cranes also were obtained – expectation values \bar{X} and coefficient of variation $Var(X)$.

In the case of loads caused by the braking of the crane truck, the parameters were calculated using the formulas:

$$\bar{X} = \frac{T_{cr}^s}{1 - 1.64 Var(X)}, \quad T_{cr}^s = 0.05 \frac{Q \cdot 9.81 + Q_{tr}}{n_0}, \quad Var(X) = 0.1, \quad (13)$$

where T_{cr}^s is the standard value of the brake load on the wheel; n_0 are number of wheels on one side of the crane.

In the course of calculations, there is also the question of the magnitude and direction of the load in the case of simultaneous braking of crane trucks at once by several contiguous cranes. Depending on the time of the beginning and end of the braking of each of them, several options are possible for the change over time of their total impact on the frame of an industrial building [9]. Therefore, the authors of the article consider it necessary to carry out calculations for all known options and to organize the search for the highest values of bending moments, based on which to carry out the design.

The proposed approach allows you to reliably design the load-bearing structures of an industrial building in accordance with the actual conditions of their work during the perception of loads caused by the braking of crane trucks.

The results of numerous theoretical and experimental studies conducted by the authors [9, 24, 28] prove that the physical nature of horizontal impacts from bridge cranes on the frame structure of an industrial building is associated not only with the braking of the crane truck but also with their movement. The kinetics of such a movement causes the appearance of lateral frictional sliding forces. These forces result from the mismatch of the plane of rotation of the crane wheel with the direction of its movement. Theoretically, the movement of a bridge crane on the traveling wheels, installed in the direction of an ideal rail track, is considered as straightforward. However, if such a movement is possible, then it is unstable. With a slight deviation from the listed conditions, the equality between the pulling forces of the drive wheels and the resistance forces of the respective sides of the crane is violated. Failure to comply with this equality indicates the presence of skew forces and transverse reactions of the track, acting on the driving wheels, which leads:

- to the appearance of rotational and transverse movements of the crane within the gaps between the flanges and the heads of the rails;
- to additional loading of metal structures of the crane, traveling wheels and crane rail track.

With regard to accounting and determining the magnitude of lateral forces arising from the movement of the crane with a bias, there is no consensus. Moreover, their values calculated by the formulas proposed by various authors [9] differ several times.

An analysis of the results showed that the values of the lateral forces exceed the braking forces acting on the transverse frames in the plane of which the bridge crane works, and the numerical characteristics of the corresponding random variables are determined:

- for cranes with a hard suspension

$$\bar{X} = 0.1 F_{mid} \sum Y; \quad Var(X) = 0.5 \quad (14)$$

where F_{mid} is the vertical wheel pressure without load with a cart located in the middle of the bridge; $\sum Y$ is the sum of the ordinates of the influence line when accounting for one crane;

– for multi-wheel cranes with flexible suspension (the number of wheels is 8 and more)

- on track sections with normal gauge

$$\bar{X} = 0.08F_{mid} \sum Y; \quad Var(X) = 0.45; \quad (15)$$

- in areas with narrowing and extending paths exceeding 40 mm

$$\bar{X} = 0.12F_{mid} \sum Y; \quad Var(X) = 0.36; \quad (16)$$

– for four-wheel cranes with flexible suspension

$$\bar{X} = 0.1\bar{F}_{max} + \frac{\alpha (\bar{F}_{max} - \bar{F}_{min}) L_{cr}}{K};$$

$$\bar{F}_{max} = \left[\frac{Q_{cr}}{2} + \frac{(\bar{Q} + Q_{tr}) (L_{cr} - a)}{L_{cr}} \right] \frac{1}{n_0};$$

$$\bar{F}_{min} = \left[\frac{Q_{cr}}{2} + \frac{(\bar{Q} + Q_{tr}) a}{L_{cr}} \right] \frac{1}{n_0};$$

$$\bar{Q} = 0.5Q, \quad (17)$$

$\bar{F}_{max}, \bar{F}_{min}$ are the mathematical expectations of vertical pressure on the wheel, respectively, on the most and least loaded side of the crane; α is the coefficient is taken to be 0.03 at the central drive of the mechanism and 0.01 – with the separate drive; a is the minimum approach of the crane hook to the axis of the crane rail.

In the course of the probabilistic calculation of the effect on the frame of the building of the ship's hull workshop of the Astrakhan Marine Plant of horizontal forces caused by the operation of bridge cranes, the values of the numerical characteristics of bending moments are determined. A graphical interpretation of the results of the study on the individual components of the crane load in the most loaded transverse frame is presented in the form of corresponding diagrams. In figure 4, the solid line shows the values obtained in the probabilistic calculation of the lateral force arising from one crane, the dotted line in the normative calculation for the braking of crane trolleys of two cranes.

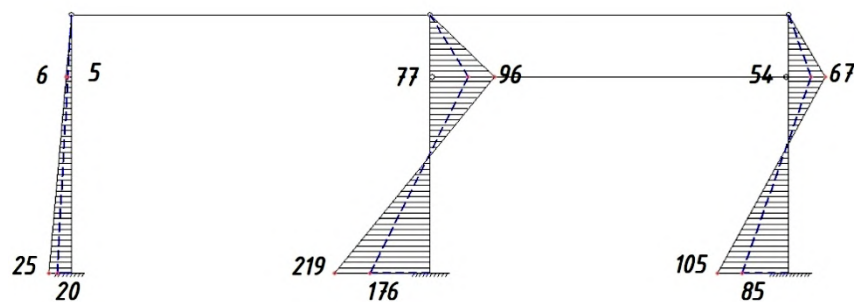


Figure 4. Diagram of bending moments from lateral force and braking of the crane truck (kN m).

Analyzing the obtained data on horizontal crane loads, we can see that the values of bending moments under the action of the lateral force of one crane, determined in the probabilistic setting, are 25 % higher compared to the values of bending moments obtained in the normative calculation from the braking of crane trucks of two cranes at once. The demonstration of the calculation results proves the need to take into account when forming combinations of the simultaneous action of the loads of all the considered components of the crane load. Each of them makes a significant contribution to the total load.

Thus, as a result of experimental and theoretical studies, refinements have been made to the previously proposed design schemes and methods for calculating industrial loads on crane loads, allowing to design the supporting structures of frames in accordance with the actual conditions of their actual operation.

In probabilistic modeling, snow load values are taken as the initial distribution of a continuous random variable of a sequence of annual maximums ($S_{m i}$) by Gumbel distribution law (7)-(8). Its parameters α and β are calculated through mathematical expectation m_{S_m} and the standard σ_{S_m} of a sample of data from meteorological observations:

$$\alpha = m_{S_m} - k_\alpha \sigma_{S_m} \quad \beta = k_\beta \sigma_{S_m} \quad (18)$$

Considering the known volume of the specified aggregate ($S_{m i}$) as N , Gumbel table coefficients k_α and k_β are approximated as:

$$k_\alpha = 0.45 + 0.34N^{-0.69} \quad k_\beta = 0.78 + 1.54N^{-0.75} \quad (19)$$

Therefore, their limit values are equal to: $k_\alpha = 0.45$ and $k_\beta = 0.78$.

For the possibility of carrying out probabilistic calculations for the perception of the snow load structure by the frame of an industrial building, we express the numerical characteristics of the random value of its annual maximums through the Gumbel distribution parameters α and β .

Taking as the value of the maximum weight of snow cover exceeded on average once $T_0 = 25$ years, the provision of snow load will be:

$$F(S_g) = 1 - \frac{1}{T_0} = 0.96. \quad (20)$$

Expressing from (8) the magnitude of the load, we obtain:

$$S_g = \alpha - \beta \ln\left(-\ln\left[F(S_g)\right]\right) \quad (21)$$

Thus, between groups of indicators ($S_g, m_{S_g}, \sigma_{S_g}$) and (α, β) there are ratios:

$$\begin{cases} S_g = \alpha - \beta \ln\left(-\ln\left[1 - \frac{1}{T_0}\right]\right) \\ m_{S_g} = \alpha + \frac{k_\alpha}{k_\beta} \beta \\ \sigma_{S_g} = \frac{1}{k_\beta} \beta \end{cases} \quad (22)$$

Considering the value of the reliability index β_{S_g} in the following form:

$$\beta_{S_g} = \frac{S_g - m_{S_g}}{\sigma_{S_g}}, \quad (23)$$

considering the derived dependences (22) and the limit values of the Gumbel coefficients k_α and k_β we have:

$$\beta_{S_g} = k_\alpha - k_\beta \ln\left(-\ln\left[1 - \frac{1}{T_0}\right]\right) = 0.45 - 0.78 \cdot \ln(-\ln 0.96) = 2.045 \quad (24)$$

When substituting a numerical value β_{S_g} in (23) a probabilistic model of snow cover weight, evenly distributed over a horizontal surface, is displayed as:

$$S_g = m_{S_g} + \beta_{S_g} \sigma_{S_g} = m_{S_g} \left(1 + \beta_{S_g} \frac{\sigma_{S_g}}{m_{S_g}} \right) \Rightarrow S_g = m_{S_g} (1 + 2.045 \cdot \text{Var}(S_g)) \quad (25)$$

where $\text{Var}(S_g)$ is the coefficient of variation of annual maximums of snow cover weight for a specific area.

Taking the average value of the coefficient of variation for most of the snow regions of the Russian Federation equal to 0.4, a numerical implementation of the presented model is obtained (Table 1).

Table 1. Indicators of the distribution of snow load.

No of snow district	Numerical characteristics		Gumbel distribution parameters	
	m_{S_g}	σ_{S_g}	α	β
I	44	17.6	36.08	13.73
II	66	26.4	54.12	20.59
III	99	39.6	81.18	30.88
IV	132	52.8	108.24	41.18
V	176	70.4	144.32	54.91
VI	220	88.0	180.40	68.64
VII	264	105.6	216.48	82.37
VIII	308	123.2	252.56	96.11

Most of the industrial buildings, the work of which framework for the action of various combinations of loads was studied in the course of research by the authors of the article, are located on the in the territory belonging to the I snow region. A graphical representation of the distribution law of the random value of annual maxima for the calculated values of the parameters (Table 1) for a given area has the following form (Fig. 5):

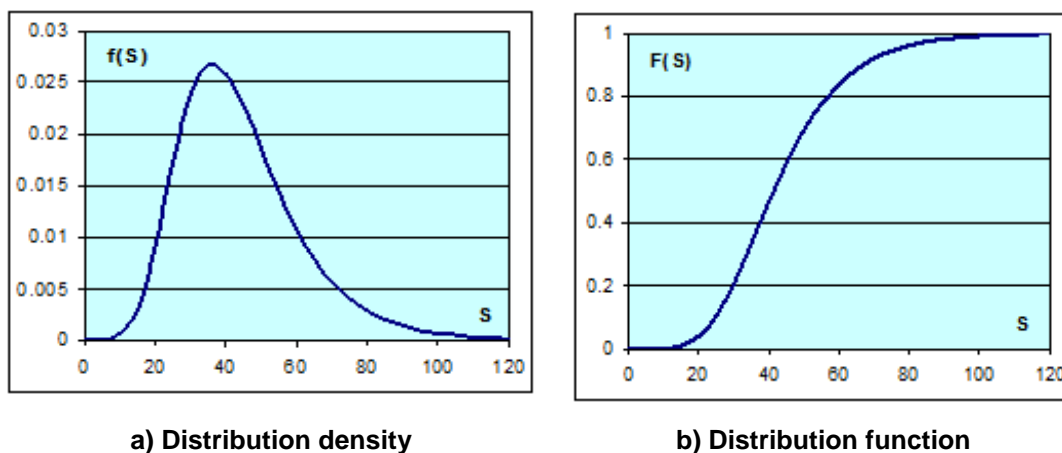


Figure 5. The random distribution of annual maxima of snow cover weight S_g (kgs/m^2) for the territory belonging to the I snow region.

The magnitude of the total snow load on the floor of a building or structure, in addition to the weight of snow cover on a horizontal surface of the earth, is influenced by a large number of other factors. They are considered in the total snow load on the coating of an industrial building by introducing coefficients μ , c_e and c_t into the design model:

$$S_{snow} = \mu c_e c_t S = \mu c_e c_t \left[\gamma_f 0.7 m_{S_g} (1 + 2.045 \cdot \text{Var}(S_g)) \right], \quad (26)$$

where μ is the coefficient taking values on the choice of the form of coverage, c_e is the coefficient taking into account the drift of snow from the surface under the action of wind and other factors, c_t is the thermal

coefficient taking into account snow thawing on non-insulated coatings of workshops with increased heat generation at roof slopes of over 3 % for removal of meltwater.

The snow load model obtained in the course of the study is in good agreement with the probabilistic approach to determining the components of the load factor based on mathematical expectations and indicators of variation of their values. It is adapted for software implementation by means of a computer through the "DINCIB-new" computational complex developed by the authors of the article.

The appearance of wind, as a natural phenomenon, is explained by the movement of air masses from high zones to lower pressure zones. The level of friction between the air flow and the surface depends on the height and density of the obstacles, which determines the magnitude and direction of the corresponding load on a particular object. Moving away from the surface of the earth, the wind speed gradually increases until a gradient level is reached, i.e. to the level at which the friction force ceases to influence the movement of air masses.

The mathematical expectations of a random wind pressure field when determining the regularities of the territorial variability of the calculated parameter are presented in the form of standard values w_0 at a height of 10 m above the ground. For example, in accordance with the standards adopted in the Russian Federation, their values can be presented in Table 2.

Table 2. The standard value of wind pressure in the regions of the Russian Federation.

Wind areas	Ia	I	II	III	IV	V	VI	VII
w_0, kPa	0.17	0.23	0.30	0.38	0.48	0.60	0.73	0.85

On the territory of each selected zone of the Russian Federation, there are areas of different type of belonging, and, consequently, different gradient levels.

To obtain calculated values and automated processing of the wind load on the blown surface area of an industrial building located at a height z , in the course of this study, the profiles of wind flow velocity at various heights were approximated (Table 3). A functional dependence has been obtained, which has a clearly expressed power-law character, since the determination coefficient R^2 is close to 1.

Table 3. Wind flow velocity at height z depending on the type of terrain.

Type A	Type B	Type C
$z_0 = 10 \text{ m}$	$z_0 = 30 \text{ m}$	$z_0 = 60 \text{ m}$
$k = \left(\frac{z}{z_0}\right)^{0.31}, R^2 = 0.9883$	$k = \left(\frac{z}{z_0}\right)^{0.39}, R^2 = 0.9976$	$k = \left(\frac{z}{z_0}\right)^{0.46}, R^2 = 0.9855$

The regression dependences of the wind pressure on the height of the stretched area of the industrial building (Table 3) obtained during the study provide a convenient form for automating the calculations.

The proportion of the velocity head of the wind, turning into pressure on the surface of the building, is expressed as the aerodynamic coefficient. Its value C is determined by:

- the direction of the undisturbed flow;
- the nature of the flow around the geometric forms of the building by the air flow;
- location of the zones of vortex formation and turbulence;
- the presence near the object of study of other obstacles, both natural and man-made.

The distribution of aerodynamic coefficients varies significantly with a small change in the force and direction of the wind flow. This fact orients further research of aerodynamic characteristics on the use of computer-aided design and simulation, implemented by a computer.

To describe the dynamic parameters of the process, presented in the form of the pulsation component of the wind load and the reactions of the structural elements of the building caused by it, the study examined random functions by the time parameter. They display the energy spectrum $S(\omega)$ of the fraction of the power of the wind flow falling on an infinitely small frequency range $d\omega$. The standards adopted in the Russian Federation are based on the use of the spectrum proposed by A. Davenport:

$$S(\omega) = \frac{8\pi u^2}{3\omega (1+u^2)^{\frac{4}{3}}}, \quad (27)$$

where ω is the circular frequency of exposure, $u = \frac{\omega L}{2\pi v_0}$ is the dimensionless design frequency, $L = 1200$ m is turbulence scale, v_0 is the average wind speed at a height of 10 m.

This representation of the spectral density considers only the change in the velocity of the wind flow in the time parameter. If we also take into account the spatial dependence, then the mutual spectrum of pulsations at two specific points in the space i and j can be analytically described [29], as:

$$S_{ij}(\omega, \chi) = \frac{2\pi u^2}{3\omega (1+u^2)^{\frac{4}{3}}} e^{-u\chi_{ij}}, \quad (28)$$

where χ_{ij} is the reduced distance between points i and j .

The aggregate of mutual spectral densities $S_{ij}(\omega, \chi)$ when choosing points of space, each of which determines the closeness of the relationship between the states of a random process $v'_i(t)$ and $v'_j(t)$ in the frequency range $[\omega, \omega + d\omega]$, allows you to set the value of the correlation coefficient of the pulsations of the wind pressure v for the entire surface of the building, perceiving the appropriate load.

An industrial building is a technical system with a large, but finite, number of degrees of freedom. For such a system, the dynamic calculation of the pulsation component of the wind load for all s -forms of natural oscillations, the frequencies of which do not exceed the limiting value f_l , i.e. the condition is met:

$$f_s < f_l < f_{s+1}. \quad (29)$$

All the buildings of the shops, the change in the stress-strain state during the operation of which was studied in the course of this study, are located in the territory of the Astrakhan region, correlated to the third wind region. Since they all belong to the class of objects with a steel frame in the presence of enclosing structures, the logarithmic decrement of oscillations is assumed to be $\delta = 0.3$, and the corresponding frequency limit is $f_l = 1.2$ Hz. The study found that for each of these industrial buildings $s > 1$.

So, for example, for the building of the ship hull workshop of the Astrakhan marine shipbuilding plant, the distribution of the first 10 circular frequencies of natural vibrations is shown in Table 4.

Table 4. Own circular oscillation frequency of the building of the ship hull workshop.

i – form number	1	2	3	4	5	6	7	8	9	10
$\omega_i, (\text{sec}^{-1})$	4.13	4.39	24.57	25.4	25.55	25.67	25.71	25.92	26.11	27.78

Consequently, $s = 2$, insofar as:

$$\omega_l = 2\pi \cdot f_l = 7,536 \text{ sec}^{-1} \Rightarrow \omega_1 < \omega_l \text{ u } \omega_2 < \omega_l. \quad (30)$$

For the adopted design schemes of single-storey industrial buildings equipped with bridge cranes, when wind load is included in the complex loading, its pulsation component at the level of z , corresponding to i -form of natural oscillations, was determined by the formula:

$$w_p^i = M \xi_i \psi_i Y_i \quad (31)$$

where M are mass of the building to which the load is applied; ξ_i is the dynamic factor for i form period; ψ_i is the main indicator that determines the magnitude of the load; Y_i is the horizontal movement of the frame with i -waveform.

The magnitude of the coefficient of dynamism at known values of the logarithmic decrement of vibrations $\delta = 0.3$ and wind load reliability indicator $\gamma_f = 1.4$ becomes dependent on the parameter

$$\varepsilon_i = \frac{\sqrt{\gamma_f k w_0}}{940 f_i} = \frac{\sqrt{\gamma_f k w_0}}{150 \omega_i} \quad (32)$$

graphical interpretation (Fig. 6) of which for the possibility of software processing by computer with varying ε_i in the range of [0; 0.2] approximate as:

$$\xi_i = -22.82\varepsilon_i^2 + 10.32\varepsilon_i + 1.03 \quad (33)$$

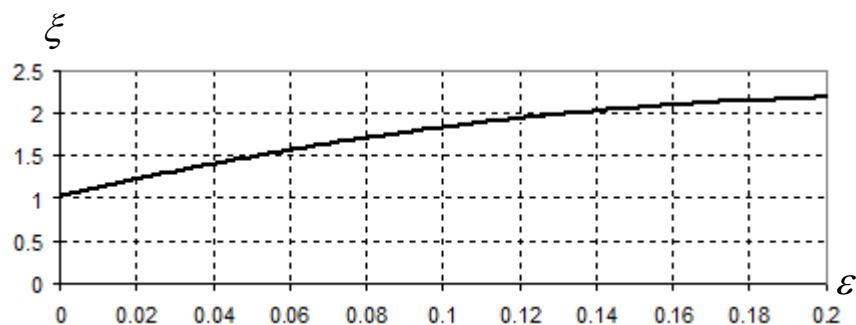


Figure 6. The coefficient of dynamic.

A dependency graph $\xi = \xi(\varepsilon, \delta)$ is correlated on the assumption of the uniformity of the distribution of pulsations of wind speed over the entire surface, perceiving the load.

Value ψ_i depends on the parameters r plots sW8plitting the industrial building, within each of which the wind load value is taken constantly. These include the resultant ripple of the specified load on the k -segment, which is determined by the product

$$w_{pk} = w_{mk} \zeta_k v_k \quad (34)$$

average static wind load w_{mk} (10), wind pressure ripple factor ζ_k and its spatial correlation of mutual spectral densities v_k (28) on this area.

Considering in the calculations the mass of each section m_k and horizontal movement of its center y_k , the dependence between the parameters when searching for an indicator ψ_i is taken as:

$$\psi_i = \frac{\sum_{k=1}^r y_{ki} w_{pk}}{\sum_{k=1}^r y_{ki}^2 m_k} \quad (35)$$

When studying the effects of wind load on the work of the frame of an industrial building, the corresponding reactions of the system elements were determined separately from the average $X^s = X(w_M)$ and the sum of the pulsating components $X^d = X\left(\sum_{i=1}^s w_p^i\right)$. The cumulative effect corresponding to the most unfavorable load value is achieved in case of coincidence of their signs:

$$X = X^s + \text{sign}(X^s) \cdot X^d. \quad (36)$$

The considered approach to the assessment of forces caused by the action of the wind, and reactions to them by the research object, is the basis of the calculation methodology, as one of the components of the generalized load, causing movements of the nodes of the design scheme, and, as a result, the change in stresses in the structural elements.

The implementation of the research concept is based on the probabilistic approach as the most appropriate for the random character of technogenic [9, 10] and extreme impacts [26, 29]. Generating the values of random variables applied crane loads, subject to the normal distribution law with known parameters of the expectation and standard deviation, each of the corresponding embedded calculation algorithms is repeated a large number of times, which allows achieving high accuracy of the results. To be able to compare them with the standard values under equal conditions, the algorithm also implies an appropriate calculation without considering the random nature of the manifestation of disturbing influences.

4. Conclusions

As conclusions on the results of the study, we highlight the following:

1. Clarifications have been made to the previously proposed design schemes and the methodology for calculating industrial buildings for crane and atmospheric loads, allowing to design the supporting structures of the frames in accordance with the actual conditions of their actual operation;
2. The necessity of calculating bending moments for all variants of the time variation of the total braking force of the trolleys of two adjacent cranes and the choice of the largest of them for loading design is substantiated;
3. The assumption is confirmed that the oscillations caused by the lateral forces during the tilted movement of the crane, directed across the rail tracks, have significantly larger amplitudes than when braking the crane truck;
4. Demonstrated good consistency of the proposed models of snow and wind loads, adapted for software implementation by means of computers, with a probabilistic approach to determining the components of the load factor.

References

1. Pichugin, S. Analysis of bridge crane loads on industrial buildings. XLIV Konferencja Naukowa KILiW PAN i KN PZITB. Poznan-Krynica. 1998. Tom VII. Pp. 171–178.
2. Pichugin, S. Probabilistic analysis on wind Load and reliability of structures. EACWE-2. Genova. Italy. 1997. Vol. 2. Pp. 1883–1890.
3. Kinash, R.I., Huk, J.S. Geographical altitude coefficient utilisation for wind gust loading determination in the mountainous terrain of the Transcarpathian region. Technical Transactions, Civil Engineering. Krakow. Poland. 2015. No. 2. Pp. 83–89.
4. Kwon, D.K., Kareem, A., Stansel, R., Ellington, B.R. Wind load factors for dynamically sensitive structures with uncertainties. Engineering Structures. 2016. Vol. 103. Pp. 53–62.
5. Baravalle, M., Kohler, J. On the probabilistic representation of the wind climate for calibration of structural design standards. Structural Safety. 2018. Vol. 70. Pp. 115–127.
6. Pichugin, S. Probabilistic description of ground snow loads for Ukraine. Snow Engineering. Recent Advanced and Developments. Rotterdam, 2000. Pp. 251–256.
7. Le, T., Lalin, V.V., Bratashov, A.A. Static accounting of highest modes in problems of structural dynamics. Magazine of Civil Engineering. 2019. 88(4). Pp. 3–13. DOI: 10.18720/MCE.88.1
8. Solovev, S.Yu., Khrapunov, E.F. Modeling of the mean wind loads on structures. Magazine of Civil Engineering. 2019. 88(4). Pp. 42–51. DOI: 10.18720/MCE.88.4
9. Zolina, T.V., Sadchikov, P.N. Modelirovanie raboty konstruksiy promyshlennogo zdaniya s uchetom izmeneniya zhestkosti v protsesse ekspluatatsii [Modeling the work of industrial building structures taking into account changes in rigidity during operation]. Vestnik MGSU [Proceedings of Moscow State University of Civil Engineering]. 2012. No. 10. Pp. 69–76. (rus) <http://vestnikmgsu.ru/ru/component/sjarchive/issue/article.display/2012/10/69-76>
10. Perelmuter, A.V., Pichugin, S.F. On the assessment of the vulnerability of building structures. Magazine of Civil Engineering. 2014. No. 5. Pp. 5–14.
11. Pichugin, S.F. Reliability estimation of industrial building structures. Magazine of Civil Engineering. 2018. 83(7). Pp. 24–37.
12. Kudzys, A.P. Otsenka nadezhnosti zhelezobetonnykh konstruksiy [Reliability estimation of reinforced concrete structures]. Vilnius: Mokslas. 1985. 156 p. (rus)
13. Cornell, C.A. Bounds on the reliability of structural systems. Journal of the Structural Division. ASCE. 1967. Vol. 93. No. ST. Pp. 171–200.
14. Bolotin, V.V. Stochastic models of fracture with applications to the reliability theory. Structural safety and reliability. Amsterdam, Oxford, New York: Elsevier. 1981. Pp. 31–56.
15. Braila, N.V., Khazieva, K.L., Staritsyna, A.A. Results of technical inspection monitoring of the operation object. Magazine of Civil Engineering. 2017. 74(6). Pp. 70–77.

16. Mushchanov, V.P., Orzhekhovskii, A.N., Zubenko, A.V., Fomenko, S.A. Refined methods for calculating and designing engineering structures. Magazine of Civil Engineering. 2018. 78(2). Pp. 101–115.
17. Danilov, A.I. Kontseptsiya upravleniya protsessom razrusheniya stroitel'nogo obyektu [The concept of controlling the process of destruction of a building object]. Industrial and Civil Engineering. 2014. No. 8. Pp. 74–77. (rus) <http://www.pgs1923.ru/russian/2014/14i08r.htm>
18. Belostotsky, A.M., Akimov, P.A., Negrozov, O.A., Petryashev, N.O., Petryashev, S.O., Sherbina, S.V., Kalichava, D.K., Kaytukov, T.B. Adaptive finite-element models in structural health monitoring systems. Magazine of Civil Engineering. 2018. 78(2). Pp. 169–178.
19. Tushnina, O.A. Finite element analysis of crane secondary truss. Magazine of Civil Engineering. 2018. 77(1). Pp. 68–89.
20. Serpik, I.N., Alekseytsev, A.V. Optimization of flat steel frame and foundation posts system. Magazine of Civil Engineering. 2016. 61(1). Pp. 14–24.
21. Alekseytsev, A.V. Evolutionary optimization of steel trusses with the nodal joints of rods. Magazine of Civil Engineering. 2013. No. 5. Pp. 28–37.
22. Tushnina, O.A., Danilov, A.I. The stiffness of rigid joints of beam with hollow section column. Magazine of Civil Engineering. 2016. 64(4). Pp. 40–51.
23. Krinitsky, E.V. Information model of the building (BIM). Magazine of Civil Engineering. 2010. No. 2. Pp. 16–18.
24. Zolina, T.V., Sadchikov, P.N. Revisiting the Reliability Assessment of frame constructions of Industrial Building. Applied Mechanics and Materials. 2015. Vols. 752-753. Pp. 1218–1223.
25. Patrikeyev, A.V., Salatov, Ye.K. Osnovy metodiki dinamicheskogo monitoringa deformatsionnykh kharakteristik zdaniy i sooruzheniy [Bases of a technique of dynamic monitoring of deformation characteristics of buildings and constructions]. Vestnik MGSU [Proceedings of Moscow State University of Civil Engineering]. 2013. No. 1. Pp. 133–138. (rus) <http://vestnikmgsu.ru/index.php/ru/archive/article/display/45/16>
26. Zolina, T.V., Sadchikov, P.N. Modelirovanie snegovoy nagruzki na pokrytie promyshlennogo zdaniya [Modeling of the Snow Load on the Roofs of Industrial Buildings]. Vestnik MGSU [Proceedings of Moscow State University of Civil Engineering]. 2016, No. 8. Pp. 25–33. (rus) <http://vestnikmgsu.ru/ru/component/sjarchive/issue/article.display/2016/8/25-33>
27. Ulybin, A.V., Vatin, N.I. Quality of visual inspection of buildings and constructions and technique of his performance. Construction of Unique Buildings and Structures. 2014. 25(10). Pp. 134–146. (rus) http://unistroy.spbstu.ru/index_2014_25/11_ulybin_25.pdf
28. Zolina, T.V., Sadchikov, P.N. Residual resource of a one-storey steel frame industrial building constructed with bridge cranes. Magazine of Civil Engineering. 2018. 84(8). Pp. 150–161.
29. Zolina, T.V., Sadchikov, P.N. Issledovanie sluchaynykh vozdeystviy vetrovoy nagruzki na rabotu karkasa odnoetazhnogo promyshlennogo zdaniya [Investigation of Random Wind Load Impacts on the Framework of a Single Storey Industrial Building]. Vestnik MGSU [Proceedings of Moscow State University of Civil Engineering]. 2016. No. 9. Pp. 15–25. (rus) <http://vestnikmgsu.ru/ru/component/sjarchive/issue/article.display/2016/9/15-25>

Contacts:

Tatiana Zolina, zolinatv@yandex.ru

Pavel Sadchikov, pn_sadchikov@mail.ru

© Zolina, T.V., Sadchikov, P.N., 2020



DOI: 10.18720/MCE.95.8

Analysis of reinforced soil sustainability while tunnel construction

A.G. Polyankin^{a*}, K.V. Korolev^b, A.O. Kuznetsov^b

^a National University of Science and Technology MISIS, Moscow, Russia

^b Siberian Transport University, Novosibirsk, Russia

* E-mail: polyankin_alex@mail.ru

Keywords: tunnels, tensile strength, reinforcement, durability, beams and girders, strength of materials, anchors

Abstract. Object – reinforced ground array stability analysis. We have not found straight and general method of analysis in theory of limit equilibrium of soils (TLES). Methods – theory of stability (Culman method), method of limit parameters of TLES. A general scheme for solving the problem of the stability of vertical slopes reinforced with horizontal rods (rough and smooth) is developed, which takes into account the behavior of reinforcing elements not only in pulling and tension, but also in the vertical direction, whereby part of the weight of the wedge of failure is transferred over its boundaries to a fixed array.

1. Introduction

Horizontal reinforcement of the soil mass with rods of circular cross-section is most often used in two cases – when fastening the sides of excavation pits – the so-called dowel fastening – and when fastening the excavation face during tunneling.

Dowel fastening became widespread first in the domestic metro construction, and then moved from there to industrial civil construction.

The technology of tunnel excavation face shoring using horizontal rods (advance support) has received the greatest industrial development in Italy. Typical examples are: Alpine tunnels (Italy-France), tunneling of the Prapontin road tunnel (Italy); construction of a single-crown station “Ubaldi” (Italy) and others. In those tunnel structures an approach was used, which was called ADECO-RS – Analysis of Controlled Deformation in Rocks and Soils. Being successfully used in various types of soils, this approach allowed to find solutions in numerous difficult tunneling situations where the application of traditional methods could no longer justify itself.

So, in [1], it is recommended that the soil of the tunnel be pre-strengthened by introducing fiberglass reinforcing elements into the core using the following methods:

- reinforcing of the tunnel working space using fiberglass elements;
- reinforcing of the tunnel working space using fiberglass elements simultaneously with creating advance temporary shotcrete shells around the working space;
- reinforcing of the tunnel working space using fiberglass elements simultaneously with creating advance temporary shells around the working space of the tunnel in the form of horizontal jet grouting;
- a combination of reinforcing the tunnel working space using with fiberglass elements and jet grouting of the soil mass, as well as simultaneously creating advance temporary shells around the tunnel working space in the form of horizontal jet grouting with fiberglass elements.

Thus, horizontal reinforcement is effectively used to strengthen the tunnel working space in underground construction, to increase the stability of the tunnel working space and has a similar principle of working with the dowel fastening of vertical slopes of excavation pits.



It should be noted that in water-saturated soils, the use of this type of reinforcement in underground construction is undesirable.

Turning to the existing methods for calculating reinforced soils, the article of V.G. Fedorovsky and S.G. Bezvovlev [2] should be noted, where the one-dimensional problem of the theory of calculating vertically reinforced foundations was formulated. Then it received significant development in the works of domestic and foreign scientists. Unfortunately, it is not directly applicable to the horizontal reinforcement problem, and here a number of issues remain, including those of a fundamental nature.

Soil reinforcement of underground structures is closely related to the problem of loss of soil stability. Comparing the methods for calculating the slope stability (for example, [3]) and the various forms of soil stability loss ahead of the face during the construction of underground structures (for example, [4, 5-8]), it is clearly seen that, in fact, very similar processes take place, therefore, similar methods for solving problems can be applied.

The papers [9, 10] are devoted to issues related to the numerical analysis of the stability of transport tunnels faces reinforced with horizontal elements [11, 12], and the work [13] is devoted to the analysis of the tunnel reinforcement schemes with horizontal reinforcing elements in cohesive soils. Additionally, the work [14] should be emphasized, in which the loss of face stability by the kinematic method of the theory of ultimate equilibrium of soils is considered.

The behavior of rods in linearly deformable media is considered in sufficient detail in [15, 16]. Of interest there is also a study [17] which examines the effect of the stress-strain state of soil located behind a face on the stability of the face. The same authors analyzed the stability situation during stepwise excavation of the face [18].

It should be noted that to date, a fairly large number of studies have already been performed, in which an analysis of a variety of contact problems in a nonlinear setting is performed [19, 20]. These solutions find quite wide practical application, however, they contain some uncertainty regarding the correctness of the description of the limit state of soil. Namely, at this state, soil masses reinforced with horizontal rods work in pits and in the faces of tunnels. And here, while one of the most popular methods are the methods of the classical Coulomb's wedge theory.

In addition to the classical Coulomb's wedge theory methods, which have received recognition and numerous experimental confirmation, for example, [21] and others, to date, linear programming methods [22], which show stable convergence with well-tested results of Coulomb's wedge theory solutions and with experimental data, are increasingly gaining confidence.

Separate consideration deserves issues related to the preparation of reinforcing elements [23], especially during tunnel face shoring. It should also be noted that in tunnel construction there are a number of technologies competing with the advance support [24, 25].

Reliability assessment of a single system "reinforcing element-soil" can be performed by standard methods of reliability of building structures [26].

The issues of assessing the stability of rocky massifs are still one of the most difficult in geomechanics and, in addition, differ in a variety of design schemes [27, 28] and force effects [29, 30]. Often they are solved only in conjunction with an analysis of the monitoring results throughout the entire tunneling [31].

Thus, a theoretical analysis of the method of fastening of soil massifs with horizontal reinforced rods, given its comparative youth, is a relevant object. So, we have to solve next tasks:

- To develop a general scheme for solving the problem of the stability of vertical slopes reinforced with horizontal rods (rough and smooth), which takes into account the behavior of reinforcing elements not only in pulling and tension, but also in the vertical direction, whereby part of the weight of the wedge of failure is transferred over its boundaries to a fixed array.
- To develop a technique for determining the force of active pressure on the retaining structures for two cases – with the presence between the horizontal reinforcing elements and the shotcreting reinforcement and the absence of such bond.
- To develop a practical recommendations for the calculation of soil massifs reinforced with horizontal or slightly inclined reinforcing elements.

2. Methods

Let us consider a solution to the stability problem of a vertical slope reinforced by horizontal rod elements of a circular cross-section, on the basis of statics equations and the Coulomb law [32].

The following designations are adopted: γ , φ and c are specific weight, angle of internal friction and soil specific cohesion; H is the slope height; p is external pressure on the edge; l_i , h_i and $d = 2r$ are the length, depth and diameter of the i -th reinforcing element; a_h , a are horizontal and vertical spacing of reinforcing elements. The horizontal spacing should ensure the stability of the tunnel face between the vertical rows of reinforcing elements.

The general behavior scheme of the reinforced soil and the failure area formation pattern is determined, first of all, by the reinforcement density. With a very high reinforcement density, the sliding surface is formed outside the reinforced soil massif, which consequently acts as a quasi-solid gravity wall [33] (Fig. 1, a).

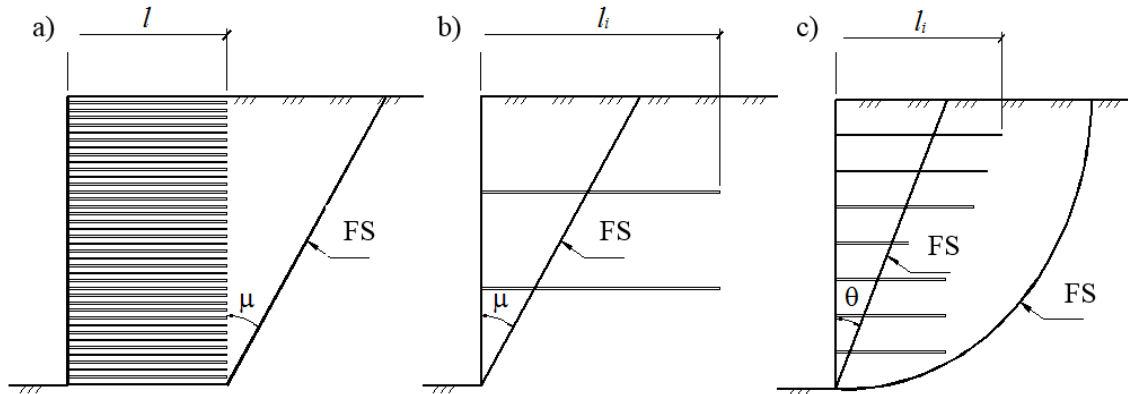


Figure 1. Failure schemes of the reinforced soil slopes with high (a), low (b), and "operating" (c) reinforcement density (FS-surface surface; $\mu = \pi/4 - \varphi/2$; $\theta < \mu$).

At a very low reinforcement density, the stability loss form of the soil massif will hardly differ from that of a homogeneous unreinforced slope, and the surface of failure intersects the reinforcing rods (Fig. 1, b). With a certain intermediate (conditionally speaking – "operating") reinforcement density, the failure can go along one of the two possible sliding surfaces – the first one crosses the reinforcing elements, and the second forms outside the reinforced soil mass (Fig. 1, c).

The intermediate scheme is of practical interest (see Fig. 1, c), since the first two are, in fact, limiting cases. Well-known methods of stability calculation can easily be performed along slip surfaces that form outside the reinforced soil massif. The main problem is considering the influence of reinforcing bars on the stability when collapsing surface crosses the reinforcing elements.

To solve this problem, we will consider the basic behavior scheme of a horizontal reinforcing element in a vertical tunnel face (Fig. 2). At the moment of the slope's stability loss, the reinforcing bar "cuts through" the wedge of failure. The force interaction of the reinforcing element and the wedge of failure is characterized by limit stresses – vertical p_u and shear τ_u , with:

$$\tau_u = \sigma_u \tan \psi, \quad (1)$$

where σ_u is the component of the limit pressure p_u normal to the reinforcing element surface; $\tan \psi$ is the friction coefficient of the reinforcing element against the ground.

As a result, the force of the "cutting" will be transmitted to the fixed soil mass:

$$Q = p_u A_{pr}, \quad M = Q \cdot l_{pr} / 2, \quad N = \tau_u A_{pr},$$

where $A_{pr} = l_{pr} \pi r$ is the contact area of the ground and reinforcing element within the wedge of failure.

Consequently, the work of the horizontal reinforcing bar will consist of transferring a part of the load from the weight G of the wedge of failure to a fixed soil mass [32].

Fig. 3 shows the design model of a reinforced slope. As mentioned above, each reinforcing element will transfer the forces Q_i , M_i , N_i to the fixed part of the foundation.

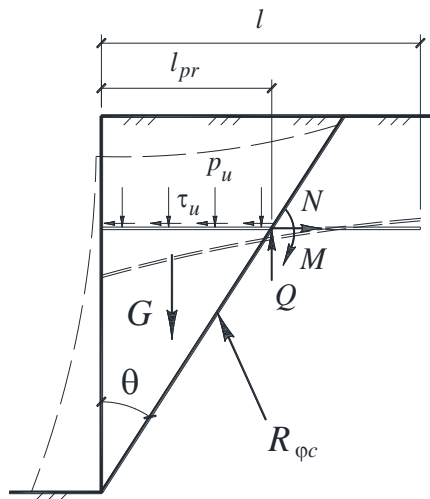


Figure 2. Principal behavior model of the reinforcing element (hatching shows a deformed view).

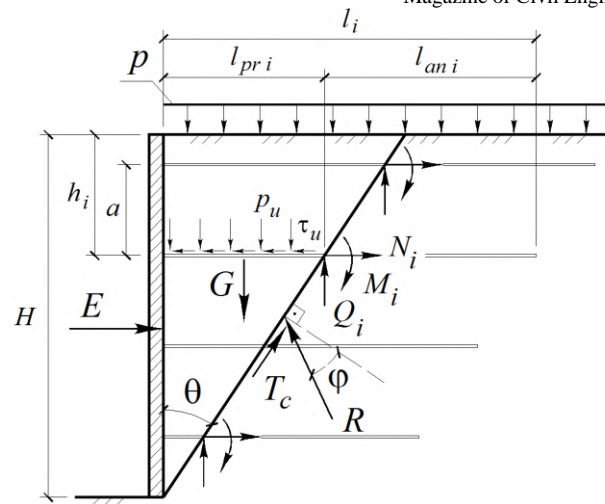


Figure 3. The design model of a vertical slope reinforced with horizontal rods.

Projecting the external forces and reactions acting on the prism at the wedge of failure at the moment of its collapse on the vertical and horizontal axes, we obtain the following equations [32]:

$$\begin{aligned} E + T_c \sin \theta - R \cos(\varphi + \theta) + \sum N_i &= 0; \\ P + G - T_c \cos \theta - R \sin(\varphi + \theta) - \sum Q_i &= 0, \end{aligned} \quad (2)$$

where $G = 0.5\gamma \cdot a_h \cdot H^2 \cdot \tan \theta$, $P = p \cdot a_h \cdot H \cdot \tan \theta$, $T_c = c \cdot a_h \cdot H / \cos \theta$, $N_i = \tau_u l_{pr,i} \pi r$, $Q_i = p_u l_{pr,i} \pi r$.

The equation of moments establishes a correspondence between the coordinates of the points of application of the forces E and R, and is not considered here.

Solving the system (2) with respect to E, we obtain

$$E = (P + G - \sum Q_i) \cot(\varphi + \theta) - \sum N_i - T_c \cos \varphi / \sin(\varphi + \theta). \quad (3)$$

The strength of the active pressure (along the length of the slope of a_h) is equal to:

$$E_a = \max E(\theta). \quad (4)$$

For absolutely smooth rods, the position of the dangerous slip line is determined by the angle $\theta = \pi/4 - \varphi/2$; for rough ones, a numerical search of θ is performed.

If $E_a \leq 0$, then the ground face is retained only by reinforcing rods, and retaining structures are only needed to ensure local soil stability (against "caving" between rods).

If $E_a > 0$, then in order to retain the ground face, in addition to reinforcement, a shotcreting reinforcement is required, but at the same time reinforcing elements reduce the value of E as compared to the unreinforced ground face. Here it seems possible to consider two design cases – when the shotcrete is connected with reinforcing elements, and when they work independently.

In the first case, collapse will not occur until the load-carrying capacity of the reinforcing elements for pulling out of the fixed ground is exceeded (it is assumed that the strength of the reinforcing elements bonds and shotcrete is sufficient):

$$E_a + \sum N_i \leq \sum N_{an,i} = \sum \tau_u A_{an,i}. \quad (5)$$

where $A_{an,i} = l_{an,i} \pi r$ is the area of contact, which is equal to the half-surface of the reinforcing element, since it, being in a fixed array, undergoes significant bending deformations under the forces Q_i and M_i (see Fig. 2); τ_u is the same as in formula (1).

When the condition (5) is satisfied, the retaining wall works virtually only for local stability. If condition (5) is not satisfied, then it is necessary to perform the calculation of the shotcreting reinforcement for the impact of the force $E_a - \sum N_{an,i}$.

In the second case (the shotcreting reinforcement and the reinforcing element are not connected), the retaining shotcreting reinforcement should be calculated for the active pressure with the resultant E_a .

The next important question is that of the value of $l_{an,i}$ of embedding of the reinforcing bar into a fixed soil mass. In principle, the value $l_{an,i}$ must provide two conditions: the rod behavior in pulling by the force N_i and the rod stability against "reversing" by the forces Q_i and M_i .

The check for pulling is carried out according to the formula

$$N_i \leq N_{an,i} = \tau_u A_{an,i}. \quad (6)$$

The check against "reversing" is expressed in ensuring the equilibrium of the part $l_{an,i}$ of the length of the reinforcing element in the embedding by the forces Q_i and M_i . This can be done in accordance with one of three schemes.

In the first scheme, it is assumed that the reinforcing element deforms in a fixed array according to the Fuss-Winkler theory, and the contact stresses reach the limit values $p_{u,b}$ at only one point (Fig. 4, a). In the second scheme, it is assumed that the contact stresses reach the limit values in individual sections, with the bottom and top limit values obviously being different – they will be denoted by $p_{u,b}$, and $p_{u,t}$ (Fig. 4, b). In the third scheme, the following limiting case is considered: in the region where the reinforcing element is pressed into the soil, stresses are equal to $p_{u,b}$, and in the region where the reinforcing element is bending upwards, "cutting" the overlying soils stresses are equal to $p_{u,t}$ (Fig. 4, c). The third scheme gives the minimum allowable amount of embedding.

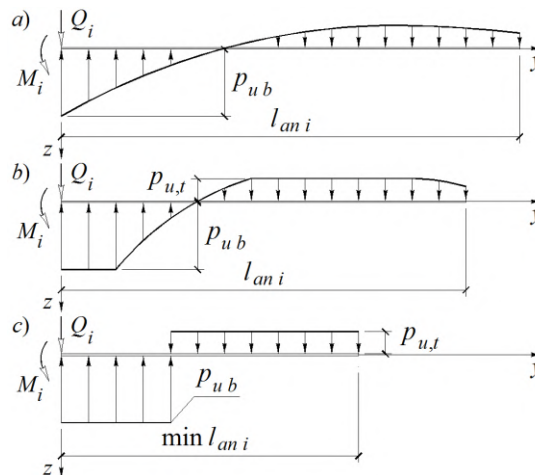


Figure 4. Schemes for determining the value of embedding the reinforcing element: a – completely safe embedding, b – with limiting pressure regions, c – minimal embedding.

In all three cases, the embedding value $l_{an,i}$ is determined from the static equilibrium of the beam, on which the force Q_i , the moment M_i and the contact stresses, whose determination has been considered earlier.

Thus, for numerical realization of the method proposed here, it is necessary to know the values of the limiting stresses at the contact "reinforced element-ground" p_u , $p_{u,b}$ and $p_{u,t}$.

3. Results and Discussion

Let us consider solutions to the theory of limiting soil equilibrium of soils (TLES) to determine the values of the limiting stresses at the "reinforced element-ground" contact and their components – vertical p_u , $p_{u,b}$, $p_{u,t}$ and normal σ_u , $\sigma_{u,b}$, $\sigma_{u,t}$ to the contact surface.

Since the sequence of boundary-value problems plays the determining role in the solutions of the TLES, it is necessary to have some initial understanding of the geometry of the limiting equilibrium regions to come up with the solution. For this purpose, we make experimental and numerical studies to investigate the formation of zones of collapse in an array around the reinforcing elements when they "cut" the soil [32].

The numerical simulation is justified by the fact that for a wide range of practically important problems of the finite element method (FEM), which does not always allow reliable values of the ultimate load to be obtained, can still give a fairly correct picture of the deformed state. Therefore, in this case, FEM can be used in combination with the experiment results for a ground failure qualitative assessment.

In both cases (both the "cutting" of the wedge of failure and the "pushing" of the fixed soils by the reinforcing element), the formation of the limiting equilibrium regions proceeds from the reinforcing element upwards, which served as the basis for further theoretical analysis by the TLES methods, determining the sequence of boundary-value problems of the TLES (Fig. 5).

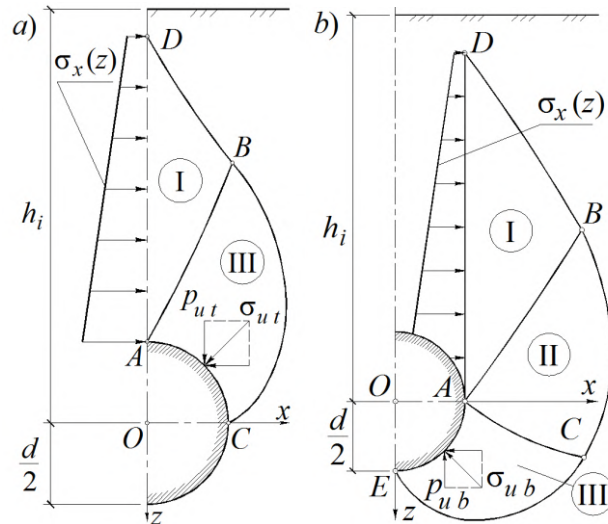


Figure 5. Solution sequence of boundary value problems: a – for p_u (or p_{ut}), b – for p_{ub} .

The solution was achieved by integrating the canonical system of equations of the static state of the granular medium, compiled from the characteristics (failure lines) of two families:

$$dx = dz \operatorname{tg}(\alpha \pm \mu), \quad d\sigma \pm 2\sigma \tan \varphi d\alpha = \gamma(dz \mp dx \tan \varphi),$$

where $\tan \alpha = 2\tau_{xz}/(\sigma_z - \sigma_x)$ is the angle between the direction of σ_1 and the Oz axis; $\sigma = (\sigma_x + \sigma_z)/2 + c \cot \varphi$ is the reduced average stress.

A feature of these schemes is the construction of a field of limiting stresses in the boundary value problem's zone III.

Fig. 6 shows the grids of the failure lines obtained for both schemes.

In both cases, the solution was detailed for two types of boundary conditions: first with taking into account the depth of the reinforcing element, if $\sigma_x(z) = \xi\gamma(h_i + z)$ at the boundary AD (where ξ is the lateral pressure coefficient); and the second without accounting for depth, if $\sigma_x(z) = 0$ at the boundary AD , which guarantees a certain margin of safety.

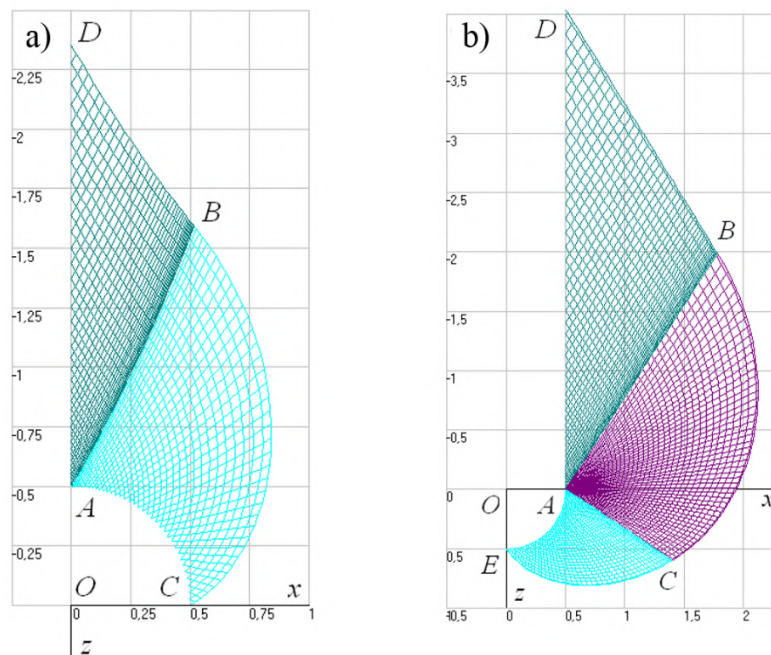


Figure 6. Examples of failure line grids: a – for p_u (or p_{ut}), b – for p_{ub} .

An analysis of the results showed that the obtained limiting stresses can be approximated by expressions in the form of the classical three-term K. Terzaghi formula. For the problem of "cutting" of the above-located soil by a reinforcing element, the expressions for the vertical and normal (to the surface of the contact) components of the limiting stresses are:

$$p_u = p_{ut} = N_\gamma \gamma d + N_q \gamma h_i + N_c c, \quad (7)$$

$$N_\gamma = [(-0.193\xi^2 - 0.127\xi + 0.32) + (0.159\xi^2 - 1.521\xi + 0.488)e^{(-6.63\xi^2 + 7.978\xi + 3.393)\tan\varphi}] / \pi$$

$$N_q = (2\xi e^{3.207\tan\varphi}) / \pi, \quad N_c = (2.13 + 4.222e^{2.372\tan\varphi}) / \pi.$$

$$\sigma_u = \sigma_{ut} = N_\gamma \gamma d + N_q \gamma h_i + N_c c, \quad (8)$$

$$N_\gamma = [(0.0884\xi^2 + 0.634\xi + 0.526) + (1.122\xi^2 - 3.935\xi + 1.219)e^{(-6.673\xi^2 + 8.327\xi + 3.806)\tan\varphi}] / \pi,$$

$$N_q = (3.14\xi e^{3.207\tan\varphi}) / \pi, \quad N_c = (4.414 + 6.97e^{2.858\tan\varphi}) / \pi.$$

Herewith the depth of the reinforcing bar must be greater than the maximum height of the development of the marginal equilibrium regions:

$$h_i > (0.206 + 0.609e^{2.38813\tan\varphi}) d.$$

Similar relations were obtained for the case of pushing the reinforcing element into the underlying soil. The required components of the ultimate stresses can be calculated by the formulas:

$$p_{ub} = N_\gamma \gamma d + N_q \gamma h_i + N_c c,$$

$$N_\gamma = [(-56.28 \cdot \xi^2 + 58.504 \cdot \xi - 2.202) +$$

$$+ (2.581 \cdot \xi^2 - 4.393 \cdot \xi + 1.341)e^{(-11.414 \cdot \xi^2 + 14.96 \cdot \xi + 7.835)\tan\varphi}] / \pi$$

$$N_q = [(0.193 \cdot \xi^2 - 0.805 \cdot \xi) + (2.14 \cdot \xi \cdot e^{7.085\tan\varphi})] / \pi,$$

$$N_c = (8.279 + 5.985e^{4.826\tan\varphi}) / \pi.$$

$$\sigma_{ub} = N_\gamma \gamma d + N_q \gamma h + N_c c,$$

$$N_\gamma = [(-62.036 \cdot \xi^2 + 64.106 \cdot \xi - 1.969) +$$

$$+ (3.011 \cdot \xi^2 - 5.129 \cdot \xi + 1.565)e^{(-11.356 \cdot \xi^2 + 14.875 \cdot \xi + 7.761)\tan\varphi}] / \pi,$$

$$N_q = [(0.222 \cdot \xi^2 - 0.067 \cdot \xi) + (3.04 \xi e^{6.891\tan\varphi})] / \pi,$$

$$N_c = (12.381 + 8.318e^{4.648\tan\varphi}) / \pi.$$

Herewith the depth of the reinforcing bar must be greater than the maximum height of the development of the marginal equilibrium regions:

$$h_i > (-0.497 + 1.333e^{2.945\tan\varphi}) d.$$

At a lower value of h_i , the contact stresses should be considered equal to the natural pressure.

To confirm the obtained theoretical data, a full-scale field experiment in the Novosibirsk region was carried out in a specially organized testing area adjacent to the construction site of a tunnel-type overpass on the Baryshevo-Orlovka-Koltsovo highway. This experiment was carried out to correct preliminary design decisions, particularly the parameters of the soil reinforcement with horizontal rods ahead of the tunnel slope (the outstripping support) and the fastening of the near-slope part of the embankment [34].

The pressure was calculated according to the proposed procedure was 32.6 kPa, and the collapse of the slope occurred when the actual loading of the pit edge was equal to 37 kPa. Since the design pressure from the external load was 70 kPa, the results of the experimental-theoretical studies were corrected accordingly.

On this basis, practical recommendations were developed for pit edge and soils calculations ahead of the tunnel face reinforced with horizontal elements. The main calculation stages in the developed practical recommendations are:

1. Collecting loads on the edge of the slope and locating them along the width of the edge (for designing the outstripping tunnel support – according to the hypothesis of arching or the scheme of natural stresses in the calculated level).
2. Preliminary assignment of geometric reinforcement parameters (diameter of reinforcing elements, vertical and horizontal spacing of reinforcing elements).
3. Determination of the limiting pressures and their components at "reinforcing element-ground" contact (see the formulas (7) ... (8)). At the same time, within the wedge of failure, the calculation of the limiting pressure for $p_{u,t}$ should be performed at $\xi = 0$.
4. Determination of the most disadvantageous position of the failure surface and the value of the resultant active pressure (see the formula (4)).
5. Correction of reinforcement parameters depending on the adopted slope reinforcement scheme (with or without a retaining wall).
6. Determination of the embedding length for reinforcing elements in the fixed ground (see Fig. 4, c).
7. Checking the reinforced soil massif as a quasi-solid retaining wall for shear along the underlying unreinforced soil.
8. Checking the reinforced soil massif as a quasi-solid retaining wall for overturning.
9. Testing the overall stability (deep-seated shift) of the reinforced soil massif as a quasi-solid retaining wall.
10. Checking material strength of the reinforcing element, as well as the wall and its connection with reinforcing elements (if available).

By varying the parameters d_a , a_h , a based on the above calculation scheme, an optimization algorithm is constructed for the entire retaining structure for one or another selected optimization parameter.

The proposed technique can also be used if the reinforced elements have a small angle of inclination to the horizon – up to 15 °.

In [14] the method face stability analysis of tunnel face is described, but tunnel face is not reinforced by beams. A finite difference procedure for deep tunnels is presented in [9]. The aims in geomechanics solved by finite element or finite difference methods have to be verified by TLES formulas.

4. Conclusions

1. A general scheme for solving the problem of the stability of vertical slopes reinforced with horizontal rods (rough and smooth) is developed, which takes into account the behavior of reinforcing elements not only in pulling and tension, but also in the vertical direction, whereby part of the weight of the wedge of failure is transferred over its boundaries to a fixed array.
2. A technique has been developed for determining the force of active pressure on the retaining structures for two cases – with the presence between the horizontal reinforcing elements and the shotcreting reinforcement and the absence of such bond. The reinforcement sufficiency condition of a soil massif is formulated without additional retaining structures.
3. In order to quantitatively evaluate the interaction between the soils of the wedge of failure and the fixed region of the foundation, on the one hand, and the reinforcing elements on the other, new rigorous solutions of the TLES are applied to the limiting state of the soil surrounding the reinforcing element of circular cross-section (with and without depth of its location). The solutions obtained are reduced to the standard form of the three-term Terzaghi formula.
4. Practical recommendations for the calculation of soil massifs reinforced with horizontal or slightly inclined reinforcing elements are developed for two main practical schemes: the stability of the foundation pit edges and the stability of the ground ahead of the face during tunnel excavation.

References

1. Lunardi, P. Progetto e costruzione di gallerie – Analisi delle deformazioni controllate nelle Rocce e nei suoli. Milano, 2006. 572 p.
2. Fedorovsky, V.G, Bezvoley, S.G. Metod analiza svaynykh poley i drugikh vertikal'no armirovannykh mass grunta [Method of pile fields and other vertically reinforced soil masses analysis]. Soil Mechanics and Foundation Engineering. 1994. No. 3. Pp. 17–27. (rus) DOI:10.1007/BF02335022
3. Senenta, S., Mollonb, G., Jimenez, R., Tunnel face stability in heavily fractured rock masses that follow the Hoek–Brown failure criterion International Journal of Rock Mechanics and Mining Sciences. 2013. 60. Pp. 440–451. DOI:10.1016/j.ijrmms.2013.01.004
4. Elkayama1, I., Klarb, A. Upper bound of tunnel face stability using asymmetric yielding. Underground Space. 2018. 3(4). Pp. 288–296. DOI:10.1016/j.undsp.2018.03.001
5. Wilson, D.W., Abbo, A.J., Sloan, S.W., Lyamin, A.V., Undrained stability of a square tunnel where the shear strength increases linearly with depth. Computers and Geotechnics. 2013. 49. Pp.314–325. DOI:10.1016/j.compgeo.2012.09.005
6. Xiang, Y., Song, W., Upper-bound limit analysis of shield tunnel stability in undrained clays using complex variable solutions for different ground-loss scenarios. International Journal of Geomechanics. 2017. 17(9). Pp.113–119. DOI:10.1061/(ASCE)GM.1943-5622.0000946
7. Zhang, C., Han, K., Zhang, D., Face stability analysis of shallow circular tunnels in cohesive frictional soils. Tunnelling and Underground Space Technology. 2015. 50. Pp. 57–63. DOI:10.1016/j.tust.2015.08.007
8. Zhang, F., Gao, Y.F., Wu, Y.X., Zhang, N. Upper-bound solutions for face stability of circular tunnels in undrained clays. Géotechnique. 2018. 68(1). Pp. 76–85. DOI:10.1680/jgeot.16.T.028
9. Oreste, P. Face stabilization of deep tunnels using longitudinal fibreglass dowels. International Journal of Rock Mechanics and Mining Sciences. 2013. 58. Pp. 127–140. DOI:10.1016/j.ijrmms.2012.07.011
10. Li, B., Hong, Y., Gao, B., Qi, T.Y., Wang, Z.Z., Zhou, J.M. Numerical parametric study on stability and deformation of tunnel face reinforced with face bolts. Tunnelling and Underground Space Technology. 2015. 47. Pp. 73–80. DOI: 10.1016/j.tust.2014.11.008
11. Paternesi, A., Schweiger, H.F., Scarpelli, G. Numerical analyses of stability and deformation behavior of reinforced and unreinforced tunnel faces. Computers and Geotechnics. 2017. 88. Pp. 256–266. DOI: 10.1016/j.compgeo.2017.04.002.
12. Maghous, S., Bernaud, D., Couto, E. Three-dimensional numerical simulation of rock deformation in bolt-supported tunnels. Tunnelling and Underground Space Technology. 2012. 31. Pp. 68–79. DOI:10.1016/j.tust.2012.04.008
13. Anagnostou, G., Perazzelli, P. Analysis method and design charts for bolt reinforcement of the tunnel face in cohesive-frictional soils. Tunnelling and Underground Space Technology. 2015. 47. 2015. Pp. 162–181. DOI:10.1016/j.tust.2014.10.007
14. Pan, Q., Dias, D. Face stability analysis for a shield-driven tunnel in anisotropic and nonhomogeneous soils by the kinematical approach International Journal of Geomechanics ASCE. 2016. 16(3). DOI:10.1061/(ASCE)GM.1943-5622.0000569
15. Klar, A., Osman, A.S. Load-displacement solutions for piles and shallow foundations based on deformation fields and energy conservation. Géotechnique. 2008. 58(7). Pp. 581–589. DOI:10.1680/geot.2008.58.7.581
16. Klar, A., Randolph, M.F. Upper-bound and load displacement solutions for laterally loaded piles in clays based on energy minimization. Géotechnique. 2008. 58(10). Pp. 815–820. DOI:10.1680/geot.2007.00197
17. Pankratenko, A., Isaev, A. The Analysis of the stress-strain state of the system "equipment complex - support - rock mass" in the bottomhole area of the shaft. E3S Web of Conferences. 2018. 41. DOI: 10.1051/e3sconf/20184101038.
18. Pankratenko, A. Vliyaniye poshagovogo vskrytiya zaboya pri prokhode krupnykh uchastkov na geomekhanicheskoye sostoyaniye porody akkomodatsionnogo massiva [The effect of step-by-step face opening during road-heading of large sections on geomechanical state of rocks of accommodating massif]. Gornyi Zhurnal. 2002. Pp. 93–99. (rus)
19. Zertsalov, M.G., Znamenskiy, V.V., Khokhlov, I.N. Interaction of drilled shafts in rock under the action of lateral load IOP Conference Series: Materials Science and Engineering. 2018. 365. 042050. DOI:10.1088/1757-899X/365/4/042050
20. Zertsalov, M.G., Merkin, V.E., and Khokhlov, I.N. The influence of the interface of drilled socketed shafts in rock. Geomechanics and Geodynamics of Rock Masses. 2018. Pp. 937–943.
21. Karaulov, A.M., Experimental and theoretical research on the bearing capacity of ring-foundation beds. Soil Mechanics and Foundation Engineering. 2005. 42(3). Pp. 75–80. DOI: 10.1007/s11204-005-0028-5
22. Karaulov, A.M. Experimental and theoretical research on the bearing capacity of ring-foundation beds. Soil Mechanics and Foundation Engineering. 2006. 43(2). Pp. 37–40. DOI: 10.1007/s11204-006-0021-7
23. Baydjanov, D.O., Abdрахmanova, K.A., Kropachev, P.A., Rakhimova G.M. Modified concrete for producing pile foundations. Magazine of Civil Engineering. 2019. 86(2). Pp. 3–10. DOI: 10.18720/MCE.86.1
24. Sabri, M.M., Shashkin, K.G. Improvement of the soil deformation modulus using an expandable polyurethane resin. Magazine of Civil Engineering. 2018. 83(7). Pp. 222–234. DOI: 10.18720/MCE.83.20
25. Sabri, M.M., Shashkin, K.G., Zakharin, E., Ulybin, A.V. Soil stabilization and foundation restoration using an expandable polyurethane resin. Magazine of Civil Engineering. 2018. 82(6). Pp. 68–80. DOI: 10.18720/MCE.82.7
26. Pichugin S.F. Reliability estimation of industrial building structures. Magazine of Civil Engineering. 2018. 83(7). Pp. 24–37. DOI:10.18720/MCE.83.3
27. Sammal, A.S., Antsiferov, S.V., Deev, P.V., Sergeev, S.V. Estimate of rock mass stability in surface-borehole mining of high-grade iron ore. IOP Conference Series: Earth and Environmental Science. 2017. 53(1). DOI:10.1088/1755-1315/53/1/012007
28. Sammal, A.S., Antsiferov, S.V. Influence of mutual position of a noncircular tunnel and a dynamic impact source on stress distribution in lining. IOP Conference Series: Earth and Environmental Science. 2018. 134(1). DOI:10.1088/1755-1315/134/1/012054.
29. Antsiferov, S.V., Sammal, A.S., Deev, P.V. Stress state estimation in multilayer support of vertical shafts, considering off-design cross-sectional deformation. IOP Conference Series: Earth and Environmental Science. 2018. 134(1). DOI:10.1088/1755-1315/134/1/012001.
30. Korovkin, V.S., Ragulin, K.G., Kuzina, A.D., Smolenkova, A.V., Orlova N.S., Computation of mooring quay in the form of pile grillage. Magazine of Civil Engineering. 2017. 71(3). Pp. 10–20. DOI: 10.18720/MCE.71.2
31. Deev P., Sammal A., Antsiferov S. Evaluation of mine support stress state on base of convergence measurement data // International Multidisciplinary Scientific GeoConference Surveying Geology and Mining Ecology Management, SGEM. 2017. 17(13). Pp. 321–326. DOI:10.5593/sgem2017/13/S03.041

32. Kuznetsov, A.O. Prakticheskaya metodologiya rascheta sklonov, armirovannykh gorizontallykh sterzhney kruglogo secheniya [Practical methodology for calculating slopes reinforced with horizontal rods of circular cross-section]. Izvestia VNIIG B.E. Vedeneeva. 2017. Pp. 88–96.
33. Ovchinnikov, I.I., Ovchinnikov, I.G. Application of nonlinear deformation model for the analysis of behavior of reinforced plates on elastic foundation, interacting with chloride-containing environments. The basic relations. Magazine of Civil Engineering. 2013. 36(1). Pp. 27–38. DOI: 10.5862/MCE.36.4
34. Oparin, V.N., Yushkin, V.F., Polyankin, G.N., Grishin, A.N., Kuznetsov, A.O., Rublev, D.E. Geomechanical monitoring of temporal lining in railway tunneling in complex geological conditions. Journal of Mining Science. 2015. 51(4). Pp. 839–859. DOI: 10.1134/S1062739115040226

Contacts:

Aleksandr Polyankin, polyankin_alex@mail.ru

Konstantin Korolev, korolev_kv@mail.ru

Anatoly Kuznetsov, kuzemon91@mail.ru

© Polyankin A.G., Korolev K.V., Kuznetsov A.O., 2020



DOI: 10.18720/MCE.95.9

Method of plates stability analysis based on the moments approximations

Yu. Ya. Tyukalov*

Vyatka State University, Kirov, Russia

* E-mail: yutvgu@mail.ru

Keywords: finite element method, plates, stability, approximations of forces, critical stress

Abstract. The paper proposes the method for calculating of thin plates stability by the finite element method based on piecewise constant approximations of the moments' fields. Using this approach may allow us to obtain the lower limit of critical stresses. We build the solution based on the extended functional of additional energy. The functional, using the method of Lagrange multipliers, includes algebraic equations of nodes equilibrium of the finite elements mesh. Using the possible displacements principle, we get equilibrium equations. The plate vertical displacements function after stability loss, is combination of linear basis functions. For rectangular and triangular finite elements there are the necessary expressions for the stresses work, acting in the plate median plane, from bending deformations. There are critical stress calculations for rectangular plates with different supporting conditions. The options for the action of compressive and shear stresses are considered. It is shown, that when the finite element mesh is refining up, the critical stress value in all the considered examples tends to the exact value from below. We perform comparison of the obtained solutions with the analytical solutions and the solutions by the program based on the finite element method in displacements. Comparison of solutions showed good accuracy in determining critical stresses by the proposed method.

1. Introduction

An analysis of elastic stability is necessary when we design many structural elements, especially thin plates. The study of the stability of elastic systems basically comes down to determining the magnitude of critical compressive loads which will lead to buckling of the structure. To ensure the margin of stability of structures, it is important to determine the lower limit of critical loads. The finite element method is one of the main methods for solving problems of stability theory, because it can be used to consider irregularities in constructions that cannot be allow in analytical methods [1, 2]. On the other hand, analytical methods using uniform approximations of displacements for the entire subject area make it possible to obtain more accurate and continuous solutions for plates with simple shapes [3, 4]. The solutions of stability problems for various structures by the finite element method in displacements are widely used [5, 6]. Such solutions are based on various functionals and use displacements fields approximations which may to allow the different deformations of structural elements [7, 8].

In [9], the solution of stability problem for spatial rod systems was obtained by the finite element method based on the forces approximations. This approach allowed to obtain the convergence of the critical load approximate value to exact value from below. To analyze the stability of the plates, the Ritz method is also often used [10–11]. Valid functions used to approximate displacements are a series of regular orthogonal polynomials which supplemented with special functions. The analysis performed in [11] shows the effectiveness and potential of the method which provides accurate results in combination with a reduced number of freedom degrees and simplified data preparation.

The stability analysis is great importance for the design of various steel plates [12–13]. In [13], the model was proposed for stability analysis of a corrugated steel plate. The proposed procedures only allow the linear elastic behavior of the material. The paper [14] is devoted to the analysis of the stability of variable thickness

Tyukalov, Yu.Ya. Method of plates stability analysis based on the moments approximations. Magazine of Civil Engineering. 2020. 95(3). Pp. 90–103. DOI: 10.18720/MCE.95.9



This work is licensed under a [CC BY-NC 4.0](https://creativecommons.org/licenses/by-nc/4.0/)

plates. To modeling plate thickness variability, quadratic functions and the same nodal parameters are used, which approximate the displacements. To confirm the reliability of the proposed method, numerical results of stability plates calculations are presented. To analyze the stability of skew plates, a differential quadrature method was proposed in [15]. A complete set of equilibrium equations, in an inclined coordinate system, of bending and torques moments, equivalent transverse forces and angular forces is obtained. The accuracy of the solution was checked by comparing the results of inclined plates calculations, which had different boundary conditions, with the results obtained by the finite element method using very fine grids.

The use of analytical methods for solving the stability problems of plates is still relevant [16–17]. The main advantage of the analytical method is that it is simple and universal and does not require any predetermined deformations functions. In [17], the generalized integral transformation method was first used to obtain an exact analytical solution to the stability loss of a rectangular thin plate. In the article [18] it is given an idea of the implementation and using of the Ritz method for the analysis of free vibrations and loss of composite plates stability. Attention was paid to the selection of approximation functions depending on the degree and type of plates anisotropy. An efficient calculation method of Ritz integrals is proposed, which allows one to process a set of admissible functions. The effect of various forms of elastic bonds, boundary conditions and the material anisotropy variants on the convergence and accuracy of the solution was investigated. Various sets of admissible functions were used - Legendre and Chebyshev polynomials, as well as trigonometric type functions. The tasks of studying shallow shells stability [19] and plates of variable stiffness [20, 21] remain relevant. Alternative variational principles, in particular the Castilian's principle [22], are also used to solve various problems of elasticity theory. An important task is to study of plates stability during heating. In [23], experimental and theoretical studies of round plates during axisymmetric heating are presented.

In articles [24, 25], piecewise constant approximations of the moment fields were used to calculate bending plates by the finite element method. It was shown, that in this case when the finite element mesh is reducing the displacements values tend to exact values from above. This shows that the solution obtained using this technique is always more flexible than accurate. Thus, it can be assumed that the use of such approximations to analyze the stability of plates will allow us to obtain the lower boundary of the critical load.

The aim of this work is to develop a method for calculating the thin plates stability, which is based on piecewise constant approximations of the moment fields. The main tasks of paper are: obtaining the necessary resolving equations for rectangular and triangular finite elements; performing test calculations of critical forces for plates with different boundary conditions; comparison of the obtained solutions with analytical solutions and solutions obtained by programs which are based on the finite element method in displacements.

2. Methods

The solution to the stability problem of thin plates corresponding to Kirchhoff's theory will be built based on the additional energy functional [1]:

$$\Pi^c = \frac{1}{2} \frac{12}{E \cdot t^3} \int_{\Omega} \left(M_x^2 + M_y^2 - 2\nu M_x M_y + 2(1+\nu) M_{xy}^2 \right) d\Omega. \quad (1)$$

E is the elastic modulus of the plate material; t is the plate thickness; ν is Poisson's ratio; M_x is bending moment directed along the X axis; M_y is bending moment directed along the Y axis; M_{xy} is torque. Bending moments are positive if they stretch the lower fibers of the plate. We write the functional (1) in matrix form:

$$\Pi^c = \frac{1}{2} \int_{\Omega} \mathbf{M}_{\Omega}^T \mathbf{E}^{-1} \mathbf{M}_{\Omega} d\Omega. \quad (2)$$

The following notation is introduced in expression (2):

$$\mathbf{M}_{\Omega} = \begin{Bmatrix} M_x \\ M_y \\ M_{xy} \end{Bmatrix}, \quad \mathbf{E}^{-1} = \frac{12}{E \cdot t^3} \begin{bmatrix} 1 & -\nu & 0 \\ -\nu & 1 & 0 \\ 0 & 0 & 2(1+\nu) \end{bmatrix}. \quad (3)$$

We shall represent the subject area as a set of rectangular and triangular finite elements. In the region of the finite element for the moments fields we use piecewise constant approximation functions (Fig. 1) [24–26].

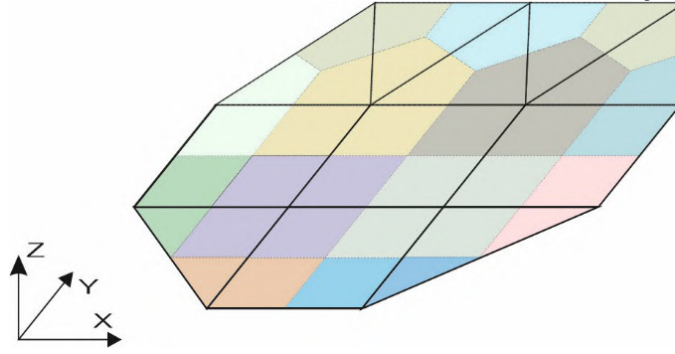


**Figure 1. Piecewise constant approximations of the moments' fields.
Areas with constant moments are shown in the same color.**

We introduce the notation for unknown nodal moments $M_{x,i}, M_{y,i}, M_{xy,i}$ and for the vector of the nodal moments to the rectangular finite element

$$\mathbf{M}_k^T = (M_{x,1} \ M_{y,1} \ M_{xy,1} \ M_{x,2} \ M_{y,2} \ M_{xy,2} \ M_{x,3} \ M_{y,3} \ M_{xy,3} \ M_{x,4} \ M_{y,4} \ M_{xy,4}). \quad (4)$$

To simplify the notation of expressions, we introduce auxiliary unit stage functions

$$\psi_i(x, y) = \begin{cases} 1, & (x, y) \in \Omega_i \\ 0, & (x, y) \notin \Omega_i \end{cases}. \quad (5)$$

Also, we introduce the corresponding diagonal matrices which correspond to the element nodes

$$\Psi_i = \begin{bmatrix} \psi_i & & & \\ & \psi_i & & \\ & & \psi_i & \\ & & & \psi_i \end{bmatrix}. \quad (6)$$

Then the approximation matrix of moments in the region of the rectangular finite element will have the simple form:

$$\mathbf{Z}_k = [\Psi_1 \ \Psi_2 \ \Psi_3 \ \Psi_4]. \quad (7)$$

For a triangular finite element, expressions (4) and (7) are written similarly. Then

$$\mathbf{M}_\Omega = \mathbf{Z}_k \mathbf{M}_k. \quad (8)$$

Using (8), we shall express the additional strain energy of the finite element in the following form:

$$\Pi_k^c = \frac{1}{2} \int_{\Omega_k} \mathbf{M}_k^T (\mathbf{Z}_k^T \mathbf{E}^{-1} \mathbf{Z}_k) \mathbf{M}_k d\Omega. \quad (9)$$

We introduce the notation for the local flexibility matrix of the finite element \mathbf{D}_k :

$$\mathbf{D}_k = \int_{\Omega_k} \mathbf{Z}_k^T \mathbf{E}^{-1} \mathbf{Z}_k d\Omega. \quad (10)$$

Note that the matrix is calculated analytically and has a block-diagonal form. Expressions of the matrix elements can be found in article [24].

From the flexibility matrices of finite elements \mathbf{D}_k , the global flexibility matrix of the construction \mathbf{D} is formed, and from the vectors \mathbf{M}_k global vector of nodal moments \mathbf{M} is formed. Using the introduced notations, we obtain the following expression of the functional (2):

$$\Pi^c = \frac{1}{2} \mathbf{M}^T \mathbf{D} \mathbf{M}. \quad (11)$$

It is important that the matrix **D** is block-diagonal and consists of square matrices measuring 3 by 3. Therefore, the matrix **D** is easily analytically reversible. This fact greatly simplifies construction of the problem solution.

In accordance with the Castigliano's principle, the moment fields must satisfy the equilibrium equations and static boundary conditions. To provide the equilibrium of the moment's fields, we compose the algebraic equilibrium equations of a grid nodes using the principle of possible displacements [24, 25].

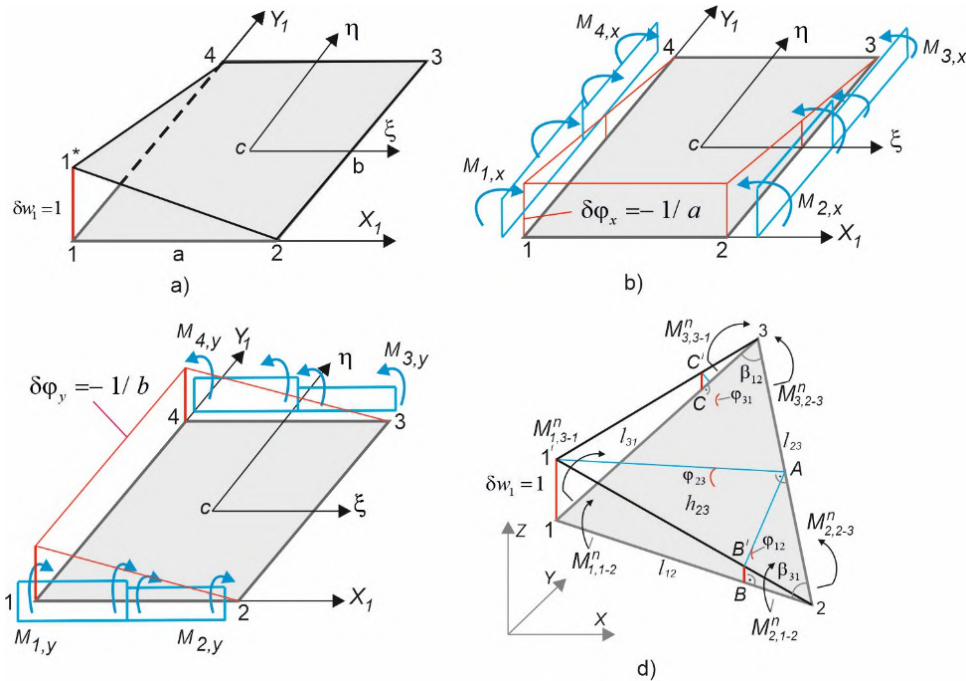


Figure 2. Possible of the node displacements:
a) possible of the node displacement for the rectangular element;
b) rotation angles of the sides which lie along the axis X_1 ;
c) rotation angles of the sides which lie along the axis Y_1 ;
d) possible displacements and rotation angles of the sides of the triangular element.

In Fig. 2 possible displacements of the node are shown. Linear functions are used to represent possible displacements at the finite element region. Therefore, the second derivatives of the possible displacements' functions will be equal to zero. Therefore, the moments which are normal to the finite element boundaries will be to do work on the corresponding rotation angles of the sides. But for a rectangular finite element, additional work will be performed by torques which will be constant over the element region.

Such equilibrium equations for finite element grid nodes are written as the system of linear homogeneous algebraic equations:

$$C_i^T M_{i,eq} = 0, \quad i \in \Xi_z. \tag{12}$$

$M_{i,eq}$ is vector of nodal moments included in the equilibrium equation of node i . The equilibrium equation for a node will include unknown moments for nodes belonging to finite elements which are adjacent to node i . C_i is vector of coefficients at unknowns which are entering the equilibrium equation. In article [24] algorithm and necessary formulas for triangular and rectangular finite elements are presented.

When solving stability problems, at nodes, which are lying on some boundaries of the subject domain, the moment normal to the boundary (13) or the moment directed along boundary (14), or both, can be equal to zero.

$$M_{n,i} = M_{x,i} \cos^2 \alpha_i + M_{y,i} \sin^2 \alpha_i - 2M_{xy,i} \sin \alpha_i \cos \alpha_i = 0. \tag{13}$$

$$M_{ns,i} = (-M_{x,i} + M_{y,i}) \sin \alpha_i \cos \alpha_i + M_{xy,i} (\cos^2 \alpha_i - \sin^2 \alpha_i) = 0. \tag{14}$$

α_i is the angle between the tangent to the boundary at node i and the global axis X ;

Using the Lagrange's multipliers method, we add the equilibrium equations (12) and the static boundary conditions (13–14) to the functional (11):

$$\Pi^c = \frac{1}{2} \mathbf{M}^T \mathbf{D} \mathbf{M} + \sum_{i \in \Omega_z} w_i \mathbf{C}_i^T \mathbf{M}_{i,eq} + \sum_{i \in \Omega_{\Gamma_n}} \varphi_{i,n} M_{n,i} + \sum_{i \in \Omega_{\Gamma_{ns}}} \varphi_{i,s} M_{ns,i}. \quad (15)$$

w_i is displacement of the node i ; $\varphi_{i,n}$, $\varphi_{i,s}$ are the Lagrange multipliers, which are additional nodal unknowns; Ω_z is set of nodes in which the vertical displacement is not equal to zero; Ω_{Γ_n} , $\Omega_{\Gamma_{ns}}$ is the sets of nodes which are lying on the boundary where the corresponding moments are equal to zero.

Expression (15) can be represented in the simpler matrix form:

$$\Pi^c = \frac{1}{2} \mathbf{M}^T \mathbf{D} \mathbf{M} + \mathbf{w}^T \mathbf{L} \mathbf{M}. \quad (16)$$

\mathbf{L} is the "equilibrium" matrix of the whole system nodes. The number of this matrix rows is equal to the sum of number unknown nodal displacements and the number of static boundary conditions (13–14). The vector \mathbf{w} includes unknown nodal displacements and Lagrange multipliers $\varphi_{i,n}$, $\varphi_{i,s}$.

To reduce the number of unknowns, one can use the penalty function method to include static boundary conditions. Then we get the following expression:

$$\Pi^c = \frac{1}{2} \mathbf{M}^T \mathbf{D} \mathbf{M} + \mathbf{w}^T \mathbf{L} \mathbf{M} + \alpha \sum_{i \in \Omega_{\Gamma_n}} M_{n,i}^2 + \alpha \sum_{i \in \Omega_{\Gamma_{ns}}} M_{ns,i}^2. \quad (17)$$

α is a large number, which is penalty parameter. In this case, the terms associated with the penalty functions are added to the elements of the matrix \mathbf{D} . Note that in this case, the matrix remains block-diagonal, and the expression of the functional takes the form (16).

If the boundary of the region is parallel to one of the global coordinate axes, then the static boundary conditions (13–14) can be allowed by excluding the corresponding unknown nodal moments. In further transformations, we will use for functional the expression (16).

As is known [1], when we solve the problem of plates stability it is necessary to consider additional tensile-compression deformities which are arising, when the plate is bending:

$$\varepsilon_{o,x} = \frac{1}{2} \left(\frac{\partial w}{\partial x} \right)^2, \varepsilon_{o,y} = \frac{1}{2} \left(\frac{\partial w}{\partial y} \right)^2, \varepsilon_{o,xy} = \frac{\partial w}{\partial x} \frac{\partial w}{\partial y}. \quad (18)$$

Deformations (18) correspond to the work of internal stresses $\sigma_x, \sigma_y, \sigma_{xy}$ acting in median plane of the plate. To obtain an expression of such work, we consider the rectangular finite element (Fig. 1). The vertical displacements of the plate, when one loss of stability, are represented by linear basis functions:

$$w(x, y) = \sum_{i=1}^4 \frac{(1 + \xi \xi_i)(1 + \eta \eta_i)}{4} \bar{w}_i, \xi = \frac{2x}{a}, \eta = \frac{2y}{b}. \quad (19)$$

\bar{w}_i is displacement of node i . Then we obtain the following expressions for derivatives included in expressions (18):

$$\frac{\partial w}{\partial x} = \sum_{i=1}^4 \frac{\xi_i (1 + \eta \eta_i)}{2a} \bar{w}_i, \frac{\partial w}{\partial y} = \sum_{i=1}^4 \frac{\eta_i (1 + \xi \xi_i)}{2b} \bar{w}_i. \quad (20)$$

The work of stresses $\sigma_x, \sigma_y, \sigma_{xy}$ is expressed by the integral over the finite element area

$$U_{\varepsilon_o}^* = \int_0^a \int_0^b t (\sigma_x \varepsilon_{o,x} + \sigma_y \varepsilon_{o,y} + \sigma_{xy} \varepsilon_{o,xy}) dx dy. \quad (21)$$

In further transformations we will use the vector of unknown nodal displacements \mathbf{w}_k and the vectors $\mathbf{N}_{k,x}$, $\mathbf{N}_{k,y}$ for finite element with index k :

$$\mathbf{w}_k = \begin{Bmatrix} \bar{w}_1 \\ \bar{w}_2 \\ \bar{w}_3 \\ \bar{w}_4 \end{Bmatrix}, \mathbf{N}_{k,x} = \begin{Bmatrix} \frac{\xi_1(1+\eta\eta_1)}{2a} \\ \frac{\xi_2(1+\eta\eta_2)}{2a} \\ \frac{\xi_3(1+\eta\eta_3)}{2a} \\ \frac{\xi_4(1+\eta\eta_4)}{2a} \end{Bmatrix}, \mathbf{N}_{k,y} = \begin{Bmatrix} \frac{\eta_1(1+\xi\xi_1)}{2b} \\ \frac{\eta_2(1+\xi\xi_2)}{2b} \\ \frac{\eta_3(1+\xi\xi_3)}{2b} \\ \frac{\eta_4(1+\xi\xi_4)}{2b} \end{Bmatrix}. \quad (22)$$

Using (22) we obtain the following matrix expressions for strains (18):

$$\varepsilon_{o,x} = \frac{1}{2} \mathbf{w}_k^T (\mathbf{N}_{k,x} \mathbf{N}_{k,x}^T) \mathbf{w}_k, \quad \varepsilon_{o,y} = \frac{1}{2} \mathbf{w}_k^T (\mathbf{N}_{k,y} \mathbf{N}_{k,y}^T) \mathbf{w}_k, \quad \varepsilon_{o,xy} = \mathbf{w}_k^T (\mathbf{N}_{k,x} \mathbf{N}_{k,y}^T) \mathbf{w}_k. \quad (23)$$

Next, we obtain the expression for the work of stresses $\sigma_x, \sigma_y, \sigma_{xy}$:

$$U_{\varepsilon_o}^* = \frac{abt}{4} \int_{-1}^1 \int_{-1}^1 t \left(\frac{1}{2} \sigma_x \mathbf{w}_k^T (\mathbf{N}_{k,x} \mathbf{N}_{k,x}^T) \mathbf{w}_k + \frac{1}{2} \sigma_y \mathbf{w}_k^T (\mathbf{N}_{k,y} \mathbf{N}_{k,y}^T) \mathbf{w}_k + \sigma_{xy} \mathbf{w}_k^T (\mathbf{N}_{k,x} \mathbf{N}_{k,y}^T) \mathbf{w}_k \right) d\xi d\eta. \quad (24)$$

To simplify we introduce the notation for the following matrices:

$$\mathbf{H}_{k,x} = \frac{abt}{4} \int_{-1}^1 \int_{-1}^1 \sigma_x \mathbf{N}_{k,x} \mathbf{N}_{k,x}^T d\xi d\eta, \quad \mathbf{H}_{k,y} = \frac{abt}{4} \int_{-1}^1 \int_{-1}^1 \sigma_y \mathbf{N}_{k,y} \mathbf{N}_{k,y}^T d\xi d\eta, \quad (25)$$

$$\mathbf{H}_{k,xy} = \frac{abt}{4} \int_{-1}^1 \int_{-1}^1 \sigma_{xy} \mathbf{N}_{k,x} \mathbf{N}_{k,y}^T d\xi d\eta.$$

After integration, we obtain the following expressions for matrix elements:

$$\mathbf{H}_{k,x} = \frac{\sigma_x bt}{6a} \begin{bmatrix} 2 & -2 & -1 & 1 \\ -2 & 2 & 1 & -1 \\ -1 & 1 & 2 & -2 \\ 1 & -1 & -2 & 2 \end{bmatrix}, \mathbf{H}_{k,y} = \frac{\sigma_y at}{6b} \begin{bmatrix} 2 & 1 & -1 & -2 \\ 1 & 2 & -2 & -1 \\ -1 & -2 & 2 & 1 \\ -2 & -1 & 1 & 2 \end{bmatrix}, \mathbf{H}_{k,xy} = \frac{\sigma_{xy} t}{4} \begin{bmatrix} 1 & 1 & -1 & -1 \\ -1 & -1 & 1 & 1 \\ -1 & -1 & 1 & 1 \\ 1 & 1 & -1 & -1 \end{bmatrix}. \quad (26)$$

$$U_{\varepsilon_o}^* = \frac{1}{2} \mathbf{w}_k^T (\mathbf{H}_{k,x} + \mathbf{H}_{k,y}) \mathbf{w}_k + \mathbf{w}_k^T \mathbf{H}_{k,xy} \mathbf{w}_k. \quad (27)$$

Calculating the derivative of additional energy, we obtain:

$$\mathbf{H}_k = \frac{dU_{\varepsilon_o}^*}{d\mathbf{w}_k} = (\mathbf{H}_{k,x} + \mathbf{H}_{k,y} + \mathbf{H}'_{k,xy}) \mathbf{w}_k, \quad \mathbf{H}'_{k,xy} = \frac{\sigma_{xy} t}{2} \begin{bmatrix} 1 & 0 & -1 & 0 \\ 0 & -1 & 0 & 1 \\ -1 & 0 & 1 & 0 \\ 0 & 1 & 0 & -1 \end{bmatrix}. \quad (28)$$

From geometric matrices of finite elements \mathbf{H}_k , the global geometric matrix \mathbf{H} is formed for entire system, and from vectors \mathbf{w}_k is formed the global vector of nodal displacements \mathbf{w} .

Using the notation introduced, we obtain the matrix expression for the work of internal stresses acting in the plate middle plane

$$U_{\varepsilon_o}^* = \frac{1}{2} \mathbf{w}^T \mathbf{H} \mathbf{w}. \quad (29)$$

Next, we obtain expressions of geometric matrices for a triangular finite element. The vertical displacement function for the triangular finite element of the plate is represented using the triangular coordinates:

$$w(x, y) = \sum_{i=1}^3 L_i(x, y) \bar{w}_i, \quad L_i(x, y) = \frac{1}{2A} (a_i + b_i x + c_i y), \quad (30)$$

$$a_i = x_{i+1}y_{i+2} - x_{i+2}y_{i+1}, \quad b_i = y_{i+1} - y_{i+2}, \quad c_i = x_{i+2} - x_{i+1}.$$

x_i, y_i is coordinates of the nodes of the finite element in the global coordinate system; \bar{w}_i is vertical displacement of the node; A is area of the finite element. The partial derivatives of the displacement functions (30) will be constant functions:

$$\frac{\partial w}{\partial x} = \frac{1}{2A} \sum_{i=1}^3 b_i \bar{w}_i, \quad \frac{\partial w}{\partial y} = \frac{1}{2A} \sum_{i=1}^3 c_i \bar{w}_i. \quad (31)$$

Vectors like (22) will have the following view:

$$\mathbf{w}_k = \begin{Bmatrix} \bar{w}_1 \\ \bar{w}_2 \\ \bar{w}_3 \end{Bmatrix}, \quad \mathbf{N}_{k,x} = \frac{1}{A} \begin{Bmatrix} b_1 \\ b_2 \\ b_3 \end{Bmatrix}, \quad \mathbf{N}_{k,y} = \frac{1}{A} \begin{Bmatrix} c_1 \\ c_2 \\ c_3 \end{Bmatrix}. \quad (32)$$

The stresses work in this case is calculated as an integral over the triangle area:

$$U_{\varepsilon_o}^* = \int_A t (\sigma_x \varepsilon_{o,x} + \sigma_y \varepsilon_{o,y} + \sigma_{xy} \varepsilon_{o,xy}) dA. \quad (33)$$

Substituting expressions for deformations (18) in (33), we obtain expressions for the geometric matrices' elements of the triangular finite element (which are like the matrices (25)):

$$\mathbf{H}_{k,x} = \frac{\sigma_x t}{4A} \begin{bmatrix} b_1^2 & b_1 b_2 & b_1 b_3 \\ b_1 b_2 & b_2^2 & b_2 b_3 \\ b_1 b_3 & b_2 b_3 & b_3^2 \end{bmatrix}, \quad \mathbf{H}_{k,y} = \frac{\sigma_y t}{4A} \begin{bmatrix} c_1^2 & c_1 c_2 & c_1 c_3 \\ c_1 c_2 & c_2^2 & c_2 c_3 \\ c_1 c_3 & c_2 c_3 & c_3^2 \end{bmatrix}, \quad \mathbf{H}_{k,xy} = \frac{\sigma_{xy} t}{4A} \begin{bmatrix} b_1 c_1 & b_1 c_2 & b_1 c_3 \\ b_2 c_1 & b_2 c_2 & b_2 c_3 \\ b_3 c_1 & b_3 c_2 & b_3 c_3 \end{bmatrix}. \quad (34)$$

Calculating the derivative of additional energy $U_{\varepsilon_o}^*$, we obtain:

$$\mathbf{H}_k = \frac{dU_{\varepsilon_o}^*}{d\mathbf{w}_k} = (\mathbf{H}_{k,x} + \mathbf{H}_{k,y} + \mathbf{H}'_{k,xy}) \mathbf{w}_k, \quad \mathbf{H}'_{k,xy} = \frac{\sigma_{xy} t}{4A} \begin{bmatrix} 2b_1 c_1 & b_1 c_2 + b_2 c_1 & b_1 c_3 + b_3 c_1 \\ b_1 c_2 + b_2 c_1 & 2b_2 c_2 & b_2 c_3 + b_3 c_2 \\ b_1 c_3 + b_3 c_1 & b_2 c_3 + b_3 c_2 & 2b_3 c_3 \end{bmatrix}. \quad (35)$$

Thus, to solve the stability problems of Kirchhoff plates, it is necessary to add to the functional (16) the work of internal stresses acting in the middle plane which is multiplied by the critical load parameter λ_{cr} . Summing up (16) and (29), we obtain the following functional for solving the plate stability problem:

$$\Pi^c = \frac{1}{2} \mathbf{M}^T \mathbf{D} \mathbf{M} + \mathbf{w}^T \mathbf{L} \mathbf{M} + \frac{\lambda_{cr}}{2} \mathbf{w}^T \mathbf{H} \mathbf{w}. \quad (36)$$

To obtain solving equations, we equate to zero derivatives (36) with respect to the vectors \mathbf{M} and \mathbf{w} :

$$\begin{aligned} \mathbf{D} \mathbf{M} + \mathbf{L}^T \mathbf{w} &= 0, \\ \mathbf{L} \mathbf{M} + \lambda_{cr} \mathbf{H} \mathbf{w} &= 0. \end{aligned} \quad (37)$$

Expressing the vector from the first equation and substituting it into the second equation, we obtain:

$$\mathbf{L} \mathbf{D}^{-1} \mathbf{L}^T \mathbf{w} - \lambda_{cr} \mathbf{H} \mathbf{w} = 0. \quad (38)$$

We introduce the notation for the product of matrices:

$$\mathbf{K} = \mathbf{L} \mathbf{D}^{-1} \mathbf{L}^T. \quad (39)$$

Using (39), we obtain the algebraic equations system for determining the critical parameter λ_{cr} :

$$\mathbf{K} \mathbf{w} = \lambda_{cr} \mathbf{H} \mathbf{w}. \quad (40)$$

As noted above, the matrix \mathbf{D} is block-diagonal form and is easily reversible analytically. The matrix \mathbf{D}^{-1} will also be block-diagonal form, therefore, the matrix \mathbf{K} is a sparse structure of nonzero elements, which significantly reduces the computational cost of solving the equations system. To calculate the elements of the matrix \mathbf{K} , you can use special algorithm to reduce the computational operations number for its formation.

To determine the critical value of the parameter, we apply the well-known reverse iterations method, which includes the following steps:

$$\left. \begin{aligned} & \text{set the vector } \mathbf{w}_0, i = 0; \\ & \text{cycle } i = i + 1; \\ & \mathbf{K}\mathbf{w}_i = \mathbf{H}\mathbf{w}_{i-1}; \\ & w_{\max} = \max |w_{i,j}|, j = 1..n; \\ & \lambda_{cr,i} = \frac{1}{w_{\max}}; \\ & \mathbf{w}_i = \frac{1}{w_{\max}} \mathbf{w}_i; \\ & \mathbf{w}_i = \frac{\mathbf{w}_i + \mathbf{w}_{i-1}}{2}; \\ & \text{cycle end, if } \frac{|\lambda_{cr,i} - \lambda_{cr,i-1}|}{\lambda_{cr,i}} \leq \varepsilon. \end{aligned} \right\} \quad (41)$$

In (41), w_{\max} is the maximum element of the nodal displacements vector \mathbf{w}_i by modulus. Parameter ε determines the calculation accuracy of the critical parameter.

3. Results and Discussion

In [27], analytical solutions are given for the Kirchhoff plates stability problems with different supporting conditions. For comparison with analytical solutions, calculations were carried out to determine the critical stresses σ_x for the hinged plates shown in Fig. 3. The calculations were performed for grids consisting of rectangular and triangular finite elements (see Fig. 3).

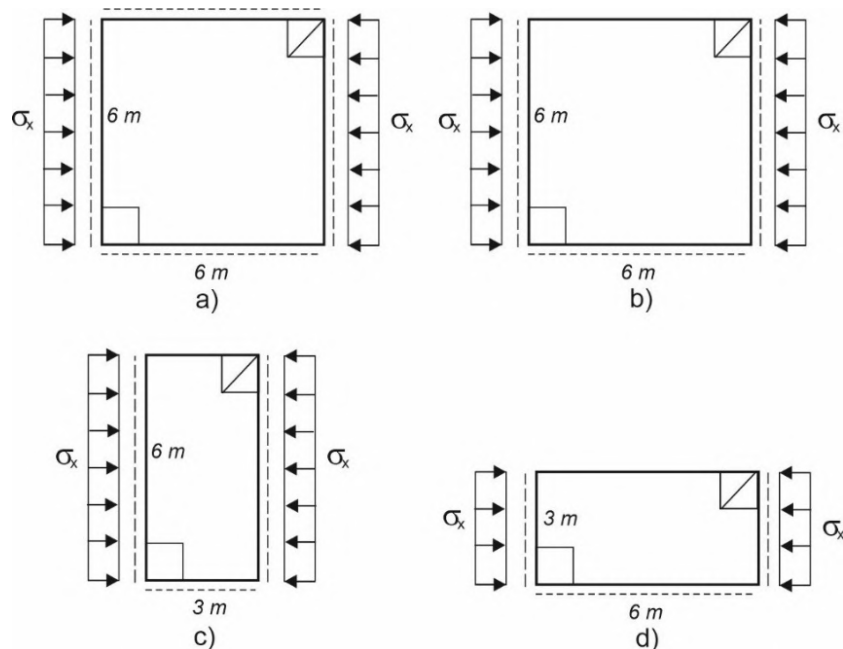


Figure 3. Hinged plates under the action of compressive load along the X axis:
a) square hinged-supported plate on all sides; b) square plate hinged-supported on three sides;
c) rectangular plate hinged-supported on three sides and the short side is free;
d) a rectangular plate hinged-supported on three sides and the long side is free.

In the calculations, the following parameters were taken for the plate: $t = 1\text{ m}$, $E = 10\text{ kN} / \text{m}^2$, $\mu = 0.3$. The hinged-supported sides of the plates are indicated by dashed line in Fig. 3. In the nodes, lying on the hinged-supported sides, moments directed perpendicular to this side were taken zero. In the nodes lying on the free side, also torques were taken zero. Tables 1–4 show the critical stress values σ_x calculated by the proposed methodology (SFEM), using the LIRA-SAPR program and obtained analytically [27].

Table 1. The critical stress $\sigma_x, \text{kN} / \text{m}^2$ for the plate in Fig. 3a.

Grid	SFEM		LIRA-SAPR	
	□	△	□	△
10x10	0.97938	0.99845	0.99373	1.01433
20x20	0.99796	1.00270	1.00157	1.00675
30x30	1.00144	1.00353	1.00305	1.00535
40x40	1.00266	1.00383	1.00357	1.00487
[27]	1.00423			

Table 2. The critical stress $\sigma_x, \text{kN} / \text{m}^2$ for the plate in Fig. 3b.

Grid	SFEM		LIRA-SAPR	
	□	△	□	△
10x10	0.33991	0.33376	0.35202	0.35360
20x20	0.34703	0.34898	0.35193	0.35231
30x30	0.34890	0.35365	0.35190	0.35207
40x40	0.34975	0.35582	0.35189	0.35199
[27]	0.361525			

Table 3. The critical stress $\sigma_x, \text{kN} / \text{m}^2$ for the plate in Fig. 3c.

Grid	SFEM		LIRA-SAPR	
	□	△	□	△
5x10	1.06470	1.06311	1.09547	1.10081
10x20	1.08211	1.08490	1.09432	1.09538
15x30	1.08660	1.09150	1.09392	1.09436
20x40	1.08859	1.09457	1.09376	1.09404
[27]	1.10465			

Table 4. The critical stress $\sigma_x, \text{kN} / \text{m}^2$ for the plate in Fig. 3d.

Grid	SFEM		LIRA-SAPR	
	□	△	□	△
10x5	1.17417	1.11743	1.33114	1.37259
20x10	1.27265	1.26725	1.33916	1.34975
30x15	1.29980	1.30917	1.34055	1.34504
40x20	1.31193	1.32751	1.34103	1.34259
[27]	1.38584			

In Fig. 4, the data from Tables 1–4 are presented in the form of graphs of the critical compression stress value. The divisions number of the plates long side is shown at the horizontal axis. The divisions number of the short side was half as much.

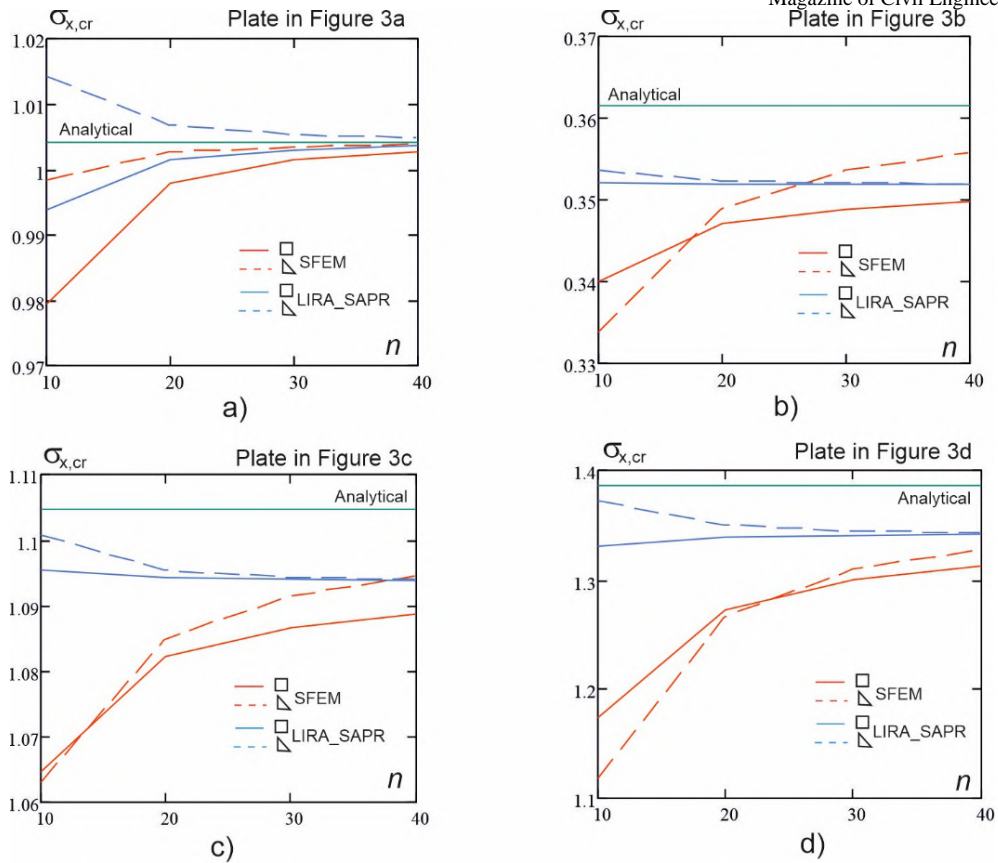


Figure 4. Graphs of the critical stress dependence on the divisions number of the plates long side, which are shown in Figure 3. Red lines are solutions obtained by the proposed SFEM method. Blue lines are LIRA-SAPR solutions. Solid lines are solutions obtained for the grid of rectangular elements. Dotted lines are solutions obtained for the grid of triangular elements. Green lines are analytical solutions [27].

The results show that the critical stresses calculated by the proposed method, when grinding up the finite elements mesh, tend to exact values from below. Thus, the proposed calculation method, based on piecewise constant approximations of the moment functions, provides the lower boundary of critical compressive stresses for the consideration plates. Such results are expected, since it was shown in [24, 25] that, using such approximations to calculate bending plates, we obtain convergence of displacements values to exact magnitudes from above. The proposed finite element model reduces the plate flexural rigidity, compared with the real rigidity, so we get lower values of critical compressive stresses. We also note that for the smallest grids, the critical stresses obtained based on the stress approximation for three plate options are closer to the analytical solutions than the solutions using the LIRA-SAPR program. Only for the plate in Fig. 3d the solution obtained by the LIRA-SAPR program is closer to the analytical one. But at the same time, when mesh grinding up the critical stress decreases and the solution moves away from the analytical one (Table 4).

Also, calculations were carried out to determine the critical stresses for plates in which one side is pinched (Fig. 5). The material characteristics were taken to be the same as in the previous example.

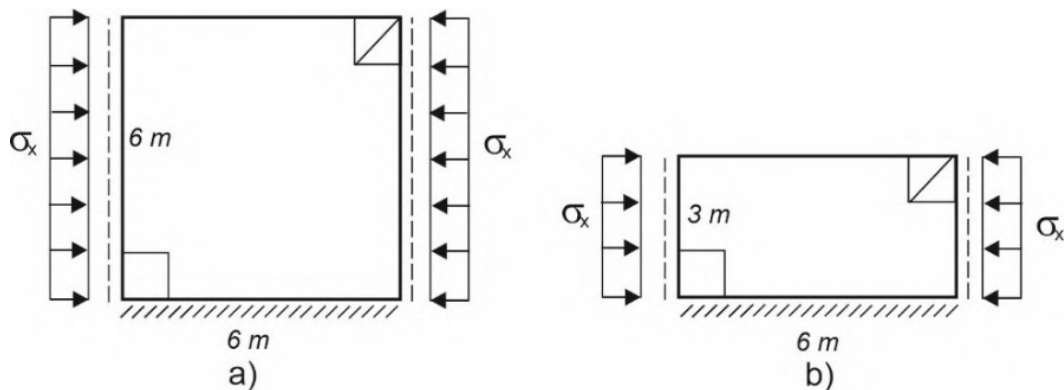


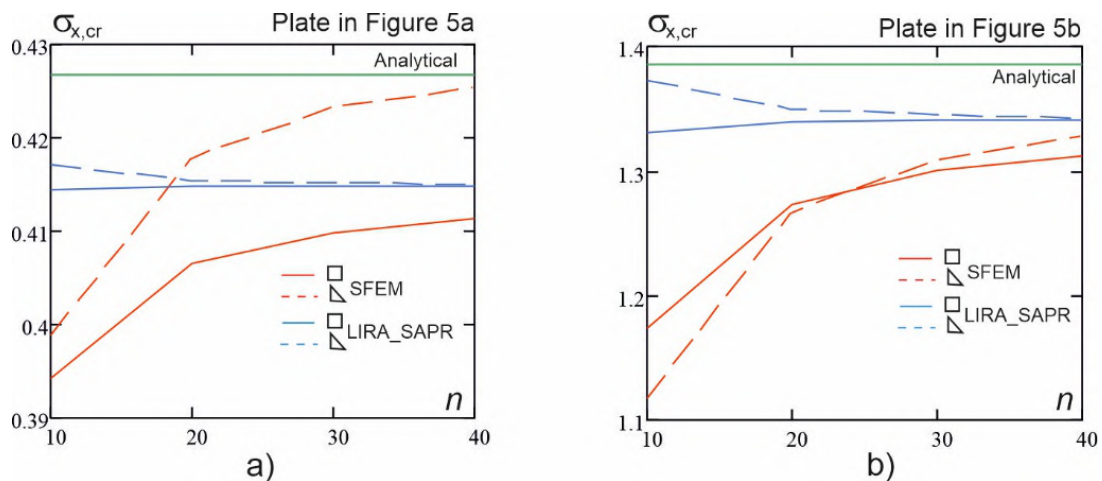
Figure 5. Plates with two hinged support sides and with one pinched side and one free.

Table 5. The critical stress $\sigma_x, kN / m^2$ for the plate in Fig. 5a.

Grid	SFEM		LIRA-SAPR	
	□	△	□	△
10x10	0.39418	0.39879	0.41440	0.41720
20x20	0.40658	0.41798	0.41477	0.41543
30x30	0.40986	0.42321	0.41483	0.41512
40x40	0.41131	0.42545	0.41485	0.41501
[27]	0.42680			

Table 6. The critical stress $\sigma_x, kN / m^2$ for the plate in Fig. 5b.

Grid	SFEM		LIRA-SAPR	
	□	△	□	△
10x10	1.17417	1.11745	1.33114	1.37259
20x20	1.27265	1.26725	1.33916	1.34975
30x30	1.29980	1.30917	1.34055	1.34504
40x40	1.31195	1.32757	1.34103	1.34259
[27]	1.38584			

**Figure 6. Graphs of the critical stress dependencies on the plate long side divisions number (Figure 5).**

The calculation results for the plate with pinched side (Fig. 5) confirm the conclusions which made at discussing the previous example results. The critical stress values obtained by the proposed method (SFEM), when grinding up the finite element mesh, approach the analytical solution from below. This direction of solution convergence provides the critical stress lower boundary. Note that in the proposed method for the displacement approximations in the finite element region, after loss of stability, simple linear functions are used. Therefore, with coarse grids, the critical forces values are calculated with a larger error, compared with the values obtained using the LIRA-SAPR program which uses displacements approximations a higher order. But, as the calculation results show, when we solve using the LIRA-SAPR program which is based on the displacements approximations we do not have a certain direction of approximate solution convergence to the exact one. In some cases, when the mesh of finite elements is refined up, the value of the critical force increases, but in many cases, it decreases (see blue lines in Fig. 4 and Fig. 6).

Also, stability calculations of hinged-supported plates by the tangent stresses action were performed (Fig. 7). The square plate (Fig. 7a) and the plate with one to two aspect ratios (Fig. 7b) were calculated. For the subject area discretization rectangular and triangular grids of finite elements were used. Calculation results comparison with the analytical solutions [27] is presented in Table 7–8 and in Fig. 8.

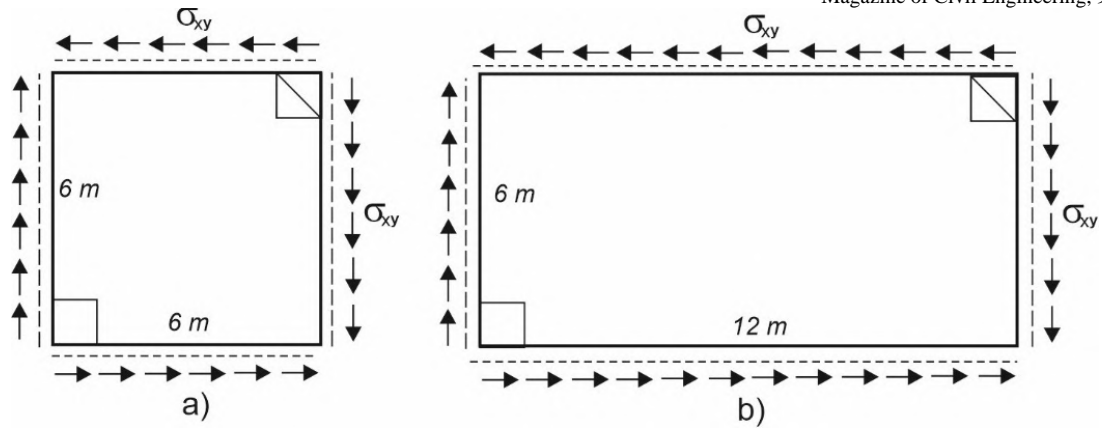


Figure 7. Hinged-supported plates. The action of tangent stresses.

Table 7. The critical stresses $\sigma_{xy}, kN / m^2$ for the plate in Fig. 7a.

Grid	SFEM		LIRA-SAPR	
	□	△	□	△
10x10	2.23904	2.24885	2.27247	2.38643
20x20	2.22525	2.31822	2.32265	2.35250
30x30	2.33737	2.33081	2.33273	2.34610
40x40	2.34287	2.34045	2.35057	2.34368
[27]	2.36497			

Table 8. The critical stresses $\sigma_{xy}, kN / m^2$ for the plate in Fig. 7b.

Grid	SFEM		LIRA-SAPR	
	□	△	□	△
10x6	1.50975	1.56137	1.55895	1.69831
20x12	1.62150	1.63299	1.62299	1.65734
30x16	1.64095	1.64727	1.63322	1.65022
40x40	1.64921	1.65315	1.63753	1.64754
[27]	1.65698			

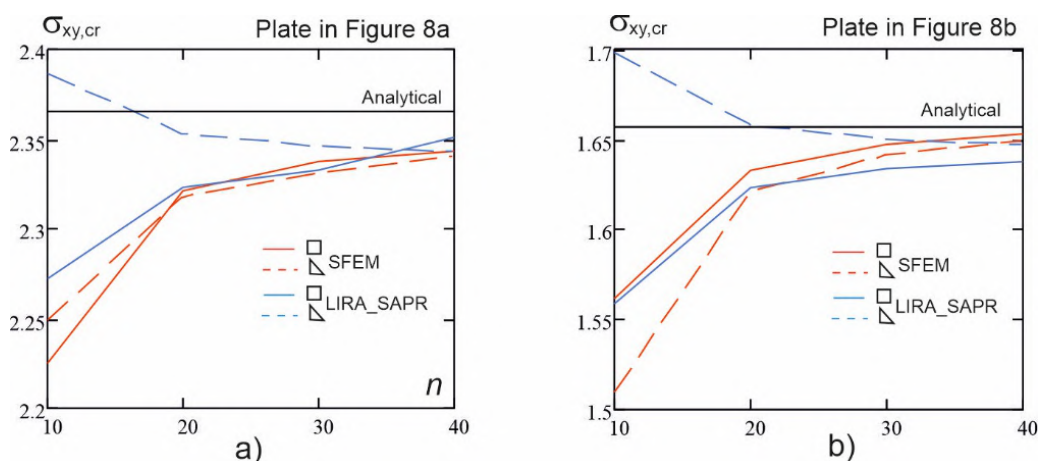


Figure 8. The critical stresses dependence graphs on the number of the long sides divisions of the shown in Figure 7 plates.

The graphs in Fig. 8 shows that the critical tangent stresses values obtained based on the stress approximation (SFEM) tend to analytical values from below when the finite element mesh is refined up. The critical tangent stresses which obtained using the LIRA-SAPR program for the triangular finite elements decrease when mesh is refined up. Thus, approximate solutions which are obtained based on the displacement approximations can converge to the exact solution from different sides.

4. Conclusion

1. The stability analysis method of thin plates, which is based on piecewise constant approximations of the moments, is proposed. The solution is based on the additional energy functional. For the finite element grid nodes, using the principle of possible displacements, algebraic equilibrium equations are formed, which are then added to the functional of additional energy by using Lagrange multipliers.

2. To calculate the work of the stresses acting in the plate median plane, the plate vertical displacements function after stability loss, is represented by linear basis functions. The necessary solving relations for rectangular and triangular finite elements are obtained.

3. According to the proposed method, critical stress calculations were performed for rectangular plates with different supporting conditions. The options for the action of compressive and shear stresses are considered. It is shown, that when the finite element mesh is refining up, the critical stress value in all the considered examples tends to the exact value from below. That direction of the solution convergence provides the lower boundary of the critical stress value.

4. The obtained solutions are compared with the analytical solutions and the solutions obtained by the LIRA-SAPR program. The solutions comparison showed good accuracy in determining critical stresses which are calculated by the proposed method.

References

- Gallagher, R.H. Finite Element Analysis: Fundamentals. Englewood Cliffs, Prentice-Hall, 1975. 420 p.
- Eslami, M.R. Buckling and Postbuckling of Beams, Plates and Shells. New York: Springer, 2018. 588 p.
- Sukhoterina, M.V., Baryshnikov, S.O., Knysh, T.P., Abdikarimov, R.A. Natural oscillations of a rectangular plates with two adjacent edges clamped // Magazine of Civil Engineering. 2018. No. 6(82). Pp. 81–94. DOI: 10.18720/MCE.82.8
- Mirsaidov, M.M., Abdikarimov, R.A., Vatin, N.I., Zhgutov, V.M., Khodzhayev, D.A., Normuminov, B.A. Nonlinear parametric oscillations of viscoelastic plate of variable thickness // Magazine of Civil Engineering. 2018. No. 6(82). Pp. 112–126. DOI: 10.18720/MCE.82.11
- Rybakov, V.A., Lalin, V.V., Ivanov, S.S., Azarov, A.A. Coordinate functions quadratic approximation in V.I. Slivker's semi-shear stability theory // Magazine of Civil Engineering. 2019. No. 5(89). Pp. 115–128. DOI: 10.18720/MCE.89.10
- Le, T., Lalin, V.V., Bratashov, A.A. Static accounting of highest modes in problems of structural dynamics // Magazine of Civil Engineering. 2019. No. 4(88). Pp. 3–13. DOI: 10.18720/MCE.88.1
- Lalin, V.V., Rybakov, V.A., Dyakov, S.F., Kudinov, V.V., Orlova, Ye.S. The semi-shear theory of V.I. Slivker for the stability problems of thin-walled bars // Magazine of Civil Engineering. 2019. No. 3(87). Pp. 66–79. DOI: 10.18720/MCE.87.6
- Tyukalov, Yu.Ya. Refined finite element of rods for stability calculation // Magazine of Civil Engineering. 2018. No. 3(79). Pp. 54–65. DOI: 10.18720/MCE.79.6
- Tyukalov, Yu.Ya. The functional of additional energy for stability analysis of spatial rod systems // Magazine of Civil Engineering. 2017. No. 2(70). Pp. 18–32. DOI: 10.18720/MCE.70.3
- Chen, D., Yang, J., Kitipornchai, S. Buckling and bending analyses of a novel functionally graded porous plate using Chebyshev-Ritz method. Archives of Civil and Mechanical Engineering. 2019. Vol. 19. Pp. 157–170.
- Milazzo, A., Benedetti, I., Gulizzi, V. A single-domain Ritz approach for buckling and post-buckling analysis of cracked plates. International Journal of Solids and Structures. 2019. Vol. 159. Pp. 221–231.
- Vu, Q.-V., Truong, V.-H., Papazafeiropoulos, G., Graciano, C., Kim, S.-E. Bend-buckling strength of steel plates with multiple longitudinal stiffeners. Journal of Constructional Steel Research. 2019. Vol. 158. Pp. 41–52.
- Gajdzicki, M., Perliński, W., Michalak, B. Stability analysis of bi-directionally corrugated steel plates with orthotropic plate model. Engineering Structures. 2018. Vol. 160. Pp. 519–534.
- Le-Manh, T., Huynh-Van, Q., Phan, T., Phan, H., Nguyen-Xuan, H. Isogeometric nonlinear bending and buckling analysis of variable-thickness composite plate structures. Composite Structures. 2017. Vol. 159. Pp. 818–826.
- Wang, X., Yuan, Z. Buckling analysis of isotropic skew plates under general in-plane loads by the modified differential quadrature method. Applied Mathematical Modelling. 2018. Vol. 56. Pp. 83–95.
- Li, S., Hu, Z., Benson, S. An analytical method to predict the buckling and collapse behaviour of plates and stiffened panels under cyclic loading. Engineering Structures. 2019. Vol. 199. Article 109627.
- Ullah, S., Zhong, Y., Zhang, J. Analytical buckling solutions of rectangular thin plates by straightforward generalized integral transform method. International Journal of Mechanical Sciences. 2019. Vol. 152. Pp. 535–544.
- Vescovini, R., Dozio, L., D'Ottavio, M., Polit, O. On the application of the Ritz method to free vibration and buckling analysis of highly anisotropic plates. Composite Structures. 2018. Vol. 192. Pp. 460–474.
- Kamenev, I.V., Semenov, A.A. Ustoychivost plogikh ortotropnykh oblochek dvoyakoy krivizny pri sharnirno-podvizhnom zakreplenii kontura [Stability of shallow orthotropic shells of double curvature during articulated-movable fastening of the contour] // Vestnik Permskogo natsionalnogo issledovatel'skogo politekhnicheskogo universiteta. Mekhanika. 2018. No. 2. Pp. 32–43. (rus) DOI: 10.15593/perm.mech/2018.2.04
- Abdikarimov, R.A., Khudayarov, B. Dynamic stability of viscoelastic flexible plates of variable stiffness under axial compression. International Applied Mechanics. 2014. Vol. 50. Pp. 389–398.
- Abdikarimov, R., Khudayarov, B., Vatin, N.I. To Calculation of Rectangular Plates on Periodic Oscillations. MATEC Web of Conferences. 2018. Vol. 245. 01003.

22. Kuznetsova, Y.S., Vorobyev, N.A., Trufanov, N.A. Application of the geometric immersion method based on the castigliano variational principle for the axisymmetric problems of elasticity theory. IOP Conference Series: Materials Science and Engineering. 2017. Pp. 012125.
23. Goldshteyn, R.V., Popov, A.L., Kozintsev, V.M., Chelyubeyev, D.A. Neosesimmetrichnaya poterya ustoychivosti pri osesimmetrichnom nagreve krugloy plastiny [Axisymmetric buckling during axisymmetric heating of a round plate] // Vestnik Permskogo natsionalnogo issledovatel'skogo politekhnicheskogo universiteta. Mekhanika. 2016. No. 2. Pp. 45–53. (rus) DOI: 10.15593/perm.mech/2016.2.04
24. Tyukalov, Yu.Ya. Finite element models in stresses for bending plates // Magazine of Civil Engineering. 2018. No. 6(82). Pp. 170–190. DOI: 10.18720/MCE.82.16
25. Tyukalov, Yu.Ya. Calculation method of bending plates with assuming shear deformations // Magazine of Civil Engineering. 2019. No. 1(85). Pp. 107–122. DOI: 10.18720/MCE.85.9
26. Tyukalov, Yu.Ya. Finite element models in stresses for plane elasticity problems // Magazine of Civil Engineering. 2018. No. 1(77). Pp. 23–37. DOI: 10.18720/MCE.77.3
27. Timoshenko, S.P. Ustoychivost sterzhney, plastin i obolochek [Stability of rods, plates and shells]. Moskow: Nauka, 1971. 808 p. (rus)

Contacts:

Yury Tyukalov, yutvgu@mail.ru

© Tyukalov Yu.Ya., 2020



DOI: 10.18720/MCE.95.10

Cold-bonded fly ash aggregate concrete

K. Usanova*, **Yu.G. Barabanshchikov**

Peter the Great St. Petersburg Polytechnic University, St. Petersburg, Russia

* E-mail: plml@mail.ru

Keywords: fly ash aggregate, cold bonded fly ash aggregate, pelletized fly ash, granulated fly ash, concrete, cement, lightweight concrete, fly ash, aggregates, concrete mixtures

Abstract. The subject of the experimental research is concrete with cold-bonded fly ash aggregate from fly ash of Novosibirskaya GRES Thermal Power Plant (Novosibirsk, Russia). Cold-bonded fly ash aggregate has the true specific gravity of 2.50 g/cm^3 , an average density of 1.53 g/cm^3 , water absorption by weight of 18.4 %, and an opened porosity of 28.15 %. Concrete with cold-bonded fly ash aggregate has a compressive strength after 28 days of 37.8 MPa, a flexural strength of 4.9 MPa, a coefficient of linear expansion of $14.8 \cdot 10^{-6} \text{ K}^{-1}$ and modulus of elasticity of $18 \cdot 10^9 \text{ Pa}$. The water presoaking of lightweight aggregate did not affect the kinetics of heat emission and, consequently, the kinetics of hydration of cement. The shrinkage of concrete with dry aggregate was higher than concrete with presoaking lightweight aggregate. Moreover, the evaporation loss was also less for concrete with dry aggregate. The shrinkage of concrete with presoaking aggregates is much less than the shrinkage of concrete with dry aggregates with the same evaporation loss. The usefulness of presoaking aggregates in working conditions, as “internal curing”, has been confirmed. This will reduce the likelihood of shrinkage cracks during concrete drying.

1. Introduction

One of the focus areas of processing ash and slag waste from thermal power plants is their use as raw materials for concrete, as well as for the production of artificial aggregates. The use of ash and slag waste in concrete technology is relevant due to the lack of natural aggregates such as gravel and crushed stone as well as the depletion of their deposits. And also, this reduces contamination of the environment.

One of the valuable components of ash and slag waste is fly ash, used in particular in the form of artificial aggregate (granules and pellets), as aggregate for concrete.

Fly ash aggregates are synthesized in two ways. The first one is the pelletization of fly ash, followed by a sintering fresh aggregate pellets at high temperatures in furnaces (sintered fly ash aggregates). The second one is the cold bonding pelletization of fly ash through moistening in a revolving tilted pan (cold-bonded fly ash aggregates).

Cold-bonded fly ash aggregate was investigated for high-performance concrete, self-compacting concrete, and lightweight concrete.

The combined use of sintered fly ash aggregate and cold-bonded fly ash aggregate in the concrete mix is considered in the study [1]. Studies [2–5] investigated the differences between properties of the lightweight concretes including either cold-bonded or sintered fly ash aggregates.

The results of studies of cold-bonded fly ash aggregate concretes are presented in [6–15], [16–24].

The results of studies of sintered fly ash aggregate concretes are presented in [25–43].

Some of the above reviewed articles use silica fume [4, 19, 23, 24, 28, 41], nanosilica [9], superplasticizer [14, 28, 41]. Also in [44, 45] steel fiber or polypropylene fiber is added to the concrete mix with fly ash lightweight aggregates.

The workability of the concrete mixture was studied in researches [1, 11, 14, 16, 21, 27, 41, 43].

The concrete properties discussed in the articles are shown in Table 1.

Usanova, K., Barabanshchikov, Yu.G. Cold-bonded fly ash aggregate concrete. Magazine of Civil Engineering. 2020. 95(3). Pp. 104–118. DOI: 10.18720/MCE.95.10



This work is licensed under a [CC BY-NC 4.0](https://creativecommons.org/licenses/by-nc/4.0/)

Table 1. The concrete properties discussed in the articles.

Concrete property	Link to article
compressive strength	[2–4, 6, 7, 9–13, 15–17, 19–24, 26–38, 40, 41, 43]
split tensile strength	[7, 12, 13, 19, 22–24, 27, 29, 32, 36, 38, 40, 43]
flexural tensile strength	[13, 24, 29, 30, 32, 36, 43]
freeze-thaw resistance	[2, 38]
water penetration	[2, 9, 28, 32]
modulus of elasticity	[2, 12, 13, 22–24, 27, 29, 36, 38, 40]
long time performance	[4, 33]
water absorption	[4, 11, 17, 43]
gas permeability	[4, 6, 9]
chloride ion permeability	[4, 6, 27, 32, 38, 39]
corrosion resistance	[4]
porosity	[17]
bond between concrete and steel	[18, 19]
drying shrinkage	[7, 20, 22, 23, 29, 33, 36, 41]
creep	[22–24]

We have done a more detailed review in [46]. Two new works have been published since the publication of this review. One of them studies the concrete mixture and properties of cold-bonded fly ash aggregate concretes [47] and the second one studies the strength assessment of fly ash lightweight aggregate concretes [48].

During the extensive studies in recent years, the basic properties of fly ash lightweight aggregate concretes were researched. The influence of the addition of fiber, superplasticizers, silica fume, and nanosilica on the characteristics of concrete mixtures and concretes was revealed. Besides, mathematical models for mechanical properties of concrete have been obtained. These models are based on empirical data, such as the modified Bolomey equation and regression dependencies. However, the reviewed papers contain no strong theory for the formation of the basic properties of such concretes depending on the design formula, which allows predicting properties in a wide range of variable parameters of the matrix and concrete aggregates.

We did not find studies on the heat of concrete hardening and studies on water presoaking lightweight aggregate concrete.

This provides a strong reason for further research.

The subject of our further research is cold-bonded fly ash aggregate concrete made from fly ash of Novosibirskaya GRES Thermal Power Plant (Novosibirsk, Russia).

The goal of the research is the development of lightweight concrete formulations based on porous aggregate which is cold-bonded fly ash aggregate and cementitious binder. Moreover, the results will be generalized to the application of fly ash from different combined heat power plants and thermal power plants.

The objectives of the work are:

1. Experimental studies of cold-bonded fly ash lightweight aggregate concretes (true specific gravity, average density, water absorption, opened porosity and other characteristics).
2. Experimental studies of mechanical properties of cold-bonded fly ash lightweight aggregate concretes (compressive strength, flexural strength, the coefficient of linear expansion, and modulus of elasticity).
3. Comparison kinetics of heat emission, kinetics of cement's hydration for concrete mixture with water presoaking lightweight aggregates, and with the dry ones.
4. A comparison deformation of shrinkage for concrete mixture with water presoaking lightweight aggregates and with dry ones.
5. Development of proposals for the use of presoaking cold-bonded fly ash aggregate in the concrete mix.

2. Materials and Methods

2.1. Testing laboratory

Fly ash aggregates were tested in Polytech-SKiM-Test laboratory of Peter the Great St. Petersburg Polytechnic University (Russia).

2.2. Concrete materials

For the production of concrete, the following materials were used:

Cement. Portland cement CEM I 42,5N manufactured by Heidelbergcement from Slantsev Cement Plant "Cesla" (Russia). Ballast content is not more than 5 %, Blaine fineness is 400 m²/kg, the medium activity of cement at the age of 2 days is 26.2 MPa, normal consistency is 24.6 %.

Fine aggregate. Sand from the Ostrovskoye deposit (Russia). Fineness modulus is 2.17 and true specific gravity is 2.79 g/cm³. Flour and clay particles content is not more than 2.0 %.

According to tests the sand meets the requirements of Russian State Standard GOST 8736-2014 "Sand for construction works. Specifications".

Coarse aggregate. Cold-bonded fly ash aggregate based on fly ash from the Novosibirskaya GRES Thermal Power Plant was made at Ural Federal University (Ekaterinburg, Russia). Pellets have a gray color, a rounded shape, and a rough surface (Fig.1). The content makes up to 99.5 % of granule fractions 5-20 mm, density grade is M900, strength grade is P200, and frost resistance grade is F15.



Figure 1. Cold-bonded fly ash aggregate used in the experiment.

Admixtures. The superplasticizer MC-PowerFlow 2695 manufactured by MC-Bauchemie was used in a mixture. It was used to provide the necessary workability and working life of concrete mix, with the minimum allowable quantity of Portland cement.

Water of mixing. Water meets the requirements of Russian State Standard GOST 23732-2011 "Water for concrete and mortars. Specifications".

2.3. Tests of concrete mix components

2.3.1. Determination of grain size of sand

The test was carried out following Russian State Standard GOST 8735-88 "Sand for construction work. Testing methods". Three sand samples were tested. The test results of the samples are presented in Table 2.

In terms of size composition, sand meets the requirements of Russian State Standard GOST 8736-2014 "Sand for construction works. Specifications". Sand refers to medium-sized sand. Fineness modulus is 2.15 (norm 2-2.5). Grain content larger than 10 mm – 1.06 % (norm ≤5); the content of grains larger than 5 mm – 3.69 % (norm ≤15); total rest on a sieve 0.63 – 37.3 % (norm 30-45); grain content less than 0.16 mm – 11.3 % (norm ≤15).

Table 2. Grain size of sand.

Grid opening size [mm]	10	5	2.5	1.25	0.63	0.315	0.16	0	Total
Residue [g]. Sample 1	47.5	35.9	159.3	259.2	445.3	885.2	504.1	288.1	2624.6
Residue [g]. Sample 2	22.5	95.7	22.5	305.8	698.2	922.2	400.9	301.5	2769.3
Residue [g] Sample 3	14.0	76.6	139.5	323.9	488.8	620.2	551.8	307.7	2522.5
Residue [g]. Average	28.0	69.4	107.1	296.3	544.1	809.2	485.6	299.1	2638.8
Residue [%]	1.06	2.63	4.06	11.23	20.62	30.67	18.40	11.33	100.0
Rest on a sieve [%]		0	4.21	11.66	21.41	31.84	19.11	11.77	100.0
Total rest on sieves [%]		0	4.21	15.87	37.28	69.12	88.23	100.00	215
Undersize [%]		100	95.79	84.13	62.72	30.88	11.77	0.00	-
									Fineness modulus
									2.15

Sand belongs to the sands of medium grain size in terms of fineness modulus.

2.3.2. Determination of average density sand grains

The test was carried out following Russian State Standard GOST 8735-88 "Sand for construction work. Testing methods". Three sand samples were tested. The test results of the samples are presented in Table 3.

Table 3. Average density sand grains.

Sample number	Mass [g]	Volume [cm ³]	Density [kg/m ³]
1	1000.0	379	2639
2	1000.0	385	2597
3	1000.0	388	2577
Average	1000.0	384	2604

The average density of sand grains is 2604 kg/m³.

2.3.3. Determination of the content of flour and clay particles of sand and clay content in lumps

The test was carried out following Russian State Standard GOST 8735-88 "Sand for construction work. Testing methods". Three sand samples were tested. The test results of the samples are presented in Table 4.

Table 4. Flour and clay particles of sand and clay content in lumps.

Sample number	Sample mass before sedimentation [g]	Residue mass after sedimentation [g]	Clay content in lumps [%]	Flour and clay particles content [%]	
				Actual	Norm
1	1000	982.8	Not	1.72	2.0
2	1000	986.2	Not	1.38	
3	1000	985.2	Not	1.48	
Average	1000	984.7	Not	1.53	

In terms of the content of flour and clay particles of sand and clay content in lumps, sand meets the requirements of Russian State Standard GOST 8736-2014 "Sand for construction works. Specifications".

2.3.4. Determination of normal consistency of cement-water paste and cement setting up time

The test was carried out following Russian State Standard GOST 30744-2001 "Cements. Methods of testing with using polyfraction standard sand". Three samples were tested for each type of test. The test results of the samples are presented in Table 5.

Table 5. Normal consistency of cement-water paste and cement setting up time.

Sample number	Normal consistency [%]	cement setting up time [h-min]	
		Initial setting time	Final set
1	25.25	2:55	6:15
2	25.75	2:50	6:30
3	25.25	3:00	6:40
Average	25.40	2:55	6:28

In terms of cement setting up time, cement meets the requirements of European Standard EN 197-1 "Cement – Part 1: Composition, specifications and conformity criteria for common cements".

2.3.5. Determination of sounding of cement

The test was carried out in accordance with Russian State Standard GOST 30744-2001 "Cements. Methods of testing with using polyfraction standard sand". Two samples were tested. The test results of the samples are presented in Table 6.

Table 6. Sounding of cement.

Sample number	Distance between pointers [mm]		Indicator of sounding of cement [mm]
	Before the test	After the test	
1	14	15	1
2	12	12	0
Average			0.5

In terms of indicator of sounding of cement, cement meets the requirements of Russian State Standard GOST 31108-2016 "Common cements. Specifications".

2.3.6. Determination of fineness of cement

The test was carried out following Russian State Standard GOST 30744-2001 "Cements. Methods of testing with using polyfraction standard sand". Three samples were tested. The test results of the samples are presented in Table 7.

Table 7. Fineness of cement.

Sample number	Sample mass [g]		Rest on a sieve No.009 [%]
	Before sieving	After sieving	
1	10.00	8.95	10.5
2	10.00	8.73	12.7
3	10.00	8.81	11.9
Average			11.7

In terms of fineness of cement, cement meets the requirements of Russian State Standard GOST 31108-2016 "Common cements. Specifications".

2.3.7. Determination of flexural strength and ultimate compressive strength of test cement beam

The test was carried out in accordance with Russian State Standard GOST 30744-2001 "Cements. Methods of testing with using polyfraction standard sand".

Specimens with dimensions of 40x40x160 mm were tested at the age of 2 and 28 days. Three specimens used for bending under tension test and six specimens used for the compressive strength test. The test results of the specimens at the age of 2 days are presented in Table 8. The test results of the specimens at the age of 28 days are presented in Table 9.

Table 8. Flexural strength and compressive strength of test cement beam at the age of 2 days.

Specimen number	Flexural strength [MPa]	Compressive strength [MPa]
1	1.94	18.0
2	2.06	19.4
3	2.00	19.0
4	-	18.6
5	-	18.3
6	-	19.4
Average	2.00	18.8

Table 9. Flexural strength and compressive strength of test cement beam at the age of 28 days.

Specimen number	Flexural strength [MPa]	Compressive strength [MPa]
1	5.06	48.2
2	4.95	48.4
3	5.16	49.1
4	-	48.8
5	-	49.0
6	-	48.4
Average	5.06	48.7

This cement meets the requirements of European Standard EN 197-1 "Cement – Part 1: Composition, specifications and conformity criteria for common cements" and refers to strength class 42.5 R.

2.3.8. Assessment of efficiency of superplasticizers

Assessment of efficiency of superplasticizers was carried out on a Southard viscosimeter for the spread of cement-water paste. The admixtures of the Muraplast, Power Floy, Glenium, Sika ViscoCrete series were tested. The most effective admixture was PF2695 produced by MS Bauchemi Russia.

Aggregates in concrete affect the behavior of polycarboxylates. It was for these reasons that the effectiveness of the selected admixtures in a sand-cement mortar with a composition of 1: 3, W/C = 0.50 with the reference sand of the Volsky field (Russia) was tested. The mortar of cement was made following Russian State Standard GOST 30744-2001 "Cements. Polyfraction sand test methods." The admixture was introduced in addition to the total number of components. The effect of the admixtures was assessed by the Hegemann cone flow after 15 drops on a flow table. The measurements were made immediately after the preparation of the mortar mix and after 2 hours. The results of these tests are presented in Table 10.

Table 10. Efficiency of superplasticizers.

Type of admixtures	The content of admixtures in % by mass of cement	spread after 15 shakes [mm]		density, [g/cm ³]	air entrainment [%]
		Right after	After 2 hours		
Power Flow PF-1130	0.9	220	170	2.13	7.4
Muraplast FK-63.30	0.9	245	205	2.06	10.5
Power Flow PF-2695	0.9	235	215	2.40	0
Power Flow 3100	0.9	210	175	2.38	0
Glenium 430	0.9	205	200	2.41	0
Muraplast FK-88	0.9	220	210	1.94	15.5
Power Flow PF-1180	0.9	206	190	2.10	9.0
Sika ViscoCrete 571	0.9	230	200	2.25	5.9

In terms of plasticization of concrete mix, the admixture Power Flow PF-2695 was the most effective according to Table 10. At the same time, this admixture showed a lack of air entrainment. It should be noted that the plasticizing ability of Muraplast FK-63.30 is slightly higher, but this should be attributed to air entrainment, which increases the workability of the concrete mix.

3. Results and Discussion

3.1. Types of tests for cold-bonded fly ash aggregate as an unconventional component of concrete mix

The following tests of the materials used were carried out following Russian State Standard GOST 9758-2012 "Non-organic porous aggregates for construction work. Test methods":

- determination of the true specific gravity of cold-bonded fly ash aggregate;
- hygroscopy of cold-bonded fly ash aggregate;
- water presoaking of aggregate depending on time;
- the average density of cold-bonded fly ash aggregate;
- water absorption of cold-bonded fly ash aggregate by weight and volume;
- the porosity of cold-bonded fly ash aggregate (including open and closed).

3.2. Physical and mechanical properties of cold-bonded fly ash aggregate

We carried out several tests of physical and mechanical properties earlier and published it in [46]. It is re-listed in Table 11 for readability.

Table 11. Physical and mechanical properties of cold-bonded fly ash aggregate.

Characteristics	Units	Values
Size fraction	mm	5-15
Bulk density	kg/m ³	970
Bulk crushing resistance	MPa	6.2
Grading, aggregate size	20 mm	0
	15 mm	4.8
	12.5 mm	26.6
	10 mm	29.7
	5 mm	37.2
	less than 5 mm	1.7
Resistance to freezing and thawing on Russian standard GOST 9758-2012	-	not less than F25

The size fraction of 5-15 mm is a characteristic of cold-bonded fly ash aggregate and it is close to the size fraction in the investigations [24, 28].

The bulk density of 970 kg/m³ corresponds to the grade of density M1000, the bulk crushing resistance of fly ash aggregate of 6.2 MPa corresponds to the grade of the strength of P250 following Russian State Standard GOST 32496-2013 "Fillers porous for light concrete. Specifications".

According to EN 13055:2016 "Lightweight aggregates", the granular material of a mineral origin has a particle density not exceeding 2000 kg/m³ or a loose bulk density not exceeding 1200 kg/m³. Thus, the fly ash aggregate meets the requirements of the European Norm as a lightweight aggregate for concrete.

Cold-bonded fly ash aggregate approximately corresponds to the aggregate in works [6–24] on the size fraction and bulk crushing resistance.

The results of new tests of cold-bonded fly ash aggregate as a coarse aggregate for concrete are presented in Table 12.

Table 12. The test results of cold-bonded fly ash lightweight aggregate.

Characteristics	Units	Values
True specific gravity	kg/m ³	2.50
Hygroscopy	%	8.52
Average density	kg/m ³	1.53
Water absorption by weight	%	18.4
Water absorption by volume	%	28.15
True porosity		38.8
opened	%	28.15
closed		10.65

The true specific gravity of other lightweight coarse aggregates (for example, porous rock crushed stone, furnace clinker, and blast furnace slag, light expanded clay aggregate, expanded perlite aggregate, haydite) is usually 2.6–2.7 g/cm³. Table 12 shows that the true specific gravity of the cold-bonded fly ash aggregate is slightly lower than the listed aggregates. It demonstrates the possibility of creating lightweight concrete with the coarse aggregate as the cold-bonded fly ash aggregate.

The water absorption by weight of the fly ash aggregate is significantly greater than that of other types of traditional aggregates, except for light expanded clay aggregate. This value of expanded clay aggregate varies over a wide range from 8 % to 20 %. Thus, certain types of expanded clay aggregate may have slightly greater water absorption by weight than the fly ash aggregate.

The true porosity of the cold-bonded fly ash aggregate is 38.8 %. Most of the pores are open for access to water. These results show the possibility of using water presoaking lightweight aggregates in concrete, which can lead to a decrease in cracking and shrinkage of concrete during the initial gain in strength.

3.3. Cold-bonded fly ash aggregate concrete mix proportion

Concrete mix proportion was carried out following Russian State Standard GOST 27006-86 "Concretes. Rules for mix proportioning". Two mixes were prepared from the previously listed materials (Table 13) for testing concrete mix and concrete specimens. The peculiarity of preparation of mix No. 2 was water presoaking

fly ash aggregate. In the beginning, mix proportion parameters were determined by calculation. Then the obtained parameters were corrected by the preparation of a trial batch of the concrete mix.

Table 13. Concrete mix proportion.

Materials	Materials consumption [kg / m ³]	
	Mix No. 1	Mix No. 2 (with water presoaking aggregate)
Cement	360	360
Sand	720	720
Cold-bonded fly ash aggregate	780	770
Water	160	180
Superplasticizer MC-PowerFlow 2695	2	2
Total	2022	2032
W / C ratio	0.44	0.50

A section of a 7x7x7 cm cube was made (Fig. 2) to check the distribution of cold-bonded fly ash aggregate over the volume of concrete mix.



Figure 2. A section of the concrete cube after compression test.

It can be seen that cold-bonded fly ash aggregate as a coarse aggregate for concrete was evenly distributed over the volume of the concrete mix.

3.4. Types of testing cold-bonded fly ash aggregate concrete specimens

The following specimens were prepared from four concrete mixes for subsequent tests (Fig. 3): cubes with a size of 7x7x7 cm (mix No. 1, No. 2), beams with a size of 4x4x16 cm (mix No. 1, No. 2), beams with a size of 7x7x28 cm (mix No. 1) and cylindrical specimens in a metal cup (mix No. 1, No. 2).



Figure 3. Cold-bonded fly ash aggregate concrete specimens.

The following tests were made on the products listed above (Table 14).

Table 14. Tests of concrete specimens.

Test type	Specimen	Dimensions [cm]	mix No.	Standard
Compressive strength	Cube	7×7×7	1, 2	GOST 10180-2012
	(at the age of 7, 28, 65 days)			
Flexural strength	Half beam	4×4×8	1	GOST 10180-2012
	Beam	4×4×16	1	GOST 10180-2012
Coefficient of linear expansion	Beam	7×7×28	1	-
Modulus of elasticity	Beam	7×7×28	1	GOST 24452-80
Shrinkage	Beam	4×4×16	1, 2	GOST 24544-81
Heat emission	Cylindrical specimens in a metal cup		1, 2	-

The test results of the concrete specimens are shown below.

3.5. Workability of concrete test results

The workability of concrete was measured in centimeters by the immersion depth in the concrete mixture of the reference cone following Russian State Standard GOST 5802-86 "Mortars. Test methods".

The workability of concrete is shown in Fig. 4a. The maximum mobility of 10.4 cm is achieved in 20 minutes after the addition of water to a concrete mix. The mixture becomes less workable than the original one in 80 minutes after the addition of water to a concrete mix and the hardening of the concrete mixture begins.

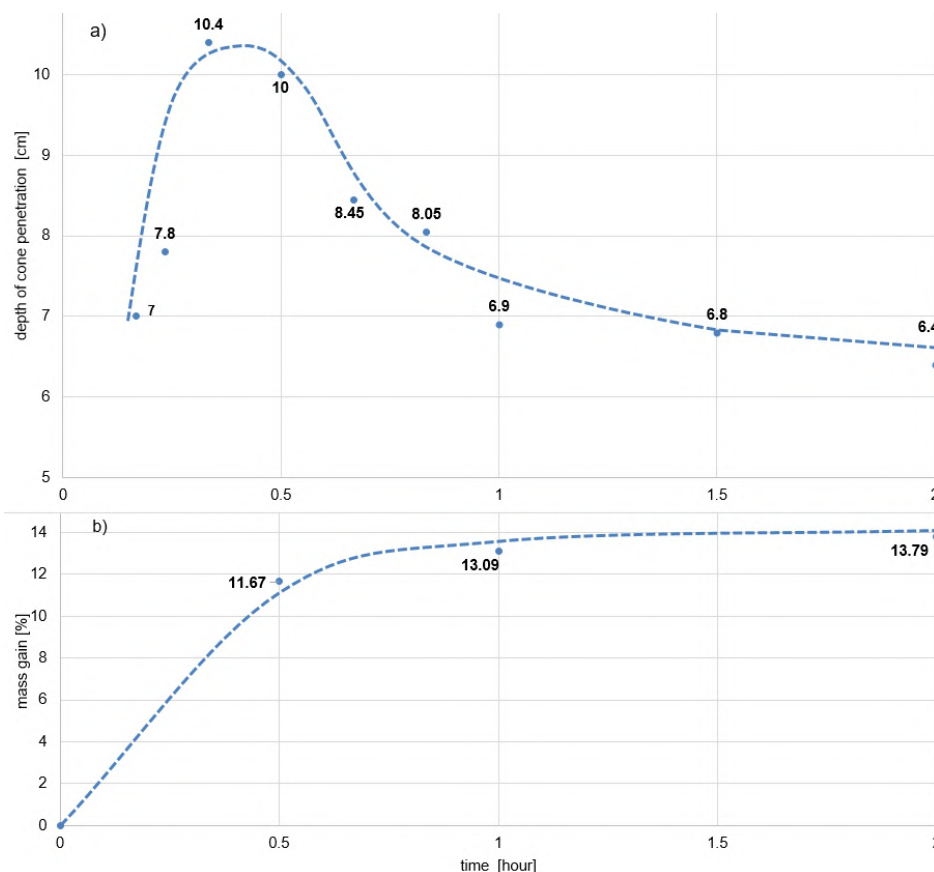


Figure 4. The effect of mixing water absorption by aggregate on the change in workability of concrete over time: a) the change in workability of concrete; b) the aggregate mass gain during water presoaking.

A decrease in the amount of free water in the concrete mixture as a result of water absorption by dry aggregate should lead to a loss of workability. However, from the diagrams in Fig. 4, it can be seen that workability of concrete increases during the first 30 minutes, and only after that workability of concrete begins to decrease. The effect of concrete mixture dilution in the first minutes after creation is typical as a result of using polycarboxylates. In this case, the dilution effect possibly combats the loss of concrete workability from

a decrease in the amount of water which gives workability to the concrete mixture. At the same time, standard test conditions give unlimited access to water during the presoaking of aggregates. For this reason, the absorption of water by aggregate is much faster than how it would be in a competitive environment of concrete mixture, where water interlayers are influenced by the holding forces of the developed surface of cement and sand.

3.6. Concrete specimens test results

3.6.1. Compressive strength

The compressive strength of concrete was determined on cubes with a size of 70.7×70.7×70.7 mm according to Russian State Standard GOST 10180-2012 "Concretes. Methods for strength determination using reference specimens". The test results of the concrete specimens for the compressive strength at the age of 7, 28, and 65 days are presented in Table 15.

Table 15. Compressive strength of concrete specimens.

Age of specimen [days]	Average compressive strength for cubes with a size of 70.7×70.7×70.7 mm [MPa]	Average compressive strength recalculated to the base specimen with a size of 150×150×150 mm [MPa]
7	35.7	30.3
28	44.5	37.8
65	50.1	42.6

The tests did not show a significant difference between the compressive strength of concrete specimens with water presoaking aggregate and the concrete specimens with dry aggregate.

Also, beam halves with a size of 40×40×80 mm were tested according to Russian State Standard GOST 310.4-81 "Cements. Methods of bending and compression strength determination". The compressive strength of these specimens was 40.4 MPa.

The obtained compressive strength after 28 days is usual for lightweight concrete [49] and equivalent to strength grade of concrete C25/30 and allows the use of this concrete as a structural one.

3.6.2. Flexural strength

The flexural strength was determined on beams of a square section with a size of 40×40×160 mm according to Russian State Standard GOST 310.4-81 "Cements. Methods of bending and compression strength determination". The flexural strength was 4.9 MPa.

3.6.3. Coefficient of linear expansion

The coefficient of linear expansion was determined on beams of a square section with a size of 70×70×280 mm. The coefficient of linear expansion was $14.8 \cdot 10^{-6} \text{ K}^{-1}$. This value should be used to determine the calculation distance between movement joints in in-situ reinforced concrete structures using this type of concrete.

3.6.4. Modulus of elasticity

The modulus of elasticity was determined according to Russian State Standard GOST 24452-80 "Concretes. Methods of prismatic, compressive strength, modulus of elasticity and Poisson's ratio determination". Beams with a size of 70×70×280 mm (Fig. 5) were tested.



Figure 5. Modulus of elasticity test.

The modulus of elasticity was $18 \cdot 10^9$ Pa according to the test results. It is typical for lightweight aggregate concrete.

Fig. 6 shows the load and unload curves of the test specimen to 40 % of the critical pressure.

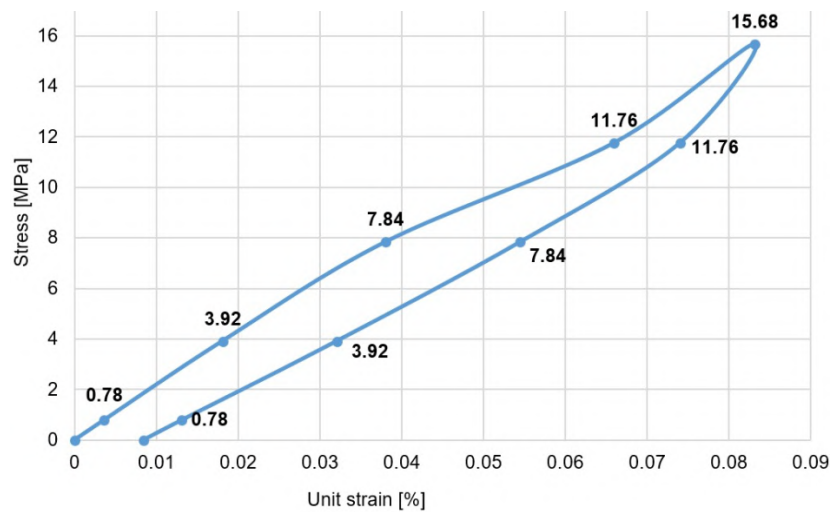


Figure 6. Stress and unit strain of concrete.

It can be seen in Fig. 6 that the unit strain after unloading was about 0.01 %.

3.6.5. Heat emission

The heat emission of concrete was determined by the thermos method at an initial temperature of 20 °C. After that, the heat emission of concrete was recalculated to the isothermal hardening mode at a temperature of 20 °C. Specimens for testing had a cylindrical shape, a volume of 0.5 l. The test was made in an aluminum cup weighing about 15 g.

Two specimens with dry aggregate and two specimens with water presoaking lightweight aggregate were tested. The test results are shown in Fig. 7.

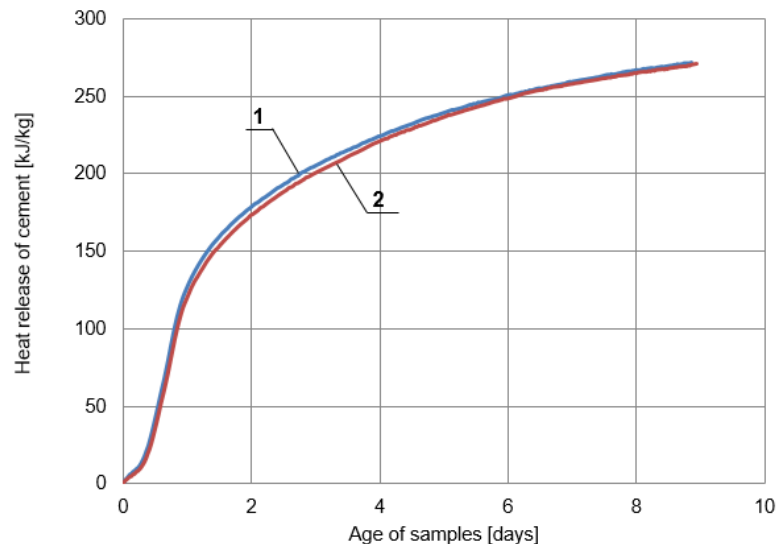


**Figure 7. The cement heat emission per mass in concrete:
1 – with the dry aggregate; 2 – with the water presoaking aggregate.**

As shown in Fig. 7 the presoaking of the aggregate did not affect the kinetics of heat emission and kinetics of hydration of cement.

3.6.6. Shrinkage of concrete

Shrinkage of concrete specimens was determined according to Russian State Standard GOST 24544-81 "Concretes. Methods of shrinkage and creep flow determination". Shrinkage of concrete was determined on specimens with air-dry aggregate (mix No. 1) and specimens with presoaking aggregate (mix No. 2) at a relative air humidity of (60 ± 5) % and a temperature of (20 ± 2) °C. The measuring device is shown in Fig. 8.



Figure 8. Shrinkage test.

The test results are shown in Fig. 9.

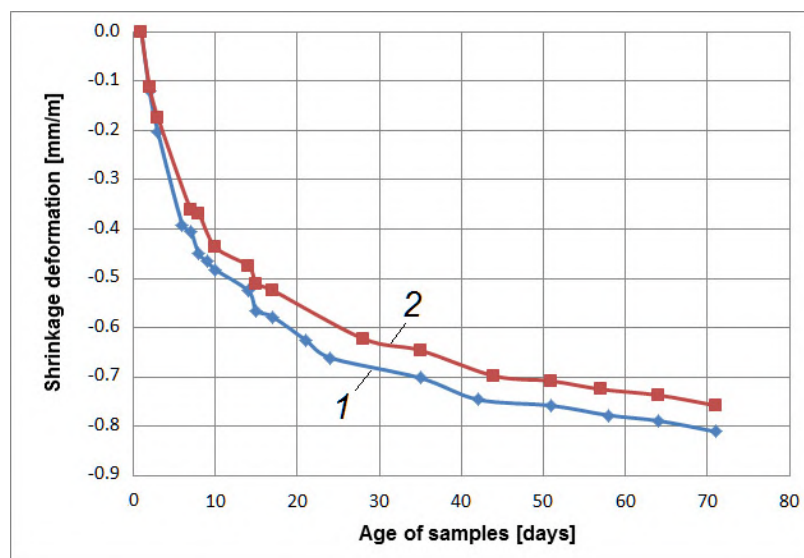


Figure 9. Shrinkage of concrete: 1 – with the dry aggregate (mix No. 1); 2 – with the water presoaking aggregate (mix No. 2).

The shrinkage of concrete with air-dry aggregate was higher than the shrinkage of concrete with presoaking aggregate. The concrete mixes differed only in the presoaking of the coarse aggregate, therefore, it is assumed that the contraction part of the shrinkage is the same for the two mixes, but the difference is dry shrinkage of concrete.

The water-cement ratio of mix No. 2 was equal to 0.5, including the water inside the aggregate. The W/C of mix No. 2 was higher than that W/C of mix No. 1 ($W/C = 0.44$). This is due to the need to obtain equally high-flow concrete mixes because water held in cold-bonded fly ash aggregate has almost no effect on the concrete mix consistency. Dry aggregate partially takes away water from cement stone during the hardening of concrete. Therefore, evaporation loss is not the only contributor to the dehydration of cement stone. Aggregate takes away water and thus shrinkage accelerates. Alternatively, the presoaking fly ash aggregate gives its water to the cement phase, and thus shrinkage decreases. This is a known occurrence and it is called "internal curing of concrete".

It should be expected that the evaporation loss of concrete mix with dry aggregate will be less than of concrete with presoaking aggregate. To verify this assumption, the specimens during the shrinkage test were periodically weighed and mass loss was calculated as a percentage of the initial mass of the specimen (Fig. 10).

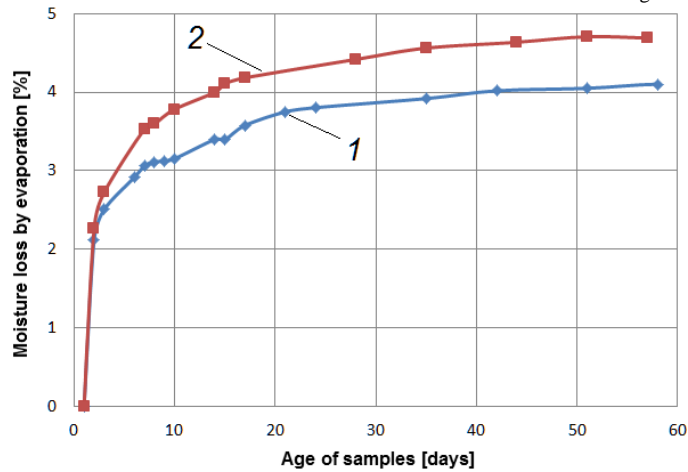


Figure 10. Evaporation loss of concrete mix during hardening in the air at a relative air humidity of $(60 \pm 5) \%$ and a temperature of $(20 \pm 2) ^\circ\text{C}$: 1 – with the dry aggregate (mix No. 1); 2 – with the water presoaking aggregate (mix No. 2).

The shrinkage of concrete in obtained dependency of evaporation loss is presented in the form of experimental curves in Fig. 11.

Two sections A and B with a sharp bend between them can be identified on these curves. The section A shows significant evaporation loss but low shrinkage. The section B shows the opposite results. In Curve 1 section A the evaporation loss is about 2.2 %, and the shrinkage is 0.12 mm/m. In the section B the shrinkage is 0.71 mm/m with almost the same evaporation loss. Many researchers [50] explain this result as follows. The drying shrinkage of the concrete is associated with capillary pressure. This capillary pressure arises with the formation of menisci of the liquid phase in the structure of cement stone. In the initial period of hardening, water fills almost all the free space in concrete (air entrainment is usually not more than 1-2 %). There are no menisci and the shrinkage develops mainly due to contraction. The total volume of the liquid phase, as a single continuum, decreases as water evaporates. At a certain point, this volume reaches a critical value, and the continuum decays while forming numerous menisci. This explains the drastic change in the curve. With a further decrease in the amount of water in concrete, the number of menisci increases, and their radii decrease. This leads to an increase in curvature pressure and the constriction of solid particles by the surface tension of the liquid.

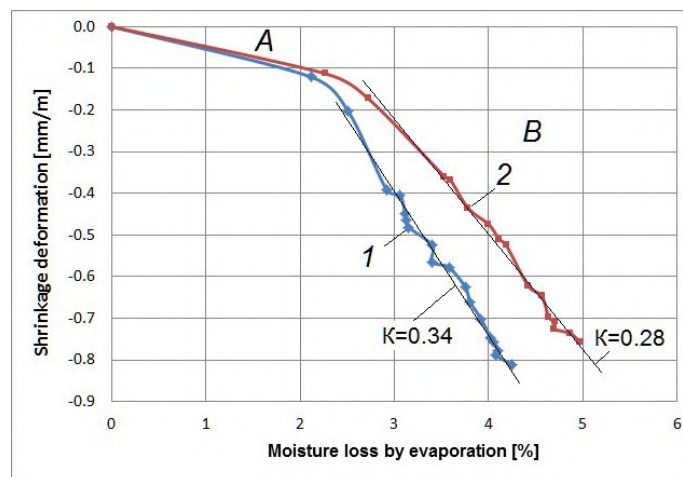


Figure 11. The shrinkage of concrete in dependency of evaporation loss: 1 – with the dry aggregates (mixture No. 1); 2 – with presoaking aggregates (mixture No. 2).

Comparison of curves 1 and 2 in Fig. 11 shows that the shrinkage of concrete with presoaking aggregates is much less than the shrinkage of concrete with dry aggregates while having the same evaporation loss. This result can be used in the working conditions to protect concrete from drying out to prevent shrinkage cracks. Based on the fact that the curves in section B of Fig. 11 are well approximated by a linear dependence, we can propose a convenient characteristic of concrete. This is the coefficient of shrinkage K , which is equal to the derivative of the shrinkage ϵ with respect to the amount of water lost c :

$$K = d\epsilon/dc.$$

In this case, concrete mix No. 2 is more preferable, because it has a smaller value of the coefficient $K = 0.28$, compared to $K = 0.34$ for concrete mix No. 1.

4. Conclusions

A brief review of publications on this topic was made. The characteristics of the fly ash aggregate from the Novosibirskaya GRES Thermal Power Plant were investigated. The characteristics of concrete mixture and concrete with cold-bonded fly ash aggregate were also investigated.

Based on the results obtained, the following conclusions can be underlined:

1. The results of a literature review show the possibility of using cold-bonded fly ash aggregate for structural concrete.
2. The accumulated experimental data is not sufficient to develop a strong theory or dependencies to predict the mechanical properties in a wide class of structural concretes. The existing attempts to derive the calculated dependencies are similar to the development of approximations (regression analysis) or the refinement of the coefficients for the Bolomey equation.
3. Cold-bonded fly ash aggregate has the true specific gravity of 2.50 g/cm^3 , an average density of 1.53 g/cm^3 , water absorption by weight of 18.4 % and an opened porosity of 28.15 %;
4. Concrete with cold-bonded fly ash aggregate has a compressive strength after 28 days of 37.8 MPa, a flexural strength of 4.9 MPa, a coefficient of linear expansion of $14.8 \cdot 10^{-6} \text{ K}^{-1}$ and a modulus of elasticity of $18 \cdot 10^9 \text{ Pa}$;
5. The water presoaking of lightweight aggregate did not affect the kinetics of heat emission and, consequently, the kinetics of hydration of cement;
6. The shrinkage of concrete with dry aggregate was higher than of concrete with presoaking lightweight aggregate. Moreover, the evaporation loss was also less for concrete with dry aggregate. The shrinkage of concrete with presoaking aggregates is much less than the shrinkage of concrete with dry aggregates while having the same evaporation loss.
7. The usefulness of presoaking aggregates in working conditions, as "internal curing", has been confirmed. This will reduce the likelihood of shrinkage cracks during concrete drying.

5. Acknowledgement

The authors would like to express their sincere thanks to Andrey I. Kalachev, Alexander V. Ukhanov, and ProfCement-Vector company for the given samples of cold-bonded lightweight fly ash aggregates.

References

1. Kumar, P.P., Rama Mohan Rao, P. Packing density of self compacting concrete using normal and lightweight aggregates. 2017. International Journal of Civil Engineering and Technology. 8 (4). Pp. 1156–1166.
2. Kockal, N.U., Ozturan, T. Durability of lightweight concretes with lightweight fly ash aggregates. 2011. Construction and Building Materials. 25 (3). Pp. 1430–1438. DOI: 10.1016/j.conbuildmat.2010.09.022
3. Gomathi, P., Sivakumar, A. Accelerated curing effects on the mechanical performance of cold bonded and sintered fly ash aggregate concrete. 2015. Construction and Building Materials. 77. Pp. 276–287. DOI: 10.1016/j.conbuildmat.2014.12.108
4. Güneyisi, E., Gesoğlu, M., Pürsünlü, Ö., Mermerdaş, K. Durability aspect of concretes composed of cold bonded and sintered fly ash lightweight aggregates. 2013. Composites Part B: Engineering. 53. Pp. 258–266. DOI: 10.1016/j.compositesb.2013.04.070
5. Kirubakaran, D., Joseravindraraaj, B. Utilization of pelletized fly ash aggregate to replace the natural aggregate: A review. 2018. International Journal of Civil Engineering and Technology. 9 (8). Pp. 147–154.
6. Gesoğlu, M., Güneyisi, E., Ali, B., Mermerdaş, K. Strength and transport properties of steam cured and water cured lightweight aggregate concretes. 2013. Construction and Building Materials. 49. Pp. 417–424. DOI: 10.1016/j.conbuildmat.2013.08.042
7. Kockal, N.U., Ozturan, T. Strength and elastic properties of structural lightweight concretes. 2011. Materials and Design. 32 (4). Pp. 2396–2403. DOI: 10.1016/j.matdes.2010.12.053
8. Kockal, N.U., Ozturan, T. Properties of lightweight concretes made from lightweight fly ash aggregates. 2009. Excellence in Concrete Construction through Innovation – Proceedings of the International Conference on Concrete Construction. Pp. 251–261.
9. Their, J.M., Özakaça, M. Developing geopolymers concrete by using cold-bonded fly ash aggregate, nano-silica, and steel fiber. 2018. Construction and Building Materials. 180. Pp. 12–22. DOI: 10.1016/j.conbuildmat.2018.05.274
10. Narattha, C., Chaipanich, A. Phase characterizations, physical properties and strength of environment-friendly cold-bonded fly ash lightweight aggregates. 2018. Journal of Cleaner Production. 171. Pp. 1094–1100. DOI: 10.1016/j.jclepro.2017.09.259
11. Venkata Suresh, G., Pavan Kumar Reddy, P., Karthikeyan, J. Effect of GGBS and Fly ash aggregates on properties of geopolymers concrete. 2016. Journal of Structural Engineering (India). 43 (5). Pp. 436–444.
12. Thomas, J., Harilal, B. Mechanical properties of cold bonded quarry dust aggregate concrete subjected to elevated temperature. 2016. Construction and Building Materials. 125. Pp. 724–730. DOI: 10.1016/j.conbuildmat.2016.08.093
13. Güneyisi, E., Gesoğlu, M., Özturan, T., Ipek, S. Fracture behavior and mechanical properties of concrete with artificial lightweight aggregate and steel fiber. 2015. Construction and Building Materials. 84. Pp. 156–168. DOI: 10.1016/j.conbuildmat.2015.03.054
14. Gesoğlu, M., Güneyisi, E., Ozturan, T., Oz, H.O., Asaad, D.S. Shear thickening intensity of self-compacting concretes containing rounded lightweight aggregates. 2015. Construction and Building Materials. 79. Pp. 40–47. DOI: 10.1016/j.conbuildmat.2015.01.012
15. Gopi, R., Revathi, V., Kanagaraj, D. Light expanded clay aggregate and fly ash aggregate as self curing agents in self compacting concrete. 2015. Asian Journal of Civil Engineering. 16 (7). Pp. 1025–1035.
16. Gomathi, P., Sivakumar, A. Synthesis of geopolymers based class-F fly ash aggregates and its composite properties in Concrete. 2014. Archives of Civil Engineering. 60 (1). Pp. 55–75. DOI: 10.2478/ace-2014-0003
17. Al Bakri, A.M.M., Kamarudin, H., Binhussain, M., Nizar, I.K., Rafiza, A.R., Zarina, Y. Comparison of geopolymers fly ash and ordinary portland cement to the strength of concrete. 2013. Advanced Science Letters. 19 (12). Pp. 3592–3595. DOI: 10.1166/asl.2013.5187

18. Güneyisi, E., Gesoğlu, M., Ipek, S. Effect of steel fiber addition and aspect ratio on bond strength of cold-bonded fly ash lightweight aggregate concretes. 2013. *Construction and Building Materials*. 47. Pp. 358–365. DOI: 10.1016/j.conbuildmat.2013.05.059
19. Gesoğlu, M., Güneyisi, E., Alzebaree, R., Mermerdaş, K. Effect of silica fume and steel fiber on the mechanical properties of the concretes produced with cold bonded fly ash aggregates. 2013. *Construction and Building Materials*. 40. Pp. 982–990. DOI: 10.1016/j.conbuildmat.2012.11.074
20. Priyadarshini, P., Mohan Ganesh, G., Santhi, A.S. Effect of cold bonded fly ash aggregates on strength & restrained shrinkage properties of concrete. 2012. *IEEE-International Conference on Advances in Engineering, Science and Management, ICAESM-2012*. Pp. 160–164.
21. Joseph, G., Ramamurthy, K. Workability and strength behaviour of concrete with cold-bonded fly ash aggregate. 2009. *Materials and Structures/Materiaux et Constructions*. 42 (2). Pp. 151–160. DOI: 10.1617/s11527-008-9374-x
22. Gesoğlu, M., Özturan, T., Güneyisi, E. Effects of cold-bonded fly ash aggregate properties on the shrinkage cracking of lightweight concretes. 2006. *Cement and Concrete Composites*. 28 (7). Pp. 598–605. DOI: 10.1016/j.cemconcomp.2006.04.002
23. Gesoğlu, M., Özturan, T., Güneyisi, E. Shrinkage cracking of lightweight concrete made with cold-bonded fly ash aggregates. 2004. *Cement and Concrete Research*. 34 (7). Pp. 1121–1130. DOI: 10.1016/j.cemconres.2003.11.024
24. Gesoğlu, M., Özturan, T., Güneyisi, E. Effect of coarse aggregate properties on the ductility of lightweight concretes. 2003. *Role of Cement Science in Sustainable Development – Proceedings of the International Symposium – Celebrating Concrete: People and Practice*. Pp. 537–546.
25. Shivaprasad, K.N., Das, B.B. Effect of Duration of Heat Curing on the Artificially Produced Fly Ash Aggregates. 2018. *IOP Conference Series: Materials Science and Engineering*. 431 (9), doi:10.1088/1757-899X/431/9/092013
26. Rajamane, N.P., Ambily, P.S. Modified Bolomey equation for strengths of lightweight concretes containing fly ash aggregates. 2012. *Magazine of Concrete Research*. 64 (4). Pp. 285–293. DOI: 10.1680/mac.11.00157
27. Dinakar, P. Properties of fly-ash lightweight aggregate concretes. 2013. *Proceedings of Institution of Civil Engineers: Construction Materials*. 166 (3). Pp. 133–140. DOI: 10.1680/coma.11.00046
28. Dash, S., Kar, B., Mukherjee, P.S. Pervious concrete using fly ash aggregate as coarse aggregate-an experimental study. 2018. *AIP Conference Proceedings*. 1953. DOI: 10.1063/1.5032808
29. Babu, B.R., Thenmozhi, R. An investigation of the mechanical properties of Sintered Fly Ash Lightweight Aggregate Concrete (SFLWAC) with steel fibers. 2018. *Archives of Civil Engineering*. 64 (1). Pp. 73–85. DOI: 10.2478/ace-2018-0005
30. Bursa, C., Tanriverdi, M., Çiçek, T. Use of fly ash aggregates in production of light-weight concrete. 2017. *IMCET 2017: New Trends in Mining – Proceedings of 25th International Mining Congress of Turkey*. Pp. 469–476.
31. Wasserman, R., Bentur, A. Effect of lightweight fly ash aggregate microstructure on the strength of concretes. 1997. *Cement and Concrete Research*. 27 (4). Pp. 525–537. DOI: 10.1016/S0008-8846(97)00019-7
32. Cerny, V., Kocianova, M., Drochytka, R. Possibilities of Lightweight High Strength Concrete Production from Sintered Fly Ash Aggregate. 2017. *Procedia Engineering*. 195. Pp. 9–16. DOI: 10.1016/j.proeng.2017.04.517
33. Kayali, O. Fly ash lightweight aggregates in high performance concrete. 2008. *Construction and Building Materials*. 22 (12). Pp. 2393–2399. DOI: 10.1016/j.conbuildmat.2007.09.001
34. Domagala, L. The effect of lightweight aggregate water absorption on the reduction of water-cement ratio in fresh concrete. 2015. *Procedia Engineering*. 108. Pp. 206–213. DOI: 10.1016/j.proeng.2015.06.139
35. Černý, V., Sokol, P., Drochytka, R. Production possibilities of concrete based on artificial fly ash aggregates. 2014. *Advanced Materials Research*. 923. Pp. 130–133. DOI: 10.4028/www.scientific.net/AMR.923.130
36. Domagala, L. Modification of properties of structural lightweight concrete with steel fibres. 2011. *Journal of Civil Engineering and Management*. 17 (1). Pp. 36–44. DOI: 10.3846/13923730.2011.553923
37. Harish, K.V., Dattatreya, J.K., Neelamegam, M. Properties of sintered fly ash aggregate concrete with and without fibre and latex. 2011. *Indian Concrete Journal*. 85 (1). Pp. 35–42.
38. Kockal, N.U., Özturan, T. Effects of lightweight fly ash aggregate properties on the behavior of lightweight concretes. 2010. *Journal of Hazardous Materials*. 179 (1–3). Pp. 954–965. DOI: 10.1016/j.jhazmat.2010.03.098
39. Kayali, O., Zhu, B. Chloride induced reinforcement corrosion in lightweight aggregate high-strength fly ash concrete. 2005. *Construction and Building Materials*. 19 (4). Pp. 327–336. DOI: 10.1016/j.conbuildmat.2004.07.003
40. Kayali, O., Haque, M.N., Zhu, B. Some characteristics of high strength fiber reinforced lightweight aggregate concrete. 2003. *Cement and Concrete Composites*. 25 (2). Pp. 207–213. DOI: 10.1016/S0958-9465(02)00016-1
41. Nair, H.K., Ramamurthy, K. Behaviour of concrete with sintered fly ash aggregate. 2010. *Indian Concrete Journal*. 84 (6). Pp. 33–38.
42. Kikuchi, M., Mukai, T. Properties of structural light-weight concrete containing sintered fly ash aggregate and clinker ash. 1986. *Transactions of the Japan Concrete Institute*. 8. Pp. 45–50.
43. Satpathy, H.P., Patel, S.K., Nayak, A.N. Development of sustainable lightweight concrete using fly ash cenosphere and sintered fly ash aggregate. 2019. *Construction and Building Materials*. 202. Pp. 636–655. DOI: 10.1016/j.conbuildmat.2019.01.034
44. Klyuev, S.V., Klyuev, A.V., Khezhev, T.A., Pukharenko, Y. High-strength fine-grained fiber concrete with combined reinforcement by fiber. 2018. *Journal of Engineering and Applied Sciences*. 13. Pp. 6407–6412. DOI: 10.3923/jeasci.2018.6407.6412
45. Lesovik, R.V., Klyuev, S.V., Klyuev, A.V., Ntrebenko, A.V., Yerofeyev, V.T., Durachenko, A.V. Fine-grain concrete reinforced by polypropylene fiber. 2015. *Research Journal of Applied Sciences*. 10 (10). Pp. 624–628. DOI: 10.3923/rjasci.2015.624.628
46. Usanova, K.Y., Barabanshchikov, Y.G., Kostyrya, S.A., Fedorenko, Y.P. Cold-bonded fly ash aggregate as a coarse aggregate of concrete. 2018. *Construction of Unique Buildings and Structures*. 72 (9). Pp. 1–16.
47. Kapustin, F.L., Kokorina, D.V., Fomina, I.V. in (2019) *IOP Conf. Ser. Mater. Sci. Eng.* DOI: 10.1088/1757-899X/481/1/012050
48. Supriya, Y., Srinivasa Reddy, V., Seshagiri Rao, M.V., Shrihari, S. Strength appraisal of light weight green concrete made with cold bonded fly ash coarse aggregate. 2019. *International Journal of Recent Technology and Engineering*. 8 (3). Pp. 5381–5385. DOI: 10.35940/ijrte.C6135.098319
49. Rybakov, V., Seliverstov, A., Petrov, D., Smirnov, A., Volkova, A. Strength characteristics of foam concrete samples with various additives. 2018. *MATEC Web of Conferences*. 245. DOI: 10.1051/mateconf/201824503015
50. Gagné, R. Shrinkage-reducing admixtures. 2016. *Science and Technology of Concrete Admixtures*. Pp. 457–469. DOI: 10.1016/B978-0-08-100693-1.00023-0

Contacts:

Kseniia Usanova, plml@mail.ru

Yuriy Barabanshchikov, ugb@mail.ru



DOI: 10.18720/MCE.95.11

Deformed state of the bases buildings and structures from weak viscoelastic soils

T.V. Maltseva^{a*}, E.R. Trefilina^b, T.V. Saltanova^b

^a Industrial University of Tyumen, Tyumen, Russia

^b Tyumen State University, Tyumen, Russia

* E-mail: maltv@utmn.ru

Keywords: soft soils, water-saturated base, stresses and deformation, viscoelasticity of the soil, modeling of bearing capacity

Abstract. The article discusses the grounds of buildings and structures from weak viscoelastic soils, the features of the theoretical justification for their deformations. The need for this study is due to the discrepancy between the theory of filtration consolidation and field and laboratory experiments. Within the framework of the proposed model, the constructions of solutions to the problems of loading the ground surface with typical loads that describe the stress-strain state of each phase of a two-phase medium (soil skeleton + pore water) with account of the residual pore pressure. The deviation of the calculated residual pore pressures from the experimental data is not more than 5 % (laboratory experiment), 7 % (full-scale experiment). The calculation method presented in the article allows predicting the deformation of the foundations of structures from weak water-saturated soils.

1. Introduction

In connection with the increase in housing and industrial construction, the problem of erecting and operating industrial and civil structures on soft water-saturated soils, as a result of the development of new territories, is becoming especially relevant. Despite the successful construction and operation of buildings and structures on soft water-saturated soils in general, in practice, one has to deal with deformations of such structures. The analysis shows that the cause of deformations which result in emergency conditions of structures is the insufficient consideration of strength properties, permeability, creep of soils [1]. For soft water-saturated soils (more than 80 % of the pores of the soil are filled with water) there are also special patterns of their deformability [2].

Speakers at international conferences devoted to these problems put forward a number of causes of deformations of structures located on the soils under consideration. They highlight three main features for soft soils. The first is the high compressibility of soils, the second is low strength, and the third is the long duration of settlement of structures [3]. In most cases, soft water-saturated soils cannot be used as the foundation of buildings and structures without their reinforcement through the use of geosynthetics, the construction of sand contour-reinforced piles, sand cushions, etc. [4–13].

Modern calculations of foundations and bases on soft water-saturated soils are carried out with account of the specifics of their properties, creep of the soil skeleton [14], compressibility of pore water [15–17] and filtration consolidation. Research into the determination of the stress-strain state of soil bases establishes the limits of applicability of methods for their calculation.

In particular, the analysis of the models of the theory of filtration consolidation based on a system of parabolic equations [18] shows that the residual pore pressures necessarily turn to zero and the two-phase system becomes a single-phase one (curve 1, Fig. 1). However, starting from some time T_{St} , field and laboratory tests [19, 20] show the presence of excessive pore pressure in a stabilized state. Filtration

Maltseva, T.V., Trefilina, E.R., Saltanova, T.V. Deformed state of the bases buildings and structures from weak viscoelastic soils. Magazine of Civil Engineering. 2020. 95(3). Pp. 119–130. DOI: 10.18720/MCE.95.11



This work is licensed under a [CC BY-NC 4.0](https://creativecommons.org/licenses/by-nc/4.0/)

consolidation models are no longer applicable to the description of the stress-strain state of a two-phase (water-saturated) base.

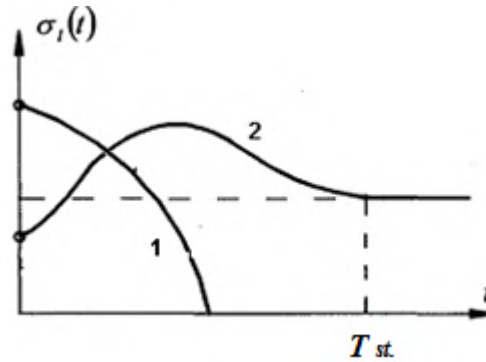


Figure 1. Change in pore pressure over time.

The article discusses a scientific direction based on a system of elliptic equations, describes residual pore pressures [18]. In accordance with the experiment, starting from a depth of 2 m from the ground surface, the qualitative character of the graph of the change in pore pressure over time has the form of curve 2 in Fig. 1. A nonmonotonic change in pore pressure over time corresponds to the consolidation process; a nonzero pore pressure corresponds to a stable state of the system. Soils with low permeability less than $5 \cdot 10^{-3}$ m/day.

According to this model, the soil is a continuous two-phase medium. The model is phenomenological, its parameters are found from experiments and it doesn't consider the mechanism of the interaction of phases based on their molecular nature.

The object of the study is a water-saturated soil base, the behavior of which under load is described from the standpoint of the mechanics of a deformable solid with account of the influence of pore water on it ("soil skeleton + pore water" two-phase system). The subject of the study is the effect of residual pore pressure on the deformed state of a water-saturated soil base.

The purpose of the study is to solve the problem of mathematical modeling of the deformed state of the soil base, taking into account the residual pore pressure at the end of the consolidation process. Within the framework of the model under consideration, the construction of solutions to the problems of loading the day surface with typical loads that describe the stress-strain state of each of the phases of a two-phase medium is carried out.

The kinematic model considered in the article describes the stress-strain state of a water-saturated soil base under load (its one-dimensional version is described in the monograph [21]) and is based on two assumptions:

1. The relative deformation of pore water ε_l (l -pore water) is proportional to the difference in pore pressure σ_1 , per length unit, i.e., the relative movement of particles of pore water is caused by pressure drop

$$(-) \varepsilon_l = \frac{h}{E_l} \frac{d\sigma_1}{dz}.$$

Relative deformation ε_l describes a local change in pore volume $dn = \varepsilon_l dz \cdot A$, where A is the cross-sectional area of the sample.

2. The relative deformation of the particles of pore water and the skeleton of the soil ε_s (s is the skeleton of the soil) are proportional and opposite in sign: $\varepsilon_s = -\varkappa \varepsilon_l$.

The parameters E_l, \varkappa are found from experiments to test large two-phase samples.

Let us consider the stress state of a water-saturated soil base as a two-phase half-space loaded with a strip load in a cylindrical coordinate system r, θ, z (a fundamental problem of the Flaman type). Statement of the boundary value problem. The normal stresses are decomposed into the sum of the stresses in the solid and liquid phases, the shear stresses in the pore fluid are set equal to zero:

$$- \text{equations of equilibrium } \frac{\partial(\sigma_{sr} - \sigma_{lr})}{\partial r} + \frac{\partial \tau_{r\theta}}{\partial \theta} + \frac{(\sigma_{sr} - \sigma_{lr}) - (\sigma_{s\theta} - \sigma_{l\theta})}{r} = 0,$$

$$\frac{\partial \tau_{r\theta}}{\partial r} + \frac{1}{r} \frac{\partial(\sigma_{s\theta} - \sigma_{l\theta})}{\partial \theta} + \frac{2\tau_{r\theta}}{r} = 0;$$

– physical equations $\sigma_{sr} = \frac{E_s}{1-\nu^2}(\varepsilon_{sr} + \nu\varepsilon_{s\theta})$, $\sigma_{s\theta} = \frac{E_s}{1-\nu^2}(\varepsilon_{s\theta} + \nu\varepsilon_{sr})$,

$$\frac{\partial \sigma_{lr}}{\partial r} = \frac{E_l}{h} \varepsilon_{lr}, \quad \frac{\partial \sigma_{l\theta}}{\partial \theta} = \frac{E_l}{h} \varepsilon_{l\theta};$$

– geometrical equations $\varepsilon_{sr} = \frac{\partial u_{sr}}{\partial r}$, $\varepsilon_{s\theta} = \frac{u_{sr}}{r} + \frac{\partial u_{s\theta}}{r \partial \theta}$,

$$\varepsilon_{lr} = \frac{\partial u_{lr}}{\partial r}, \quad \varepsilon_{l\theta} = \frac{u_{lr}}{r} + \frac{\partial u_{l\theta}}{r \partial \theta},$$

$$\gamma_{sr\theta} = \frac{\partial u_{sr}}{r \partial \theta} + \frac{\partial u_{s\theta}}{\partial r} - \frac{u_{s\theta}}{r};$$

– kinematic equations $\varepsilon_{sr} = -\varkappa \varepsilon_{lr}$, $\varepsilon_{s\theta} = -\varkappa \varepsilon_{l\theta}$.

Boundary conditions:

$$\theta = \pm \frac{\pi}{2} \quad \left. \begin{array}{l} (\sigma_{s\theta} - \sigma_{l\theta}) = 0, \quad \tau_{r\theta} = 0, \quad u_{sr} \\ \theta = 0 = 0; \quad \sigma_{lr}|_{r=\rho} = 0. \\ r = L \end{array} \right\}$$

We consider the *Boussinesq* problem about the action of a concentrated force F on an elastic half-space in the spherical coordinates R, θ, φ and generalize its fundamental solution to a two-phase half-space.

The statement of a Boussinesq type boundary value problem:

$$\frac{\partial(\sigma_{sR} - \sigma_{lR})}{\partial R} + \frac{1}{R \sin \theta} \frac{1}{R} \frac{\partial \tau_{\phi R}}{\partial \phi} + \frac{1}{R} \frac{\partial \tau_{R\theta}}{\partial \theta} + \frac{2(\sigma_{sR} - \sigma_{lR}) - (\sigma_{s\phi} - \sigma_{l\phi}) - (\sigma_{s\theta} - \sigma_{l\theta}) + \tau_{R\theta} \operatorname{ctg} \theta}{R} = 0$$

$$\frac{\partial \tau_{R\phi}}{\partial R} + \frac{1}{R \sin \theta} \frac{1}{R} \frac{\partial(\sigma_{s\phi} - \sigma_{l\phi})}{\partial \phi} + \frac{1}{R} \frac{\partial \tau_{\phi\theta}}{\partial \theta} + \frac{3\tau_{R\phi} + 2\tau_{\phi\theta} \operatorname{ctg} \theta}{R} = 0,$$

$$\frac{\partial \tau_{R\theta}}{\partial R} + \frac{1}{R \sin \theta} \frac{1}{R} \frac{\partial \tau_{\theta\phi}}{\partial \phi} + \frac{1}{R} \frac{\partial(\sigma_{s\theta} - \sigma_{l\theta})}{\partial \theta} + \frac{(\sigma_{s\theta} - \sigma_{l\theta} - (\sigma_{s\phi} - \sigma_{l\phi})) \operatorname{ctg} \theta + 3\tau_{R\theta}}{R} = 0,$$

$$\nabla^2(\sigma_{sR} - \sigma_{lR} + (\sigma_{s\theta} - \sigma_{l\theta}) + (\sigma_{s\phi} - \sigma_{l\phi})) = 0,$$

$$(\sigma_{s\theta} - \sigma_{l\theta}) = -(\sigma_{s\phi} - \sigma_{l\phi}), \quad \tau_{\theta\phi} = 0, \quad \tau_{R\theta} = 0.$$

In order to set the boundary conditions, we select two hemispheres: S_1 of a small radius (ρ) and S_2 of a large radius (L). We replace the concentrated force F with the equivalent load distributed over the surface S_1 : $\sigma_{sR}|_{S_1} = -\sigma_0$, displacements u_{sR} on the surface of the sphere S_2 are taken equal to zero: $u_{sR}|_{S_2} = 0$. On the daylight surface, stresses in the liquid phase are taken to zero.

2. Methods

We will calculate the stress-strain state of a water-saturated soil base by means of expanding the well-known Flamant solution for an elastic single-phase half-plane:

$$\sigma_r = \frac{-2F \cos \theta}{\pi r}, \quad \sigma_\theta = 0, \quad \tau_{r\theta} = 0.$$

This solution, which uses the hypotheses and equations of the one-dimensional version of the kinematic model, is decomposed into the solutions for each phase separately:

$$\begin{aligned} \sigma_r &= \sigma_{sr} - \sigma_{lr}, \\ \varepsilon_l &= \frac{h}{E_l} \frac{d\sigma_l}{dz}, \quad \varepsilon_s = \frac{1-\nu^2}{E_s} \sigma_s, \\ \varepsilon_l &= \frac{du_l}{dz}, \quad \varepsilon_s = \frac{du_s}{dz}, \quad \varepsilon_s = -\nu \varepsilon_l. \end{aligned}$$

The system of equations is reduced to one differential equation of the first order in the displacements of the solid phase. Its solution has the following form:

$$u_{sr} = \frac{2F(1-\nu^2)\cos\theta}{\pi E_s} \cdot e^{-a^2 r} \left[\ln \frac{R}{a^2 r} - \int \frac{e^{a^2 r} - 1}{r} dr \right],$$

We determine the tangential displacements of the solid phase:

$$u_{s\theta} = \frac{2F \sin \theta}{\pi E_s} \left(\nu(1+\nu) + (1-\nu(1+\nu)a^2 r) \cdot e^{-a^2 r} \left[\ln \frac{R}{a^2 r} - \int \frac{e^{a^2 r} - 1}{r} dr \right] \right).$$

Basing on this fundamental solution, we get a solution for a number of problems, which are given below.

The calculation of the elastic two-phase half-space in the stabilized state is carried out by expanding the well-known Boussinesq solution into two phases [18] (similar to the expansion of the Flamant solution):

$$\sigma_{sR} - \sigma_{lR} = -\frac{3F}{2\pi} \cdot \frac{\cos \theta}{R^2}.$$

This equation is the equation of static equilibrium. We supplement it with the equations of the kinematic model for the one-dimensional case and the stabilized state (as in the case of the Flamant solution expansion), reduce the system to a first-order differential equation for the displacements of the solid phase, after integration of which we have the calculation formula for the displacements:

$$u_{sR} = \frac{3F \cos \theta}{2\pi E_s} \cdot \left(e^{-a^2 L} \cdot \int_{\rho}^L \frac{e^{a^2 R}}{R^2} dR - e^{-a^2 R} \cdot \int_{\rho}^R \frac{e^{a^2 R}}{R^2} dR \right).$$

In a known manner, one can go from spherical coordinates to cylindrical coordinates and obtain the corresponding formulas for the stresses in the skeleton and pore fluid.

For example, we obtained normal vertical stresses in the problem of a uniformly distributed load:

$$\sigma_{lz} = \frac{2q}{\pi} \cdot a^2 \int_{-b}^b \frac{z^3}{r^3} \cdot e^{-a^2 r} \left[\ln \frac{r}{\rho} + \int_{\rho}^r \frac{e^{a^2 \xi} - 1}{\xi} d\xi \right] d\eta,$$

$$\sigma_{sz} = -\frac{2q}{\pi} \cdot \int_{-b}^b \left(\frac{z^3}{r^4} - a^2 \cdot \frac{z^3 e^{-a^2 r}}{r^3} \left[\ln \frac{r}{\rho} + \int_{\rho}^r \frac{e^{a^2 \xi} - 1}{\xi} d\xi \right] \right) d\eta,$$

$$\rho \leq \xi \leq r, \quad r = \sqrt{(x - \eta)^2 + z^2}.$$

The obtained analytical dependences make it possible to construct graphs of changes in stresses and displacements in depth (along the OZ axis) and horizontally. Replacing the integral with a variable upper limit with an approximate expression with an error estimate allowed us to speed up the computational process while maintaining an acceptable accuracy of 3 %.

Solving problems with account of the viscoelastic properties of the soil and changes in the stress-strain state of the soil base in time. One of the stages of the study was the study of changes in pore stress over time. For this study, we turned to the linear hereditary theory of viscoelasticity. In order to switch from the image to the original, we used the broken line method proposed by L.E. Maltsev.

The essence of the broken line method is that the function of four arguments $F^*(x, y, z, p)$ is transferred to the function of one argument $F^*(p)$ by means of replacing spatial coordinates at a fixed point with coordinates $x = x_i, y = y_i, z = z_i$ ($i = \overline{1, n}$) with the numbers. A system of fixed spatial points for which it is interesting to obtain (expand) a solution in time in each problem is selected individually. The function known in the images $0 \leq p$ is approximated by a function of a special form:

$$\phi^*(p) = \phi(0) \cdot \left(1 - \sum_{i=0}^n (c_i - c_{i+1}) \frac{1}{p} e^{-pT_i} \right), \quad 0 \leq p \leq \infty, \quad T_0 = 0, c_0 = 0, c_{i+1} = 0$$

The original function $\phi(t)$ is known in advance and looks like a broken line:

$$\phi(t) = \phi(0) \cdot \left(h(t) - \sum_{i=0}^n (c_i - c_{i+1})(t - T_i)h(t - T_i) \right).$$

Here $h(t)$ is the Heaviside function, $\phi(0), c_i, T_i$ are the desired parameters of the broken line. The parameter $\phi(0)$ is necessarily dimensional, c_i, T_i are dimensionless. The arguments t and p are also dimensionless.

Advantages of writing a function as a broken line:

the possibility of approximation with a given accuracy (the number of links can be increased);

the presence of an elementary image according to Laplace-Carson.

The disadvantages of writing include the following: at the point $t = 0$ the broken line will have a finite derivative, and with the function $F(t)$ a derivative may be infinite; the broken line reaching the asymptotic value occurs at the final value t .

Let us consider how the pore pressure of a half-plane loaded with a uniformly distributed load changes at the initial stage of time.

In the section, $z = 1/5b$ we fix the coordinate point ($z = 1/5b, x = 0$), for which we show the change in pore stresses in time. In the elastic solution for $\sigma_{lz}(z_3 = 1/5b, x = 0)$, in accordance with the Volterra principle we make a change of notation $a^2 \rightarrow [a^2(p)]^*$, and obtain the solution to the viscoelastic problem in the images:

$$\sigma_{lz}^* = \frac{2q}{\pi} \cdot (a^2)^* \cdot \int_{-b}^b \frac{(1/5b)^3}{r^3} \cdot e^{-(a^2)^* r} \left[\ln \frac{r}{\rho} + \int_{\rho}^r \frac{e^{(a^2)^* \xi} - 1}{\xi} d\xi \right] d\eta, \quad r = \sqrt{\eta^2 + (1/5b)^2}.$$

In accordance with the broken line method, we present the desired original in the form of a broken line:

$$\bar{\sigma}_{lz}(t) = \sigma(0) \cdot \left(1 - \sum_{i=0}^5 (c_i - c_{i+1})(t - T_i)h(t - T_i) \right), \quad c_0 = c_6 = T_0 = 0,$$

in which the parameters $\sigma(0), c_i$ are the desired ones, and T_i are given as for the well-known original $a^2(t)$.

We rewrite this spline in images

$$\bar{\sigma}_{lz}^*(p) = \sigma(0) \cdot \left(1 - \sum_{i=0}^5 (c_i - c_{i+1}) \frac{1}{p} e^{-pT_i} \right).$$

In order to determine the unknown parameters, we compose a system of linear algebraic equations using the conditions for the broken line to coincide in images with the known right-hand side on the point system $p = P_j$:

$$\bar{\sigma}_{lz}^*(p = P_j) = \sigma_{lz}^*(p = P_j), \quad j = 1, \dots, k.$$

The points are selected in a special way, for example, $p_j = \frac{\ln T_j - \ln T_{j-1}}{T_j - T_{j-1}}$, $T_0 = 10^{-5}$.

We repeat similar arguments for other points of the half-space.

3. Results and Discussion

Let us consider the results of calculating normal vertical stresses in the problem of a uniformly distributed load (Fig. 2).

$$\sigma_{lz} = \frac{2q}{\pi} \cdot a^2 \int_{-b}^b \frac{z^3}{r^3} \cdot e^{-a^2 r} \left[\ln \frac{r}{\rho} + \int_{\rho}^r \frac{e^{a^2 \xi} - 1}{\xi} d\xi \right] d\eta,$$

$$\sigma_{sz} = -\frac{2q}{\pi} \cdot \int_{-b}^b \left(\frac{z^3}{r^4} - a^2 \cdot \frac{z^3 e^{-a^2 r}}{r^3} \left[\ln \frac{r}{\rho} + \int_{\rho}^r \frac{e^{a^2 \xi} - 1}{\xi} d\xi \right] \right) d\eta,$$

$$\rho \leq \xi \leq r, \quad r = \sqrt{(x - \eta)^2 + z^2}.$$

The obtained analytical dependences make it possible to construct graphs of changes in stresses and displacements in depth (along the OZ axis) and horizontally.

Below are the graphs of normal stresses in different sections (Fig. 3).

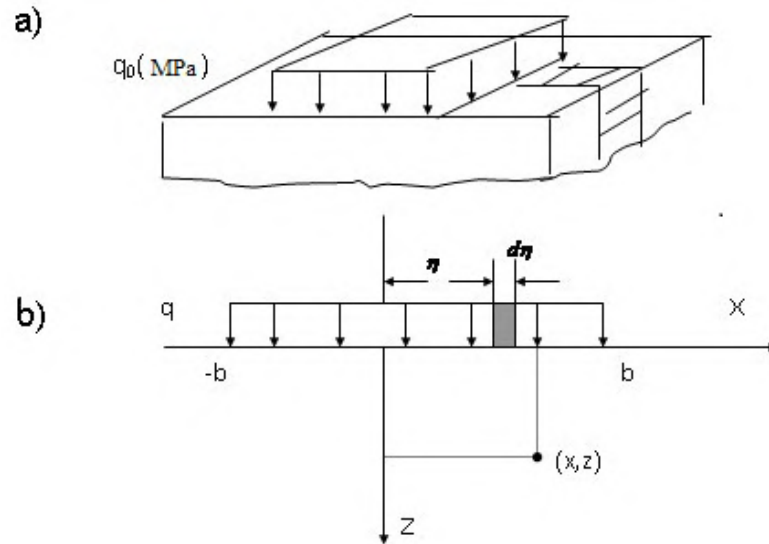


Figure 2. a) Effect of a uniformly distributed load on half-space;
 b) Transition from distributed load to concentrated force.

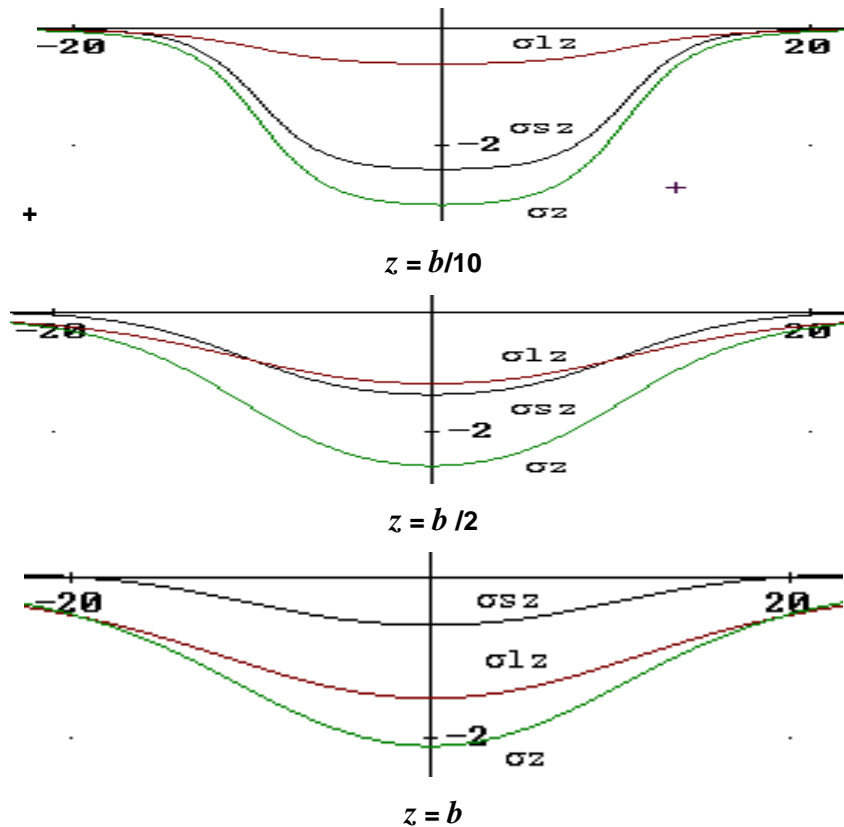


Figure 3. Change in vertical stresses in solid, σ_{sz} , liquid σ_{lz} phases and the total ones σ_z .

In the central part of the loaded area, pore water is more strongly clamped by soil and therefore its bearing capacity is greater than at the periphery. After analyzing the latter graphs of normal stresses, we conclude that at a distance of $z = b$ most of the external load falls on the liquid phase. This once again confirms the carrying capacity of the liquid phase.

In the process of research, we solved the problems of the action of two or more structures on a two-phase base.

Let us consider the problem of determining the stress-strain state of the base from the action of two uniformly distributed loads (Fig. 4). This problem models the mutual influence of two closely standing buildings (flat case). In this case, the stresses and displacements at point M are found through the principle of superposition (summation) of two forces. In order to do this, we first need to place the origin of coordinates at the point of application of force $dF_1 = q_1 d\xi$ and find the coordinates of the point $M(x - \xi_1, z)$. Then we

transfer the coordinates system to the point of application of force $dF_2 = q_2 d\xi$ and determine the new coordinates of the point $M(x - \xi_2, z)$.

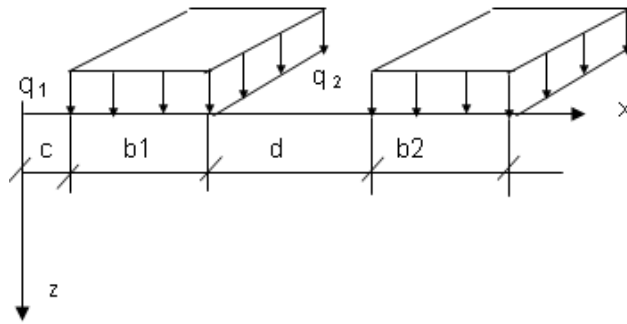


Figure 4. Action of two evenly distributed loads on the base.

Below are the formulas for the stresses:

$$\sigma_{sz} = -\frac{2q_1}{\pi} \int_c^{c+b_1} f_1(x, z, \xi) d\xi - \frac{2q_2}{\pi} \int_{c+b_1+d}^{c+b_1+d+b_2} f_1(x, z, \xi) d\xi,$$

$$\sigma_{lz} = \frac{2q_1}{\pi} \int_c^{c+b_1} f_2(x, z, \xi) d\xi + \frac{2q_2}{\pi} \int_{c+b_1+d}^{c+b_1+d+b_2} f_2(x, z, \xi) d\xi,$$

and the corresponding graphs of displacements and stresses in Fig. 5, 6, 7.

The study of the dependence of stresses in solid and liquid phases on the distance between the objects showed that with the separation of objects from each other, normal stresses in the solid phase found by the kinematic model fade out 40 % faster than similar stresses found by the Flaman solution.

Basing on the expansion of the fundamental solution for the two-phase half-space, we considered several problems: about the action of the load distributed over rectangular and circular platforms, and about the action of the load from the interaction of two objects (spatial case). We completed the calculation of the stress and strain state for all cases. $z = 2 \text{ m}$, $d = 2 \text{ m}$, $d = 4 \text{ m}$, $d = 6 \text{ m}$.

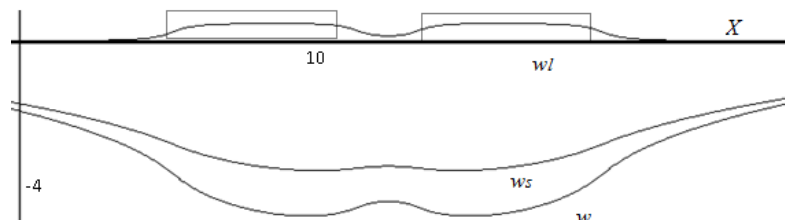


Figure 5. Vertical displacements of points in the section $z = 0.5 \text{ m}$, w_s, w_l is according to the kinematic model, w – by the Flaman solution.

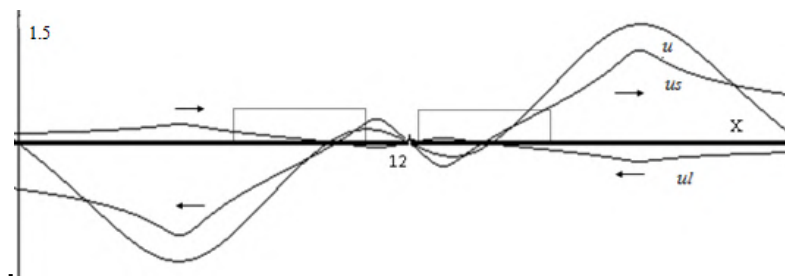


Figure 6. Horizontal displacements of points in the section $z = 0.5 \text{ m}$.

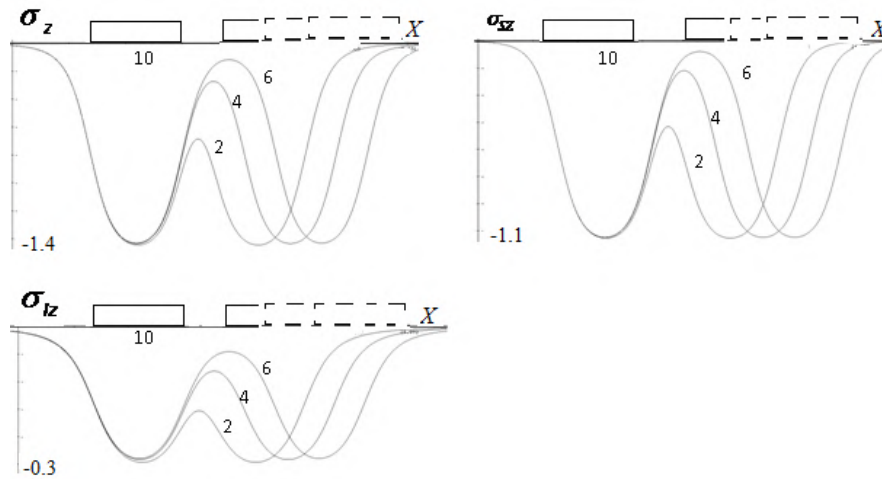


Figure 7. Dependence of stresses in the cross section $z = 2$ m on the distance between the objects $d = 2$ m, $d = 4$ m, $d = 6$ m.

The problem of the action of a concentrated force F on an elastic two-phase half-space is considered above. Here are the graphs of normal stresses in fractions of force F in different sections (Fig. 8):

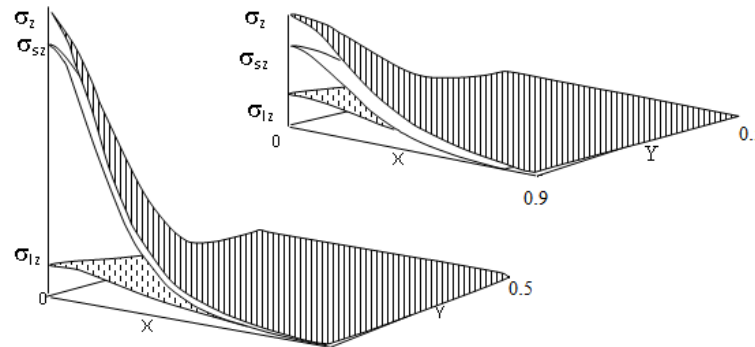


Figure 8. Change in vertical stresses in solid σ_{sz} , liquid σ_{lz} phases and the total ones σ_z in sections $z = 1, z = 5$.

Fig. 9 shows the graphs of displacements from the action of a load distributed over a rectangle with a parameter $a^2 = 0.1(1/m)$ and different values of the coordinate Z .

$$u_s = \frac{F(1+\nu)}{2\pi E_s} \int_{-b}^b \int_{-l}^l \left(\frac{1}{R^2} - a^2 e^{-a^2 R} \int_0^R \frac{e^{a^2 R}}{\rho R^2} dR \right) \left(\frac{zr}{R} - \frac{(1-2\nu)Rr}{R+z} \right) d\xi d\eta.$$

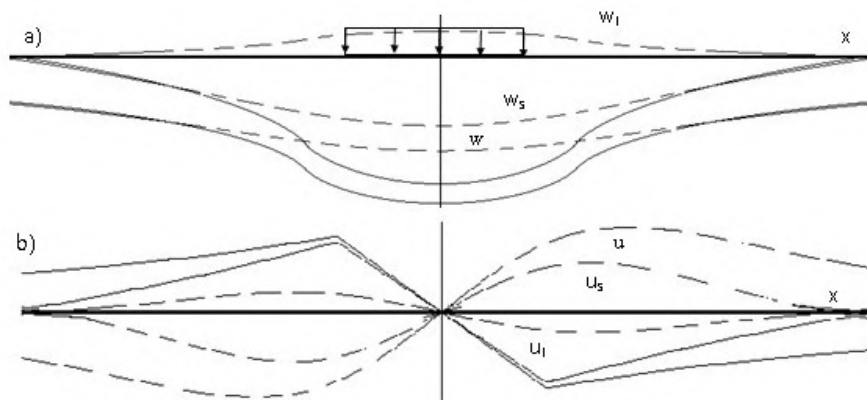


Figure 9. Graphs a) vertical and b) horizontal movements along the X axis for $z = 0$ (—) and $z = 2$ (---) by the Boussinesq solution (u, w) and by the kinematic model.

It follows from the graphs that the vertical displacements of the skeleton due to the unloading contribution of the liquid phase on the axis of symmetry for $z = 2$ decreased by 30 %. The maximum values of the horizontal movements of the skeleton decreased by 40 %.

The vertical stresses in the solid phase decrease faster than the total ones, therefore, the vertical displacements of the skeleton particles decrease faster than the vertical displacements obtained by the Boussinesq solution. Consequently, taking account of the liquid phase leads to the fact that the two-phase base becomes more rigid compared to the single-phase base. Fig. 11 shows graphs of pore pressures which vary over time.

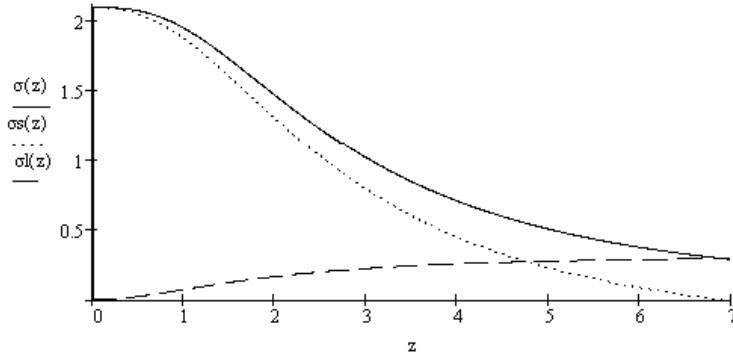


Figure 10. Distribution of stresses in depth at points under the center of the circle: total – σ , in solid σ_s and liquid σ_l phases.

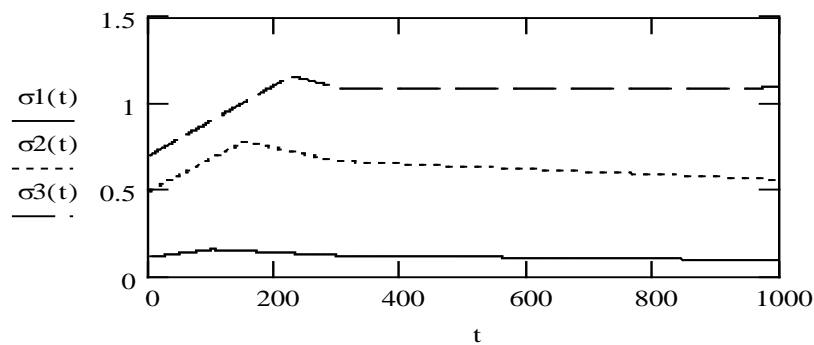


Figure 11. Change in time of pore pressure at points: $x = 0$, $z_1 = 1/5b$ (---), $z_2 = b$ (...), $z_3 = 5b$ (—).

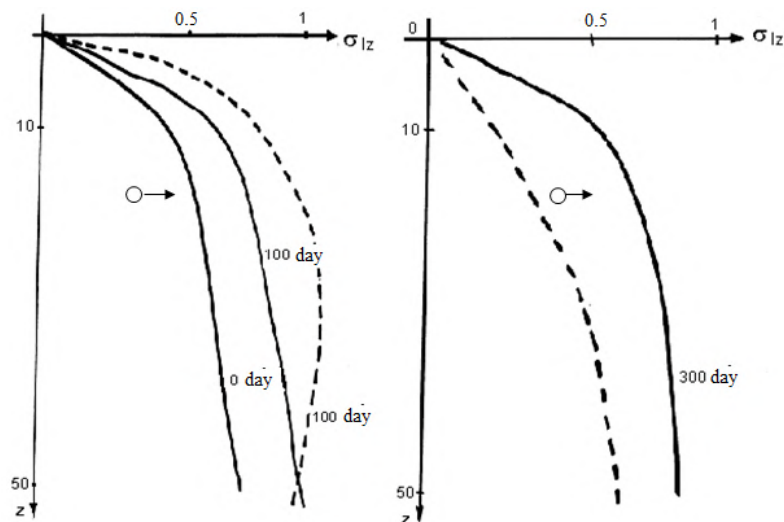


Figure 12. Comparison of the research results of pore pressure according to two models: (- - -) – according to the theory of filtration consolidation; (—) – according to the kinematic model.

For all fixed spatial points, the pore pressure varies nonmonotonically over time. The non-uniformity of the change in pore pressure at a constant load over time reflects the peculiarity of a two-phase system. The process of pressure redistribution between phases is nonmonotonic. The maximum value of pore pressure lags in time with increasing depth, i.e. for $z = 1/5b$ the maximum value of pore pressure is reached at time

$t = 100$ days, and for $z = 5b$ the maximum is reached after 200 days. This effect was first established by L.S. Amaryan in experiments with monolithic large-sized samples.

Let us compare the obtained solution with the well-known theoretical result of V.G. Korotkin given in the monograph [22]. In the problem we investigate the distribution of pore pressure in depth during the filtration consolidation of the base from the action of a uniformly distributed load. The soil characteristics are given: $a = 0.01 \text{ cm}^2/\text{kg}$, $\varepsilon_0 = 1$, $\kappa = 1.16 \cdot 10^{-6} \text{ cm}\cdot\text{s}$, the width of the strip foundation is $b = 10 \text{ m}$. The book contains graphs of pore pressure for time $T = 100, 300, 1000$ и 10000 days, plotted in shares $p \cdot b/q$. The comparison was carried out only for $T = 100$ и 300 days, because for $T = 1000$ days the consolidation process almost ends and the pore pressure differs little from zero. For $T = 10000$ according to the theory of filtration consolidation, the pore pressure vanishes (Fig. 12).

4. Conclusion

1. The reliability of the model under consideration is shown by comparing the theoretical pore pressures with the data of a laboratory experiment LS Amaryan conducted on a sample of water-saturated peat [18]. The greatest discrepancy of 18 % is observed at the points of maximum pore pressure function. For the asymptotic value of the pore pressure function (i.e., residual pore pressure), the discrepancy between the calculated and experimental data is not more than 5 %. Comparison with the results of a full-scale experiment F.F. Zekhnueva the maximum discrepancy at the points of maximum pore pressure was 23 % and the discrepancy in residual pore pressures was 7 %.

2. In problems of the Flaman type and Boussinesq type, the stress and strain state analytically accurately decomposes into two phases (soil skeleton + pore water). From a comparison of surface sediment for single-phase and two-phase bodies, it follows that the influence of pore water on the soil skeleton manifests itself in their rapid decrease to 40 %.

3. The solution of problems in a viscoelastic formulation by the broken line method allowed us to describe the consolidation process over time and compare the result with the well-known solution obtained by the theory of filtration consolidation. For all fixed spatial points, the pore pressure varies nonmonotonically with time, and the initial value is less than the final value corresponding to a stabilized state. The non-uniformity of the change in pore pressure at a constant load over time reflects the experimentally defined feature of a two-phase system. In all solutions, we numerically analyzed and graphically presented the reduction of stresses and displacements in the skeleton due to the unloading effect of pore water. Pore pressures can reach up to 70 % of the total stresses.

4. New analytical formulas are obtained for stresses and displacements in the soil skeleton and pore water when loaded with typical loads. The solutions, in contrast to single-phase soil, take into account the influence of pore water, that is, they determine the deformed condition of the base from two-phase viscoelastic soil. The calculation formulas for the final sediments corresponding to the stabilized state of the base, without a description of the consolidation process, are recommended to be used at the design stage of buildings. This will allow taking into account the influence of pore water on the soil skeleton and providing for measures to improve the safety of their construction and operation.

References

1. Nguyen, P.D. The dependence of the strength properties of soil on its physical state. Magazine of Civil Engineering. 2012. 35(9). Pp. 23–28. DOI: 10.5862/MCE.35.3
2. Liu, E.L., Lai, Y.M., Wong, H., Feng, J.L. An elastoplastic model for saturated freezing soils based on thermo-poromechanics. International Journal of Plasticity. 2018. 107. Pp. 246–285. DOI: 10.1016/j.ijplas.2018.04.007
3. Abelev, M.Yu. Features of the construction of structures on soft water-saturated soils. Industrial and Civil Engineering. 2010. 3. Pp. 12–13.
4. Oyegbile, B., Oyegbile, B.A. Applications of geosynthetic membranes in soil stabilization and coastal defense structures. International Journal of Sustainable Built Environment. 2017. 6(2). Pp. 636–662. DOI: 10.1016/j.ijsbe.2017.04.001
5. Usmanov, R., Mrdak, I., Vatin, N., Murgu, I.V. Reinforced soil beds on weak soils. Applied Mechanics and Materials. 2014. 633–634. Pp. 932–935. DOI: 10.4028/www.scientific.net/AMM.633-634.932
6. Mirsaidov, M.M., Sultanov, T.Z. Use of linear heredity theory of viscoelasticity for dynamic analysis of earthen structures. Soil Mechanics and Foundation Engineering. 2013. 49(6). Pp. 250–256. DOI:10.1007/s11204-013-9198-8
7. Sultanov, T.Z., Khodzhaev, D.A., Mirsaidov, M.M. The assessment of dynamic behavior of heterogeneous systems taking into account non-linear viscoelastic properties of soil. Magazine of Civil Engineering. 2014. 45(1). DOI: 10.5862/MCE.45.9
8. Mirsaidov, M.M., Sultanov, T.Z. Assessment of stress-strain state of earth dams with allowance for non-linear strain of material and large strains. Magazine of Civil Engineering. 2014. 49(5). Pp. 73–82+136–137. DOI: 10.5862/MCE.49.8
9. Khudayarov, B.A., Turaev, F.Z. Nonlinear vibrations of fluid transporting pipelines on a viscoelastic foundation. Magazine of Civil Engineering. 2019. 86(2). Pp. 30–45. DOI: 10.18720/MCE.86.4

10. Maltseva, T., Saltanova, T., Chernykh, A. Modelling a Reinforced Sandy Pile Rheology when Reacting with Water-saturated Ground. *Procedia Engineering*. 2016. 165. Pp. 839–844. DOI: 10.1016/j.proeng.2016.11.782
11. Maltseva, T., Saltanova, T. Modelling of Water-Saturated Grounds under a Curved Section of an Oil and Gas Pipeline. *MATEC Web of Conferences*. 2016. 73. DOI: 10.1051/mateconf/20167301022
12. Zhi Yong Ai, Ye Cheng Dai, Yi Chong Cheng. Time-dependent analysis of axially loaded piles in transversely isotropic saturated viscoelastic soils. *Engineering Analysis with Boundary Elements*. 2019. 101. Pp. 173–187. DOI: 10.1016/j.engabound.2019.01.004
13. Sinyakov, L., Garmanov, G., Melentev, A. Strengthening and Stabilization of the Weak Water Saturated Soils Using Stone Columns. *MATEC Web of Conferences*. 2016. 73. DOI: 10.1051/mateconf/20167301003
14. Maltseva, T., Nabokov, A., Chernykh, A. Reinforced Sandy Piles for Low-Rise Buildings. *Procedia Engineering*. 2015. 117. DOI: 10.1016/j.proeng.2015.08.08.15
15. Buhartsev, V.N., Nguyen Tkhay Khoang. Estimation of the soil body stability. *Magazine of Civil Engineering*. 2012. 35(9). Pp. 41–48. DOI: 10.5862/MCE.35.6
16. Smolin, Yu.P., Vostrikov, K.V. Compaction of saturated soils with regard to compressible pore fluid and soil creep. *Bulletin of Tomsk State University of Architecture and Civil Engineering. Journal of Construction and Architecture*. 2019. 21(5). Pp. 192–199. DOI: 10.31675/1607-1859-2019-21-5-192-199
17. Guan-lin, Y., Bin, Y. Investigation of the overconsolidation and structural behavior of Shanghai clays by element testing and constitutive modeling. *Shanghai, China, Tongji University*. 2016. 1(1). Pp. 62–77. DOI: 10.1016/j.undsp.2016.08.001
18. Maltseva, T. Mathematical modeling of water-saturated soil basements. *Advances in Intelligent Systems and Computing*. 2020. 982. Pp. 872–884. DOI: 10.1007/978-3-030-19756-8_84
19. Bugrov, A.K., Golli, A.V., Kagan, A.A. et al. Field studies of the stress-strain state and consolidation of beds of the system of flood-protection structures in Saint-Petersburg. *Soil Mech Found Eng*. 1997. 34. Pp. 1–8. DOI: 10.1007/BF02465082
20. Vorontsov, V.V., Nabokov, A.V., Ovchinnikov, V.P., Tverdokhle, S.A. The results of compression of weak water-saturated clay macro-samples through using a "soil castle". *Scientific and Technical Bulletin of the Volga Region*. 2015. 1. Pp. 60–65.
21. Maltsev, L.E., Bai, V.F., Maltseva, T.V. Kinematic model of soil and biomaterials, 2002. 336 p.
22. Tsytoovich, N.A., Zaretsky, Yu.K., Malyshev, M.V. et al. The forecast rate of subsidence of structures foundations. *Stroyizdat*, 1967. 238 p.

Contacts:

Tatyana Maltseva, maltv@utmn.ru

Elena Trefilina, e3filina@mail.ru

Tatyana Saltanova, tsaltanova@mail.ru

© Maltseva T.V., Trefilina E.R., Saltanova T.V., 2020



DOI: 10.18720/MCE.95.12

Winter greenhouse combined heating system

M.V. Pavlov*, **D.F. Karpov**, **A.A. Sinitsyn**, **A.G. Gudkov**

Vologda State University, Vologda, Russia

* E-mail: pavlov_kaftgv@mail.ru

Keywords: energy consumption, heat transfer, infrared radiation technology, soil, greenhouse

Abstract. Energy preservation and reduction in greenhouse gas emissions into the atmosphere can be partially gained through decentralization of heat supply. In the case of cultivation facilities, a solution is a combined heating system which includes soil infrared heating and air heating in the winter greenhouse up to the required values by means of autonomous convective heaters. Upon analysing domestic and foreign scientific publications, there has not been found any comprehensive calculation method of the combined heating system. The target of research is normally one of the space heating ways: either radiant or convective. The calculation method considered in the article is based on the solution of the coupled equations set of the greenhouse heat and material balances, its walling and soil surface. It takes into consideration both the features of radiant heat transfer between distant bodies, and convective air heating from heaters. The developed calculation method has been tested using the modern industrial greenhouse “Fermer 7.5” for year-round cultivation of crops. As shown by the results of software calculations, at low temperatures of the outside air, the heat power of winter greenhouse radiant heating should be twice as high as the heat consumption for convective heating of the cultivation facility. There have been obtained heat power change patterns of the winter greenhouse combined heating system depending on a number of important factors, such as: temperature of the outside air; walling thermal resistance; absorption coefficient of the soil surface. Due to the fact that according to the calculations results, the heat loss via the winter greenhouse ventilation proved to be significant, it makes sense to consider further the option of preheating outdoor air necessary for air exchange indoors.

1. Introduction

Heating of cultivation facilities during the cold period plays an important role in year-round cultivation of flowers, vegetables, seedlings, etc. The greenhouse heating costs make up about 30–50 % of the production costs, which is explained using glass and polycarbonate of low thermal properties for walling [1, 2]. The search for alternative materials, which can minimize energy needs in space heating and significantly improve conditions for growing plants, is underway, but at the moment there is no comprehensive solution to the problem [3, 4]. This applies to the search for optimal space planning designs of winter greenhouses as well: finding the correct shape and orientation of the facility by the cardinal directions for different climatic conditions [5]. In any case, the use of efficient heat supply of winter greenhouses is a priority in the greenhouse industry of the country. In the last century convective heating methods (heating internal air, but not soil) were actively used for greenhouses. They are not quite efficient, especially during the vegetative period, as the main part of heat is located in the upper zone of the facility, and not close to the soil surface where the plants grow [6]. Nowadays, there are some innovative technologies for cultivation facilities heat supply, based, for example, on the use of solar radiation [7–9], low grade heat of the environment and soil (heat pumps) [10–13] or geothermal energy sources [14–16]. It is often economically feasible to heat winter greenhouses using thermal energy from third-party production processes or from local heat sources [17]. Despite the fact that these heating systems have their distinctive advantages due to their nature, it is necessary, first of all, to focus on the greenhouses heating methods, which to a lesser extent depend on geographical conditions and environmental factors. These include radiant heating systems of winter greenhouses operating on fuel gas [18, 19]. However, as shown by the conducted research [20], the use of only infrared soil heating in the greenhouse does not allow to maintain the targeted indoor thermal conditions at low outdoor temperatures.



It is commonly known that a heating system is designed to create the necessary indoor thermal conditions. This also applies to cultivation facilities as in case of winter greenhouses heated in the cold period. Table 1 presents, as an example, the required microclimate parameters in year-round vegetable greenhouses prior to fructification.

Table 1. Greenhouse temperature and humidity conditions (before fructification).

Plant	Air temperature, °C			Soil temperature, °C	Relative humidity, %
	day		night		
	sunny	overcast			
Cucumber (winter-spring cycle)	22–24	20–22	17–18	20–24	70–75
Cucumber (autumn cycle)	25–26	22–23	19–20	22–24	70–75
Tomato (winter-spring cycle)	22–24	19–20	16–17	18–20	60–65
Tomato (autumn cycle)	24–26	18–20	16–18	18–19	60–70
Lettuce	20–23	16–18	10	15–16	70–80
Radish	20–22	7–9	5–6	15–16	60–70
Dill, spinach	17–18	8–12	5–6	15–16	65–80

According to Table 1, unlike conventional agricultural buildings and facilities, winter greenhouses need to maintain the required thermal conditions not only of the space itself, but also of the soil. A water (or air) heating system with additional soil heating, which is basically a system of pipelines laid in the soil, is an obsolete option. These include such disadvantages as: large quantity of metal per structure (10–12 kg/m²) and slow response of the system; complexity of installation (underground piping, installation of a heating unit, etc.); need for a remote heat source; high energy consumption for circulation of the coolant; different coolant temperatures in the heating system circuits (above the surface and under it); possible leakage of water into the soil layer in case of pipelines damage, etc. In addition, most of the existing winter greenhouses with traditional heating systems were built before the implementation of modern energy-saving programs and, as a result, the amount of energy consumed in such cultivation facilities is much higher compared to the new agricultural sites [21]. The use of only radiant heating in the greenhouse also cannot be a solution, since most of the heat is spent on soil heating, and the inside air temperature, as a consequence, is relatively low (below the standard values given in Table 1).

In this case it is important to consider a combined heating system, which, in addition to convective space heating, also involves radiant heat flow generated by the overhead dark infrared emitters. Besides, the use of gas infrared emitters will allow, through decentralization of heat supply and relatively cheap fuel gas, to reduce the heat load of the convective heating system designed to heat the air, and reduce consumption of non-renewable fuel and energy resources. Gas-fired radiant heating will provide crops in the greenhouse with additional carbon dioxide (CO₂), which is necessary for photosynthesis reaction. This type of combined heating system will generate economic benefits due to the reduction in convective heat output (during less cold months of the heating period).

The research target is a combined heating system of the winter greenhouse with overhead gas infrared emitters for soil heating and convective heaters designed for maintaining the required temperature of the indoor air.

The research is focused on the patterns of heat power changes of the winter greenhouse combined heating system depending on environmental factors, walling design features and heat absorbing properties of the soil surface under conditions of ventilation and soil irrigation.

The purpose of the study is to develop a method of calculation of the winter greenhouse combined heating system, which includes overhead infrared radiators with convective heaters and is designed for maintaining the required heat and humidity conditions of the indoor space and the soil in the cultivation facility.

To achieve this purpose it is necessary to solve the following tasks:

1. Determine the main heat and mass transfer processes occurring in the winter greenhouse while using the combined heating system.

2. To compose a system of coupled equations of heat and mass transfer in the winter greenhouse with combined heating taking into account incoming and outgoing fluxes of heat and mass.

3. To test the developed calculation method of the combined heating system using a modern industrial greenhouse as an example.

4. To study the effect of various factors on the heat power of the winter greenhouse combined heating system with the help of the developed calculation method.

2. Methods

Fig. 1 shows the schematic diagram of the winter greenhouse combined heating system under steady-state heat and humidity conditions.

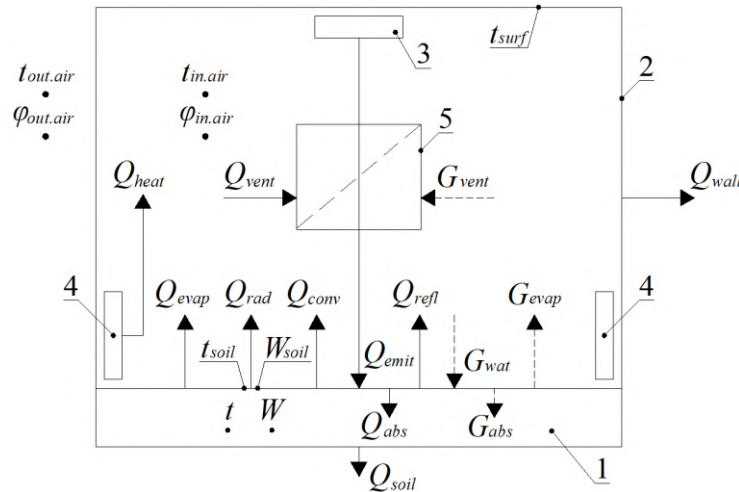


Figure 1. Calculation model of the winter greenhouse combined heating system:
1 – soil; 2 – walling; 3 – infrared radiation source (emitter);
4 – convective heaters; 5 – ventilation (supply, exhaust).

Under steady-state heat and humidity conditions in the winter greenhouse (Fig. 1), the heat balance equation can be written as follows, W:

$$Q_{emit} + Q_{heat} = Q_{wall} + Q_{vent} + Q_{soil}, \quad (1)$$

where Q_{emit} is the radiant heat flux coming from the emitter 3, W;

Q_{heat} is the convective heat flux coming from the heaters 4, W;

Q_{wall} is the heat loss by heat transfer through the greenhouse walling 2, W;

Q_{vent} is the heat loss with the ventilation air leaving the greenhouse through the exhaust ventilation aperture 5, W;

Q_{soil} is the heat loss into the deep soil horizons, W.

In the combined heating system, the thermal power Q_{heat} , W, of the convective heaters 4 is to maintain the required thermal conditions in the greenhouse and is used for heating the indoor air up to the target temperature (Table 1).

Heat loss Q_{wall} through the walling 2 of the winter greenhouse, W, can be found using the heat transfer equation:

$$Q_{wall} = \frac{t_{in.air} - t_{out.air}}{R_t} F_{wall} (1 + \beta_{inf}), \quad (2)$$

where $t_{in.air}$ is the indoor air temperature, °C;

$t_{out.air}$ is the outside air temperature, °C;

R_t is resistance to the greenhouse walling heat transfer 2, m²·K/W;

F_{wall} is the total area of the greenhouse walling, m²;

β_{inf} is a coefficient that factors in the additional heat energy consumption for heating the infiltrating air, usually taken to be 0.2.

Heat losses with the ventilation air leaving the greenhouse Q_{vent} , W, under balanced ventilation are numerically equal to the heat consumption for heating the supply air coming from outside into the winter greenhouse through the ventilation aperture 5:

$$Q_{vent} = G_{air} (h_{in.air} - h_{out.air}), \quad (3)$$

where G_{air} is the mass flow rate of the dry part of moist air participating in the greenhouse air exchange, kg/s;

$h_{in.air}$ and $h_{out.air}$ are specific enthalpy of indoor and outdoor humid air respectively, J/kg.

Heat losses into the soil Q_{soil} , W, due to their smallness are calculated in a simplified way by the equation:

$$Q_{soil} = (t_{in.air} - t_{out.air}) \sum_{i=1}^n \left(\frac{F_i}{R_i} \right), \quad (4)$$

where F_i is the projected area of the i -th soil zone in the greenhouse with their total number n , m²;

R_i is resistance to heat transfer of the i -th soil zone in the greenhouse with their total number n , m²·K/W.

The winter greenhouse material balance equation (Fig. 1) will be as follows, kg/s:

$$G_{evap} = G_{vent}, \quad (5)$$

where G_{evap} is the moisture evaporation from the soil surface 1, kg/s;

G_{vent} is the moisture loss with the exhaust air leaving the greenhouse through the exhaust ventilation aperture 5, kg/s.

The set of winter greenhouse walling thermal balance equations 2 (Fig. 1) includes the expression (2) and the formula, W:

$$Q_{wall} = \left(1 - \frac{A_1}{1 - k_{refl}} \right) Q_{emit} + Q_{rad} + Q_{conv2}, \quad (6)$$

where $k_{refl} = (1 - A_1)(1 - A_2)\varphi_{21}[1 - \varphi_{22}(1 - A_2)]^{-1}$ is a coefficient that factors in the repeated reflection of thermal radiation from the soil surface 1 and the internal surface of the greenhouse walling 2;

A_1 and A_2 are absorption coefficients of the soil surface 1 and the greenhouse walling internal surface 2 respectively;

φ_{21} is a radiation coefficient from the greenhouse walling internal surface 2 to the soil surface 1;

φ_{22} is a self-radiation coefficient of the greenhouse walling internal surface 2;

Q_{rad} is the resultant thermal radiation between the soil surface 1 and the greenhouse walling internal surface 2, W;

Q_{conv2} is a convective component of heat transfer between the indoor air and the greenhouse walling internal surface 2, W.

In formula (6) the resultant thermal radiation between the soil surface 1 and the greenhouse walling internal surface 2 provided that the angular radiation coefficient $\varphi_{12} = 1$, is calculated using the following equation, W:

$$Q_{rad} = c_0 \varepsilon_{12} F_{surf} \left[\left(\frac{T_{surf}}{100} \right)^4 - \left(\frac{T_{wall}}{100} \right)^4 \right], \quad (7)$$

where c_0 is a black body radiation coefficient, 5.67 W/(m²·K⁴);

ε_{12} is the reduced relative coefficient of the soil surface thermal radiation 1 and the greenhouse walling internal surface 2;

F_{surf} is the soil surface area 1 in the greenhouse, m²;

$T_{surf} = t_{surf} + 273.15$ and $T_{wall} = t_{wall} + 273.15$ are the absolute temperatures of the soil surface 1 and of the greenhouse walling internal surface 2 respectively, K.

The heat balance equation of the soil surface 1 in the winter greenhouse (Fig. 1) will be as follows, W:

$$\frac{A_1 Q_{emit}}{1 - k_{refl}} = Q_{rad} + Q_{conv1} + Q_{evap} + Q_{soil}, \quad (8)$$

where Q_{conv1} is the heat flux caused by convective heat transfer between the soil surface 1 and the surface air in the greenhouse (in Fig. 1 is marked as Q_{conv}), W;

Q_{evap} is the heat flux spent on moisture evaporation from the soil surface 1, W.

The material balance equation of the soil surface 1 in the winter greenhouse (Fig. 1) is as follows, kg/s:

$$G_{wat} = G_{evap}, \quad (9)$$

where G_{wat} is the water flow for watering the soil 1, kg/s.

On the right side of equation (9) there must also be water flow G_{abs} , kg/s, absorbed by plants. At this stage, we assume that plants are temporarily absent in the greenhouse (fetal period, until fruitification), so the value $G_{abs} \approx 0$.

3. Results and Discussion

Let us consider the solution of the coupled equations set of the greenhouse thermal and material balances, its walling and soil when utilizing the combined heating system for space heating using the industrial greenhouse "Fermer 7.5" (Fig. 2) as an example.

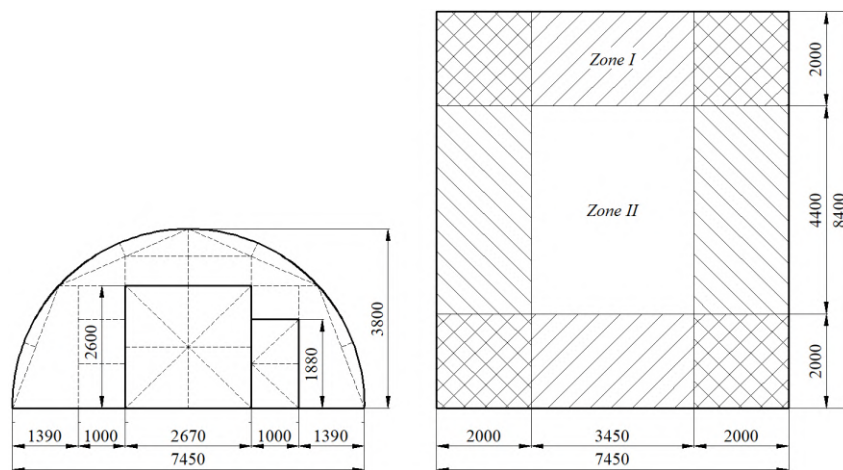


Figure 2. Industrial greenhouse "Fermer 7.5" and the soil zone layout chart.

Initial data to perform the calculation:

- Greenhouse dimensions: width $a = 7.45$ m; length $b = 8.40$ m; height $h = 3.80$ m.
- Ventilation apertures dimensions:
 - for air inflow: width $a_{in} = 1.0$ m; height $h_{in} = 1.88$ m; opening rate $\chi_{in} = 0.25$; quantity $N_{in} = 1$;
 - for air exhaust: width $a_{ex} = 0.75$ m; height $h_{ex} = 1.0$ m; opening rate $\chi_{ex} = 1$; quantity $N_{ex} = 2$.
- The soil surface parameters (tomatoes before fruitification in winter-spring cycle, according to Table 1): temperature $t_{surf} = 20$ °C; absorption coefficient $A_1 = 0.65$ (reflection coefficient $R_1 = 0.35$); thermal radiation coefficient (emissivity factor) $\varepsilon_1 = A_1 = 0.65$.
- Walling parameters: material – cellular polycarbonate with walling heat transfer resistance $R_{wall} = 0.45$ m²·K/W; absorption coefficient $A_2 = 0.94$ (reflection coefficient $R_2 = 0.06$); thermal radiation coefficient (emissivity factor) $\varepsilon_2 = A_2 = 0.94$.
- Design parameters of the internal air (Table 1): temperature $t_{in.air} = 22$ °C; relative humidity $\varphi_{in.air} = 60$ %.

6. Design parameters of the outdoor air for the climatic conditions of the city of Vologda (Russia): temperature $t_{out.air} = -32$ °C; relative humidity $\varphi_{out.air} = 85$ %.

7. Ventilation parameters: natural ventilation; design height of the ventilation system $\Delta h = 0.45$ m.

8. Irrigation parameters: soil irrigation coefficient $k_{irr} = 1$ (the whole soil surface in the greenhouse is irrigated).

The calculation of the combined heating system of the industrial greenhouse "Fermer 7.5" (Fig. 2) has been performed in the mathematical editor "Mathcad".

Further to the program calculation of the combined heating system of the industrial greenhouse "Fermer 7.5" the following results were obtained:

1. Temperature of the greenhouse walling internal surface $t_{wall} \approx 22$ °C.

2. The required power of infrared radiation $Q_{emit} \approx 44.2$ kW (thermal density $q_{emit} \approx 705.8$ W/m²) and convective space heating $Q_{heat} \approx 22.2$ kW (specific convective heat $q_{heat} \approx 121.1$ W/m³). If we compare the thermal density found $q_{emit} \approx 705.8$ W/m² with the results of other researchers, it is comparable to the specific installed heat power of infrared emitters 706 W/m², intended for heating plants in greenhouses [22]. The total heat power of the winter greenhouse combined heating system is $Q_{tot} \approx 66.4$ kW.

3. Heat loss: through the greenhouse walling $Q_{wall} \approx 14.7$ kW; with the ventilation air going from the greenhouse into the environment, $Q_{vent} \approx 49.8$ kW (with the flow of dry air equal to $G_{air} \approx 2264$ kg/h); into the soil $Q_{soil} \approx 1.82$ kW.

4. Heat loss from heat exchange by radiation between the greenhouse walling internal surface and the soil surface $Q_{rad} \approx 0.46$ kW (in this case $t_{wall} > t_{surf}$, °C).

5. Heat loss from convective heat transfer between the indoor air and the soil surface in the greenhouse $Q_{conv1} \approx 0.30$ kW (provided that $t_{in.air} > t_{surf}$, °C); between the indoor air and the greenhouse walling internal surface is almost absent, i.e. $Q_{conv2} \approx 0$.

6. Heat loss caused by the moisture evaporation process from the soil surface in the greenhouse amounted to $Q_{evap} \approx 27.9$ kW.

7. The required water flow rate for watering the soil $G_{wat} \approx 41.0$ kg/h.

Fig. 3 shows the dependence of the design heat power of the winter greenhouse combined heating system (Fig. 2) on the outside air temperature $t_{out.air}$, °C, during the heating period.

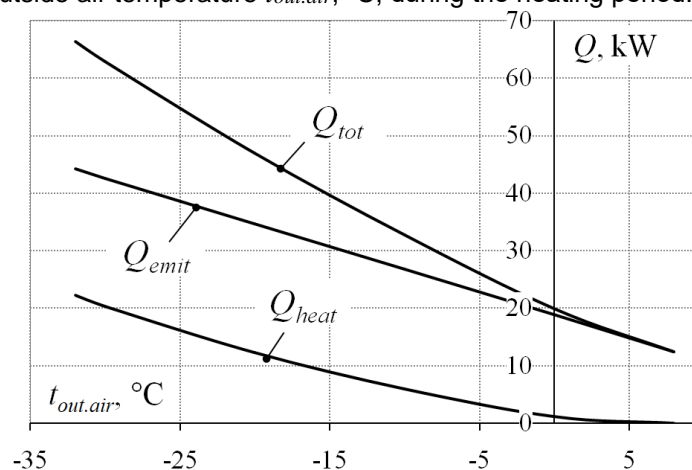


Figure 3. Heating system capacity $Q = Q(t_{out.air})$.

As is clear from Fig. 3, the increase in the outside air temperature $t_{out.air}$, °C, leads to the decrease in the total heat power of the combined heating system Q_{tot} , kW. This is due to the fact that the increase in temperature $t_{out.air}$ naturally results in heat loss reduction through the greenhouse walling Q_{wall} , for air exchange Q_{vent} and into the soil Q_{soil} . According to the greenhouse heat balance equation (1), the design heat power of the heating system should be reduced.

The relationship between the design heat power of the winter greenhouse combined heating system and the walling thermal resistance R_t , m²·K/W, is shown in Fig. 4.

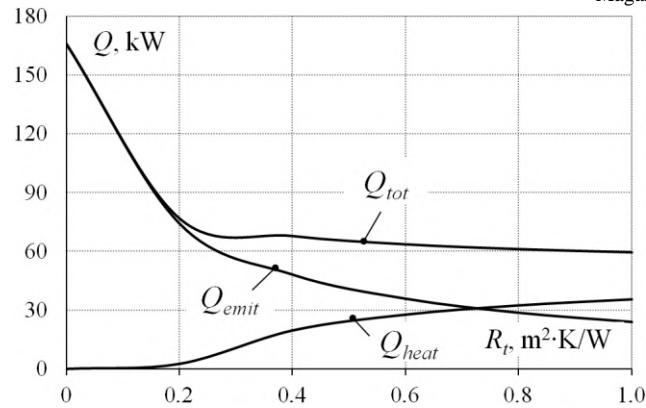


Figure 4. Heating system capacity of $Q = Q(R_t)$ type.

The walling thermal resistance R_t , $\text{m}^2\cdot\text{K}/\text{W}$, plays an important role in creating the required microclimate in the winter greenhouse. The use of ultra-thin translucent covering materials in the cold season, especially in the northern regions of the country with severe climate, is impractical. The greenhouse walling is one of the main problems in the cultivation facilities construction from the point of view of energy saving, as it should simultaneously effectively transmit sunlight (have a high light transmittance coefficient) and perform heat shielding functions. Even modern materials, such as cellular polycarbonate with closed cellular structure (honeycomb), have relatively low thermal insulation qualities (for example, at a significant thickness of the cellular polycarbonate sheet $\delta_{wall} = 32$ mm the R_t value does not exceed 0.83 $\text{m}^2\cdot\text{K}/\text{W}$). In accordance with Fig. 4, the increase in the thermal resistance R_t will naturally lead to a decrease in the design heat power of the heating system. It is worth noting that the total heat flux Q_{tot} , kW, decreases less intensively at $R_t > 0$ values, which are usually found in practical work. This is due to the fact that at the design temperature of the outside air $t_{out.air} = -32$ °C, the main part of the heat is used for ventilation in order to provide the necessary air exchange indoors. In addition, there is a gradual redistribution of the heat load for heating needs: in order to obtain the total heat power Q_{tot} while reducing the radiant component Q_{emit} , there is a natural increase in convective heat flux Q_{heat} .

The heat and mass balances of the soil, and therefore the greenhouse as a whole while heated are affected by the ability of the soil surface to absorb (or reflect) thermal energy. Fig. 5 shows the relationship between the heat power of the winter greenhouse combined heating system and the absorption coefficient of the soil surface A , %.

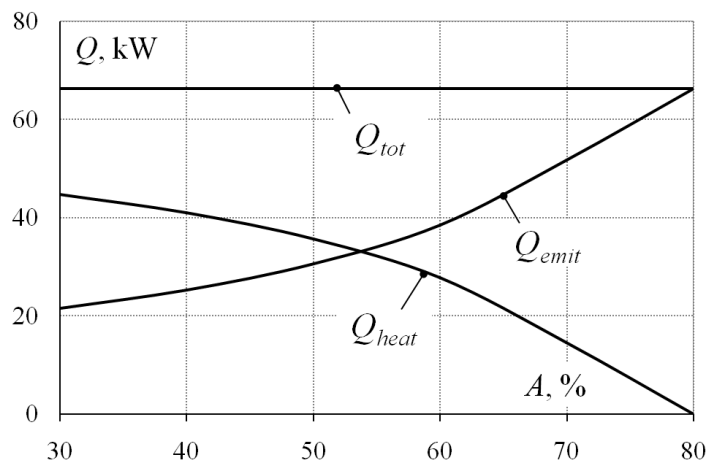


Figure 5. Heating system capacity of $Q = Q(A)$ type.

The total heat power of the winter greenhouse combined heating system Q_{tot} , kW, does not depend on the absorption capacity of the soil surface A , %. As it is known, heating is intended to compensate for heat losses into the environment in order to maintain a given microclimate indoors (Table 1). Heat fluxes Q_{wall} , kW, Q_{vent} and Q_{soil} do not depend on the absorption coefficient A and their values remain constant in this case. Then according to the equation (1), the design heat power Q_{tot} must also be a constant value. In order to maintain the required temperature of the indoor air and soil, the heat power Q_{emit} , according to the formula (6), should increase together with the absorption coefficient A rise. At the constant total heat power of the

heating system Q_{tot} , the increase of radiant component Q_{emit} will naturally lead to a decrease in the heat power of convective heating Q_{heat} .

4. Conclusions

1. There has been developed a calculation method of the winter greenhouse combined heating system which includes both overhead infrared radiators for heating the soil surface, and convective heaters for heating the indoor air.

2. When using radiant heating of the winter greenhouse, the following effects on the indoor thermal conditions have been factored in: the effect of infrared radiation repeated reflections and the walling self-radiation.

3. The equations set of heat and mass fluxes reflects the relation between evaporative processes on the soil surface and their influence on the indoor thermal processes.

4. The calculation method has been tested using a modern industrial greenhouse "Fermer 7.5" taking into account the initial data for a given region of construction.

5. It has been established that at low outdoor temperatures in case of indoor air ventilation heat consumption for heating needs is rather significant (≈ 66.4 kW). The heat load ratio of radiant heating to convective heating stands approximately at two to one.

6. The obtained change patterns of the heat power of the winter greenhouse combined heating system depending on a number of key factors allow to estimate the feasibility of using this heating method for specified climatic conditions. In addition, based on the constructed patterns it is possible to create an engineering calculation method of the combined heating system, as the program calculation requires a certain amount of time and the appropriate skill level of a technician. This method may include a graph for finding the base value of the heating system capacity, as well as a number of auxiliary patterns to determine the adjusting coefficients that take into account various factors.

7. Considering that the heat losses by ventilation turned out to be significant (75 % of the total heat losses), the authors of the work are planning to further research a possibility of preliminary heating the outside air up to the design temperature for the indoor air exchange needs.

References

- Shvedkoj, D.A., Barabanov, V.G. Using sensor of heat losses in the system of automatic support of temperature in the thermal room. *Izvestiya Volgogradskogo gosudarstvennogo tekhnicheskogo universiteta*. 2019. No. 1(224). Pp. 80–82. (rus)
- Kavga, A., Angastiniotis, N., Trypanagnostopoulos, G., Pantelakis, S. Regulated transparent insulation for greenhouse covers through the use of tailor-made bimodal nanoparticle formations. *Acta Horti*. 2017. No. 1170. Pp. 321–328. DOI: 10.17660/ActaHorti.2017.1170.39
- Kavga, A., Souliotis, M., Koumoulose, E.P., Fokaides, P.A., Charitidis, C.A. Environmental and nanomechanical testing of an alternative polymer nanocomposite greenhouse covering material. *Solar energy*. 2018. Vol. 159. Pp. 1–9. DOI: 10.1016/j.solener.2017.10.073
- Baxevanou, C., Fidaros, D., Bartzanasa, Th., Constantinos, K. Yearly numerical evaluation of greenhouse cover materials. *Computers and electronics in agriculture*. 2018. Vol. 149. Pp. 54–70. DOI: 10.1016/j.compag.2017.12.006
- Choab, N., Allouhi, A., Maakoul, A.E., Kousksou, T., Saadeddine S., Jamil, Ab. Review on greenhouse microclimate and application: Design parameters, thermal modeling and simulation, climate controlling technologies. *Solar Energy*. 2019. Vol. 191. Pp. 109–137. DOI: 10.1016/j.solener.2019.08.042
- Trypanagnostopoulos, G., Kavga, A., Souliotis, M., Tripanagnostopoulos, Y. Greenhouse performance results for roof installed photovoltaics. *Renewable Energy*. Vol. 111. Pp. 724–731. DOI: 10.1016/j.renene.2017.04.066
- Bargach, M.N., Dahman, A.S., Boukallouch, M.A. Heating system using flat plate collectors to improve the inside greenhouse microclimate in Morocco. *Renewable energy*. 1999. No. 3. Vol. 18. Pp. 367–381. DOI: 10.1016/S0960-1481(98)00803-9
- Sonneveld, P.J., Swinkels, G.L.A.M., Bot, G.P.A., Flamand, G. Feasibility study for combining cooling and high grade energy production in a solar greenhouse. *Biosystems engineering*. 2010. No. 1. Vol. 105. Pp. 51–58. DOI: 10.1016/j.biosystemseng.2009.09.012
- Esmaeli, H., Roshandel, R. Optimal design for solar greenhouses based on climate conditions. *Renewable energy*. 2020. No. 3. Vol. 145. Pp. 1255–1265. DOI: 10.1016/j.renene.2019.06.090
- Tong, Y., Nishioka, N., Ohyama, K., Kozai, T. Greenhouse heating using heat pumps with a high coefficient of performance (COP). *Biosystems engineering*. 2010. No. 4. Vol. 106. Pp. 405–411. DOI: 10.1016/j.biosystemseng.2010.05.003
- Okushima, L., Mears, D.R., Sase, S., Takakura, T., Moriyama, H., Furuno, Sh., Ishii, M. Capacities for heat pump cooling systems for greenhouses in Japan. *Journal of the Society of Agricultural Structures*. 2014. No.2. Vol.45.
- Shatalov, I.K., Shatalova, I.I. The effectiveness of innovative technologies for energy supply of greenhouses. *Vestnik Rossijskogo universiteta druzhby narodov. Seriya: inzhenernye issledovaniya*. 2017. No. 2. Vol. 18. Pp. 275–285. DOI: 10.22363/2312-8143-2017-18-2-275-285. (rus)
- D'Arpa, St., Colangelo, G., Starace, G., Petrosillo, I., Bruno, D.E., Uricchio, V., Zurlini, G. Heating requirements in greenhouse farming in southern Italy: evaluation of ground-source heat pump utilization compared to traditional heating systems. *Energy Efficiency*. No. 5. Vol. 9. Pp. 1065–1085. DOI: 10.1007/s12053-015-9410-y
- Karytsas, C., Mendrinou, D., Goldbrunner, J. Low enthalpy geothermal energy utilisation schemes for greenhouse and district heating at Traianoupolis Evros, Greece. *Geothermics*. 2003. No. 1. Vol. 32. Pp. 69–78. DOI: 10.1016/S0375-6505(02)00051-2

15. Bošnjaković, Ml. Lacković, I., Grdić, I. The greenhouses soil heating by geothermal energy. 5th International Scientific and Expert Conference of The TEAM Society (TEAM 2013). 2013. Vol. 5. Pp. 138–141.
16. Zui, V. Geothermal resources of Belarus and their utilization. Monitoring. Nauka i tehnologij. 2017. No. 3(32). Pp. 30–36.
17. Sethia, V.P., Sharma, S.K. Survey and evaluation of heating technologies for worldwide agricultural greenhouse applications. Solar Energy. 2008. No. 9. Vol. 82. Pp. 832–859. DOI: 10.1016/j.solener.2007.03.004
18. Kavga, A. Karanastasi, E., Konstas, I. Panidis, Th. Performance of an infrared heating system in a production greenhouse. IFAC Proceedings Volumes. 2013. No. 18. Vol. 46. Pp. 235–240. DOI: 10.3182/20130828-2-SF-3019.00017
19. Meyer, G.E., Fletcher, M.R., Fitzgerald, J.B. Calibration and use of a pyroelectric thermal camera and imaging system for greenhouse infrared heating evaluation. Computers and electronics in agriculture. 1994. No. 3. Vol. 10. Pp. 215–227. DOI: 10.1016/0168-1699(94)90042-6
20. Pavlov, M., Lukin, S., Derevianko, O. Modeling of greenhouse radiant heating. MATEC Web of Conferences. 2018. Vol. 193. DOI: 10.1051/mateconf/2018193030
21. Gorshkov, A.S., Vatin, N.I., Rymkevich, P.P., Kydrevich, O.O. Payback period of investments in energy saving. Magazine of Civil Engineering. 2018. No. 2(78). Pp. 65–75. DOI: 10.18720/MCE.78.5
22. Dolgikh, P.P., Samoilov, M.V. Obluchenie i obogrev rastenij v teplicah [Irradiation and heating plants in greenhouses]. Vestnik NGIEI. 2016. No. 4 (59). Pp. 71–86. (rus)

Contacts:

Mikhail Pavlov, pavlov_kaftgv@mail.ru

Denis Karpov, karpov_denis_85@mail.ru

Anton Sinitsyn, patinfo@mail.ru

Alexander Gudkov, agud@list.ru

© Pavlov, M.V., Karpov, D.F., Sinitsyn, A.A., Gudkov, A.G., 2020



ПОЛИТЕХ
Санкт-Петербургский
политехнический университет
Петра Великого

Инженерно-строительный институт
Центр дополнительных профессиональных программ

195251, г. Санкт-Петербург, Политехническая ул., 29,
тел/факс: 552-94-60, www.stroikursi.spbstu.ru,
stroikursi@mail.ru

Приглашает специалистов проектных и строительных организаций,
не имеющих базового профильного высшего образования
на курсы профессиональной переподготовки (от 500 часов)
по направлению «Строительство» по программам:

П-01 «Промышленное и гражданское строительство»

Программа включает учебные разделы:

- Основы строительного дела
- Инженерное оборудование зданий и сооружений
- Технология и контроль качества строительства
- Основы проектирования зданий и сооружений
- Автоматизация проектных работ с использованием AutoCAD
- Автоматизация сметного дела в строительстве
- Управление строительной организацией
- Управление инвестиционно-строительными проектами. Выполнение функций технического заказчика

П-02 «Экономика и управление в строительстве»

Программа включает учебные разделы:

- Основы строительного дела
- Инженерное оборудование зданий и сооружений
- Технология и контроль качества строительства
- Управление инвестиционно-строительными проектами. Выполнение функций технического заказчика и генерального подрядчика
- Управление строительной организацией
- Экономика и ценообразование в строительстве
- Управление строительной организацией
- Организация, управление и планирование в строительстве
- Автоматизация сметного дела в строительстве

П-03 «Инженерные системы зданий и сооружений»

Программа включает учебные разделы:

- Основы механики жидкости и газа
- Инженерное оборудование зданий и сооружений
- Проектирование, монтаж и эксплуатация систем вентиляции и кондиционирования
- Проектирование, монтаж и эксплуатация систем отопления и теплоснабжения
- Проектирование, монтаж и эксплуатация систем водоснабжения и водоотведения
- Автоматизация проектных работ с использованием AutoCAD
- Электроснабжение и электрооборудование объектов

П-04 «Проектирование и конструирование зданий и сооружений»

Программа включает учебные разделы:

- Основы сопротивления материалов и механики стержневых систем
- Проектирование и расчет оснований и фундаментов зданий и сооружений
- Проектирование и расчет железобетонных конструкций
- Проектирование и расчет металлических конструкций
- Проектирование зданий и сооружений с использованием AutoCAD
- Расчет строительных конструкций с использованием SCAD Office

П-05 «Контроль качества строительства»

Программа включает учебные разделы:

- Основы строительного дела
- Инженерное оборудование зданий и сооружений
- Технология и контроль качества строительства
- Проектирование и расчет железобетонных конструкций
- Проектирование и расчет металлических конструкций
- Обследование строительных конструкций зданий и сооружений
- Выполнение функций технического заказчика и генерального подрядчика

По окончании курса слушателю выдается диплом о профессиональной переподготовке
установленного образца, дающий право на ведение профессиональной деятельности

